



Grant Agreement No.: 226479

SafeLand

Living with landslide risk in Europe: Assessment, effects of global change, and risk management strategies

7th Framework Programme
Cooperation Theme 6 Environment (including climate change)
Sub-Activity 6.1.3 Natural Hazards

Deliverable D1.7

Landslide runout: Review of analytical/empirical models for subaerial slides, submarine slides and snow avalanche. Numerical modelling. Software tools, material models, validation and benchmarking for selected case studies

Including:

Appendix I: Overview of run-out models for landslide hazard and risk assessment

Appendix II Landslide runout: Guidelines for using a simple propagation code

Work Package 1.5 Runout Models

Deliverable/Work Package Leader: FUNAB

Revision: 02

April 2012

Rev.	Deliverable Responsible	Controlled by	Date
0	Manuel Pastor	Giovanni Crosta	22 Feb 2010
1	Manuel Pastor	Giovanni Crosta	24 April 2010
2	Manuel Pastor, Byron Quan Luna	Dieter Issler	30 April 2012

SUMMARY

The modelling of rapid catastrophic landslides is of paramount importance for risk management in populated areas. It is important to produce risks maps leading to urban planning legislation and mitigation measures. To attain such a goal and to assess the effects of mitigation measures, data provided by experience and modelling are necessary. This work package WP 1.5 and this deliverable D 1.7 aims to present models to describe the physical processes involved in landslide propagation, especially in the case of rapid landslides. The results will be used to do complete hazard and risk zonation. The tools allow predicting the velocity and thickness of landslides, as well as the running up along valley flanks and obstacles of different shape and position.

We describe here (i) a set of hierarchically structured mathematical models describing the basic phenomena taking part in propagation phenomena, (ii) rheological models describing the behaviour of fluidized soils, (iii) numerical models for propagation, and (iv) applications.

Note about contributors

The following organisations contributed to the work described in this deliverable:

Lead partner responsible for the deliverable:

FUNAB

Fundación Agustín de Betancourt ETS de Ingenieros de Caminos
Universidad Politécnica de Madrid (Spain)

Deliverable prepared by:

- (i) FUNAB (M.Pastor, T.Blanc, D.Manzanal, V.Drempetic, M.J.Pastor
And M. Sánchez)
- (ii) UNIMIB (G.Crosta, S.Imposimato, D.Roddeman)
- (iii) BRGM (E.Foester, H.Kobayashi, M.Delattre)
- (iv) ICG (D.Issler)

Partner responsible for quality control:

UNIMIB

Deliverable reviewed by:
Giovanni Crosta

Other contributors:

UNISA (L.Cascini, G.Sorbino, S.Cuomo)
UPC (E.Alonso, N.Pinyol)

CONTENTS

1	Introduction	5
1.1	references	7
2	Mathematical model	9
2.1	Introduction.....	9
2.2	A Hierarchical set of models for the coupled behaviour of geomaterials	10
2.2.1	General Model.....	10
2.2.2	A w-u-pw model for the dynamic behaviour of non saturated soils with zero air pressure	12
2.2.3	A u- pw model for unsaturated and saturated soils	14
2.2.4	Remarks	16
2.3	Propagation-consolidation model for shallow landslides	17
2.4	Depth integrated models	20
2.4.1	Introduction.....	20
2.4.2	Balance of mass	22
2.4.3	Balance of linear momentum	22
2.4.4	A note on normal accelerations and stresses at the basal surface	24
2.4.5	Consolidation equation	27
2.4.6	Quasi Lagrangian formulation	31
2.5	References.....	32
3	Behaviour of fluidized geomaterials: Rheological and constitutive modelling.....	35
3.1	Introduction.....	35
3.2	mechanisms of fluidization of geomaterials	35
3.3	Rheometers and the behaviour of fluidized geomaterials.....	35
3.4	Rheological models.....	40
3.4.1	General framework.....	40
3.4.2	Newtonian fluids	45
3.4.3	Bagnold fluids	46
3.4.4	Bingham fluids	48
3.4.5	Generalized viscoplastic model of Chen and Ling	51
3.5	Depth integrated Rheological Models	55
3.5.1	Introduction.....	55
3.5.2	The Infinite Landslide model.....	57
3.5.3	Newtonian fluids	60
3.5.4	Bingham fluids	62
3.5.5	Bagnold Fluids	72
3.5.6	Generalized Viscoplastic Flow Model of Chen and Lin.....	79
3.5.7	The Herschel-Bulkley fluid.....	93
3.5.8	The frictional fluid	94
3.6	References.....	96

4	Numerical models for landslide run out	99
4.1	Introduction.....	99
4.2	Meshless technique: the sph method. Application to depth integrated models.	101
4.2.1	Introduction.....	101
4.2.2	Fundamentals: integral approximations.....	102
4.2.3	SPH discretization in continuum mechanics.....	107
4.2.4	SPH discretization of depth integrated equations	115
4.2.5	Examples and applications.....	121
4.2.6	References.....	132
4.3	Meshless technique: the EFGM method to model run out by integrated models.....	136
4.3.1	Introduction.....	136
4.3.2	Description of the EFG method.....	136
4.3.3	EFGM discretization of depth integrated equations.....	144
4.3.4	References.....	146
4.4	Finite element modelling of run out of fast landslides	146
4.4.1	Introduction.....	147
4.4.2	Model equation: the 1D convective transport.....	149
4.4.3	Finite elements that work: the Taylor Galerkin scheme.	150
4.4.4	Examples and applications.....	159
4.4.5	References.....	170
4.5	Granular flows on erodible and non erodible surfaces	171
4.5.1	Introduction.....	172
4.5.2	Granular Step Collapse	178
4.5.3	Collapse of a granular step on erodible layer.....	198
4.5.4	Arvel case study.....	216
4.5.5	Discussion and conclusions	228
4.5.6	References.....	234
4.6	CaLIBRATION OF RHEOLOGICAL PARAMETERS FOR VOLCANIC AND GLACIAL ROCK AVALANCHES	240
4.6.1	Introduction.....	240
4.6.2	Volcanic debris avalanches.....	242
4.6.3	Glacial Rock avalanches	251
4.6.4	DISCUSSIONS AND CONCLUSIONS	259
4.6.5	REFERENCES.....	261

Appendix I: Overview of run-out models for landslide hazard and risk assessment

Appendix II Landslide runout: Guidelines for using a simple propagation code

1 INTRODUCTION

Fast landslides, avalanches, lahars and debris flows are geophysical, gravity driven flows causing extensive loss of human life and economic damage throughout the world every year. They involve phase changes from solid to fluid at the triggering stage and from fluid to solid when the motion stops. The interaction between solid grains and pore water is of paramount importance. Indeed, the mechanical behaviour of soil-water mixtures does not depend on total stresses, but on effective stresses, which are obtained by subtracting the pore pressure hydrostatic tensor from the total stress tensor.

Slope failures can be triggered by different causes: (i) changes of effective stresses induced by changes of load (earthquakes), pore pressures (rain), or changes of geometry (erosion), and (ii) material degradation due to weathering. There exist several alternative classifications of landslides according to their shape, morphology, velocity of propagation, etc. Two interesting types are slides and flows. In the former, deformation is concentrated in a narrow zone, the failure surface. Kinematics can be approximately described as the movement of a rigid mass along the failure surface. This mechanism of failure is associated to concepts such as material softening, strain localization and shear bands. Flows are usually produced in loose metastable deposits, where failure is of diffuse type. The tendency of the soil to compact results on the generation of high pore pressures and a decrease of the effective confining pressure which causes in some cases liquefaction. As the fluidized material propagates, phenomena of dissipation of pore pressures and dilatancy take place.

Geotechnical engineers are concerned with the analysis of geostructures under design loads and the prediction of the conditions under which failure will take place, in order to assess (i) how far are design conditions from failure (safety factor), and (ii) the failure mechanism. Knowledge of the latter allows the reinforcement of weak zones. Because of this focus, post failure phenomena are seldom studied. However, there are cases where the analysis of post failure phenomena is of paramount importance, such as fast catastrophic landslides traveling long distances at high speeds which present a high destruction power.

The study of failure conditions has attracted the attention of researchers since the early works of Coulomb (1773). Historically, three main lines of dealing with the problem and obtaining solutions were followed: (i) The slip line method, (ii) Limit theorems for plastic collapse, and (iii) limit equilibrium methods. All of them provide information on failure loads and mechanisms, but not on post failure phenomena, and because of both the type of material behavior assumed and the kinematics of failure, cannot be applied in all cases, as explained below.

Both the limit theorems of plastic collapse and the limit equilibrium methods are based on two assumptions (i) failure conditions takes place at the strength envelope, and (ii) there exists a surface where failure takes place. This corresponds to a type of failure which is referred to as “localized”. These conditions are not always satisfied, as in the case loose, collapsible materials, where instability and failure are observed at effective stresses below Mohr Coulomb strength envelope, and where failure is observed to occur in a much larger volume of soil. This type of failure has been described as “diffuse”.

Localized failure is found in overconsolidated materials presenting softening, while the diffuse mode is typical of soils having a low relative density and tending to compact when sheared. Failure takes place not in a narrow limited zone, but in a much larger mass of soil. Pore pressures developed may cause liquefaction of the soil or conditions close to it. This mechanism is believed to play an important role in landslides of the flow type.

Localized failure is characterized by a concentration of strain in very narrow and limited zones, where the phenomenon is idealized assuming there exist a discontinuity in the strain or its rate (weak discontinuity). In the case of soils, the most frequent case is that of discontinuities in the shear strain, which are referred to as shear bands. They can evolve into discontinuities in the displacement and velocity fields (strong discontinuity). Failure mechanism is interpreted as a relative sliding of two regions where deformations are small.

Diffuse failure is related to instabilities of material behavior in loose soils. The study of these instabilities is still a young area of research. It is worth mentioning the work of Darve (1995) and Nova (1994) on constitutive instabilities and di Prisco et al. (1995) on the stability of shallow submerged slopes where liquefaction induced by sea waves can be triggered, and Darve and Laouafa (2000, 2001) and Fernández Merodo et al (2004) on diffuse mechanisms of failure in catastrophic landslides. An updated account of work done in this area can be found in Nicot and Wan (2008).

In the case of landslides, there exist several alternative classifications. The main types of landslides, are the following: (a) Fall, (b) Topple, (c) Slides, (d) Lateral spreading, (e) Flows, and (f) complex movements. Of course, this is a simplification of the complex pattern which is often observed in reality. For instance, we could mention the case of rockfalls where the falling blocks can break into smaller ones due to fragmentation. What it is interesting is that slides have a failure mechanism of localized type while flows are related to diffuse modes of failure. In the case of slides, a mass of soil moves along a surface below which material deforms much less. Depending on the shape of the sliding surface, slides are said to be translational or rotational. Localized failure is typical of overconsolidated materials presenting material softening.

Concerning modeling, it is important to note that even if simplified methods are still in use to provide a first estimation of the failure conditions, the most widespread approach is based today on mathematical, constitutive, and numerical modeling. In the case of diffuse failure, the key ingredient is constitutive modeling.

Once failure has been triggered, material can flow in a fluid like manner. Flowslides are a particular case of fast propagating mass movements, characterized by an important coupling between the solid skeleton and the pore fluids resulting on high pore pressures on the basal surface. These pore pressures generated during the initiation phase dissipate during propagation, being the consolidation and the propagation times of the same order of magnitude. It is possible therefore to have flowslides in a dry collapsible material, as it will be shown later. This is an important difference with other phenomena. In the case of dry granular avalanches, the permeability can be large enough as to dissipate the generated pore pressures in the body of the avalanche. Falling blocks disaggregate and evolve into granular fluids. The process of grain breakage provides energy to the system, increasing its mobility which results

on apparent friction angles smaller than the basal friction angle. In the case of mudflows, very fluid mixtures of fine grained soils such as clays and water, the material is often studied as a monophasic cohesive-frictional fluid. Debris flows are mixtures of water and soil, originated by rain and eroded soil –or shallow landslides-. In some cases, large blocks entrained in the flow can hit structures causing their collapse. Lahars are special cases of debris flows in loose volcanic soils.

Modelling of these phenomena present important difficulties, and in the most general case, the analysis has to be based on a thermodynamically consistent formulation of mixture theory (Schneider and Hutter 2009). This is the first difficulty encountered in the analysis, and in practical cases depth integrated models (Savage and Hutter, 1991) are used as they provide a good combination of accuracy and computational cost. It interesting to notice that while coupling of solids and pore fluids has been known in Geomechanics since the early work of Biot (1955) and considerable progress has been done later (Zienkiewicz and Shiomi 1984, Zienkiewicz et al 1980, 1999, Coussy 1995, de Boer 2000) it has not been applied to fast landslides until recently (Hutchinson 1986, Iverson and LaHusen 1989, Iverson 1993, Iverson and Denlinger 2001, Pastor et al 2002, 2009)

The second difficulty concerns rheological modeling, which are still based on simple shear or rheometrical flows experiments carried out in laboratories. Due to the limitation imposed by their size, it has not been possible so far to perform tests with real materials found in landslides.

Concerning numerical modeling, fully coupled models are still not available. The numerical models used consider the mixture as a single phase. They can be either eulerian, and then the free surface has to be tracked using special techniques such as Volume of Fluid (VOF) or Level Set (Quecedo et al. 2004) with a high computational cost, or lagrangian, where the meshless methods such as the SPH are a very interesting alternative.

Finally, one important limitation is the lack of a constitutive model able to describe the behaviour of the material in the whole range, from solid to fluid. In traditional soil mechanics, most of today's used constitutive models are elastoplastic. There abound models able to reproduce most salient aspects of cohesive and frictional soils, including liquefaction. The transition from a soil at Critical State conditions to a fluidized mixture is an area where much research is still needed.

1.1 REFERENCES

M.A.Biot, (1955). Theory of elasticity and consolidation for a porous anisotropic solid. **Journal of Applied Physics** 26 (1955) 182 – 185

Coulomb, C.A., **Mem.Math. et Phys.** 7, 343, (1773)

Coussy, O. *Mechanics of Porous Media*. John Wiley and Sons, Chichester (1995).

Darve, F., Liquefaction phenomenon of granular materials and constitutive instability, **Int. J. Eng. Comp.** 7, pp 5-28 (1995)

de Boer, R. *Theory of porous media*. Springer-Verlag, Berlin (2000)

-
- Di Prisco, C., Mantiotti, R. and Nova, R., Theoretical investigation of undrained stability of shallow submerged slopes, **Geotechnique** 45, pp 479-496, 1995
- Darve, F., and Laouafa, F., Instabilities in granular materials and application to landslides, *Mech. Coh.-Frict. Mater.* 5 (8), pp. 627-652 (2000)
- Fernández Merodo, J.A., Pastor, M., Mira, P., Tonni, L., Herreros, I., González, E., and Tamagnini, R., “Modelling of diffuse failure mechanisms of catastrophic landslides ” , **Comp.Methods Appl. Mech.Engrg.**, 193, 2911-2939 (2004)
- Hutchinson, J.N. ,A sliding-consolidation model for flow slides, *Can.Geotech.J.*, 23 115-126 (1986)
- Iverson, R.M. “Differential equations governing slip-induced pore pressure fluctuations in a water-saturated granular medium”, **Mathematical Geology** 25 (8), 1027–1048 (1993)
- Iverson, R.M. and LaHusen, R.G. “Dynamic pore-pressure fluctuations in rapidly shearing granular materials”, *Science* 246, 796–799 (1989)
- Nicot, F. and Wan, R. (Eds) *Micromécanique de la rupture dans les milieux granulaires*, Hermes Science Lavoisier 2008
- Nova, R. “Controllability of the incremental response of soil specimens subjected to arbitrary loading programmes”, **J.Mech.Behav.Mater.** 5, pp. 193-201 (1994)
- M.Pastor, M.Qucedo, J.A.Fernández Merodo, I.Herreros, E. González and P.Mira, Modelling Tailing Dams and mine waste dumps failures. **Geotechnique**, Vol.LII, (2002) N.8, 579 – 592
- M.Pastor, T.Blanc, M.J.Pastor, A depth integrated viscoplastic model for dilatant saturated cohesive-frictional fluidized mixtures: application to fast catastrophic landslides, **J. Non-Newtonian Fluid Mech.** 158 (2009) 142-153
- Pastor M., Haddad B., Sorbino G., Cuomo S., Drempetic, V., “A depth integrated coupled SPH model for flow-like landslides and related phenomena” , **Int. J. Num. Anal. Meth. Geomechanics** 33, 2, 143-172, 2009
- Qucedo, M. , Pastor, M. and Herreros, I., “Numerical modelling of impulse wave generated by fast landslides”, **Int. J. Num. Meth. Eng.**, 59: 1633-1656 (2004)
- Savage, S.B. and Hutter, K. “The dynamics of avalanches of granular materials from initiation to runout. Part I: Analysis”. **Acta Mechanica** 86 201 – 223 (1991)
- Schneider, L. and Hutter, K., *Solid-Fluid Mixtures of Frictional Materials in Geophysical Context based on a concise thermodynamic analysis*, *Advances in Geophysical and Environmental Mechanics and Mathematics Series*, Springer (2009, to appear)
- Zienkiewicz, O.C., and Shiomi, T., Dynamic behaviour of saturated porous media: The generalised Biot formulation and its numerical solution. **International Journal of Numerical and Analytical Methods in Geomechanics**, 8 71-96 (1984) .
- Zienkiewicz, O.C., Chang, C.T. and Bettess, P. (1980), Drained, undrained, consolidating dynamic behaviour assumptions in soils. **Geotechnique** 30, 385-395
- Zienkiewicz, O.C., Chan, A.H.C., Pastor, M., Shrefler, B.A., and Shiomi, T. (1999), **Computational Geomechanics**, J.Wiley and Sons

2 MATHEMATICAL MODEL

2.1 INTRODUCTION

Soils and rocks are geomaterials with voids which can be filled with water, air, and other fluids. They are, therefore, multiphase materials, exhibiting a mechanical behaviour governed by the coupling between all the phases. Pore pressures of fluids filling the voids play a paramount role in the behaviour of a soil structure, and indeed, their variations can induce failure. If we consider the soil as a mixture, we will have equations describing: (i) balance of mass for all phases, i.e., solid skeleton, water and air, in the case of non saturated soils (ii) balance of linear momentum for pore fluids and for the mixture, and (iii) constitutive equations. A crucial point is the choice between eulerian and lagrangian formulations. In soil mechanics, the approach followed most often is mixed, lagrangian for the skeleton and eulerian for the relative movement of the pore fluids relative to the soil skeleton. In many occasions, convective terms can be neglected.

The first mathematical model describing the coupling between solid and fluid phases was proposed by Biot (1941,1955) for linear elastic materials. This work was followed by further development at Swansea University, where Zienkiewicz and coworkers (1980, 1984, 1990a, 1990b, 2000) extended the theory to non-linear materials and large deformation problems. It is also worth mentioning the work of Lewis and Schrefler (1998), Coussy (1995) and de Boer (2000). It can be concluded that the geotechnical community have incorporated coupled formulations to describe the behaviour of foundations and geostructures. Indeed, analyses of earth dams, slope failures and landslide triggering mechanisms have been carried out using such techniques during last decades.

This theoretical framework has not been applied to model the propagation of landslides until recently. We can mention here the work of Hutchinson (1986), who proposed a sliding consolidation model to predict run out of landslides, Iverson and Denlinger (2001), and Pastor et al. (2002).

This Chapter is devoted to present different alternative models which can be used to describe the coupling between solid skeleton and pore fluids in geomaterials, both in solid and fluidized states. We have chosen an approach closer to mixture theories than to the more classical approach used in computational geotechnics, as it provides a more general description which can be used not only for the initiation of failure but also for propagation of catastrophic landslides.

The Chapter begins with a Section where we present those basic concepts and theorems of continuum mechanics which will be applied later. Next, a second Section is devoted to derive the general model, valid for multiphase mixtures of solid particles and pore fluids such as water, mud or air. From here, some simplifications can be made. If we assume that the velocity of the pore fluids relative to soil skeleton is small, we can derive models formulated in terms of velocities of soil skeleton and pressures of the pore fluids such as the u - p model of Biot-Zienkiewicz, cast in terms of velocities, or the v - p variation written in terms of velocities, which is more convenient for fluidized geomaterials.

In a large number of fast catastrophic landslides, the depth is small in comparison to the length or the width of the moving mass. It is possible, under certain assumptions, to integrate the balance equations in depth, arriving to depth integrated models. The Chapter will end with a Section devoted to these models, which provide an excellent combination of accuracy and computational effort.

2.2 A HIERARCHICAL SET OF MODELS FOR THE COUPLED BEHAVIOUR OF GEOMATERIALS

The purpose of this Section is to present in a unified manner the equations describing the coupling of fluid and solid phases in soils, both for triggering and run out phases. We will start by recalling the general equations which can be used in the most general case, where the relative motion of the fluid phases with respect to the solid particles is relevant.

2.2.1 General Model

The general model consists of the following equations:

(a) Balance of mass for the constituents and the mixture

$$\frac{D^{(\alpha)}}{Dt}(nS_{\alpha}\rho_{\alpha}) + nS_{\alpha}\rho_{\alpha}\operatorname{div}v_{\alpha} = 0 \quad (2.2.1a)$$

$$\frac{D^{(s)}}{Dt}[(1-n)\rho_s] + (1-n)\rho_s\operatorname{div}v_s = 0 \quad (2.2.1b)$$

$$\frac{D^{(s)}\rho}{Dt} + \rho\operatorname{div}v_s + \sum_{\alpha=1}^{N_{\alpha}}\operatorname{div}(\rho_{\alpha}w_{\alpha}) = 0 \quad (2.2.1c)$$

(b) Balance of linear momentum, equations (2.2.2.a) and (2.2.2.b) for the constituents and (2.2.2.c) for the mixture.

$$\rho_{\alpha}\frac{D^{(\alpha)}v_{\alpha}}{Dt} = \operatorname{div}\sigma_{\alpha} + \rho_{\alpha}b + R_{\alpha} \quad (2.2.2.a)$$

$$\rho_s\frac{D^{(s)}v_s}{Dt} = \operatorname{div}\sigma_s + \rho_s R_s \quad (2.2.2.b)$$

with

$$R_\alpha = -k_\alpha^{-1} w_\alpha = -k_\alpha^{-1} n S_\alpha (v_\alpha - v_s) \quad (2.2.2.c)$$

$$\rho \frac{D^{(s)} v_s}{Dt} + c.t.1 = \rho b + \text{div } \sigma + c.t.2 \quad (2.2.d)$$

where the correcting terms are given by:

$$c.t.1 = \sum_{\alpha=1}^{N_\alpha} n S_\alpha \rho_\alpha \left\{ \frac{D^{(s)}}{Dt} \left(\frac{w_\alpha}{n S_\alpha} \right) + \frac{w_\alpha}{n S_\alpha} \text{grad } v_s + \frac{w_\alpha}{n S_\alpha} \text{grad} \left(\frac{w_\alpha}{n S_\alpha} \right) \right\} \quad (2.2.2.e)$$

and

$$c.t.2 = \sigma_s \cdot \text{grad } n - \sum_{\alpha=1}^{N_\alpha} \sigma_\alpha \cdot \text{grad} (n S_\alpha) \quad (2.2.2.f)$$

These equations have to be complemented with suitable constitutive or rheological laws allowing determining the state of stress for all constituents.

Debris flows are mixtures of air, water and solid particles. We can assume that density of water remains constant, air pressure is zero (atmospheric), and write the balance equations as:

$$\begin{aligned} \frac{D^{(w)}}{Dt} (n S_w \rho_w) + n S_w \rho_w \text{div } v_w &= 0 \\ \frac{D^{(s)}}{Dt} [(1-n) \rho_s] + (1-n) \rho_s \text{div } v_s &= 0 \end{aligned} \quad (2.2.3)$$

$$\rho_s \frac{D^{(w)} v_w}{Dt} = -\text{grad } p_w + \rho_w b + R_w$$

$$\rho_s \frac{D^{(s)} v_s}{Dt} = \text{div } \sigma_s + \rho_s b + R_s$$

where the coupling terms are given by:

$$R_s = -\frac{n}{1-n} S_w k_w^{-1} w_w \quad (2.2.4)$$

$$R_w = -k_w^{-1} w_w$$

Concerning the stresses σ_s , they can be obtained or updated using a suitable constitutive equation. If the grains are in contact, we could use the relation between σ_s and the effective stress tensor:

$$\sigma' = (1-n)\{\sigma_s + \bar{p}I\} \quad (2.2.5)$$

An interesting limiting case is that of mudflows with high water contents and fine solid particles which are frequently considered as a fluid obeying a rheological law of Bingham type. The equations are in this case:

$$\frac{D^{(s)}\rho}{Dt} + \rho \operatorname{div} v_s = 0 \quad (2.2.6a)$$

as $\sum_{\alpha=1}^{N_a} \operatorname{div}(\rho_{\alpha} w_{\alpha})$ can be assumed to be zero, and

$$\rho_s \frac{D^{(s)}v_s}{Dt} = \rho b + \operatorname{div} \sigma \quad (2.2.6b)$$

where σ is obtained through the rheological law.

2.2.2 A w-u-pw model for the dynamic behaviour of non saturated soils with zero air pressure

The model presented in the preceding section can be used when the movement of all fluid and solid phases is relevant, which is the case of debris flows or mixtures of mobilized rock fragments and water where the permeability is high. Indeed, it is more convenient to think in terms of a mixture than of a solid skeleton with interstitial fluids filling its voids. In some occasions, the phenomenon can be described by the movement of a solid skeleton and the movement of the pore fluids relative to it. This is the case of most geotechnical problems.

In this case the equations can be cast in terms of the displacements or velocities of solid skeleton, the velocities of the pore water relative to the skeleton and the averaged pore pressure \bar{p} , defined as:

$$\bar{p} = S_a p_a + S_w p_w$$

If the air is at atmospheric pressure, the averaged pressure is

$$\bar{p} = S_w p_w$$

This model is referred to as $u - \bar{p} - w$. It was introduced by Zienkiewicz and Shiomi (1984) for the case of saturated soils. The case of non-saturated soils with air at atmospheric pressure

was proposed by Zienkiewicz et al (1990b). We will derive this model as a particular case of the general model proposed above. The basic equations are:

(a) Balance of mass for the pore water.

$$\begin{aligned} \operatorname{div}(w) + S_w \operatorname{div} v_s + \left\{ S_w^2 \frac{1-n}{K_s} + S_w \frac{n}{K_w} \right\} \frac{D^{(s)} p_w}{Dt} \\ + \left\{ C_s \left(1 + \frac{1-n}{n} S_w \frac{p_w}{K_w} \right) \right\} \frac{D^{(s)} p_w}{Dt} = 0 \end{aligned} \quad (2.2.7)$$

(b) Balance of linear momentum for the pore water.

$$\begin{aligned} \rho_w \frac{D^{(s)} v_s}{Dt} + \rho_w \left\{ \frac{D^{(s)}}{Dt} \left(\frac{w}{nS_w} \right) + \frac{w}{nS_w} \operatorname{grad} v_s + \frac{w_w}{nS_w} \operatorname{grad} \left(\frac{w_w}{nS_w} \right) \right\} \\ = -\operatorname{grad} p_w + \rho_w b + R_w \end{aligned} \quad (2.2.8)$$

where $R_w = -k_\alpha^{-1} w$

(c) Balance of linear momentum for the mixture,

$$\rho \frac{D^{(s)} v_s}{Dt} + c.t.1 = \rho b + \operatorname{div} \sigma + c.t.2 \quad (2.2.9)$$

where the correcting terms are given now by:

$$c.t.1 = nS_w \rho_w \left\{ \frac{D^{(s)}}{Dt} \left(\frac{w}{nS_w} \right) + \frac{w}{nS_w} \operatorname{grad} v_s + \frac{w}{nS_w} \operatorname{grad} \left(\frac{w}{nS_w} \right) \right\}$$

and

$$c.t.2 = \sigma_s \cdot \operatorname{grad} n - p_w \cdot \operatorname{grad} (nS_w)$$

In conclusion, the $v-p_w-w$ model for non saturated soils with air at atmospheric pressures consists of equations (4.5-4.7). A particular case of great interest is that of saturated soils, where the model reduces to:

$$\operatorname{div}(w) + \operatorname{div} v_s + \left\{ \frac{1-n}{K_s} + \frac{n}{K_w} \right\} \frac{D^{(s)} p_w}{Dt} = 0 \quad (2.2.10)$$

$$\rho_w \frac{D^{(s)}v_s}{Dt} + c.t. = -\text{grad } p_w + \rho_w b + R_w \quad (2.2.11)$$

where the correcting term is:

$$c.t. = \rho_w \left\{ \frac{D^{(s)}}{Dt} \left(\frac{w}{n} \right) + \frac{w}{n} \text{grad } v_s + \frac{w_w}{n} \text{grad} \left(\frac{w_w}{n} \right) \right\}$$

and

$$\rho_s \frac{D^{(s)}v_s}{Dt} + c.t.1 = \rho b + \text{div } \sigma + c.t.2$$

where the correcting terms are now given by:

$$c.t.1 = n \rho_w \left\{ \frac{D^{(s)}}{Dt} \left(\frac{w}{n} \right) + \frac{w}{n} \text{grad } v_s + \frac{w}{n} \text{grad} \left(\frac{w}{n} \right) \right\}$$

and

$$c.t.2 = \sigma_s \cdot \text{grad } n - p_w \cdot \text{grad}(n)$$

This model consists on the three equations of balance given above, plus a suitable constitutive or rheological law providing the stress tensor and a kinematical relation relating displacements or velocities to strain or rate of deformation tensors. The main variables are (i) the velocity of solid skeleton v_s , the Darcy velocity of the pore water w , and the pore pressure p_w .

Under certain assumptions, which were analyzed for soil mechanics problems by Zienkiewicz, Chang and Bettess (1980), it is possible to eliminate the Darcy velocity from the model. This is the most celebrated $u - p_w$ model of Zienkiewicz, which will be described next.

2.2.3 A $u - p_w$ model for unsaturated and saturated soils

If we assume that relative velocities and accelerations of fluids relative to solid skeleton are small, the model can be cast in terms of velocity of the solid skeleton and Darcy's velocities of pore fluids. We will consider first the balance of mass and linear momentum equations for the pore water, which will be written as:

$$\operatorname{div}(w) + S_w \operatorname{div} v_s + \frac{1}{Q^*} \frac{D^{(s)} p_w}{Dt} = 0 \quad (2.2.12)$$

where we have introduced

$$\frac{1}{Q^*} = \left\{ S_w^2 \frac{1-n}{K_s} + S_w \frac{n}{K_w} \right\} + \left\{ C_s \left(1 + \frac{1-n}{n} S_w \frac{p_w}{K_w} \right) \right\}$$

and

$$\begin{aligned} \rho_w \frac{D^{(s)} v_s}{Dt} + \rho_w \left\{ \frac{D^{(s)}}{Dt} \left(\frac{w}{nS_w} \right) + \frac{w}{nS_w} \operatorname{grad} v_s + \frac{w_w}{nS_w} \operatorname{grad} \left(\frac{w_w}{nS_w} \right) \right\} \\ = -\operatorname{grad} p_w + \rho_w b - k_\alpha^{-1} w \end{aligned} \quad (2.2.13)$$

From (4.6), we can obtain the Darcy velocity as:

$$\begin{aligned} w = k_w \{ -\operatorname{grad} p_w + \rho_w b \} - k_w \rho_w \frac{D^{(s)} v_s}{Dt} \\ - k_w \left\{ \rho_w \frac{D^{(s)}}{Dt} \left(\frac{w}{nS_w} \right) + \frac{\rho_w w}{nS_w} \operatorname{grad} v_s + \frac{\rho_w w}{nS_w} \operatorname{grad} \left(\frac{w}{nS_w} \right) \right\} \end{aligned}$$

We can see that the terms of the second row involve products of the Darcy velocity by the permeability. If this group of terms can be neglected, we can substitute the value of w :

$$w = k_w \{ -\operatorname{grad} p_w + \rho_w b \} - k_w \rho_w \frac{D^{(s)} v_s}{Dt} \quad (2.2.14)$$

in the balance equation (4.10):

$$\operatorname{div}(w) + S_w \operatorname{div} v_s + \frac{1}{Q^*} \frac{D^{(s)} p_w}{Dt} = 0$$

The result is:

$$-\operatorname{div}(k_w \operatorname{grad} p_w) + S_w \operatorname{div} v_s + \frac{1}{Q^*} \frac{D^{(s)} p_w}{Dt} + \operatorname{div}(\rho_w b) - \operatorname{div}(k_w \rho_w \frac{D^{(s)} v_s}{Dt}) = 0 \quad (2.2.15)$$

It is interesting to note that the divergence of the body forces is zero except in cases such as centrifuge testing machines, where the centripetal acceleration depends on the position. The last term is frequently omitted in the analysis, resulting on:

$$-\text{div}(k_w \text{grad } p_w) + S_w \text{div } v_s + \frac{1}{Q^*} \frac{D^{(s)} p_w}{Dt} = 0 \quad (2.2.16)$$

Concerning the balance of momentum for the mixture, equation (4.7) simplifies to:

$$\rho \frac{D^{(s)} v_s}{Dt} = \rho b + \text{div } \sigma \quad (2.2.17)$$

where the correcting terms have been neglected.

The $u - p_w$ model consists of equations (2.2.16) and (2.2.17), plus the constitutive and kinematical relations described above.

In the case of saturated materials, equation (2.2.16) simplifies to:

$$-\text{div}(k_w \text{grad } p_w) + \text{div } v_s + \frac{1}{Q} \frac{D^{(s)} p_w}{Dt} = 0 \quad (2.2.18)$$

with

$$\frac{1}{Q} = \frac{n}{K_w} + \frac{1-n}{K_s}$$

2.2.4 Remarks

An important case is that of dry soils where the time scale of air pore pressure dissipation is similar to that of propagation of the landslide. In this case, pore pressures of the pore air can play a paramount role, and in the limit it is possible to arrive at "dry liquefaction". The equations can be easily derived from those of (b), assuming there is only one fluid phase, i.e. the air, substituting now density, permeability and volumetric stiffness of the water by those of the air. So far, we have considered coupling between the soil grains and the pore pressures. There are two limit cases where the soil can be approximated as a single phase material:

(i) Flow of dry granular materials with high permeability. The permeability is high enough so that the consolidation time is much smaller than the time of propagation, the material behaves as "drained".

(ii) Flow of slurries with a high water content, where the time of dissipation is much higher than that of propagation. The behaviour can be assumed to be of undrained type. Material behaviour can be approximated using rheological models such as Bingham, etc.

In both cases, it is usually assumed that material density does not change. This approach can be justified in the case (i) by the existence of a "critical void ratio".

2.3 PROPAGATION-CONSOLIDATION MODEL FOR SHALLOW LANDSLIDES

So far we have described general models which can be applied to general problems in soil mechanics. The analysis of landslides, due to their shape and geometrical properties allow some interesting simplifications. First of all, we will arrive to “propagation-consolidation” models, where pore pressure dissipation takes place along the normal to the terrain surface, and next, we will describe depth integrated models, where the three dimensional problem is transformed into a two dimensional form. The starting point is the balance equations for a saturated soil obtained above:

$$\rho \frac{D^{(s)} v^s}{Dt} = \rho b + \text{div } \sigma$$

$$\text{div } (-k_w \text{grad } p_w) + \text{div } v^s = 0$$

where we have neglected the term $\frac{1}{Q} \frac{Dp_w}{Dt}$.

These equations are completed with the constitutive/rheological equations and the kinematical relations relating strains and their rate to displacements or velocities.

One important aspect is that fast landslides involve two physical phenomena which appear in above equations: (i) consolidation and dissipation of pore pressures, and (ii) propagation. In order to gain insight on the relative importance of all terms, we will express above equations in non-dimensional form as proposed by Hutter and Koch (1991), introducing a characteristic length of the landslide L and H a characteristic depth of the sliding mass, and the ratio $\varepsilon=H/L$. In typical cases, L will be of the order of 10^2m and H of the order of 5 m . Therefore, ε will be small.

We will introduce next some characteristic magnitudes of the slide. First, we will use L as a characteristic length, and H a characteristic depth of the flow. In most cases, the ratio $\varepsilon=H/L$ can be assumed to be small (shallow landslides). The time scale is $T=\sqrt{L/g}$, and a typical velocity $v=\sqrt{gL}$. Finally, the stresses and pressures will be compared to the reference pressure $\rho_0 gH$, where ρ_0 is a reference density. The x_1 and x_2 axes will be chosen on a plane close to that of the slope, or a horizontal one, and the x_3 axis will be normal to this plane. The v - p_w model can be cast in a non dimensional form by introducing

$$\begin{aligned} \hat{x}_1 &= x_1/L & \hat{x}_2 &= x_2/L & \hat{x}_3 &= x_3/L \\ \hat{v}_1 &= v_1/\sqrt{gL} & \hat{v}_2 &= v_2/\sqrt{gL} & \hat{v}_3 &= \varepsilon v_3/\sqrt{gL} \\ \hat{\sigma} &= \sigma/\rho_0 gH & \hat{p}_w &= p_w/\rho_0 gH \end{aligned}$$

The non dimensional form of the balance of mass and momentum can be written as:

$$\text{div } \hat{v} = \theta \left(\varepsilon^2 \frac{\partial^2 \hat{p}_w}{\partial \hat{x}_1^2} + \varepsilon^2 \frac{\partial^2 \hat{p}_w}{\partial \hat{x}_2^2} + \frac{\partial^2 \hat{p}_w}{\partial \hat{x}_3^2} \right) \quad (2.3.19)$$

which reduces to

$$\text{div } \hat{\mathbf{v}} = \theta \frac{\partial^2 \hat{p}_w}{\partial \hat{x}_3^2} \quad (2.3.20)$$

for shallow landslides. In above, we have introduced the non dimensional magnitude θ given by

$$\theta = \left(\frac{\sqrt{L/g}}{H/(k_w \rho_0 g)} \right) \quad (2.3.21)$$

Assuming the same typical values for L and H , and a permeability such that $k_w \rho_0 g$ is of the order of 10^{-11} ms^{-1} , it can be seen that θ will be close to 10^{-11} . Typical values are 10^{-9} for clays, 10^{-7} for silts, 10^{-5} for fine sands and 10^{-1} for gravels. Therefore, equation (2.3.19) can be approximated by

$$\text{div } \hat{\mathbf{v}} = \theta \frac{\partial^2 \hat{p}_w}{\partial \hat{x}_3^2} \quad (2.3.22)$$

The component along x_3 of the balance of momentum equation for the mixture results in

$$\varepsilon \left\{ \frac{\partial \hat{u}_3}{\partial \hat{t}} + \text{grad } \hat{u}_3 \cdot \hat{\mathbf{u}} \right\} = -1 + \left[\varepsilon \frac{\partial \hat{\sigma}_{13}}{\partial \hat{x}_1} + \varepsilon \frac{\partial \hat{\sigma}_{23}}{\partial \hat{x}_2} + \frac{\partial \hat{\sigma}_{33}}{\partial \hat{x}_3} \right]$$

where we have assumed that gravity acts along the axis x_3 , and therefore, $\hat{\mathbf{b}}_3 = -\hat{\mathbf{g}} = -1$. If we assume that ε is small, above equation reduces to

$$-1 + \frac{\partial \hat{\sigma}_{33}}{\partial \hat{x}_3} = 0$$

Or, in terms of effective stresses:

$$-1 + \frac{\partial \hat{\sigma}'_{33}}{\partial \hat{x}_3} - \frac{\partial \hat{p}_w}{\partial \hat{x}_3} = 0$$

From here, the dimensional equations are:

$$\begin{aligned}
 \operatorname{div} \mathbf{v} &= \frac{\partial}{\partial x_3} \left(-k_w \frac{\partial p_w}{\partial x_3} \right) \\
 -\rho g + \frac{\partial \sigma_{33}}{\partial x_3} &= 0 \\
 -\rho g + \frac{\partial \sigma'_{33}}{\partial x_3} - \frac{\partial p_w}{\partial x_3} &= 0
 \end{aligned} \tag{2.3.23}$$

We will assume next that the velocity field can be decomposed as

$$\mathbf{v} = \mathbf{v}_0 + \mathbf{v}_1 \tag{2.3.24}$$

and the pore pressure field will be assumed to be of the form

$$p_w = p_{w0} + p_{w1} \tag{2.3.25}$$

where p_{w0} is a hydrostatic field varying linearly from zero at the surface to $\rho g h$ at the bottom. From here we obtain

$$\begin{aligned}
 \operatorname{div} \hat{\mathbf{v}}_0 + \operatorname{div} \hat{\mathbf{v}}_1 &= \theta \left(\frac{\partial^2 \hat{p}_{w0}}{\partial \hat{x}_3^2} + \frac{\partial^2 \hat{p}_{w1}}{\partial \hat{x}_3^2} \right) \\
 &= \theta \frac{\partial^2 \hat{p}_{w1}}{\partial \hat{x}_3^2}
 \end{aligned} \tag{2.3.26}$$

And we will assume

$$\begin{aligned}
 \operatorname{div} \hat{\mathbf{v}}_0 &= 0 \\
 \operatorname{div} \hat{\mathbf{v}}_1 &= \theta \frac{\partial^2 \hat{p}_w}{\partial \hat{x}_3^2}
 \end{aligned} \tag{2.3.27}$$

In this way, we can identify the perturbed field \mathbf{v}_1 as the velocity field corresponding to consolidation and \mathbf{v}_0 as the velocity field corresponding to propagation. This result is of paramount importance, and clarifies the assumptions which should be made when modelling these phenomena. First of all, incompressibility is not a feature of rheological soil behaviour, but a consequence of the coupled behaviour between the pore fluid and the soil skeleton. Indeed, this will explain the "undrained" behavior in simple shear devices, where pressures depend on shear strain rate.

If we now approximate the divergence as

$$\operatorname{div} \mathbf{v}_1 = \frac{1}{E_m} \frac{Dp_w}{Dt}$$

where E_m is the oedometric modulus of soil skeleton, we arrive to

$$\frac{1}{E_m} \frac{Dp_w}{Dt} = \frac{\partial}{\partial x_3} \left(k_w \frac{\partial p_w}{\partial x_3} \right) \quad (2.3.28)$$

where p_w depends on x_1 , x_2 , x_3 and t . This equation is the well known 1D consolidation equation which is found in geotechnical engineering text books. Sometimes is written as:

$$\frac{Dp_w}{Dt} = \frac{\partial}{\partial x_3} \left(c_v \frac{\partial p_w}{\partial x_3} \right) \quad (2.3.29)$$

where we have introduced the coefficient of vertical consolidation c_v

$$c_v = E_m k_w = \frac{E_m \bar{k}_w}{\rho_w g}$$

with dimensions $L^2 T^{-1}$

The equations of the propagation-consolidation model are:

$$\rho \frac{Dv_0}{Dt} = \rho b + \text{div } \sigma \quad (2.3.30a)$$

with

$$\text{div } v_0 = 0 \quad (2.3.30b)$$

and

$$\frac{Dp_w}{Dt} = \frac{\partial}{\partial x_3} \left(c_v \frac{\partial p_w}{\partial x_3} \right)$$

2.4 DEPTH INTEGRATED MODELS

2.4.1 Introduction

Many fast, catastrophic landslides have average depths which are small in comparison with their length or width. In this case, it is possible to simplify the 3D propagation-consolidation model described in Section 2 by integrating the equations along the vertical axis. The

resulting 2D depth integrated model presents an excellent combination of accuracy and simplicity providing important information such as velocity of propagation, time to reach a particular place, depth of the flow at a certain location, etc. Most of the depth integrated models available in the literature do not take into account basal pore pressure, although they play a paramount role. The purpose of this Section is to present a depth integrated model which takes into account pore pressure dissipation during the propagation phase. The Section is structured as follows. After an introduction where we recall the basic equations of the propagation-consolidation model, we obtain integrate along the vertical direction the balance of mass and momentum equations of the mixture, paying attention to the centrifugal acceleration effects caused by the terrain curvature. Next, we will obtain a depth integrated equation for the vertical consolidation equation. Finally, we will consider how to formulate the eulerian model in a “pseudo-lagrangian” or arbitrary lagrangian-eulerian (ALE) framework.

The equations of the depth averaged model are obtained integrating along X_3 the balance of mass and momentum equations, and taking into account Leibniz's rule:

$$\int_a^b \frac{\partial}{\partial s} F(r, s) dr = \frac{\partial}{\partial s} \int_a^b F(r, s) dr - F(b, s) \frac{\partial b}{\partial s} + F(a, s) \frac{\partial a}{\partial s}$$

We will use the reference system given in Fig.3.1 where we have depicted some magnitudes of interest which will be used in this section.

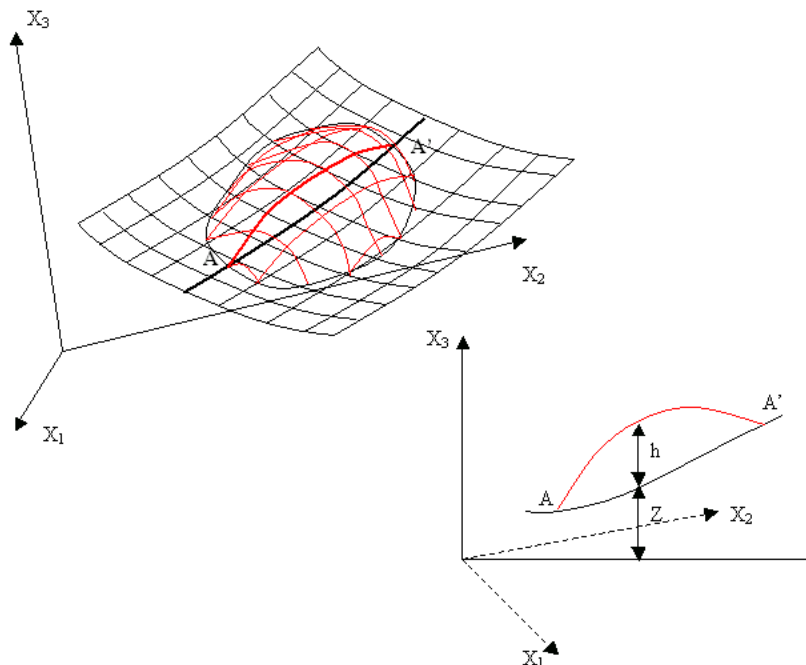


Fig. 3.1. Reference system and notation used in the analysis

2.4.2 Balance of mass

The balance of mass equation is obtained by integrating along depth eqn. (2.3.30b) and applying Leibnitz's rule. We obtain:

$\frac{\partial h}{\partial t} + \frac{\partial}{\partial x_j} (\bar{v}_j h) = e_R$	(2.4.31)
---	----------

where the erosion rate e_R is defined as:

$$e_R = -\frac{\partial Z}{\partial t}$$

2.4.3 Balance of linear momentum

Next, we will integrate along depth the balance of linear momentum equations

$$\rho \frac{\partial v_i}{\partial t} + \rho \frac{\partial}{\partial x_j} (v_i v_j) = \frac{\partial}{\partial x_j} (\sigma_{ij}) + \rho b_i \quad i = 1, 3$$

arriving, after integration along depth to:

$\frac{\partial}{\partial t} (h \bar{v}_i) + (1 + \alpha) \frac{\partial}{\partial x_j} (h \bar{v}_i \bar{v}_j) = b_i h + \frac{1}{\rho} \frac{\partial}{\partial x_j} (h \bar{\sigma}_{ij}) + \frac{1}{\rho} N^A t_i^A + \frac{1}{\rho} N^B t_i^B - e_R \bar{v}_i$	(2.4.32)
---	----------

There are some important remarks concerning this equation:

(R1) The correction coefficient α is often neglected. It depends on the rheological model describing the fluid behaviour. In the case of a Newtonian fluid it can be estimated as $\alpha = 0.2$.

(R2) The surface forces at the top are usually assumed to be zero. However, in some cases such as submarine landslides, they should be taken into account. Concerning the forces in the bottom, they depend on the rheological model used.

(R3) We have included the divergence of the averaged stresses as a source term on the right hand side, but it contains a pressure term which will result on a flux which should form part of the L.H.S. A classical case is that of an inviscid fluid, where:

$$\sigma_{ij} = -p\delta_{ij}$$

with

$$p = -\rho b_3 (Z + h - x_3) \quad (\text{Note that } b_3 \text{ is } -g \text{ when the axis } x_3 \text{ is vertical and points upwards})$$

The averaged pressure results:

$$\bar{p} = -\frac{1}{2} \rho b_3 h$$

from where the divergence of the stress tensor is:

$$\frac{\partial}{\partial x_j} (h \bar{\sigma}_{ij}) = \frac{\partial}{\partial x_j} \left(\frac{1}{2} \rho b_3 h^2 \delta_{ij} \right) = \frac{\partial}{\partial x_i} \left(\frac{1}{2} \rho b_3 h^2 \right) \quad (2.4.33)$$

The balance of linear momentum is written as:

$$\frac{\partial}{\partial t} (h \bar{v}_i) + \frac{\partial}{\partial x_j} \left(h \bar{v}_i \bar{v}_j - \frac{1}{2} b_3 h^2 \delta_{ij} \right) = -\alpha \frac{\partial}{\partial x_j} (h \bar{v}_i \bar{v}_j) + b_i h + \frac{1}{\rho} |N^A| t_i^A + \frac{1}{\rho} |N^B| t_i^B \quad (2.4.34a)$$

where we can see the flux term including both convective terms and a pressure gradient. All terms in the right hand side can be considered as sources.

This formulation can be extended to general conditions by introducing the decomposition:

$$\sigma_{ij} = -p^* \delta_{ij} + \sigma_{ij}^*$$

where we have introduced the pressure p^* defined as:

$$p^* = -\rho b_3 (Z + h - x_3)$$

In above decomposition, it is important to notice that σ_{ij}^* is not a deviatoric tensor. From here, we can obtain the depth averaged magnitudes:

$$\bar{p} = \frac{1}{2} \rho b_3 h \quad \bar{\sigma}_{ij}^* = \bar{\sigma}_{ij} + \bar{p} \delta_{ij}$$

The balance of momentum equation is then written as:

$\frac{\partial}{\partial t}(h\bar{v}_i) + \frac{\partial}{\partial x_j} \left(h\bar{v}_i\bar{v}_j - \frac{1}{2}b_3h^2\delta_{ij} \right) =$ $-\alpha \frac{\partial}{\partial x_j} (h\bar{v}_i\bar{v}_j) + \frac{1}{\rho} \frac{\partial}{\partial x_j} (h\bar{\sigma}_{ij}^*) + b_i h + \frac{1}{\rho} N^A t_i^A + \frac{1}{\rho} N^B t_i^B$	(2.4.35)
---	----------

2.4.4 A note on normal accelerations and stresses at the basal surface

In the depth integrated model the flow velocities are parallels to the plane x_1, x_2 . However, fast flows propagate downhill on curved beds with large gradients, flow velocities are parallel to the bed of the slide. Changes of gradient slope and curvature produce a pore pressure distribution different to the hydrostatic one, therefore these effects must be incorporated to the general equations.

A one dimensional lagrangian model that takes into account the slope and curvature effect was proposed by Savage and Hutter (1991). They showed that the curvature effect leads to a vertical stress increment, above all in granular materials.

The movement equations were also solved by Hungr (1995) using a lagrangian finite differences scheme. The mass was divided in a number of blocks in contact each others, which could deform during the propagation. The curvature effect was incorporated into the bottom friction force adding to the normal component, the contribution of the centrifuge force.

If a frictional material is considered, the curvature effect can be taken into account through the methods proposed by Savage and Hutter, Hungr, and Quecedo and Pastor (2003), where the authors use a reference system with axes oriented along the main curvature directions of the basal surface and the normal to it. This reference system has been used by Quecedo and Pastor in order to model bidimensional fast flows using a eulerian formulation. One of the conclusions of this work was that the main difference between the classical approach and the proposed formulation based in curvilinear coordinates was the presence of a centripetal acceleration which caused differences on the normal stresses at the basal surface and on bottom friction in the case of frictional fluids.

The purpose of this Section is to propose a simple approach based on the work of Quecedo and Pastor which can be easily implemented in numerical models to account for the centrifuge effects.

We will denote by α, β and η the coordinates along the axes oriented along the two main curvature directions and the normal to the basal surface. The distribution of the stress component $\sigma_{\eta\eta}$ is given by (Quecedo and Pastor 2003):

$$\sigma_{\eta\eta}(\eta) = \sigma_{\eta\eta}^A - \rho[\chi_\alpha \bar{v}_\alpha^2 + \chi_\beta \bar{v}_\beta^2 + b \cdot n](h' - \eta) \quad (2.4.36)$$

where:

- $\sigma_{\eta\eta}^A$ is the stress at the surface
- $\bar{v}_\alpha^2, \bar{v}_\beta^2$ are the averaged velocities along directions α, β
- χ_α, χ_β are the curvature radii along the two principal directions
- h' is the depth of the flow along axis η
- b is the vector of body forces
- n is the unit vector normal to the basal surface, given by:

$$n = \frac{1}{\left\{1 + \left(\frac{\partial Z}{\partial x_1}\right)^2 + \left(\frac{\partial Z}{\partial x_2}\right)^2\right\}^{\frac{1}{2}}} \begin{pmatrix} -\frac{\partial Z}{\partial x_1} \\ -\frac{\partial Z}{\partial x_2} \\ 1 \end{pmatrix} \quad (2.4.37)$$

The interested reader can find in Quecedo and Pastor details of the derivation.

The normal stress on the basal surface is therefore given by:

$$\sigma_{\eta\eta}^B = \sigma_{\eta\eta}^A - \rho[\chi_\alpha \bar{v}_\alpha^2 + \chi_\beta \bar{v}_\beta^2 + b \cdot n] h' \quad (2.4.38)$$

Care should be taken when using this expression in depth integrated models, because (i) the velocities are parallel to the basal surface and (ii) h' is not equal to h , but:

$$h = h' n_3$$

In order to implement this effect in the depth integrated model described here, we will obtain:

(i) The modulus of the averaged velocity \bar{V} , assuming it is tangent to the basal surface. As the averaged velocity is orthogonal to n , we can obtain the vertical component from:

$$\bar{v}_1 n_1 + \bar{v}_2 n_2 + \bar{v}_3 n_3 = 0$$

from where:

$$\bar{V} = (\bar{v}_1^2 + \bar{v}_2^2 + \bar{v}_3^2)^{1/2} \quad (2.4.39)$$

(ii) The main radius of curvature in the direction of the flow. Referring to figure 2, where we have re defined the angle α as the angle between the flow velocity and the main curvature direction, we will obtain the radius R as:

$$K = \frac{1}{R} = \frac{L \cos^2 \alpha + M \cos \alpha \sin \alpha + N \sin^2 \alpha}{E \cos^2 \alpha + F \cos \alpha \sin \alpha + G \sin^2 \alpha} = \frac{L + M \lambda + N \lambda^2}{E + F \lambda + G \lambda^2} \quad (2.4.40)$$

where:

$$\lambda = \tan \alpha$$

$$L = n^T \cdot X_{uu} \quad M = n^T \cdot X_{uv} \quad N = n^T \cdot X_{vv}$$

$$E = X_u^T \cdot X_u \quad F = X_u^T \cdot X_v \quad G = X_v^T \cdot X_v$$

In above, we have used:

$$X_u^T = \left(1, 0, \frac{\partial Z}{\partial x_1} \right) \quad X_v^T = \left(0, 1, \frac{\partial Z}{\partial x_2} \right)$$

$$X_{uu}^T = \left(0, 0, \frac{\partial^2 Z}{\partial x_1^2} \right) \quad X_{uv}^T = \left(0, 0, \frac{\partial^2 Z}{\partial x_1 \partial x_2} \right) \quad X_{vv}^T = \left(0, 0, \frac{\partial^2 Z}{\partial x_2^2} \right)$$

and:

$$E = \left(1 + \left(\frac{\partial Z}{\partial x_1} \right)^2 \right) \quad F = \left(\frac{\partial Z}{\partial x_1} \frac{\partial Z}{\partial x_2} \right) \quad G = \left(1 + \left(\frac{\partial Z}{\partial x_2} \right)^2 \right)$$

$$L = \frac{\frac{\partial^2 Z}{\partial x_1^2}}{\left\{ 1 + \left(\frac{\partial Z}{\partial x_1} \right)^2 + \left(\frac{\partial Z}{\partial x_2} \right)^2 \right\}^{\frac{1}{2}}} \quad M = \frac{\frac{\partial^2 Z}{\partial x_1 \partial x_2}}{\left\{ 1 + \left(\frac{\partial Z}{\partial x_1} \right)^2 + \left(\frac{\partial Z}{\partial x_2} \right)^2 \right\}^{\frac{1}{2}}} \quad N = \frac{\frac{\partial^2 Z}{\partial x_2^2}}{\left\{ 1 + \left(\frac{\partial Z}{\partial x_1} \right)^2 + \left(\frac{\partial Z}{\partial x_2} \right)^2 \right\}^{\frac{1}{2}}}$$

Once that we have obtained the averaged velocity and the radius of curvature, we can write the normal stress on the basal surface as:

$$\sigma_{\eta\eta}^B = \sigma_{\eta\eta}^A - \rho \left[\frac{\bar{V}^2}{R} + b \cdot n \right] \frac{h}{n_3} \quad (2.4.41)$$

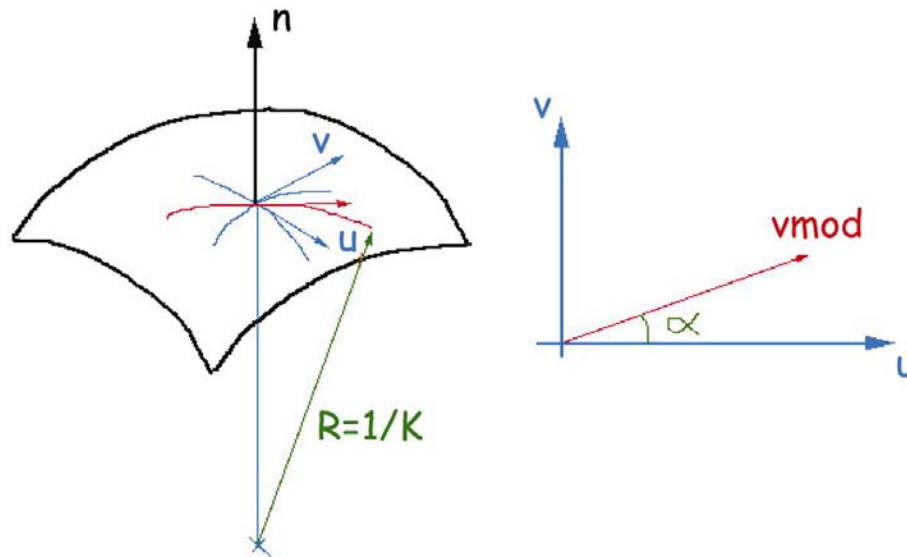


Figure 3.2. Curvature approximation

2.4.5 Consolidation equation

We will begin by recalling the vertical consolidation equation

$$\frac{Dp_w}{Dt} = \frac{\partial}{\partial x_3} \left(c_v \frac{\partial p_w}{\partial x_3} \right) \quad (2.4.42)$$

which can be cast as:

$$\frac{\partial p_w}{\partial t} + v_j \frac{\partial p_w}{\partial x_j} = \frac{\partial}{\partial x_3} \left(c_v \frac{\partial p_w}{\partial x_3} \right) \quad j = 1, 2$$

or, taking into account the incompressibility condition:

$$\frac{\partial p_w}{\partial t} + \frac{\partial}{\partial x_j} (v_j p_w) = \frac{\partial}{\partial x_3} \left(c_v \frac{\partial p_w}{\partial x_3} \right) \quad j = 1, 2 \quad (2.4.43)$$

Integration along x_3 of the left hand side gives the following terms:

$$\int_Z^{Z+h} \frac{\partial p_w}{\partial t} dx_3 = \frac{\partial}{\partial t} \int_Z^{Z+h} p_w dx_3 - p_w \frac{\partial(Z+h)}{\partial t} \Big|_{Z+h} + p_w \frac{\partial Z}{\partial t} \Big|_Z$$

$$\int_Z^{Z+h} \frac{\partial}{\partial x_j} (v_j p_w) dx_3 = \frac{\partial}{\partial x_j} \int_Z^{Z+h} v_j p_w dx_3 - v_j p_w \frac{\partial(Z+h)}{\partial x_j} \Big|_{Z+h} + v_j p_w \frac{\partial Z}{\partial x_j} \Big|_Z \quad j=1,2$$

$$\int_Z^{Z+h} \frac{\partial}{\partial x_3} (v_3 p_w) dx_3 = v_3 p_w \Big|_{Z+h} - v_3 p_w \Big|_Z$$

The terms in the preceding equations will be grouped and evaluated as:

$$-p_w \frac{\partial(Z+h)}{\partial t} \Big|_{Z+h} - v_j p_w \frac{\partial(Z+h)}{\partial x_j} \Big|_{Z+h} + v_3 p_w \Big|_{Z+h} = 0 \quad (2.4.44a)$$

$$p_w \frac{\partial Z}{\partial t} \Big|_Z + v_j p_w \frac{\partial Z}{\partial x_j} \Big|_Z - v_3 p_w \Big|_Z = 0 \quad (2.4.44b)$$

where we have used equations (5.3) and (5.4) which refer to the velocities at the surface and the basal surface,

$$\frac{\partial}{\partial t} \int_Z^{Z+h} p_w dx_3 = \frac{\partial}{\partial t} (\bar{p}_w h) \quad (2.4.45)$$

In above, we have introduced the averaged pore pressure \bar{p}_w . Finally, in order to evaluate the integral

$$\frac{\partial}{\partial x_j} \int_Z^{Z+h} v_j p_w dx_3$$

we will use the decomposition of the velocities and pressures:

$$p_w = \bar{p}_w + p_w'$$

$$v_j = \bar{v}_j + v_j'$$

Substituting into the integral, we obtain:

$$\frac{\partial}{\partial x_j} \int_Z^{Z+h} v_j p_w dx_3 = \frac{\partial}{\partial x_j} \left(\int_Z^{Z+h} \bar{v}_j \bar{p}_w dx_3 \right) + \frac{\partial}{\partial x_j} \left(\int_Z^{Z+h} v_j' p_w' dx_3 \right)$$

$$\frac{\partial}{\partial x_j} \int_Z^{Z+h} v_j p_w dx_3 = \frac{\partial}{\partial x_j} (\bar{v}_j \bar{p}_w h) + C.T. \quad (2.4.46)$$

where the correcting term $\frac{\partial}{\partial x_j} \left(\int_Z^{Z+h} v_j' p_w' dx_3 \right)$ will be evaluate using the rheological properties of the fluid.

In above we have used the identities:

$$\frac{\partial}{\partial x_j} \int_Z^{Z+h} \bar{v}_j p_w' dx_3 = 0 \quad \frac{\partial}{\partial x_j} \int_Z^{Z+h} v_j' \bar{p}_w dx_3 = 0$$

The right hands side $\frac{\partial}{\partial x_3} \left(c_v \frac{\partial p_w}{\partial x_3} \right)$ is integrated along x_3 in an immediate manner:

$$\int_Z^{Z+h} \frac{\partial}{\partial x_3} \left(c_v \frac{\partial p_w}{\partial x_3} \right) dx_3 = c_v \frac{\partial p_w}{\partial x_3} \Big|_Z^{Z+h} \quad (2.4.47)$$

Finally, we arrive to:

$\frac{\partial}{\partial t} (\bar{p}_w h) + \frac{\partial}{\partial x_j} (\bar{v}_j \bar{p}_w h) = c_v \frac{\partial p_w}{\partial x_3} \Big _Z^{Z+h} + C.T.$	(2.4.48)
--	----------

which is the vertical consolidation equation integrated along x_3 .

Next, we will assume that the pore pressure can be approximated as:

$$p_w(x_1, x_2, x_3, t) = \sum_{k=1}^{N_{pw}} P_k(x_1, x_2, t) N_k(x_3) \quad (2.4.49)$$

where we have used shape functions along x_3 fulfilling the boundary conditions. We can assume in most cases that the pore pressure at the surface is zero and the influx at the basal surface is zero. In this case, the shape functions can be chosen as:

$$N_k(x_3) = \cos \frac{(2k-1)}{2h} \pi (x_3 - Z) \quad k = 1, N_{pw} \quad (2.4.50)$$

The first term is given by:

$$N_1(x_3) = \cos \frac{\pi}{2h}(x_3 - Z) \quad (2.4.51)$$

If we limit the analysis to a single Fourier component, the pore pressure is:

$$p_w(x_1, x_2, x_3, t) = P_1(x_1, x_2, t) \cos \frac{\pi}{2h}(x_3 - Z) \quad (2.4.52)$$

from where we obtain:

$$\begin{aligned} \bar{p}_w &= \int_Z^{Z+h} p_w dx_3 = \int_Z^{Z+h} P_1(x_1, x_2, t) N_1(x_3) dx_3 \\ &= P_1(x_1, x_2, t) \int_Z^{Z+h} \cos \frac{\pi}{2h}(x_3 - Z) dx_3 \\ &= \frac{2}{\pi} P_1 \end{aligned} \quad (2.4.53)$$

Concerning the left hand side of equation (2.4.48), we will substitute the averaged pore pressure by its approximation given by (2.4.53):

$$\frac{\partial}{\partial t}(\bar{p}_w h) = \frac{2}{\pi} \frac{\partial}{\partial t}(P_1 h) \quad (2.4.54)$$

$$\frac{\partial}{\partial x_j}(\bar{v}_j \bar{p}_w h) = \frac{2}{\pi} \frac{\partial}{\partial x_j}(\bar{v}_j P_1 h) \quad j = 1, 2 \quad (2.4.55)$$

The term $c_v \frac{\partial p_w}{\partial x_3} \Big|_Z^{Z+h}$ is obtained substituting (2.4.52):

$$c_v \frac{\partial p_w}{\partial x_3} \Big|_Z^{Z+h} = -\frac{\pi}{2h} c_v P_1 \quad (2.4.56)$$

Collecting the terms obtained in (2.4.53-2.4.56), we obtain:

$$\frac{2}{\pi} \frac{\partial}{\partial t}(P_1 h) + \frac{2}{\pi} \frac{\partial}{\partial x_j}(\bar{v}_j P_1 h) + C.T. = -\frac{\pi}{2h} c_v P_1$$

from where:

$\frac{\partial}{\partial t}(P_1 h) + \frac{\partial}{\partial x_j}(\bar{v}_j P_1 h) + \frac{\pi}{2} C.T. = -\frac{\pi^2}{4h} c_v P_1$	(2.4.57)
--	----------

2.4.6 Quasi Lagrangian formulation

Sometimes, it has been found convenient to refer to an equivalent 2D continuum having as velocities of their material points the depth integrated velocities. This cannot be considered as a Lagrangian formulation, because the moving points have no exact connection with material particles. It can be denominated either “quasi lagrangian”, or arbitrary lagrangian eulerian (ALE) formulation.

To derive a quasi lagrangian formulation of the depth integrated equations, we will first introduce a “quasi material derivative” as:

$$\frac{\bar{d}}{dt} = \frac{\partial}{\partial t} + \bar{v}_j \frac{\partial}{\partial x_j} \tag{2.4.58}$$

The balance of mass equation

$$\frac{\partial h}{\partial t} + \frac{\partial}{\partial x_j}(\bar{v}_j h) = e_R$$

will be written as

$$\frac{\partial h}{\partial t} + \bar{v}_j \frac{\partial h}{\partial x_j} + h \frac{\partial \bar{v}_j}{\partial x_j} = e_R \tag{2.4.59}$$

from where we obtain the “quasi lagrangian” form of the balance of mass, depth integrated equation :

$\frac{\bar{d}h}{dt} + h \frac{\partial \bar{v}_j}{\partial x_j} = e_R$	(2.4.60)
---	----------

In a similar way, the balance of momentum equation

$$\frac{\partial}{\partial t}(h \bar{v}_i) + \frac{\partial}{\partial x_j} \left(h \bar{v}_i \bar{v}_j - \frac{1}{2} b_3 h^2 \delta_{ij} \right) = \alpha \frac{\partial}{\partial x_j} (h \bar{v}_i \bar{v}_j) + b_i h + \frac{1}{\rho} |N^A| t_i^A + \frac{1}{\rho} |N^B| t_i^B - e_R \bar{v}_i$$

can be transformed into:

$$h \frac{\bar{d}}{dt} \bar{v}_i - \frac{\partial}{\partial x_i} \left(\frac{1}{2} b_3 h^2 \right) = -e_R \bar{v}_i - \alpha \frac{\partial}{\partial x_j} (h \bar{v}_i \bar{v}_j) + \frac{1}{\rho} \frac{\partial}{\partial x_j} (h \bar{\sigma}_{ij}^*) + b_i h + \frac{1}{\rho} |N^A| t_i^A + \frac{1}{\rho} |N^B| t_i^B \quad (2.4.61)$$

Finally, the vertical consolidation equation

$$\frac{\partial}{\partial t} (P_1 h) + \frac{\partial}{\partial x_j} (\bar{v}_j P_1 h) + \frac{\pi}{2} C.T. = -\frac{\pi^2}{4h} c_v P_1$$

will be transformed as follows:

$$\frac{\partial}{\partial t} (P_1 h) + \frac{\partial}{\partial x_j} (\bar{v}_j P_1 h) + \frac{\pi}{2} C.T. = -\frac{\pi^2}{4h} c_v P_1$$

$$h \left\{ \frac{\partial P_1}{\partial t} + \bar{v}_j \frac{\partial P_1}{\partial x_j} \right\} + P_1 \left\{ \frac{\partial h}{\partial t} + \frac{\partial}{\partial x_j} (\bar{v}_j h) \right\} + \frac{\pi}{2} C.T. = -\frac{\pi^2}{4h} c_v P_1$$

from where, we obtain:

$$\frac{\bar{d}P_1}{dt} + \frac{1}{h} P_1 e_R + \frac{\pi}{2h} C.T. = -\frac{\pi^2}{4h^2} c_v P_1 \quad (2.4.62)$$

which is the quasi lagrangian form of the vertically integrated 1D consolidation equation.

2.5 REFERENCES

Biot, M.A.(1941) General theory of three-dimensional consolidation. **J.Appl.Phys.** 12, 155-164.

Biot, M.A.(1955) Theory of elasticity and consolidation for a porous anisotropic solid. **J.Appl.Phys.** 26, 182-185

Coussy,O. (1995), Mechanics of Porous Media, John Wiley and Sons, Chichester.

de Boer, R. (2000), Theory of porous media, Springer-Verlag, Berlin.

Hutchinson, J.N. (1986). "A sliding-consolidation model for flow slides", **Can.Geotech.J.**, 23, 115-126

Hungr, O. (1995): "A model for the runout analysis of rapid flow slides, debris flows and avalanches", **Can.Geotech.J.** 32, pp 610-623.

Hutter, K. & Koch, T. (1991). "Motion of a granular avalanche in an exponentially curved chute: experiments and theoretical predictions", **Phil. Trans. R. Soc.London**, A 334, pp 93-138.

Iverson, R.I., and Denlinger, R.P. (2001), "Flow of variably fluidized granular masses across three dimensional terrain. 1. Coulomb mixture theory", **J.Geophys.Res.** 106, N0.B1, 537-552

Lewis, R.L. and Schrefler, B.A. (1998), The Finite Element Method in the Static and Dynamic Deformation and Consolidation of Porous Media, J.Wiley and Sons.

Pastor, M., Quecedo,M., Fernández Merodo, J.A., Herreros, M^a.I., González, E. And Mira, P. (2002), Modelling Tailing Dams and mine waste dumps failures, **Geotechnique**, Vol.LII, N.8, 579-592, 2002

Quecedo, M. and Pastor,M. (2003): "Finite Element modelling of free surface flows on inclined and curved beds" **Journal of Computational Physics** Vol. 189, Issue 1, pp 45-62, July 2003

Savage, S.B. and Hutter, K. (1991). "The dynamics of avalanches of granular materials from initiation to runout. Part I: Analysis", *Acta Mechanica* 86, pp 201-223.

Zienkiewicz, O.C., Chang, C.T. and Bettess, P.(1980). Drained, undrained, consolidating dynamic behaviour assumptions in soils. **Geotechnique** 30, 385-395 .

Zienkiewicz, O.C. and Shiomi, T. (1984), Dynamic behaviour of saturated porous media: The generalised Biot formulation and its numerical solution. **Int.J.Num.Anal.Meth.Geomech.**,8, 71-96.

Zienkiewicz, O.C., Chan, A.H.C., Pastor, M., Paul, D.K and Shiomi (1990a), T. Static and dynamic behaviour of soils: a rational approach to quantitative solutions. I. Fully saturated problems. **Proc.R.Soc.Lond.** A 429, 285-309.

Zienkiewicz, O.C, Xie, Y.M., Schrefler, B.A., Ledesma, A. and Bicanic. (1990b), N . Static and dynamic behaviour of soils: a rational approach to quantitative solutions. II. Semi-saturated problems, **Proc.R. Soc.Lond.** A 429, 311-321.

Zienkiewicz, O.C., Chan, A.H.C., Pastor, M., Shrefler, B.A., and Shiomi, T. (2000), **Computational Geomechanics**, J.Wiley and Sons

3 BEHAVIOUR OF FLUIDIZED GEOMATERIALS: RHEOLOGICAL AND CONSTITUTIVE MODELLING

3.1 INTRODUCTION

Mathematical models described in the preceding Section have to be completed using constitutive or rheological models relating stress and strain tensors. In the case of solid soils, great effort has been devoted in the past decades to develop accurate constitutive models accounting for the more important aspects of soil behaviour, and today there is a wide choice between many elastoplastic, viscoplastic, hypoplastic, non linear incremental and generalized plasticity models, just to mention some of them.

One important limitation is that, so far, no satisfactory model able to reproduce the behaviour of soil mixtures under the full range of strain rates which appear in fast slope movement problems has been developed. After liquefaction or fluidization has taken place, the soil behaves in a fluid like manner, and models used here are different from those used for reproducing the triggering mechanism. Indeed, both classes of models for solid or fluidized soils are often referred to as “constitutive equations” and “rheological models”.

The purpose of this Chapter is to present models able to describe -with different degrees of approximation- the behaviour of fluidized soils. We will begin by discussing the process of fluidization or liquefaction. In a second Section, we will describe some available laboratory testing apparatuses which allow determining the properties of these fluidized materials, together with some basic features of their behaviour. From here, we will continue by introducing a general framework within which rheological laws such as newtonian, Bagnold or Bingham fluids can be derived as particular cases. Finally, we will describe depth integrated rheological models.

3.2 MECHANISMS OF FLUIDIZATION OF GEOMATERIALS

Classical geotechnical analysis stops at failure. Beyond it, there are important difficulties from all points of view: experimental, constitutive, and numerical. Experimentalists find that specimens are not homogeneous in the case of localized failure, and therefore it is a difficult task to obtain reliable measurements of stress and strain. Moreover, the test apparatuses are not designed to follow the important strain which develops. Constitutive modellers do not go further because of the lack of experimental data. The situation is not much different for numerical analysts, who will find here large deformations. Numerical methods such as finite elements need to use special techniques. If the formulation is of lagrangian type, the mesh can be severely distorted, and either adaptive remeshing or arbitrary lagrangian eulerian techniques have to be used. If an eulerian formulation is used, the material movement has to be tracked in the fixed mesh. Tracking of free surfaces requires also the use of techniques such as the level set.

3.3 RHEOMETERS AND THE BEHAVIOUR OF FLUIDIZED GEOMATERIALS

To develop suitable constitutive relations it is necessary to have experimental results obtained under controlled conditions. It is convenient to use simple stress and strain rate fields to obtain the basic features of the model. At a latter stage, more complex tests can be introduced to improve our understanding.

Testing apparatuses used to reproduce simple flows are called rheometers. Most of them aim to obtain fluid viscosity -or relations between shear stress and rate of shear strain-. Simplest conditions are those of simple shear flows, where the fluid is sheared on a plane XZ, the velocity being parallel to X (Figure 3.3.1)

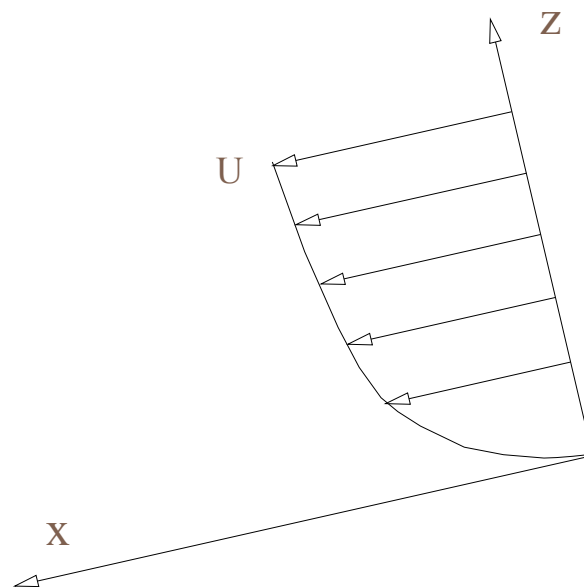


Fig.3.3.1 Simple shear flow: velocity is constant along X axis

One important limitation of the laboratory rheometers is their size. Sometimes, debris flows include large solid particles such as boulders. In order to have a representative volume inside the rheometer, we will need to have a certain number of particles across the sheared zone, which will not be always possible.

The study of the flow of granular materials of very small diameter (in the mm range) in a viscous fluid can provide insight into the basic features of flow. From here, constitutive equations for larger grains can be developed, provided they are validated against data obtained either in large scale laboratory flumes or in real debris or mudflows.

One of the first rheometers built to study the flow of granular particles is due to Bagnold (Bagnold 1954). A sketch of this rheometer can be seen in Fig.3.3.2

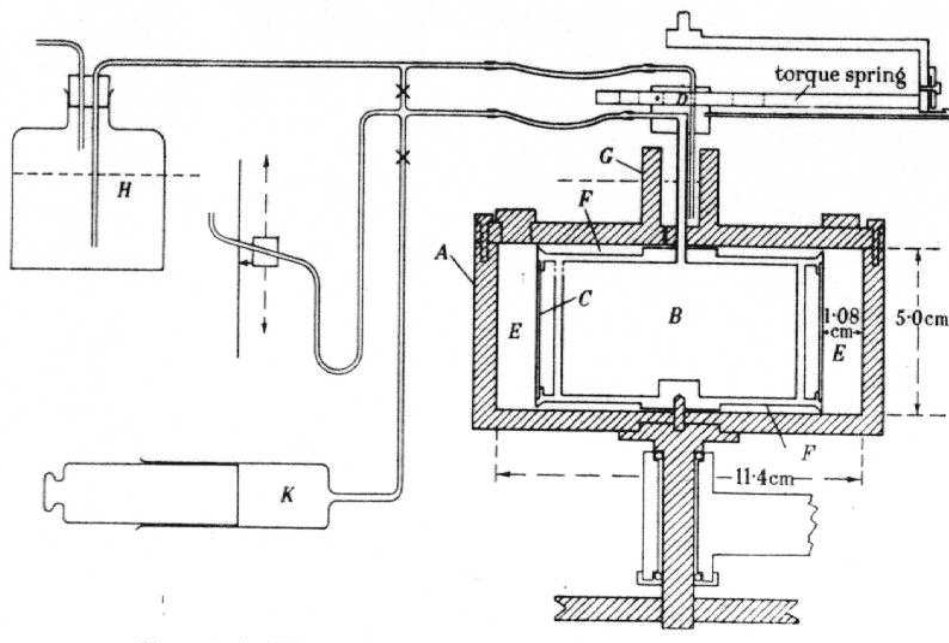


Figure 3.3.2. Bagnold's rheometer (Bagnold, 1954)

Bagnold used the annular space between two drums to create a simple shear Couette flow when the outer drum rotated keeping the inner stationary. The granular material consisted on 0.132 cm. diameter spherical droplets of a mixture of paraffin wax and lead stearate, with a density equal to that of water.

Other experimental devices which are worth mentioning are those of Hanes and Inman (1985) and the rolling sleeve rheometer of Johnson and Martosudarmo (1997).

In Bagnold's rheometer, it is possible to study the influence of grains concentration, shear strain rate and fluid viscosity. The main results obtained in his pioneering work are:

- (i) For a given mixture, there are two regimes:
 - (a) The inertia regime, where the effects of collisions between grains are dominant and the shear stress is proportional to the square of the shear strain rate.
 - (b) The macro viscous regime, where viscosity effects dominate and the relation between shear stress and strain rate is linear.
- (ii) Shearing causes an extra pressure of dispersive nature, which was found to be proportional to the shear stress.

Figs 3.3.3 and 3.3.4 (Bagnold 1954) show the dependence of the shear and normal stresses on the rate of shear strain. In both figures, σ is the density, D the particle diameter, and T and P the shear and normal stresses respectively. To characterize concentration, Bagnold used the linear concentration λ defined as:

$$\frac{1}{\lambda} = \left(\frac{C_{\max}}{C} \right)^{\frac{1}{3}} - 1 \quad (3.3.1)$$

where C and C_{\max} are the concentration and the maximum possible concentration, which for spheres is $\frac{\pi}{3\sqrt{2}} = 0.74$.

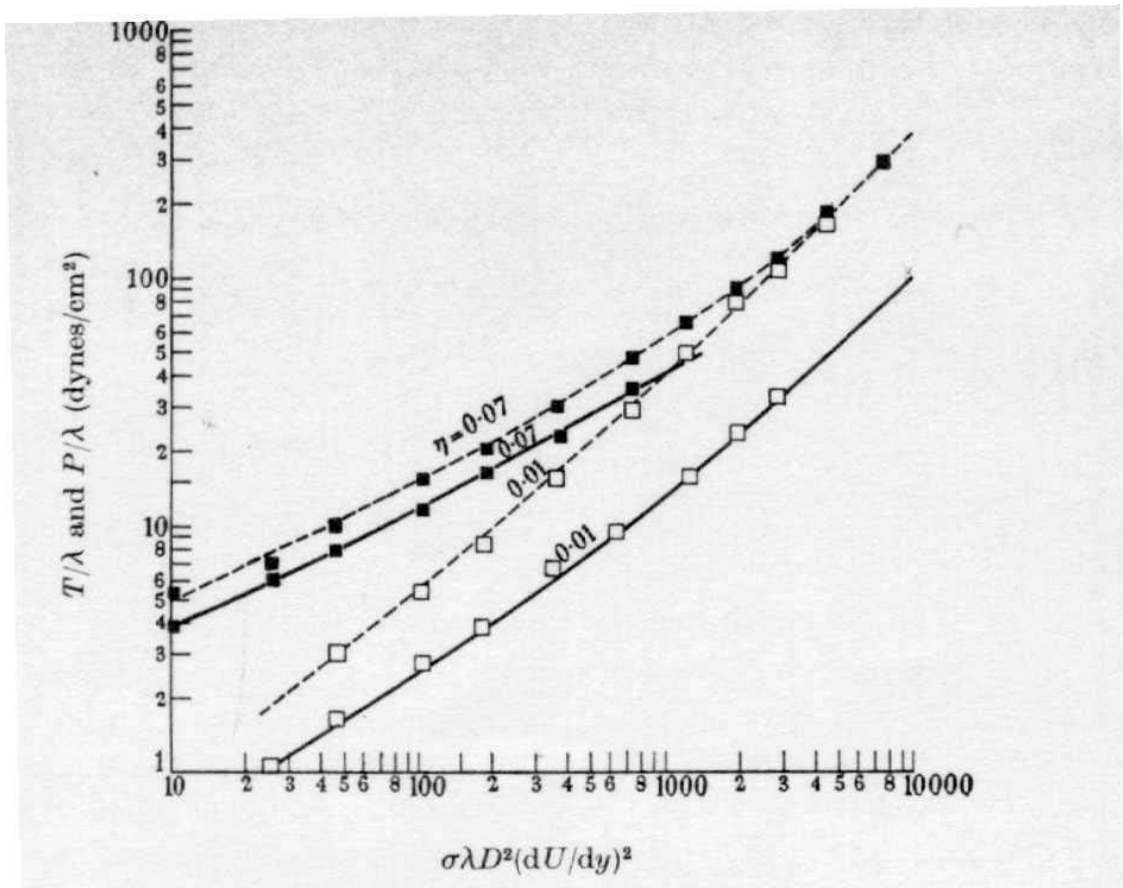


Figure 3.3.3. Shear stress vs. shear strain rate at different linear concentrations.

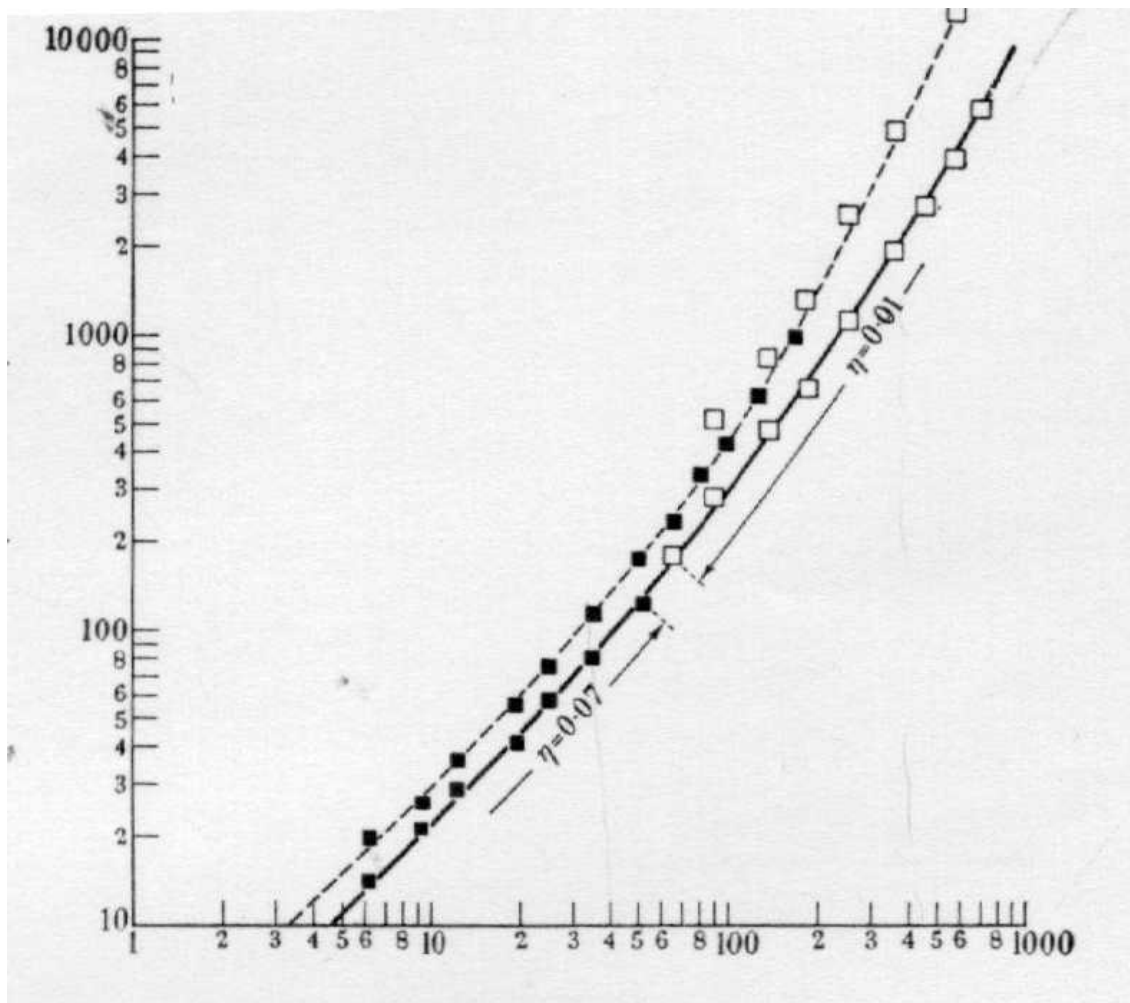


Figure 3.3.4. Dispersive pressure for different linear concentrations.

Bagnold (1966) suggested two critical values of λ , 17 for general shearing and 14 for fluidization.

So far, we have presented rheometers where simple shear flows are approximated with a reasonable degree of accuracy. Sometimes, researchers favour rheometers with more complex stress and rate of strain fields, such as rotating drums, inclined planes, silos, etc. The interested reader will find in the collective work of the research group MIDI (2004) an interesting description of these devices together with basic aspects of the observed behaviour. We include in figure 3.5 an sketch of two such rheometers.

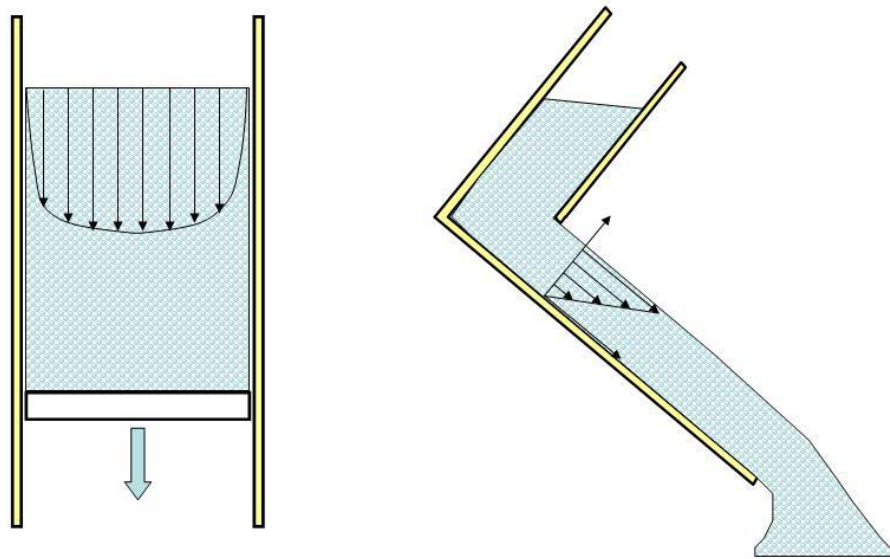


Figure 3.3.5 Vertical chute and inclined plane rheometers (MIDI 2004)

3.4 RHEOLOGICAL MODELS

3.4.1 General framework

Once downhill movement has started, material behaviour becomes more and more "fluid-like". The problem of modelling such fluid is complex, and it will depend on the type of mixture. In the simplest case of a flow of a granular material without interstitial water, it could be thought of being composed of a single phase. However, the flow presents inverse segregation, and the coarsest fraction will move upwards. Therefore, this phenomenon cannot be modelled if the assumption of a single phase material is made. The problem gets more complicated if an interstitial fluid such as water or mud is present.

A first simplification commonly found in literature consists in studying the overall mixture behaviour, formulating ad-hoc models for it. This approach precludes the relative movement of the interstitial fluid relative to the solid fraction, and does not allow modelling of stabilization of the flow using bottom drainage systems.

Next refinement consists on considering two phases, a granular skeleton with voids filled with either water or mud. If the shear strength of the fluid phase can be neglected, the stress tensor in the mixture can be decomposed into a "pore pressure" and an effective stress.

The purpose of this Section is to present some of the models which have been used in the past, providing values of their material parameters whenever they are available. Most of them

have been formulated in terms of total stresses for one phase, but they can be generalized including the stresses of the fluid. It seems reasonable to consider one phase in the case of mudflows, and two in the case of debris flows. The difference could be the ability of the fluid phase to percolate through the solid.

One of the main difficulties to develop suitable rheological models is the limitations of the existing rheometers in applying general stress and rate of deformation fields. This situation is much different from that found in soil mechanics, where today it is possible to control three independent magnitudes such as principal stresses or invariants. There exist devices where it is possible to explore the effect of rotation of principal stresses axes, the structural and induced anisotropy, etc.

In the case of fluidized geomaterials, the stress conditions are rather simple, such as the simple shear which has been already described, and most of simplifications used in the analysis are caused by a lack of available data rather than founded in experiments.

If we assume that the fluid is isotropic, and we want to express the stress as a function of the rate of deformation tensor, it is possible to use the so called “representation theorems”. Following Malvern (1969) the stress tensor can be expressed as:

$$\sigma = -pI - \Phi_0 I + \Phi_1 d + \Phi_2 d^2 \quad (3.4.1)$$

where p is a “thermodynamic” pressure, I the identity tensor, d the rate of deformation tensor, and Φ_k $k = 0..2$ scalar functions of the invariants of d :

$$\Phi_k = \Phi_k(I_{1d}, I_{2d}, I_{3d})$$

The invariants are defined as:

$$I_{kd} = \frac{1}{k} \text{tr}(d^k) \quad (3.4.2)$$

In most of models it is assumed that the flow is incompressible, and therefore $I_{1d} = 0$. This is consistent with the decomposition into propagation and vertical consolidation described in the preceding Chapter, and also with the fact that soils fails at constant volume. However, the reader should be aware that this is just an assumption which has proven accurate only under certain assumptions. We will assume in what follows that the flow is incompressible. Moreover, due to the lack of experimental evidence, we will assume that there is no dependence on I_{3d} . In our opinion, this assumption which is found in most of available models has to be devoted more attention. In the case of soils and granular materials in solid state, this assumption leads to important errors, such as different friction angles at critical state at compression and extension. In consequence, we will assume:

$$\Phi_k = \Phi_k(I_{2d})$$

The stress tensor can be decomposed into hydrostatic and deviatoric components as:

$$\sigma = -\hat{p}I + s \quad (3.4.3)$$

where:

$$\hat{p} = -\frac{1}{3}\text{tr}(\sigma)$$

$$s = \sigma + \hat{p}I$$

The hydrostatic component can be obtained as:

$$\begin{aligned} \hat{p} &= -\frac{1}{3}(-3p - 3\Phi_0 + \Phi_2\text{tr}(d^2)) \\ &= p + \Phi_0 - \frac{2}{3}\Phi_2 I_{2d} \end{aligned} \quad (3.4.4)$$

In above, we have used the definition of I_{2d} (3.4.2):

$$I_{2d} = \frac{1}{2}\text{tr}(d^2)$$

Finally, the deviatoric component can be easily obtained as:

$$s = -\frac{2}{3}\Phi_2 I_{2d}I + \Phi_1 d + \Phi_2 d^2 \quad (3.4.5)$$

It is important to notice that, as the flow is isochoric, the hydrostatic component of the rate of deformation tensor is zero, and d is a deviatoric tensor. Therefore,

$$d = \text{dev}(d) \quad (3.4.6)$$

and (3.4.5) can be written as:

$$s = -\frac{2}{3}\Phi_2 I_{2d}I + \Phi_1 \text{dev}(d) + \Phi_2 d^2 \quad (3.4.7)$$

The stress is given by:

$$\sigma = -pI - \Phi_0 I + \Phi_1 \text{dev}(d) + \Phi_2 d^2 \quad (3.4.8a)$$

An alternative is:

$$\sigma = -pI - \Phi_0 I + \Phi_1 \text{dev}(d) + \Phi_2 \{\text{dev}(d)\}^2 \quad (3.4.8b)$$

We will consider next two particular cases of motion: simple shear flow and a general 2D plane flow.

The simple shear flow will be assumed to take place in the $X_1 X_3$ plane (figure 4.1), with a velocity field of the form:

$$\begin{aligned} v_1 &= v_1(x_3) \\ v_2 &= v_3 = 0 \end{aligned} \quad (3.4.9)$$

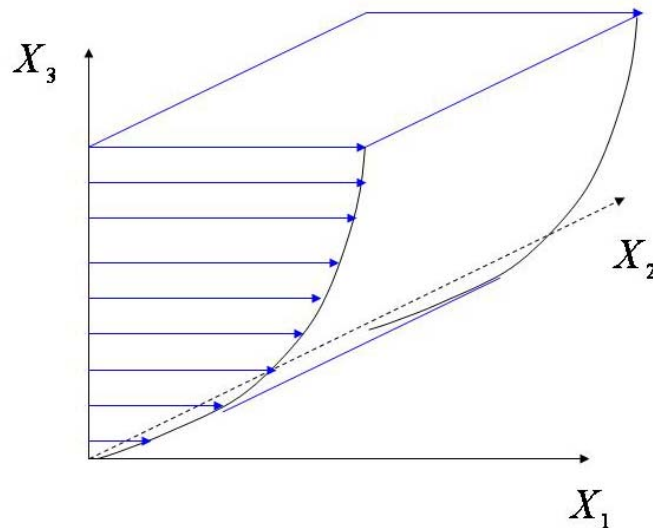


Figure 3.4.1 Simple shear flow

The rate of deformation tensor is:

$$d = \begin{pmatrix} 0 & 0 & \frac{1}{2} \frac{\partial v_1}{\partial x_3} \\ 0 & 0 & 0 \\ \frac{1}{2} \frac{\partial v_1}{\partial x_3} & 0 & 0 \end{pmatrix} \quad (3.4.10a)$$

and d^2 is given by:

$$d^2 = \begin{pmatrix} \frac{1}{4} \left(\frac{\partial v_1}{\partial x_3} \right)^2 & 0 & 0 \\ 0 & 0 & 0 \\ 0 & 0 & \frac{1}{4} \left(\frac{\partial v_1}{\partial x_3} \right)^2 \end{pmatrix} \quad (3.4.10b)$$

The second invariant I_{2d} is:

$$I_{2d} = \frac{1}{2} \text{tr}(d^2) = \frac{1}{4} \left(\frac{\partial v_1}{\partial x_3} \right)^2 \quad (3.4.10c)$$

The stress tensor is given by:

$$\sigma = -pI - \Phi_0 I + \Phi_1 \begin{pmatrix} 0 & 0 & \frac{1}{2} \frac{\partial v_1}{\partial x_3} \\ 0 & 0 & 0 \\ \frac{1}{2} \frac{\partial v_1}{\partial x_3} & 0 & 0 \end{pmatrix} + \Phi_2 \begin{pmatrix} \frac{1}{4} \left(\frac{\partial v_1}{\partial x_3} \right)^2 & 0 & 0 \\ 0 & 0 & 0 \\ 0 & 0 & \frac{1}{4} \left(\frac{\partial v_1}{\partial x_3} \right)^2 \end{pmatrix} \quad (3.4.11)$$

from where we obtain the components:

$$\begin{aligned} \sigma_{11} = \sigma_{33} &= -p - \Phi_0 + \frac{1}{4} \Phi_2 \left(\frac{\partial v_1}{\partial x_3} \right)^2 \\ \sigma_{22} &= -p - \Phi_0 \\ \sigma_{13} = \sigma_{31} &= \frac{1}{2} \Phi_1 \frac{\partial v_1}{\partial x_3} \end{aligned} \quad (3.4.12)$$

where $\Phi_k = \Phi_k(I_{2d}) \quad k = 0..2$

It is important to notice that, in addition to having shear stresses which depend on the rate of shear strain $\frac{\partial v_1}{\partial x_3}$ we find that the normal stresses σ_{11} and σ_{33} depend also on it. This contribution is often referred to as “dispersive stresses”.

The expression of the stress components (3.4.12) will be used to generalize the results obtained in simple shear flow rheometers to more general stress conditions.

The second case which will be considered here is that of a **isochoric 2D flow**, which we will assume to take place in the plane $X_1 X_3$. The rate of deformation tensor is now given by:

$$d = \begin{pmatrix} d_{11} & 0 & d_{13} \\ 0 & 0 & 0 \\ d_{31} & 0 & d_{33} \end{pmatrix} \quad (3.4.13a)$$

with $d_{11} + d_{33} = 0$. From here, we obtain:

$$d^2 = \begin{pmatrix} d_{11}^2 + d_{13}^2 & 0 & d_{13}(d_{11} + d_{33}) \\ 0 & 0 & 0 \\ d_{13}(d_{11} + d_{33}) & 0 & d_{33}^2 + d_{13}^2 \end{pmatrix} = \begin{pmatrix} d_{11}^2 + d_{13}^2 & 0 & 0 \\ 0 & 0 & 0 \\ 0 & 0 & d_{33}^2 + d_{13}^2 \end{pmatrix} \quad (3.4.13b)$$

The components of the stress tensor are given now by:

$$\sigma = -pI - \Phi_0 I + \Phi_1 \begin{pmatrix} d_{11} & 0 & d_{13} \\ 0 & 0 & 0 \\ d_{31} & 0 & d_{33} \end{pmatrix} + \Phi_2 \begin{pmatrix} d_{11}^2 + d_{13}^2 & 0 & 0 \\ 0 & 0 & 0 \\ 0 & 0 & d_{33}^2 + d_{13}^2 \end{pmatrix} \quad (3.4.14)$$

from where we obtain:

$$\begin{aligned} \sigma_{11} &= -p - \Phi_0 + \Phi_1 d_{11} + \Phi_2 (d_{11}^2 + d_{13}^2) \\ \sigma_{33} &= -p - \Phi_0 + \Phi_1 d_{33} + \Phi_2 (d_{33}^2 + d_{13}^2) \\ &= -p - \Phi_0 - \Phi_1 d_{11} + \Phi_2 (d_{11}^2 + d_{13}^2) \\ \sigma_{22} &= -p - \Phi_0 \\ \sigma_{13} &= \sigma_{31} = \Phi_1 d_{13} \\ \sigma_{12} &= \sigma_{23} = 0 \end{aligned} \quad (3.4.15)$$

Again, we find (i) a shear stress depending only on d_{13} , and (ii) dispersive stress terms which depend on $\Phi_2 (d_{11}^2 + d_{13}^2)$

3.4.2 Newtonian fluids

The Newtonian fluid is a simple rheological model characterized by one single constitutive parameter, the fluid viscosity. In the case of a simple shear flow, the shear stress is given by:

$$\sigma_{13} = \mu \frac{\partial v_1}{\partial x_3} \quad (3.4.16)$$

where we have introduced the viscosity coefficient μ with units Pa.s in the MKS system. Typical values of μ are:

Material	μ (Pa.s)
Air	10^{-6}
Water	10^{-3}
Mud	10^{-2}

where it should be remembered that viscosity depends on temperature.

If we compare (3.4.16) to (3.4.8), we can identify:

$$\mu \frac{\partial v_1}{\partial x_3} = \frac{1}{2} \Phi_1 \frac{\partial v_1}{\partial x_3} \quad (3.4.17)$$

from where $\Phi_1 = 2\mu$. The newtonian fluid model can be written in general conditions as:

$$\sigma = -pI + 2\mu \text{dev}(d) \quad (3.4.18)$$

3.4.3 Bagnold fluids

Bagnold proposed a model valid for simple shear conditions which explained the behaviour observed in his rheometer. The tests were conducted at constant volume, and he identified two different flow regimes, which he denoted as “macro-viscous” and “inertial”, depending on whether fluid viscosity or grain inertia dominated. The transition was characterized by a value of the non dimensional number N_B in the range 40-450. The Bagnold number N_B is defined as:

$$N_B = \frac{\lambda^{1/2} \rho c^2 \left(\frac{\partial v_1}{\partial x_3} \right)}{\mu} \quad (3.4.19)$$

where c is the diameter of the spheres, and λ the linear concentration given in (3.4.1).

Bagnold proposed the following expressions for shear and normal stresses in the inertia regime:

$$\begin{aligned}\sigma_{13} &= a_i \sin \alpha_i \rho \lambda^2 c^2 \left(\frac{\partial v_1}{\partial x_3} \right)^2 \\ \sigma_{33} &= p + a_i \cos \alpha_i \rho \lambda^2 c^2 \left(\frac{\partial v_1}{\partial x_3} \right)^2\end{aligned}\tag{3.4.19}$$

where $a_i = 0.042$ and $\tan \alpha_i = 0.4$, The equations are valid for $\lambda \geq 12$. In above, p is the thermodynamic pressure introduced in (3.4.2). We have reproduced the experimental results obtained by Bagnold in Figs. 3.3.3 and 3.3.4. There, the shear stress and the normal stress are given for different values of the linear concentration ranging from 17 to 1.3. The legend ‘‘a’’ denotes the behaviour of plain water. It is also worth mentioning that Bagnold took compression components as negative.

Equations (3.4.19) show a dependence on the normal stress σ_{33} on the rate of shear deformation $\frac{\partial v_1}{\partial x_3}$. This component is referred to as ‘‘dispersive pressure’’, and it can be observed under isochoric conditions. Should the test have been run under constant pressure conditions, we would have observed a dilation or increase of void ratio.

If we compare above expressions with (3.4.11)

$$\sigma = -pI - \Phi_0 I + \Phi_1 \begin{pmatrix} 0 & 0 & \frac{1}{2} \frac{\partial v_1}{\partial x_3} \\ 0 & 0 & 0 \\ \frac{1}{2} \frac{\partial v_1}{\partial x_3} & 0 & 0 \end{pmatrix} + \Phi_2 \begin{pmatrix} \frac{1}{4} \left(\frac{\partial v_1}{\partial x_3} \right)^2 & 0 & 0 \\ 0 & 0 & 0 \\ 0 & 0 & \frac{1}{4} \left(\frac{\partial v_1}{\partial x_3} \right)^2 \end{pmatrix}$$

we can identify:

$$\begin{aligned}\sigma_{33} &= -p - \Phi_0 + \frac{1}{4} \Phi_2 \left(\frac{\partial v_1}{\partial x_3} \right)^2 = -p - a_i \cos \alpha_i \rho \lambda^2 c^2 \left(\frac{\partial v_1}{\partial x_3} \right)^2 \\ \sigma_{13} = \sigma_{31} &= \frac{1}{2} \Phi_1 \frac{\partial v_1}{\partial x_3} = \sigma_{13}^{urb} + a_i \sin \alpha_i \rho \lambda^2 c^2 \left(\frac{\partial v_1}{\partial x_3} \right)^2\end{aligned}$$

from where

$$\Phi_0 = 0$$

$$\Phi_1 = 2a_i \sin \alpha_i \rho \lambda^2 c^2 \left(\frac{\partial v_1}{\partial x_3} \right) = 4a_i \sin \alpha_i \rho \lambda^2 c^2 (I_{2D})^{\frac{1}{2}} \quad (3.4.20)$$

$$\Phi_2 = -4a_i \cos \alpha_i \rho \lambda^2 c^2$$

In above, we have used the value of I_{2D} for simple shear flows given in (3.4.10c).

From here, we can derive the general rheological model of a Bagnold fluid:

$$\sigma = -pI + \Phi_1 \text{dev}(d) + \Phi_2 d^2$$

$$\sigma = -pI + \left\{ 4a_i \sin \alpha_i \rho \lambda^2 c^2 (I_{2D})^{\frac{1}{2}} \right\} \text{dev}(d) - \left\{ 4a_i \cos \alpha_i \rho \lambda^2 c^2 \right\} d^2 \quad (3.4.21)$$

Again, it is important to remark that Bagnold model has been obtained for a granular fluid *under constant volume conditions*, and special care should be taken when generalizing it to more general situations.

3.4.4 Bingham fluids

So far, we have considered Newtonian and Bagnold fluids, which deforms when subjected to shear stress. The Bingham fluid model introduces a threshold for the shear stress below which no flow occurs. It provides an explanation to phenomena such as stoppage of flows and formation of plug regions.

The rheological law for simple shear conditions can be written as:

$$\begin{aligned} \left(\frac{\partial v_1}{\partial x_3} \right) &= \frac{1}{\mu} (\sigma_{13} - \tau_y) & \sigma_{13} > \tau_y \\ &= 0 & \sigma_{13} \leq \tau_y \end{aligned} \quad (3.4.22)$$

or

$$\sigma_{13} = \tau_y + \mu \frac{\partial v_1}{\partial x_3} \quad (3.4.23)$$

Following the same method as in previous cases, we can identify the components of the general rheological law. Observing the equations:

$$\sigma_{33} = -p - \Phi_0 + \frac{1}{4} \Phi_2 \left(\frac{\partial v_1}{\partial x_3} \right)^2 = -p$$

$$\sigma_{13} = \sigma_{31} = \frac{1}{2} \Phi_1 \frac{\partial v_1}{\partial x_3} = \tau_y + \mu \frac{\partial v_1}{\partial x_3}$$

we obtain:

$$\Phi_0 = \Phi_2 = 0$$

$$\Phi_1 = 2 \frac{1}{(\partial v_1 / \partial x_3)} \left(\tau_y + \mu \frac{\partial v_1}{\partial x_3} \right)$$

from where

$$\Phi_1 = \frac{2\tau_y}{(\partial v_1 / \partial x_3)} + 2\mu$$

and, using the value of I_{2D} for simple shear flows given in (3.4.10c):

$$\Phi_1 = \frac{\tau_y}{\sqrt{I_{2D}}} + 2\mu \tag{3.4.24}$$

The Bingham model for general flow condition is, therefore:

$$\sigma = -pI + \left(\frac{\tau_y}{\sqrt{I_{2D}}} + 2\mu \right) \text{dev}(d) \tag{3.4.25}$$

In the context of landslides, Bingham models have been used to model mixtures of fine grained soils with high water contents. Several researchers have provided values which can illustrate their ranges.

Rickenmann and Koch (1997) have taken values of τ_y and μ in the ranges 100-800 Pa and 400-800 Pa.s respectively, for simulations of debris flows which occurred in Kamikamihori (Japan) and Saas (Switzerland) valleys. They concluded that the use of Bingham models results on higher velocities of propagation than those predicted by other models.

It is also interesting to consider the values reported by Jan (1997), obtained from other works:

Author	ρ (Kg / m ³)	τ_y (Pa)	μ (Pa.s)
Jan		100 to 160	40-60
Johnson	2000 to 2400	60; 170 to 500	45

Sharp& Nobles	2400		20-60
Pierson	2090	130-240	210-810

Jin and Fread (1997) reported the following values for different sites:

Site	$\rho(Kg/m^3)$	$\tau_y(Pa)$	$\mu(Pa.s)$
Anhui	1570	38	2.1
Aberfan	1764	4794	958
Rudd Creek	1575	956	958

It is interesting to note that the selection of a particular rheological model is difficult, and several models can provide similar results. This is the case of the Aberfan flowslide, where basal pore pressures played an important role. This flowslide can be modelled using either a Bingham model or a frictional fluid model with dissipation of pore pressures, but in our opinion, the latter approach represents better what happened.

The basic Bingham model has been extended in the past decades to account for effects such as non linear viscosity components, for instance. One such extension is based on the following simple shear law:

$$\sigma_{13} = \tau_y + \mu \left(\frac{\partial v_1}{\partial x_3} \right)^\eta \quad (3.4.26)$$

where η is a material model. Bingham model is recovered by setting $\eta = 1$.

This law can be easily generalized to 3D situations as:

$$\sigma = -pI + \left\{ \frac{\tau_y}{\sqrt{I_{2D}}} + 2\mu(4I_{2D})^{\frac{\eta-2}{2}} \right\} \text{dev}(d) \quad (3.4.27)$$

The Herschel_Bulkley law described by Laigle and Coussot (1994) is a particular case of (4.26) where a value of $\eta > 1$ has been chosen. The authors used it for mudflows and muddy debris flows.

An interesting improvement for simple shear conditions proposed by Julien and Lan (1991) was the law:

$$\sigma_{13} = \tau_y + \mu \frac{\partial v_1}{\partial x_3} + \nu \left(\frac{\partial v_1}{\partial x_3} \right)^2 \quad (3.4.28)$$

The parameter ν is given by:

$$\nu = \rho l_m^2 + \hat{a}_i \rho_s \lambda^2 d_s^2 \quad (3.4.29)$$

In above:

- (i) l_m is the mixing length, which can be approximated as $0.4h$ where h is the flow depth of the landslide.
- (ii) \hat{a}_i is a material parameter which is close to 0.01 in most cases. Indeed, it correspond to $a_i \sin \alpha_i$ in Bagnolds model.

Again, the model can be generalized to 3D situations as:

$$\sigma = -pI + \left(\frac{\tau_y}{\sqrt{I_{2D}}} + 2\mu + 4\nu\sqrt{I_{2D}} \right) \text{dev}(d) \quad (3.4.30)$$

3.4.5 Generalized viscoplastic model of Chen and Ling

Chen and Ling (1996) proposed a model which could embrace as particular cases many rheological models. The basic idea was to generalize the following relations, valid for simple shear conditions:

$$\begin{aligned} \sigma_{13} &= s + \mu_1 \left(\frac{\partial v_1}{\partial x_3} \right)^{\eta_1} \\ \sigma_{33} &= -p + \frac{1}{3} \mu_2 \left(\frac{\partial v_1}{\partial x_3} \right)^{\eta_2} \end{aligned} \quad (3.4.31)$$

where μ_1 , μ_2 , η_1 and η_2 are model parameters for which they proposed ad-hoc expressions, and s is a yield stress of Mohr-Coulomb type:

$$s = c \cos \phi + p \sin \phi \quad (3.4.32)$$

with c and ϕ being the cohesion and the friction angle. From here, and using the method shown in the preceding models, we can identify:

$$\Phi_1 = \frac{s}{\sqrt{I_{2D}}} + 2\mu_1 (4I_{2D})^{\frac{\eta_1-1}{2}} \quad (3.4.33)$$

and

$$\Phi_2 = \frac{4}{3} \mu_2 \left(\frac{\partial v_1}{\partial x_3} \right)^{\eta_2-2} = \frac{4}{3} \mu_2 (4I_{2D})^{\frac{\eta_2-2}{2}}$$

The resulting general law is, therefore,

$$\sigma = -pI + \left\{ \frac{s}{\sqrt{I_{2D}}} + 2\mu_1 (4I_{2D})^{\frac{\eta_1-1}{2}} \right\} d + \left\{ \frac{4}{3} \mu_2 (I_{2D})^{\frac{\eta_2-2}{2}} \right\} d^2 \quad (3.4.34a)$$

or, taking into account that for simple shear flows $d = \text{dev}(d)$,

$$\sigma = -pI + \left\{ \frac{s}{\sqrt{I_{2D}}} + 2\mu_1 (4I_{2D})^{\frac{\eta_1-1}{2}} \right\} \text{dev}(d) + \left\{ \frac{4}{3} \mu_2 (I_{2D})^{\frac{\eta_2-2}{2}} \right\} d^2 \quad (3.4.34b)$$

It can be seen that above expression does not depend on the third invariant of the rate of deformation tensor, the reason being related to the fact that this invariant is zero in simple shear flows, which are the conditions in most of existing rheometers.

We leave as an exercise to the reader to derive the preceding models as particular cases of this general viscoplastic flow model.

One point of great importance is the consistency of the conditions when the rate of deformation is very small, $d \rightarrow 0$. All terms in (4.34) become zero, except $\frac{s}{\sqrt{I_{2D}}}$ and the pressure term. In the limit, we obtain

$$\lim_{d \rightarrow 0} \sigma = -pI + \frac{s}{\sqrt{I_{2D}}} d \quad (3.4.35)$$

We can see that the stress will depend on the direction of the rate of deformation tensor, as

$\frac{s}{\sqrt{I_{2D}}}$ is a scalar. In the case of a simple shear flow, where

$$\sqrt{I_{2D}} = \frac{1}{2} \left(\frac{\partial v_1}{\partial x_3} \right)$$

the components of the stress tensor are:

$$\begin{aligned} \sigma_{11} &= \sigma_{33} = -p \\ \sigma_{13} &= s = c \cos \phi + p \sin \phi \end{aligned} \quad (3.4.36)$$

which do not satisfy the Mohr-Coulomb on the plane $X_1 X_3$ but on a plane inclined $\frac{\pi}{2} + \frac{\phi}{2}$ criterion. Moreover, if these results are to be related to classical solid or soil mechanics approaches, some inconsistencies have to be removed from the model. Chen and Ling proposed to relax the conditions $d_{11} = 0$ $d_{33} = 0$ for the simple shear flow. Under plane strain conditions, the stress components are given by:

$$\begin{aligned}\sigma_{11} &= -p + (c \cos \phi + p \sin \phi) \frac{d_{11}}{\sqrt{d_{11}^2 + d_{13}^2}} \\ \sigma_{33} &= -p + (c \cos \phi + p \sin \phi) \frac{d_{33}}{\sqrt{d_{11}^2 + d_{13}^2}} \\ \sigma_{13} &= (c \cos \phi + p \sin \phi) \frac{d_{13}}{\sqrt{d_{11}^2 + d_{13}^2}}\end{aligned}\tag{3.4.37}$$

To derive above relations, we have used (3.4.14), which particularizes here to:

$$\sigma = -pI + \Phi_1 \begin{pmatrix} d_{11} & 0 & d_{13} \\ 0 & 0 & 0 \\ d_{31} & 0 & d_{33} \end{pmatrix}$$

together with (3.4.33)

$$\Phi_1 = \frac{s}{\sqrt{I_{2D}}} + 2\mu_1 (4I_{2D})^{\frac{\eta-1}{2}}$$

where

$$\sqrt{I_{2d}} = \sqrt{d_{11}^2 + d_{13}^2}$$

and the incompressibility condition $d_{11} + d_{33} = 0$

If we introduce the angle β as:

$$\begin{aligned}\lim_{d \rightarrow 0} \frac{d_{11}}{\sqrt{d_{11}^2 + d_{13}^2}} &= \cos \beta \\ \lim_{d \rightarrow 0} \frac{d_{13}}{\sqrt{d_{11}^2 + d_{13}^2}} &= \sin \beta\end{aligned}\tag{3.4.38}$$

we obtain, after substituting in (3.4.37)

$$\begin{aligned}\sigma_{11} &= -p - (c \cos \phi + p \sin \phi) \cos \beta \\ \sigma_{33} &= -p + (c \cos \phi + p \sin \phi) \cos \beta \\ \sigma_{13} &= (c \cos \phi + p \sin \phi) \sin \beta\end{aligned}\tag{3.4.39}$$

where we have taken into account that $d_{33} = -d_{11}$

These stress components fulfil Mohr Coulomb criterion as:

$$(\sigma_{11} + p)^2 + \sigma_{13}^2 = (c \cos \phi + p \sin \phi)^2 = s^2\tag{3.4.40}$$

as we can check in Figure 3.4.2:

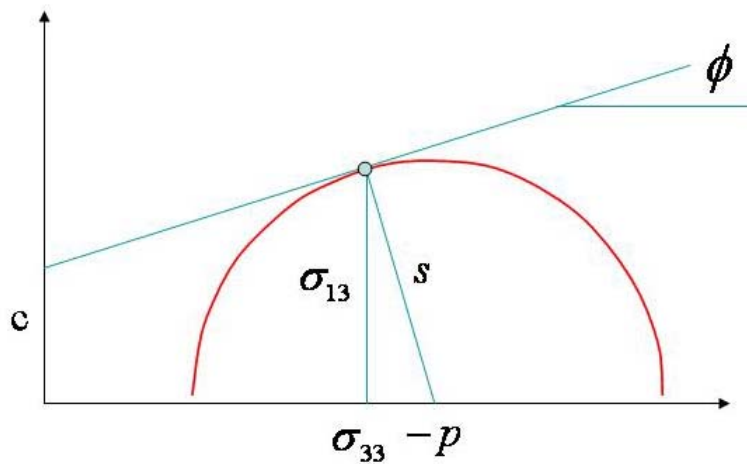


Figure 3.4.2 Mohr-Coulomb criterion for the 2D incompressible flow of a Chen and Ling fluid in the limit case $d \rightarrow 0$

Another interesting aspect is that $|\sigma_{11}| < |\sigma_{33}|$ if $\cos \beta > 0$, i.e. $D_{11} > 0$ (active state), and $|\sigma_{11}| > |\sigma_{33}|$ if $\cos \beta < 0$, i.e. $D_{11} < 0$ (passive state).

These results can be interpreted in a more general manner. There exists a process of fluidization or liquefaction in which the solid is transformed into a fluid. Failure of the soil takes place at the Critical State, with zero volume change. Rate of deformation fulfils the incompressibility condition, and it is close to the limit $d \rightarrow 0$. If the velocity and rate of deformation increases, the stress will abandon the yield surface, and material behaviour will be governed by the general equations (3.4.34).

There are other models which can be mentioned within this framework, such as that proposed by Johnson (1996). It is also worth mentioning the general model proposed by Hutter and co workers (Hutter et al 1996), who proposed to decompose the stress tensor of the granular phase into static and dynamic components as:

$$\begin{aligned}\sigma^{static} &= -p^{static} I + 2\mu^{static} d \\ \sigma^{dynamic} &= -p^{dynamic} I + 2\mu^{dynamic} d + 4\eta d^2\end{aligned}\tag{3.4.41}$$

3.5 DEPTH INTEGRATED RHEOLOGICAL MODELS

3.5.1 Introduction

Fast landslides, avalanches and debris flows are complex 3D phenomena which can be described by alternative models with different accuracy. In the more general situation, the equations of balance of linear momentum for all components of the mixture include the partial stresses, which have to be specified from the flow kinematics. In the preceding Section we have presented several rheological models which allow determination of the stress tensor once the rate of deformation tensor is known.

This approach is complex and expensive in computer time. As an alternative, we have introduced the depth integrated models, where velocities and stresses are integrated along the vertical axis. The equations are cast in terms of depth of flow and averaged velocities and stresses, and include the surface forces on the surface and the bottom.

We will recall here for completeness the depth integrated balance of momentum equations obtained in the Chapter devoted to describe the different alternative mathematical models available to describe fast landslides.

The basic equation is:

$$\frac{\partial}{\partial t}(h\bar{v}_i) + (1 + \alpha) \frac{\partial}{\partial x_j}(h\bar{v}_i\bar{v}_j) = b_i h + \frac{\partial}{\partial x_j}(h\bar{\sigma}_{ij}) + |N^A| t_i^A + |N^B| t_i^B\tag{3.5.1a}$$

or the alternative form

$$\begin{aligned}\frac{\partial}{\partial t}(h\bar{v}_i) + \frac{\partial}{\partial x_j} \left(h\bar{v}_i\bar{v}_j - \frac{1}{2} \rho b_3 h^2 \delta_{ij} \right) \\ = -\alpha \frac{\partial}{\partial x_j}(h\bar{v}_i\bar{v}_j) + \frac{\partial}{\partial x_j}(h\bar{\sigma}_{ij}^*) + b_i h + |N^A| t_i^A + |N^B| t_i^B\end{aligned}\tag{3.5.1b}$$

where it is important to notice:

(i) The forces at the basal surface t_i^B , which depend on the stresses.

(ii) The correction factor α defined from:

$$\int_Z^{Z+h} v_i^* v_j^* dx_3 = \alpha \bar{v}_i \bar{v}_j \quad (3.5.2)$$

where v_i^* is related to the depth averaged velocity as:

$$v_i(x_1, x_2, x_3) = \bar{v}_i(x_1, x_2) + v_i^*(x_1, x_2, x_3)$$

(iii) The depth integrated stress tensors $\bar{\sigma}_{ij}$ and $\bar{\sigma}_{ij}^*$ which has been obtained using the decomposition:

$$\sigma_{ij} = -p^* \delta_{ij} + \sigma_{ij}^* \quad (3.5.3a)$$

where

$$p^* = -\rho b_3 (Z + h - x_3)$$

After averaging along depth, we arrive to:

$$\bar{\sigma}_{ij} = -\bar{p} \delta_{ij} + \bar{\sigma}_{ij}^* \quad (3.5.3b)$$

with:

$$\begin{aligned} \bar{p} &= -\frac{1}{2} \rho b_3 h \\ \bar{\sigma}_{ij}^* &= \int_Z^{Z+h} \sigma_{ij}^* dx_3 \end{aligned} \quad (3.5.3c)$$

The original 3D equations have been greatly simplified as the resulting model is 2D, but the problem now is how to determine the correction factor α defined in (3.5.2), the basal forces per unit area t_i^B and the depth integrated stresses (3.5.3b) without having information of the 3D flow structure, which has been lost in the averaging process.

A possible solution which is widely used consist of assuming that the flow at a given point and time, with known depth and depth averaged velocities has the same vertical structure than a uniform, steady state flow. In the case of fast landslides this model is often referred to as the infinite landslide, as it is assumed to have constant depth and move at constant velocity along a constant slope.

In addition to provide depth integrated stresses and basal friction, the infinite landslide model can be used in order to (i) determine the conditions at which a landslide is triggered, and (ii) provide a first estimate of paths and velocities.

This Section is devoted to present the infinite landslide model and the method to obtain basal friction and depth averaged stresses.

3.5.2 The Infinite Landslide model

In what follows, we will assume that our infinite landslide takes place along a plane with constant slope. We will use the notation introduced in figure 3.5.1, where there are depicted the main variables which will be used in the analysis.

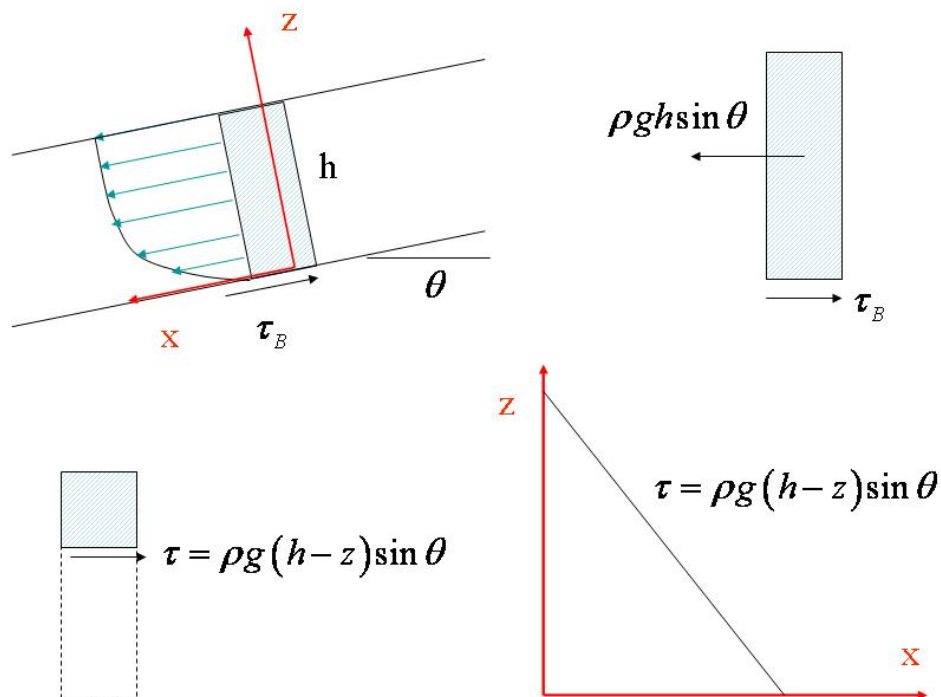


Figure 3.5.1 Infinite landslide

In the figure, we have considered a column of material of unit length and depth h . The flow structure is that of a simple shear flow. As acceleration along x axis is zero, we can write the equilibrium of the whole column as:

$$\rho g h \sin \theta = \tau_B \quad (3.5.4)$$

where ρ is the mixture density, g the gravity acceleration, θ the slope and τ_B the bottom friction. By considering the equilibrium of a part of the column extending from the surface to a depth $(h-z)$, we can obtain the shear stress as a function of z as:

$$\tau = \rho g (h-z) \sin \theta = \tau_B \left(1 - \frac{z}{h}\right) \quad (3.5.5)$$

Therefore, the shear stress varies linearly from zero at the surface to a maximum at the bottom given by eqn (5.4). This shear stress can be related to the rate of shear strain using the models described in the preceding Section. The ordinary differential integration can be integrated to yield the velocity profile, from which we can obtain the depth averaged velocity. Finally, the shear stress at the bottom will be obtained after elimination of the slope angle. We will apply this method to the rheological models described in the preceding Section.

Once we have obtained the velocity $v(\xi)$ where $\xi = \frac{z}{h}$, we can write the velocity as a function of the average velocity:

$$v(\xi) = \bar{v} f(\xi) \quad (3.5.6a)$$

where $f(\xi)$ is a function which depends on the rheological model. From here, we have:

$$v(\xi) = \bar{v} + v^*(\xi)$$

and

$$v^*(\xi) = \bar{v} (f(\xi) - 1) \quad (3.5.6b)$$

To obtain α in (3.5.2), we use above equation for the components of velocity:

$$v_i^* = \bar{v}_i (f(\xi) - 1) \quad v_j^* = \bar{v}_j (f(\xi) - 1)$$

from where we arrive to:

$$\alpha = \frac{\int_Z^{Z+h} v_i^* v_j^* dx_3}{\bar{v}_i \bar{v}_j} = \int_0^1 (f(\xi) - 1)^2 d\xi \quad (3.5.7)$$

Therefore, the correction factor α is obtained from the information provided by the infinite landslide model.

Finally, we will analyze the depth averaged stresses. Our purpose is to relate it to a depth integrated rate of deformation tensor. The starting point is the general rheological law (3.4.8):

$$\sigma = -pI + \Phi_0 I + \Phi_1 \text{dev}(d) + \Phi_2 d^2$$

where

$$\Phi_k = \Phi_k(I_{2D})$$

If we average along depth (4.8), the averaged magnitudes will not satisfy the averaged equation, i.e.

$$\bar{\sigma} \neq -\bar{p}I + \bar{\Phi}_0 I + \bar{\Phi}_1 \text{dev}(\bar{d}) + \bar{\Phi}_2 \bar{d}^2$$

unless the equation is linear, which only happens if Φ_0 and Φ_2 are zero and Φ_1 is constant. Should these conditions were satisfied, we could write:

$$\bar{\sigma} = -\bar{p}I + \Phi_1 \text{dev}(\bar{d})$$

To obtain the averaged components of the rate of deformation tensor d_{ij} , we will first consider the case $i, j = 1, 2$, where:

$$\bar{d}_{ij} = \frac{1}{2h} \left(\int_Z^{Z+h} \frac{\partial v_i}{\partial x_j} dx_3 + \int_Z^{Z+h} \frac{\partial v_j}{\partial x_i} dx_3 \right) \quad (3.5.8)$$

In the case of the simple shear flow or infinite landslide we are considering, we are using a reference system where the integral $\frac{1}{h} \int_Z^{Z+h} \frac{\partial v_i}{\partial x_j} dx_3$ is evaluated as:

$$\frac{1}{h} \int_0^h \frac{\partial v}{\partial x} dz = \frac{1}{h} \left\{ \frac{\partial}{\partial x} \int_0^h v dz - v \frac{\partial h}{\partial x} \Big|_h \right\}$$

from where:

$$\frac{1}{h} \int_0^h \frac{\partial v}{\partial x} dz = \frac{\partial \bar{v}}{\partial x}$$

as the depth of the flow does not depends on x .

This can be generalized to:

$$\frac{1}{h} \int_Z^{Z+h} \frac{\partial v_i}{\partial x_j} dx_3 = \frac{\partial \bar{v}_i}{\partial x_j} \quad \frac{1}{h} \int_Z^{Z+h} \frac{\partial v_j}{\partial x_i} dx_3 = \frac{\partial \bar{v}_j}{\partial x_i}$$

From here, substituting into (3.5.8), we arrive to:

$$\bar{d}_{ij} = \frac{1}{2} \left(\frac{\partial \bar{v}_i}{\partial x_j} + \frac{\partial \bar{v}_j}{\partial x_i} \right) \quad i, j = 1, 2 \quad (3.5.9)$$

The component \bar{d}_{33} is obtained in a straight forwards manner as follows:

$$\bar{d}_{33} = \frac{1}{h} \int_Z^{Z+h} \frac{\partial v_3}{\partial x_3} dx_3 = \frac{1}{h} (v_3|_{Z+h} - v_3|_Z) \approx \frac{1}{h} \frac{\partial h}{\partial t} \quad (3.5.10)$$

Finally, the components \bar{d}_{i3} with $i = 1, 2$, can be calculated using the assumption that the flow is that of an infinite landslide:

$$\bar{d}_{i3} = \frac{1}{h} \left\{ \int_Z^{Z+h} \frac{\partial v_i}{\partial x_3} dx_3 + \int_Z^{Z+h} \frac{\partial v_3}{\partial x_i} dx_3 \right\}$$

The second term is zero, as v_3 does not depend on x_i , and we arrive to:

$$\bar{d}_{i3} = \frac{1}{h} \int_Z^{Z+h} \frac{\partial v_i}{\partial x_3} dx_3 \quad (3.5.11)$$

which will be evaluated for the particular rheological model being used.

3.5.3 Newtonian fluids

For Newtonian fluids, the shear stress is given by (3.4.16) which will be written here as:

$$\tau = \mu \frac{\partial v}{\partial z} \quad (3.5.12)$$

from where:

$$\tau_B \left(1 - \frac{z}{h} \right) = \mu \frac{\partial v}{\partial z} \quad (3.5.13)$$

which can be integrated easily. The resulting velocity is:

$$v = \frac{\tau_B}{\mu} \left(z - \frac{z^2}{2h} \right) = \frac{\tau_B h}{\mu} \left(1 - \frac{z}{2h} \right) \frac{z}{h} \quad (3.5.14)$$

where we have taken into account that the velocity is zero at the basal surface. We can obtain the depth integrated velocity as:

$$\bar{v} = \frac{1}{h} \int_0^h v(z) dz = \frac{\tau_B h}{3\mu} \quad (3.5.15)$$

Therefore, the shear stress at the bottom is given by:

$$\tau_B = \frac{3\mu \bar{v}}{h} \quad (3.5.16)$$

From these results, we can conclude that an infinite slide in a Newtonian fluid (i) will be triggered when the slope is not zero, and, (ii) will not stop until the slope is zero.

Concerning the correction factor α in the balance of momentum equation, we will obtain it using (5.7)

$$\alpha = \frac{\int_Z^{Z+h} v_i^* v_j^* dx_3}{\bar{v}_i \bar{v}_j} = \int_Z^{Z+h} (f(\xi) - 1)^2 dx_3$$

where $\xi = x/h$ and the function $f(\xi)$ is determined from:

$$v = \frac{\tau_B h}{\mu} \left(1 - \frac{z}{2h}\right) \frac{z}{h} = 3\bar{v} \left(\xi - \frac{\xi^2}{2}\right)$$

$$v^* = \bar{v} \left(-1 + 3\xi - \frac{3\xi^2}{2}\right)$$

which results on:

$$\alpha = \frac{\int_Z^{Z+h} v_i^* v_j^* dx_3}{\bar{v}_i \bar{v}_j} = \int_Z^{Z+h} \left(-1 + \xi - \frac{\xi^2}{2}\right)^2 d\xi = 0.2 \quad (3.5.17)$$

The term \bar{d}_{13} is given by (5.11):

$$\bar{d}_{13} = \frac{1}{h} \int_Z^{Z+h} \frac{\partial v_i}{\partial x_3} dx_3$$

In our case, we will use the rheological law and the linearity of the shear stress profile, arriving to:

$$\bar{d}_{13} = \frac{3\bar{v}_i}{2h} \quad (3.5.18)$$

3.5.4 Bingham fluids

3.5.4.1 Rheology and flow structure

The rheological law governing the behaviour of a Bingham fluid was given in (3.4.23) as:

$$\tau = \tau_y + \mu \frac{\partial v}{\partial z} \quad (3.5.19)$$

The flow structure, in the general case, will consist of two separate parts, which have been depicted in Figure 3.5.2. In the upper part, from points S to P, the mobilized shear stress is smaller than τ_y . Therefore $\frac{\partial v}{\partial z} = 0$ and the velocity is constant in this region, which is referred to as a “plug”. From P to B, the mobilized shear stress is larger than τ_y , and a shear zone develops, with:

$$\frac{\partial v}{\partial z} = \frac{1}{\mu} (\tau - \tau_y) \quad (3.5.20)$$

It can be seen that, for a given slope, the height of the plug will depend on the yield stress τ_y . There is a limit height below which the flow will freeze. Therefore, if we think of a Bingham fluid flowing in a channel, it will stop at the moment when the height is smaller than $\frac{\tau_y}{\rho g \sin \theta}$. If more material arrives later, the height will be larger than the critical value and the flow will start moving again. This phenomenon has been reported in Chinese rivers.

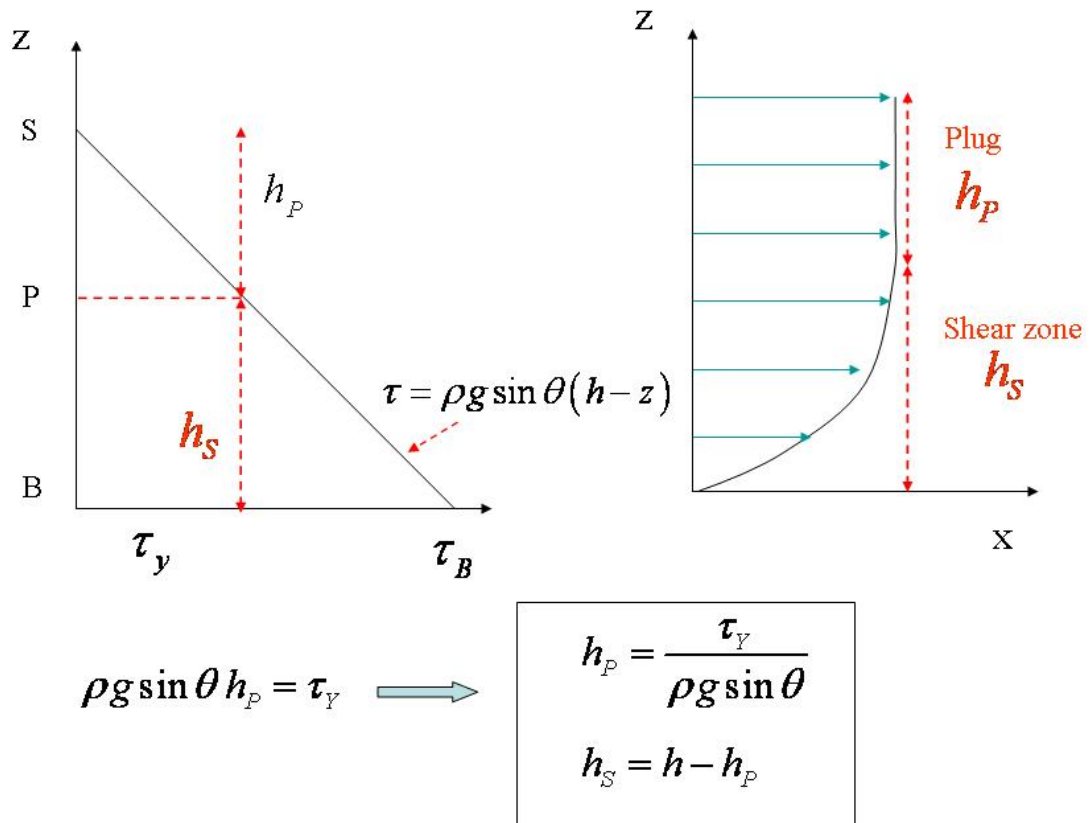


Figure 3.5.2 Flow structure of a Bingham fluid in a infinite simple shear flow

Some relations of interest which will be used later are the following:

$$h_p = \frac{\tau_y}{\rho g \sin \theta} = h \frac{\tau_y}{\tau_B} \tag{3.5.21a}$$

$$h_s = h \left(1 - \frac{\tau_y}{\tau_B} \right)$$

We will define the relative plug height η as:

$$\eta = \frac{h_p}{h} = \left(1 - \frac{h_s}{h} \right) = \left(1 - \frac{\tau_y}{\tau_B} \right) \tag{3.5.21b}$$

To obtain the velocity profile, we integrate:

$$\mu \frac{\partial v}{\partial z} = \tau - \tau_Y = (\tau_B - \tau_Y)(1 - \xi) \quad (3.5.22)$$

where $\xi = x/h_s$. In above we have used a geometrical relationship which is obtained considering the sketch given in figure 3.5.3 below.

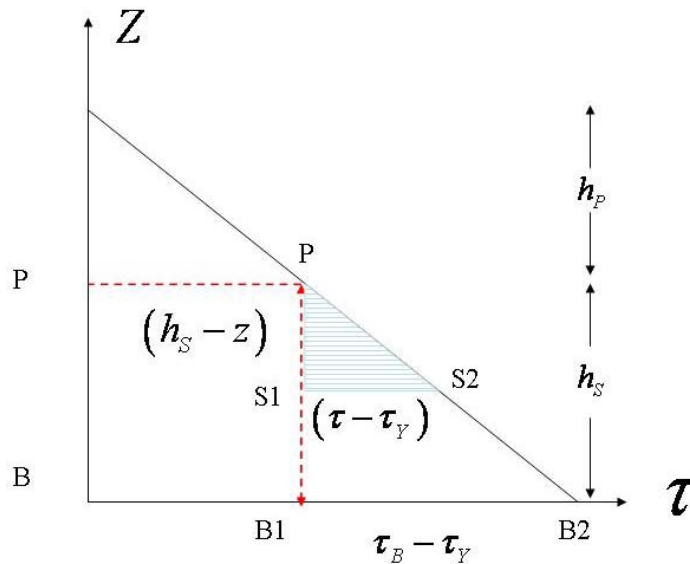


Figure 3.5.3 Profile of shear stress

Considering the triangles $PB1B2$ and $PS1S2$ we can write:

$$\frac{h_s - z}{h_s} = \frac{\tau - \tau_Y}{\tau_B - \tau_Y}$$

from where:

$$\tau - \tau_Y = (\tau_B - \tau_Y)(1 - \xi)$$

Integrating (3.5.22) with respect to z , we obtain the velocity as:

$$v = \frac{\tau_B - \tau_Y}{\mu} h_s \left(\xi - \frac{\xi^2}{2} \right) \quad (3.5.23a)$$

The plug velocity corresponds to $\xi = 1$, i.e.,

$$v_p = \frac{\tau_B - \tau_Y}{2\mu} h_s \quad (3.5.24a)$$

From here, we can express the velocity as:

$$v = 2v_p \left(\xi - \frac{\xi^2}{2} \right) \quad (3.5.24b)$$

To obtain the average velocity, we will use again a simple geometrical consideration. The profile of velocity consists of two parts, the plug and the shear zone (Figure 3.5.4).

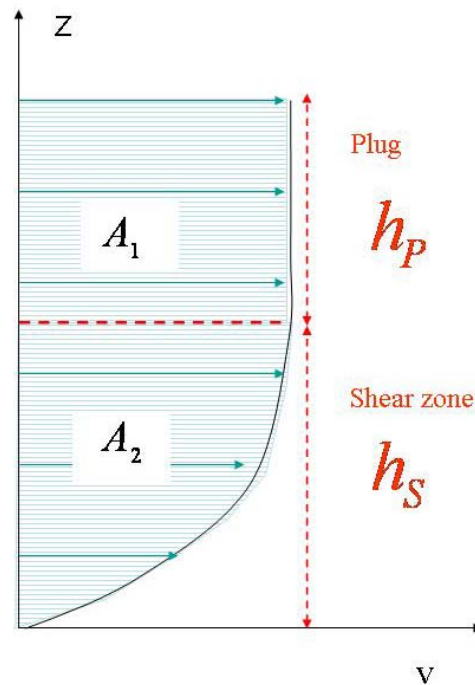


Figure 3.5.4 Profile of velocity

The average velocity is computed as:

$$\bar{v} = \frac{1}{h} \left\{ \int_0^{h_s} v dz + \int_{h_s}^{h_p} v dz \right\} = \frac{1}{h} (A_1 + A_2)$$

where A_1 and A_2 are the areas depicted in the figure, which are a rectangle and a second order parabola. We obtain:

$$\bar{v} = \frac{1}{h} \left(\eta h v_p + \frac{2}{3} (1-\eta) h v_p \right) = \frac{v_p}{3} (\eta + 2) \quad (3.5.25)$$

3.5.4.2 Basal friction

To obtain the basal friction, we will transform (3.5.25) into a more convenient form. After some algebra, we arrive to:

$$\bar{v} = \frac{\tau_B h}{6\mu} \left(1 - \frac{\tau_Y}{\tau_B} \right)^2 \left(2 + \frac{\tau_Y}{\tau_B} \right) \quad (3.5.26)$$

This equation can be written as:

$$\frac{6\mu\bar{v}}{h\tau_Y} \eta = (1-\eta)^2 (2+\eta)$$

This equation can be further simplified introducing the non dimensional number a

$$a = \frac{6\mu\bar{v}}{h\tau_Y}$$

which is related to the Bingham number B by:

$$B = \frac{4h\tau_Y}{\mu\bar{v}} = \frac{24}{a}$$

The non dimensional number a is equal to zero for purely cohesive fluids and tends to infinity for purely viscous fluids. After substitution, we obtain the following third order polynomial:

$$P_3(\eta) := \eta^3 - (3+a)\eta + 2 = 0 \quad (3.5.27)$$

Therefore, the basal friction cannot be obtained in a straightforward manner, and we will have to find the roots of $P_3(\eta)$ where $\eta = h_p / h$ and The solution of (3.5.27) lies in the interval $[0,1]$. Once we have computed η , we obtain the basal friction term as:

$$\tau_B = \tau_Y \frac{h}{h_p} = \frac{\tau_Y}{\eta}$$

To obtain the roots of the polynomial we can use Cardano's formula, which requires to transform the equation into the canonical form $\eta^3 + p\eta + q = 0$. In our case, the equation is already in canonical form. The first root ξ_1 is:

$$\eta_1 = \sqrt[3]{-\frac{q}{2} + \sqrt{R}} + \sqrt[3]{-\frac{q}{2} - \sqrt{R}}$$

where the discriminant R is

$$R = \left(\frac{q}{2}\right)^2 + \left(\frac{p}{3}\right)^3$$

The remaining roots are obtained as:

$$\eta_{2,3} = -\frac{\eta_1}{2} \pm \sqrt{\left(\frac{\eta_1}{2}\right)^2 + \frac{q}{\eta_1}}$$

In our case, the discriminant is:

$$R = \left(\frac{2}{2}\right)^2 - \left(1 + \frac{a}{3}\right)^3 < 0$$

and therefore we will have three complex valued solutions for η_1 . Because of this complexity, the friction term has been obtained either finding the root belonging to $[0,1]$ using an iterative method such as Newton-Raphson or by using one of the approximate solutions:

(i) Jin and Fread (1977) proposed the following semi empirical law:

$$\eta = \frac{\tau_Y}{\tau_B} = \left(1 + \frac{(m+1)(m+2)}{(0.74 + 0.656m)} \frac{\bar{v}}{h \left(\frac{\tau_Y}{\mu}\right)^m} \right)^{\frac{1}{m+0.15}}$$

which for $m = 1$ can be applied to a Bingham fluid:

$$\eta = \frac{\tau_Y}{\tau_B} = \left(1 + \frac{1}{1.396} a \right)^{\frac{1}{1.15}} \quad (3.5.28)$$

(ii) Fread (1988) proposed the following estimate value:

$$\eta = \left(\frac{3}{2} + \frac{3\bar{v}\mu}{\tau_y h} \right)^{-1} = \frac{2}{3+a} \quad (3.5.29)$$

which was implemented in the code NWS_DAMBRK.

(iii) Jeyapalan, Duncan and Seed proposed the simple law:

$$\eta = \frac{3}{3+a} \quad (3.5.30)$$

The accuracy of these approximations can be seen in Figure 3.5.5, where we have plotted the relative height of the plug ξ as function of the non dimensional number a .

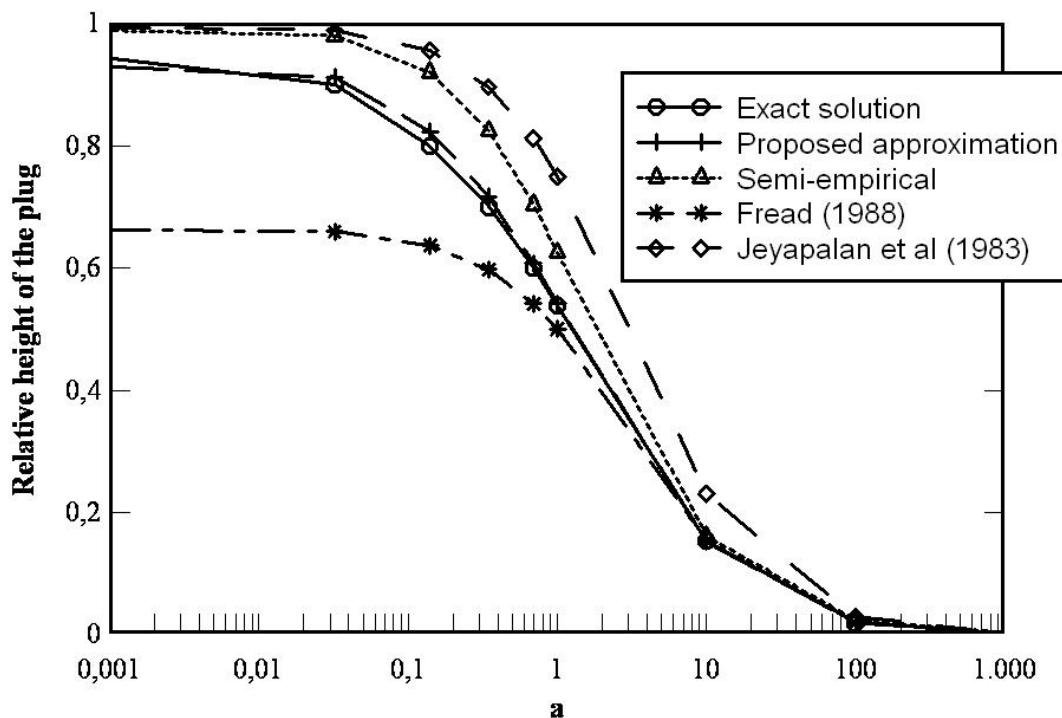


Figure 3.5.5 Alternative approximations to basal friction on Bingham fluids

The authors (Pastor et al. 2004) have proposed a simple yet accurate approximation based on using a polynomial economization technique which consists on obtaining the second order polynomial $P_2(\eta)$ which is the best approximation to $P_3(\xi)$ in the sense of the uniform distance in the interval $[0,1]$.

The error $E = P_3(\eta) - P_2(\eta)$ is given by:

$$E = \frac{1}{3!} \frac{d^3 P_3(\eta)}{d\eta^3} \Pi(\eta) \quad (3.5.31)$$

where

$$\Pi(\eta) = (\eta_0 - \eta)(\eta_1 - \eta)(\eta_2 - \eta)$$

with η_0, η_1 and η_2 being the points used in the interpolation, i.e., the points where both polynomials coincide. The maximum error can be minimized if η_0, η_1 and η_2 are chosen as the roots of the third Tchebichef polynomial T_3 , which is written in terms of $t \in [-1, 1]$ as:

$$T_3(t) = 4t^3 - t^2$$

or

$$T_3(\eta) = 32\eta^3 - 48\eta^2 + 18\eta - 1 \quad \eta \in [0, 1]$$

The error is obtained using (3.5.31):

$$E = \eta^3 - \frac{3}{2}\eta^2 + \frac{9}{16}\eta - \frac{1}{16}$$

and once $E(\eta)$ is known, we obtain $P_2(\eta)$ as

$$P_2(\eta) = P_3(\eta) - E = \frac{3}{2}\eta^2 - \left(\frac{57}{16} + a\right)\eta + \frac{65}{32} \quad (3.5.32)$$

The maximum error is $1/32$ in $[0, 1]$.

Therefore, the approximation consists of solving the second order equation

$$\frac{3}{2}\eta^2 - \left(\frac{57}{16} + a\right)\eta + \frac{65}{32} = 0 \quad (3.5.33)$$

The accuracy of this approximation can be observed in figure 3.5.3, providing an excellent approximation in the whole range of values of a .

3.5.4.3 Momentum correction factor

To obtain the correction factor α for the balance of linear momentum, we will use the alternative definition:

$$\alpha = \frac{1}{h} \frac{\int_0^h v^2 dz}{\bar{v}^2} - 1 \quad (3.5.34)$$

which can be derived easily from its original definition:

$$\alpha \bar{v}^2 = \frac{1}{h} \int_0^h (v - \bar{v})^2 dz$$

It is convenient to use the definitions of the velocity and the average velocity in terms of the plug velocity (3.5.24b) and (3.5.25). After some algebra, we obtain:

$$\alpha = \frac{3}{5} \left\{ \frac{(7\eta + 8)}{(\eta + 2)^2} \right\} - 1 \quad (3.5.35)$$

We have depicted in Figure 5.6 the values of the correction factor as a function of the non dimensional plug height.

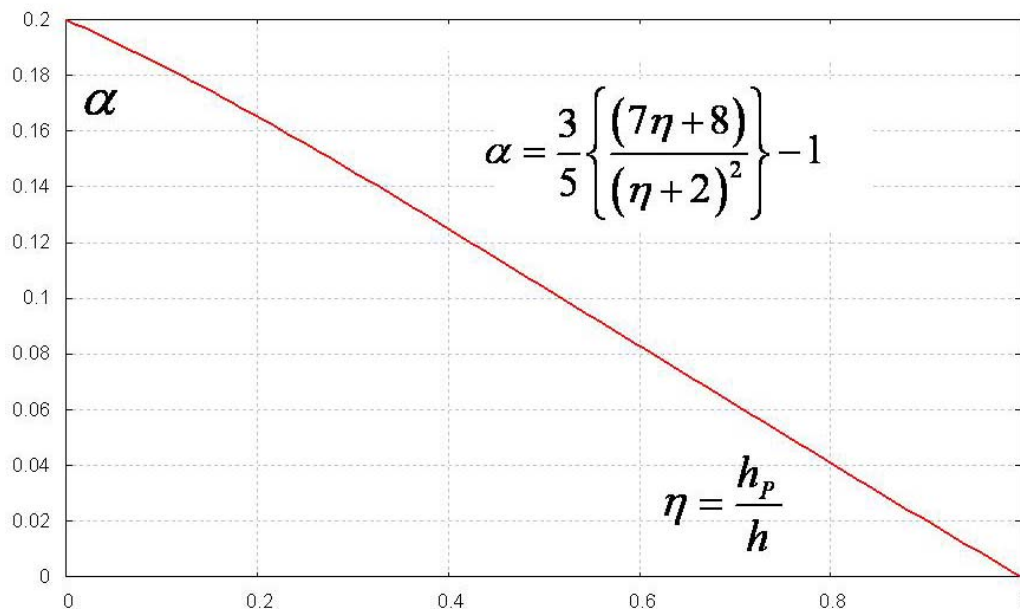


Figure 3.5.6 Correction factor for a Bingham fluid

We can see it varies linearly from 0.2 in the case of a Newtonian fluid with $\tau_y = 0$ to zero in the case of $h_p = h$.

3.5.4.4 Depth averaged stresses

The depth averaged stress tensor will be assumed to be:

$$\bar{\sigma} = -\bar{p}I + \left(\frac{\tau_y}{\sqrt{I_{2D}}} + 2\mu \right) \text{dev}(\bar{d}) \quad (3.5.36)$$

where the averaged pressure is given by

$$\bar{p} = \frac{1}{2} \rho b_3 (Z + h - x_3) \quad (3.5.37)$$

The components of the depth averaged rate of deformation tensor are obtained as explained in Section 3.5.2:

$$\bar{d}_{ij} = \frac{1}{2} \left(\frac{\partial \bar{v}_i}{\partial x_j} + \frac{\partial \bar{v}_j}{\partial x_i} \right) \quad i, j = 1, 2$$

$$\bar{d}_{33} = \frac{1}{h} \int_Z^{Z+h} \frac{\partial v_3}{\partial x_3} dx_3 = \frac{1}{h} (v_3|_{Z+h} - v_3|_Z) \approx \frac{1}{h} \frac{\partial h}{\partial t}$$

$$\bar{d}_{13} = \frac{1}{h} \int_Z^{Z+h} \frac{\partial v_i}{\partial x_3} dx_3$$

The latter can be easily obtained as:

$$\bar{d}_{13} = \frac{\tau_B}{2\mu} (1-\eta)^2 \quad (3.5.38)$$

where we have used:

$$\begin{aligned} \frac{\partial v}{\partial z} &= \frac{\tau_B - \tau_Y}{\mu} (1-\xi) & z \leq h_s \\ &= 0 & h_s < z \leq h \end{aligned}$$

3.5.5 Bagnold Fluids

3.5.5.1 Introductory remarks

We will assume that the soil is saturated, has a porosity n and consists of particles having a density ρ_s .

The components of the stress tensor for a Bagnold fluid were given in (3.4.19)-(3.4.21). We will write them for completeness below:

$$\sigma_{13} = a_i \sin \alpha_i \rho \lambda^2 c^2 \left(\frac{\partial v_1}{\partial x_3} \right)^2$$
$$\sigma_{33} = p + a_i \cos \alpha_i \rho \lambda^2 c^2 \left(\frac{\partial v_1}{\partial x_3} \right)^2$$

where we have assumed compression stresses are positive. In order to simplify the notation, we will write the stresses as:

$$\tau = \mu_B \sin \phi_B \left(\frac{\partial v}{\partial z} \right)^2$$
$$\sigma_v = p + \mu_B \cos \phi_B \left(\frac{\partial v}{\partial z} \right)^2 \tag{3.5.39}$$
$$\sigma_h = \sigma_v$$

where we have introduced the material parameter

$$\mu_B = a_i \rho \lambda^2 c^2 \tag{3.5.40}$$

and denoted $\phi_B = \alpha_i$

There are some remarks concerning the stress state. First of all, the model was proposed by Bagnold who performed experiments on grains with the same density than water, in order to avoid the effects of a variation of vertical and horizontal stresses due to gravity. When the mixture is at rest, the stress tensor is hydrostatic, all the components σ_{ii} of the total stress tensor being equal to p . If we consider a granular mixture which is starting to move, this stress state is not valid unless the soil has liquefied, i.e., the mean effective confining pressure is zero.

The total vertical stress in the soil phase is given by:

$$\sigma_v / g(h-z) = (1-n)\rho'_s = \rho'_d \quad (3.5.41)$$

where the submerged density of soil particles ρ'_s is

$$\rho'_s = \rho_s - \rho_w \quad (3.5.42a)$$

and

$$\rho'_d = (1-n)\rho'_s \quad (3.5.42b)$$

If the soil has liquefied, the increment in pore pressure should be equal to σ_v . The total pore pressure will be:

$$\begin{aligned} p_w / g(h-z) &= \rho_w + (1-n)\rho'_s \\ &= \rho_w + (1-n)(\rho_s - \rho_w) \\ &= \rho \end{aligned} \quad (3.5.43)$$

The total pressure acting on the basal surface is obtained by adding the contributions of solid and fluid phases. Therefore, the pressure term which appears in (3.5.39) is given by:

$$p = g(h-z)\{(1-n)\rho_s + n\rho\} \quad (3.5.44)$$

If we plot the stress path in the (σ, τ) plane when the rotation speed in the rheometer is increasing, we obtain the results shown in Fig. 3.5.7. Starting from the point O, the effective stress state (p', τ) moves along a straight line with slope ϕ_B . The Mohr circle lies outside this line, and indeed it is tangent to a straight line having a slope $\tan \phi_{dyn}$ given by:

$$\sin \phi_{dyn} = \tan \phi_B \quad (3.5.44)$$

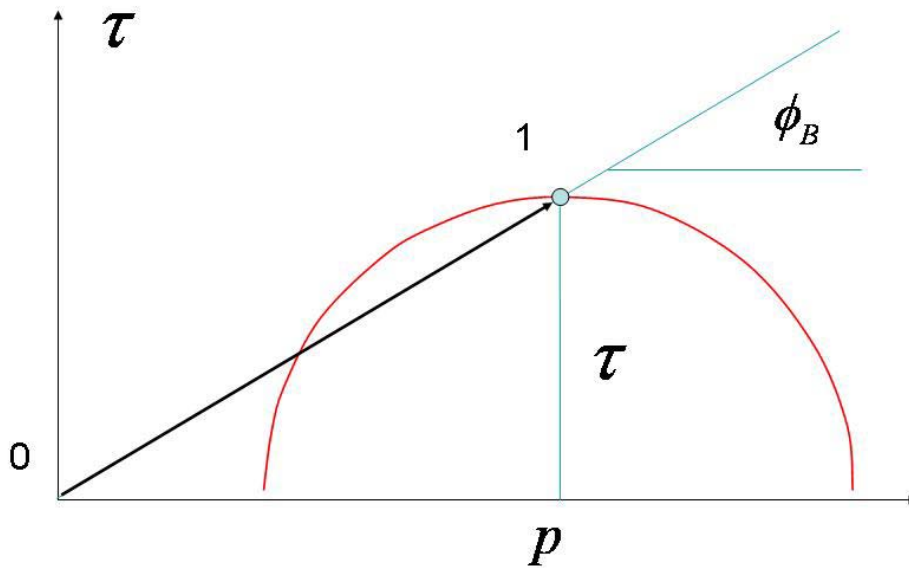


Figure 3.5.7 Stress path in the (p', τ) plane for a Bagnold's fluid

So far, we have avoided proposing any relation relating angles ϕ_B and ϕ_{dyn} to the residual angle of friction of the granular material we are considering. Indeed, the latter can be higher. In this case, the stress state would be outside the Mohr-Coulomb failure surface, which is consistent with viscoplasticity. We should keep in mind that Bagnold measured stresses once dynamic equilibrium had been reached, and it is possible that stress states of higher intensity exist.

3.5.5.2 Flow structure and basal friction

The vertical distribution of shear stress was obtained in (3.5.5):

$$\tau = \tau_b \left(1 - \frac{z}{h}\right) = \tau_b (1 - \xi)$$

where the shear stress is given by (3.5.39)

$$\tau = \mu_B \sin \phi_B \left(\frac{\partial v}{\partial z}\right)^2$$

From above expressions, after integration with respect to ξ , and using the boundary condition $v(0) = 0$, we arrive to:

$$v = \frac{2h}{3} \sqrt{\frac{\tau_b}{\mu_B \sin \phi_B}} \left\{ 1 - (1 - \xi)^{\frac{3}{2}} \right\} \quad (3.5.45)$$

If we denote the maximum velocity, which takes place at the surface, by v_p the velocity is:

$$v = v_p \left\{ 1 - (1 - \xi)^{\frac{3}{2}} \right\} \quad (3.5.46)$$

with

$$v_p = \frac{2h}{3} \sqrt{\frac{\tau_b}{\mu_B \sin \phi_B}} \quad (3.5.47)$$

The averaged velocity \bar{v} is obtained by integrating along the vertical direction the velocity, and it is given by:

$$\bar{v} = \frac{3}{5} v_p = \frac{2h}{5} \sqrt{\frac{\tau_b}{\mu_B \sin \phi_B}} \quad (3.5.48)$$

From here, it is immediate to obtain the basal friction as:

$$\tau_b = \frac{25}{4} \mu_B \sin \phi_B \frac{\bar{v}^2}{h^2} \quad (3.5.49)$$

3.5.5.3 Momentum correction factor

The correction factor in the depth averaged momentum equation will be obtained using (3.5.34):

$$\alpha = \frac{1}{h} \frac{1}{\bar{v}^2} \int_0^1 (v - \bar{v})^2 h d\xi = \frac{\int_0^1 v^2 d\xi}{\bar{v}^2} - 1$$

In our case, we have:

$$\int_0^1 v^2 d\xi = \frac{9}{20} h v_p^2$$

from where the momentum correction factor is obtained as:

$$\alpha = 0.25$$

3.5.5.4 Depth averaged stresses

The stress tensor was found to be given by (4.21):

$$\sigma = -pI + \left\{ 4a_i \sin \alpha_i \rho \lambda^2 c^2 (I_{2D})^{\frac{1}{2}} \right\} \text{dev}(d) - \left\{ 4a_i \cos \alpha_i \rho \lambda^2 c^2 \right\} d^2$$

or, with the notation introduced here:

$$\sigma = -pI + \left\{ 4\mu_B \sin \phi_B (I_{2D})^{\frac{1}{2}} \right\} \text{dev}(d) - \left\{ 4\mu_B \cos \phi_B \right\} d^2 \quad (3.5.50)$$

Please note that according that, as explained above, $\bar{p} = g(h-z)(\rho + n\rho'_d)$, where $g(h-z)n\rho'_d$ is the excess pore pressure which has caused liquefaction.

The depth averaged stress tensor will be assumed to be:

$$\bar{\sigma} = -\bar{p}I + \left\{ 4\mu_B \sin \phi_B (\bar{I}_{2d})^{\frac{1}{2}} \right\} \text{dev}(\bar{d}) - \left\{ 4\mu_B \cos \phi_B \right\} \bar{d}^2 \quad (3.5.51)$$

We will consider first the linear term $\left\{ 4\mu_B \sin \phi_B (\bar{I}_{2d})^{\frac{1}{2}} \right\} \text{dev}(\bar{d})$. According to (3.5.9), the components of the averaged rate of deformation tensor

$$\bar{d}_{ij} = \frac{1}{2} \left(\frac{\partial \bar{v}_i}{\partial x_j} + \frac{\partial \bar{v}_j}{\partial x_i} \right) \quad i, j = 1, 2$$

can be obtained from the averaged velocities. In order to evaluate \bar{I}_{2d} we will need the components involving the vertical direction $\bar{d}_{13}, \bar{d}_{23}$ and \bar{d}_{33} .

The latter was proposed to be approximated by (3.5.37):

$$\bar{d}_{33} = \frac{1}{h} \frac{\partial h}{\partial t}$$

Concerning $\bar{d}_{13}, \bar{d}_{23}$ they are approximated as:

$$\bar{d}_{k3} = \frac{1}{h} \int_0^h \frac{\partial v_k}{\partial x_3} dz \quad k = 1, 2$$

In the case of the infinite landslide, above integral is obtained easily by integrating along the vertical direction, resulting on:

$$\bar{d}_{k3} = \frac{5 \bar{v}_k}{3 h} \quad k = 1, 2 \quad (3.5.52)$$

Next, we will obtain the quadratic term $-\{4\mu_B \cos \phi_B\} \bar{d}^2$. Note that \bar{d}^2 is the average of d^2 and not the second power of the averaged tensor.

We will use an auxiliary reference system (x, y, z) , where $z \equiv x_3$, x is horizontal and parallel to the averaged horizontal velocity \bar{v} , and y orthogonal to x and z . We will further assume that the flow structure is that of a simple shear flow (infinite landslide). In this reference system, \bar{d}^2 only has two non zero components, $\bar{d}_{xx}^2 = \bar{d}_{zz}^2$ which are given by:

$$\bar{d}_{xx}^2 = \frac{1}{h} \int_0^h \left(\frac{\partial v}{\partial z} \right)^2 dz \quad (3.5.53)$$

The integral can be easily computed, using (3.5.5) and (3.5.39):

$$\tau = \tau_b \left(1 - \frac{z}{h} \right) = \tau_b (1 - \xi)$$

from where:

$$\left(\frac{\partial v}{\partial z} \right)^2 = \frac{\tau_b}{\mu_B \sin \phi_B} (1 - \xi) \quad (3.5.54)$$

Substituting in (3.5.53), and integrating, we obtain:

$$\bar{d}_{xx}^2 = \frac{\tau_b}{2\mu_B \sin \phi_B}$$

This expression can be written in a more convenient way taking into account (5.49) which relates the basal shear to the averaged velocity. The result is:

$$\bar{d}_{xx}^2 = \frac{25 \bar{v}^2}{8 h^2} \quad (3.5.55)$$

from where we obtain the contribution of this quadratic term to the stress tensor as:

$$\sigma_{xx}^{dyn} = \frac{25}{8} \frac{\bar{v}^2}{h^2} \mu_B \cos \phi_B \quad (3.5.56)$$

This component has to be changed back to the reference system (x_1, x_2, x_3) and added to the term

$$\frac{\partial}{\partial x_j} \left(h \overline{\sigma_{ij}^*} \right)$$

3.5.5.5 Generalization

If we use an exponent m different from 2 in Bagnold model:

$$\begin{aligned} \tau &= \mu_B \sin \phi_B \left(\frac{\partial v}{\partial z} \right)^m \\ \sigma_v &= p + \mu_B \cos \phi_B \left(\frac{\partial v}{\partial z} \right)^m \\ \sigma_h &= \sigma_v \end{aligned} \quad (3.5.57)$$

we obtain:

(i) The velocity profile is:

$$v = v_P \left\{ 1 - (1 - \xi)^{\frac{m+1}{m}} \right\} \quad (3.5.58)$$

where

$$v_P = \frac{m}{m+1} h \left(\frac{\tau_b}{\mu_B \sin \phi_B} \right)^{\frac{1}{m}} \quad (3.5.59)$$

(ii) The averaged velocity is:

$$\bar{v} = \frac{m+1}{2m+1} v_P \quad (3.5.60)$$

(iii) The bottom friction is:

$$\tau_b = \left(\frac{2m+1}{m} \right)^m \frac{\mu_B \bar{v}^m}{h^m} \quad (3.5.61)$$

(iv) The momentum correction factor is given by:

$$\alpha = \frac{m}{3m + 2} \quad (3.5.62)$$

This relation is depicted in Figure 3.5.8. The value of the correction factor increases with the exponent m , reaching a maximum asymptotic value of $1/3$.

(v) The dynamic contribution to the averaged stress along the direction of the flow is:

$$\sigma_{xx}^{dyn} = \frac{1}{2} \left(\frac{2m+1}{m} \right)^m \mu_B \cos \phi_B \frac{\bar{v}^m}{h^m} \quad (3.5.63)$$

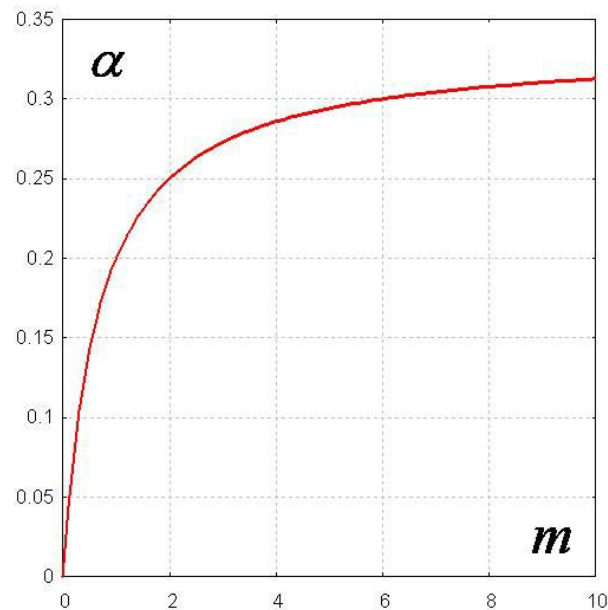


Figure 3.5.8 Momentum correction factor

3.5.6 Generalized Viscoplastic Flow Model of Chen and Lin

3.5.6.1 Introductory remarks

This model was developed assuming that the soil is either dry or saturated with a hydrostatic pore pressure $p_w = \rho_w g(h - z)$. Therefore, total and effective stresses coincide. We will extend here the model to a more general situation where an excess of pore pressure exists.

The Generalized Viscoplastic Flow model proposed by Chen and Ling (1996), which was given in (3.4.34)

$$\sigma = -pI + \left\{ \frac{s}{\sqrt{I_{2D}}} + 2\mu_1 (4I_{2D})^{\frac{\eta_1-1}{2}} \right\} \text{dev}(d) + \left\{ \frac{4}{3} \mu_2 (I_{2D})^{\frac{\eta_2-2}{2}} \right\} d^2$$

particularizes to

$$\begin{aligned} \tau &= s + \mu_1 \left(\frac{\partial v}{\partial z} \right)^{\eta_1} \\ \sigma_v = \sigma_h &= p + \frac{1}{3} \mu_2 \left(\frac{\partial v}{\partial z} \right)^{\eta_2} \end{aligned} \tag{3.5.64a}$$

in the case of the infinite landslide considered here. In above, we have taken compressions as positive; s represents the strength or failure conditions of the fluidized mixture:

$$s = c \cos \phi + p' \sin \phi \tag{3.5.64b}$$

with c and ϕ being the cohesion and the friction angle. In above, μ_1 , μ_2 , η_1 and η_2 are model parameters.

In above, the pressure term p is obtained by adding up the contributions from:

(i) soil skeleton

$$p^{(s)} = (1 - n) \rho_s g(h - z) \tag{3.5.65a}$$

(ii) hydrostatic component of pore water pressure

$$p^{(w)} = n \rho_w g(h - z) \tag{3.5.65b}$$

(iii) excess pore water pressure

$$\Delta p^{(w)} = \beta_w p^{(w)} \tag{3.5.65c}$$

where we have introduced the variable β_w to describe the excess pore pressure as a fraction β_w of the hydrostatic pore pressure.

Therefore,

$$\begin{aligned} p &= g(h-z)\{(1-n)\rho_s + n\rho_s + \beta_w n\rho_s\} \\ &= g(h-z)(\rho + \beta_w n\rho_s) \end{aligned} \quad (3.5.66d)$$

Concerning the strength term s it is important to notice that the frictional part depends on the effective stress, which is given by:

$$\begin{aligned} p' &= g(h-z)\{(\rho_s - \rho_w)(1-n) - \beta_w \rho_w\} \\ &= g(h-z)(\rho'_d - \beta_w \rho_w) \end{aligned} \quad (3.5.67)$$

We will study here the particular case:

$$\begin{aligned} \mu_1 &= \mu_C \sin \phi_C \\ \frac{1}{3} \mu_2 &= \mu_C \cos \phi_C \\ \eta_1 &= \eta_2 = m \end{aligned} \quad (3.5.68a)$$

from where

$$\begin{aligned} \tau &= s + \mu_C \sin \phi_C \left(\frac{\partial v}{\partial z} \right)^m \\ \sigma_v = \sigma_h &= p + \mu_C \cos \phi_C \left(\frac{\partial v}{\partial z} \right)^m \end{aligned} \quad (3.5.68b)$$

To better understand this equation, we have represented in figure 3.5.9 the stress conditions at failure (p, τ) and the stress path followed when the rate of shear strain increases.

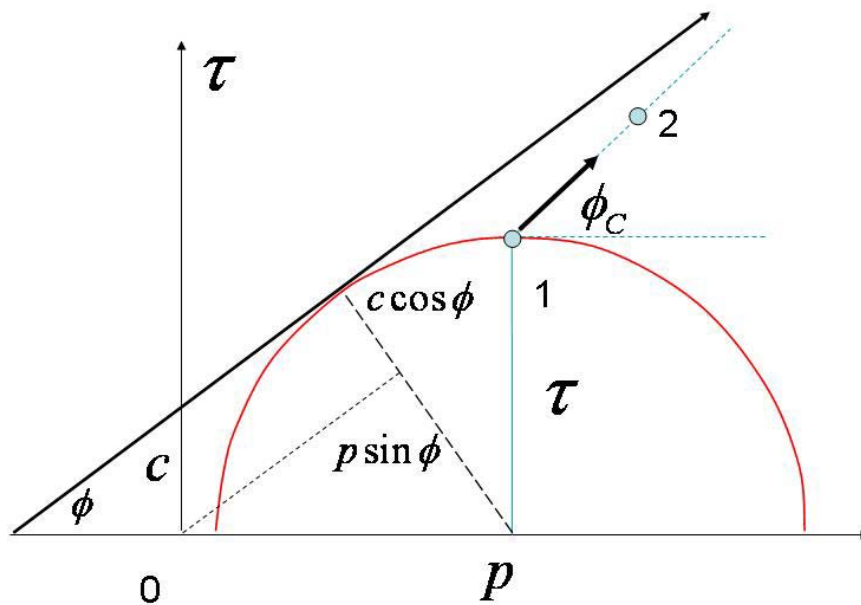


Figure 3.5.9 Stress conditions at failure and stress path of the fluidized mixture

We can observe several interesting facts.

- (i) The conditions (p, τ) depicted in the figure fulfil the Mohr circle conditions at failure. Chen model predicts $\sigma_v = \sigma_h$.
- (ii) The dynamic stress follows a straight line with origin at point 1, progressing to point 2, etc, as the shear component of the rate of deformation tensor increases. The angle is ϕ_c , which has to be greater or equal to ϕ
- (iii) It is more logical to think that failure conditions take place at a state of stress $(\sigma_h \neq \sigma_v; \tau)$. The dynamic stress path will follow Chen's law, but the initial residual conditions can change.

3.5.6.2 Flow structure

First of all, we will consider the vertical distribution of shear stress and strength s of the fluidized soil, which have been depicted in Figure 3.5.10. The shear stress increases with depth according to the law:

$$\tau(z) = \{(1-n)\rho_s + n\rho_w\} g(h-z) \sin \theta = \rho g(h-z) \sin \theta \quad (3.5.69)$$

while the shear strength distribution is:

$$\begin{aligned} s(z) &= c \cos \phi + p' \sin \phi \\ &= c \cos \phi + g(h-z)(\rho'_d - \beta_w \rho_w) \cos \theta \sin \phi \end{aligned} \quad (3.5.70)$$

For convenience we will introduce $\rho'_d^* = \rho'_d - \beta_w \rho_w$

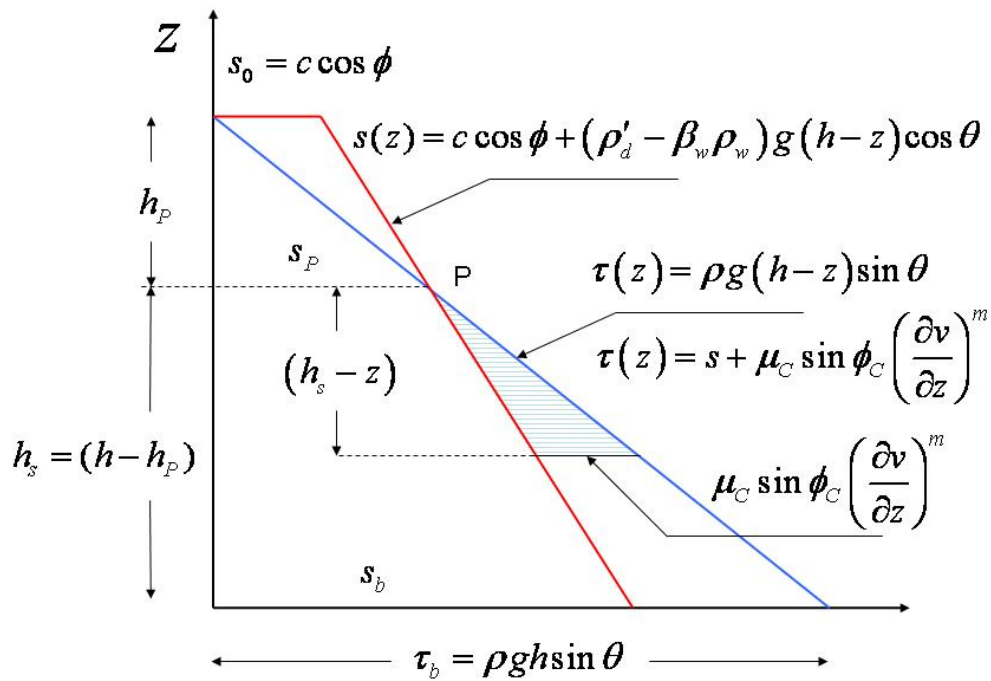


Figure 3.5.10 Shear strength and shear stress distributions for the infinite landslide with Chen and Ling model

The point P at which the shear strength is equal to the shear stress characterizes the plug. All the material above P will flow with a constant velocity v_p , while the fluidized soil below P will be sheared. The height of the plug is obtained from equations (3.5.69) and (3.5.70):

$$c \cos \phi + \rho'_d^* g h_p \cos \theta = \rho g h_p \sin \theta$$

The height of the plug is, therefore:

$$h_p = \frac{s_0 h}{\rho g h \left(\sin \theta - \frac{\rho'_d^*}{\rho} \cos \theta \sin \phi \right)}$$

from where:

$$h_p = \frac{s_0 h}{\rho g h \sin \theta \left(1 - \frac{\rho_d^* \cos \theta}{\rho \sin \theta} \sin \phi \right)} = \frac{s_0 h}{\tau_b \left(1 - \frac{\rho_d' \cos \theta}{\rho \sin \theta} \sin \phi \right)}$$

and

$$h_p = \frac{s_0 h}{\tau_b \left(\frac{\tan \theta - \frac{\rho_d^* \sin \phi}{\rho}}{\tan \theta} \right)} \quad (3.5.71)$$

which can be written in a more compact manner as:

$$h_p = \frac{s_0 h}{\tau_b^*} \quad (3.5.72)$$

with:

$$\tau_b^* = \tau_b \left(\frac{\tan \theta - \frac{\rho_d^* \sin \phi}{\rho}}{\tan \theta} \right) \quad (3.5.73)$$

Once h_p has been determined, we will study the velocity distribution in the shear zone extending from the bottom to the beginning of the plug at point P.

We will introduce the non dimensional vertical coordinate ξ in the shear zone as:

$$\xi = \frac{z}{h_s} \quad (3.5.74a)$$

and the relative plug height η

$$\eta = \frac{h_p}{h} \quad (3.5.74b)$$

If we consider the two triangles with a vertex at P depicted in fig.3.5.10, we have the following proportionality relation:

$$\frac{\mu_c \sin \phi_c \left(\frac{\partial v}{\partial z} \right)^m}{s_0} = \frac{(h_s - z)}{h_p} \quad (3.5.75)$$

from where we obtain

$$\frac{\partial v}{\partial z} = \left(\frac{s_0 h_s}{\mu_c \sin \phi_c h_p} \right)^{\frac{1}{m}} (1 - \xi)^{\frac{1}{m}} \quad (3.5.76)$$

Above equation can be integrated, and the resulting velocity profile is:

$$v = v_p \left\{ 1 - (1 - \xi)^{\frac{m+1}{m}} \right\} \quad (3.5.77)$$

where the plug velocity is:

$$v_p = \frac{m}{m+1} h_s \left(\frac{s_0 h_s}{\mu_c \sin \phi_c h_p} \right)^{\frac{1}{m}} \quad (3.5.78)$$

The flow structure is similar to the one depicted in figure 3.5.4 for Bingham fluids, with a plug and a shear part. The averaged velocity can be calculated following the same method, as:

$$\bar{v} = \frac{1}{h} \left\{ \int_0^{h_s} v dz + \int_{h_s}^{h_p} v dz \right\} = \frac{1}{h} (A_1 + A_2)$$

where A_1 and A_2 are the areas depicted in figure 5.4. We obtain:

$$A_1 = \eta h v_p$$

$$A_2 = \frac{m+1}{2m+1} v_p (1-\eta) h_s$$

and

$$\bar{v} = \frac{v_p}{2m+1} (m\eta + m + 1) \quad (3.5.79)$$

3.5.6.3 Basal friction

If we consider the triangles PA_1A_2 and PB_1B_2 depicted in Figure 3.5.11, we can express the basal friction as:

$$\tau_b = s_b + s_0 \left(\frac{1-\eta}{\eta} \right) \quad (3.5.80)$$

In this expression, both s_0 and s_b are known:

$$s_0 = c \cos \phi_C$$

$$s_b = s_0 + \rho_d^* g h \cos \theta$$

but we have to obtain the relative height of the plug η .

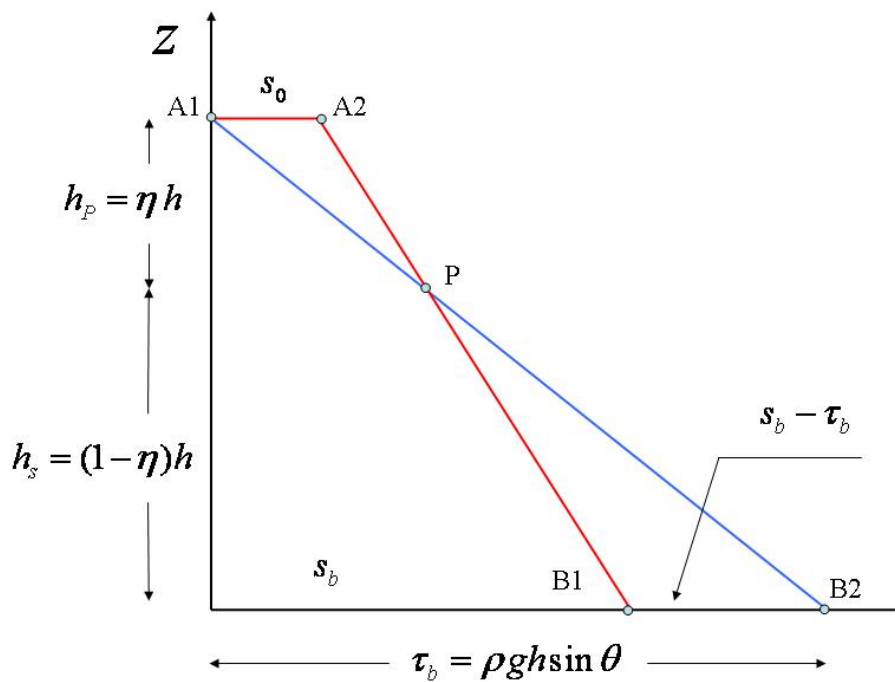


Figure 3.5.11 Obtaining basal friction

In depth integrated models, we have to determine the basal friction from the known averaged velocity \bar{v} . We will start with equation (3.5.79)

$$\bar{v} = \frac{v_p}{2m+1} (m\eta + m + 1)$$

where the plug velocity given in (3.5.78)

$$v_P = \frac{m}{m+1} h_s \left(\frac{s_0 h_s}{\mu_C \sin \phi_C h_P} \right)^{\frac{1}{m}}$$

will be elaborated taking into account that

$$h_s \left(\frac{h_s}{h_P} \right)^{\frac{1}{m}} = \left(\frac{h_s}{h} \right) \left(\frac{h_s}{h} \right)^{\frac{1}{m}} \left(\frac{h_P}{h} \right)^{\frac{1}{m}} = (1-\eta)^{\frac{m+1}{m}} \eta^{-\frac{1}{m}}$$

We obtain

$$\bar{v} = \frac{m}{(m+1)(2m+1)} \left(\frac{s_0}{\mu_C \sin \phi_C} \right) \left\{ \frac{(1-\eta)^{\frac{m+1}{m}}}{\eta^{\frac{1}{m}}} (m\eta + m + 1) \right\} \quad (3.5.81)$$

which relates the averaged velocity to the relative height of the plug η . If we introduce the non dimensional number a

$$a = \frac{(m+1)(2m+1)}{m} \left(\frac{\mu_C \sin \phi_C}{s_0} \right)^{1/m} \frac{1}{h} \bar{v} \quad (3.5.82)$$

equation (5.81) can be written as:

$$(1-\eta)^{m+1} (m\eta + m + 1)^m - a\eta = 0 \quad (3.5.83)$$

which is a polynomial of degree $2m + 1$.

The root of this polynomial belonging to $[0,1]$ is the non dimensional plug height, knowing which we can determine the basal friction using (3.5.80). The situation is the same described for Bingham fluids. The computational cost of having to find this root at all point s of the computational mesh and every time step is very high.

One interesting case is that of $m = 2$, which can be viewed as a generalization of Bagnold model. The polynomial is now:

$$P_5(\eta) = (1-\eta)^3 (2\eta + 3)^2 - a\eta = 0 \quad (3.5.84)$$

with

$$a = \frac{15}{2} \left(\frac{\mu_c \sin \phi_c}{s_0} \right)^{1/2} \frac{\bar{v}}{h} \quad (3.5.85)$$

In order to speed up computations in numerical models, there are several alternatives.

We will consider first to build a second order polynomial which is the best approximation of the fifth order polynomial $P_5(\eta)$ in the minimax sense. The method consists on writing $P_5(\eta)$ in a Tchebichef base $\{U_0(\eta)..U_5(\eta)\}$, and then to prune the terms in $\{U_3(\eta), U_4(\eta), U_5(\eta)\}$. The resulting polynomial $P_2(\eta)$ is the best approximation of $P_5(\eta)$. This technique is known as polynomial economization.

The steps are the following:

(i) Build a Tchebichef base in $[0,1]$

We will use the recurrence relation:

$$U_{n+1} = (2\eta - 1)U_n - U_{n-1} \quad (3.5.86)$$

with

$$\begin{aligned} U_0 &= 1 \\ U_1 &= 2\eta - 1 \end{aligned} \quad (3.5.87)$$

We obtain:

$$\begin{aligned} U_2 &= 8\eta^2 - 8\eta + 1 \\ U_3 &= 32\eta^3 - 48\eta^2 + 18\eta - 1 \\ U_4 &= 128\eta^4 - 256\eta^3 + 160\eta^2 - 32\eta + 1 \\ U_5 &= 512\eta^5 - 1280\eta^4 + 1120\eta^3 - 400\eta^2 + 50\eta - 1 \end{aligned} \quad (3.5.88)$$

(ii) We will obtain polynomials $P_4(\eta)$, $P_3(\eta)$ and finally, $P_2(\eta)$

$$P_2(\eta) = 10\eta^2 - (a + 19.2188)\eta + 9.1875 = 0 \quad (3.5.89)$$

The problem has been reduced to obtain the root of (5.89) belonging to $[0,1]$

We have plotted in Figure 3.5.12 polynomials $P_5(\eta)$ and $P_2(\eta)$ for different values of a .

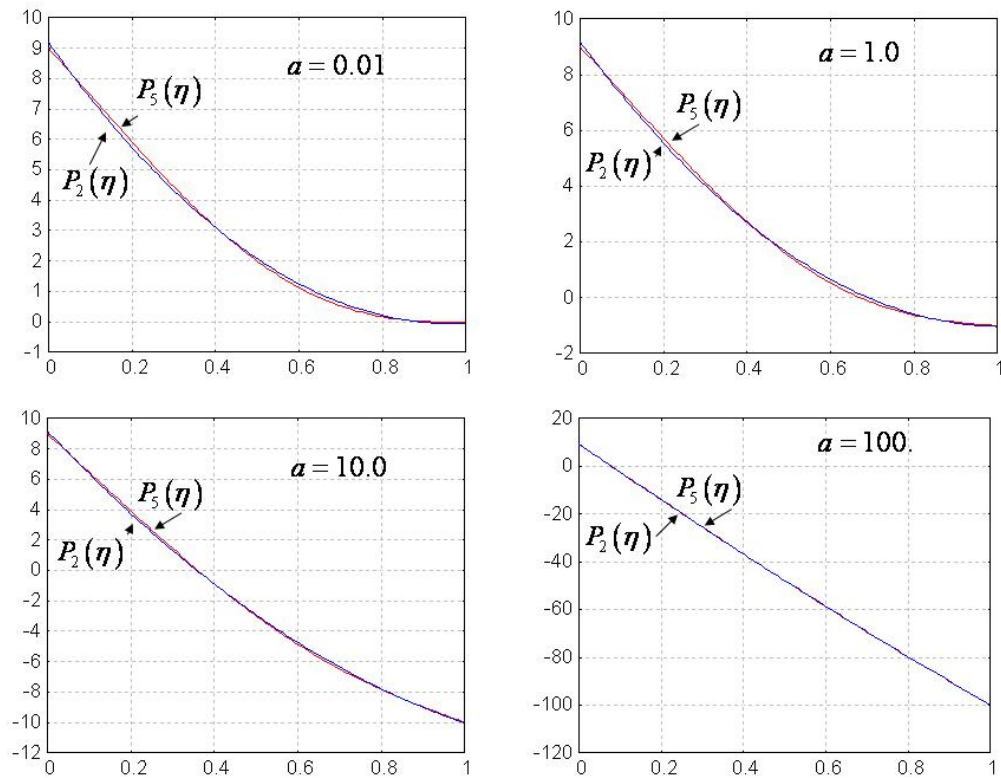


Figure 3.5.12 Polynomials $P_5(\eta)$ and $P_2(\eta)$

It is interesting to note that the approximating polynomials are accurate approximations of $P_5(\eta)$, except for very low values of α , where we find a 5% error. This case correspond to cohesive fluids with a small viscosity. We give more details in figure 5.13, where we have plotted the root against the parameter α .

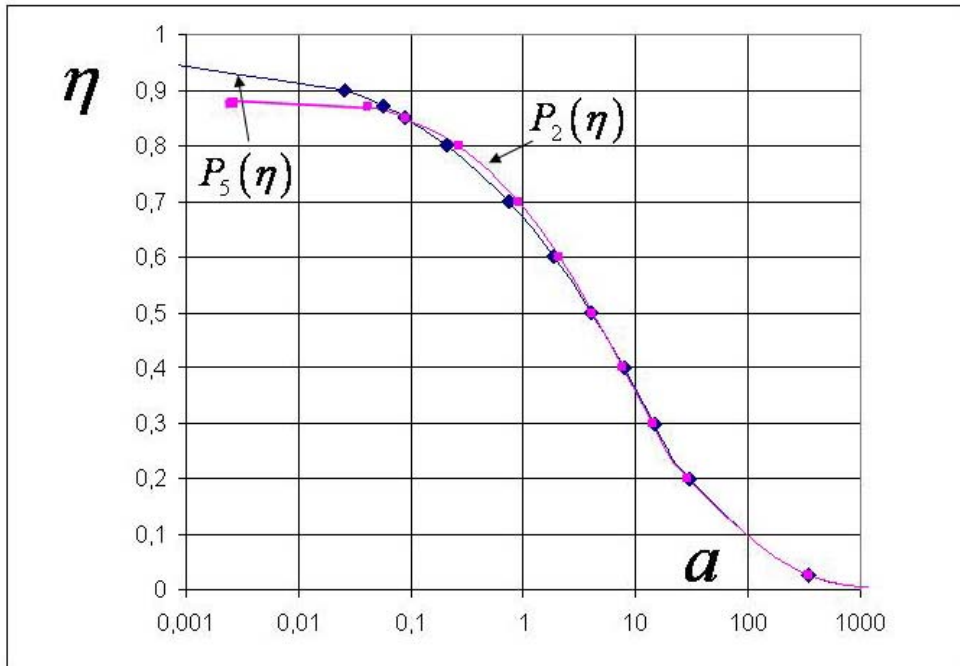


Figure 3.5.13 Relative height of the plug in Chen and Ling model. Exact and approximated solution.

3.5.6.4 Momentum Correction factor

We have seen that the momentum correction factor is given by (3.5.34):

$$\alpha = \frac{1}{h} \frac{\int_0^h v^2 dz}{\bar{v}^2} - 1$$

We will compute the integral considering the two areas shown in fig.3.5.4. It results:

$$\frac{1}{h} \int_{h_s}^h v^2 dz = v_p^2 \eta$$

for the area A_1 , and

$$\frac{1}{h} \int_0^{h_s} v^2 dz = v_p^2 (1 - \eta) \frac{2(m+1)^2}{(2m+1)(3m+2)}$$

for A_2 . From here, and after some algebra, we arrive to:

$$\alpha = \frac{\left\{ \eta + (1-\eta) \frac{2(m+1)^2}{(3m+2)(2m+1)} \right\}}{\left\{ \eta + (1-\eta) \frac{(m+1)}{(2m+1)} \right\}^2} - 1 \quad (3.5.90)$$

In the case $m = 2$, above expression particularizes to:

$$\alpha = \frac{5}{4} \left\{ \frac{9+11\eta}{(3+2\eta)^2} \right\} - 1 \quad (3.5.91)$$

3.5.6.5 Depth averaged stresses

Let us recall that the version of the Chen and Ling rheological model we are considering here can be obtained by substituting in (3.4.34)

$$\sigma = -pI + \left\{ \frac{s}{\sqrt{I_{2D}}} + 2\mu_1 (4I_{2D})^{\frac{\eta_1-1}{2}} \right\} \text{dev}(d) + \left\{ \frac{4}{3} \mu_2 (I_{2D})^{\frac{\eta_2-2}{2}} \right\} d^2$$

the values of the rheological parameters given in (3.5.68):

$$\begin{aligned} \mu_1 &= \mu_c \sin \phi_c \\ \frac{1}{3} \mu_2 &= \mu_c \cos \phi_c \\ \eta_1 &= \eta_2 = m \end{aligned}$$

from where:

$$\sigma = -pI + \left\{ \frac{s}{\sqrt{I_{2D}}} + 2\mu_c \sin \phi_c (4I_{2D})^{\frac{m-1}{2}} \right\} \text{dev}(d) + \left\{ 4\mu_c \cos \phi_c (I_{2D})^{\frac{m-2}{2}} \right\} d^2 \quad (3.5.92)$$

The pressure is given by (3.5.66d) as:

$$\begin{aligned} p &= g(h-z) \{ (1-n) \rho_s + n \rho_s + \beta_w n \rho_s \} \\ &= g(h-z) (\rho + \beta_w n \rho_s) \end{aligned}$$

We will assume that the depth averaged tensor is given by:

$$\bar{\sigma} = -\bar{p}I + \left\{ \frac{\bar{s}}{\sqrt{I_{2D}}} + 2\mu_c \sin \phi_c \left(4\overline{I_{2D}} \right)^{\frac{m-1}{2}} \right\} \text{dev}(\bar{d}) + \left\{ 4\mu_c \cos \phi_c \left(\overline{I_{2D}} \right)^{\frac{m-2}{2}} \right\} \bar{d}^2 \quad (3.5.93)$$

Therefore, to obtain the depth averaged stress tensor, we will have to evaluate the following items:

(i) The depth averaged strength \bar{s} , which can be easily computed as:

$$\bar{s} = \frac{1}{2} h (s_0 + s_b) \quad (3.5.94)$$

(ii) \bar{d}_{k3} $k=1,2$, which is obtained as:

$$\bar{d}_{k3} = \frac{1}{h} \int_0^h \frac{\partial v_k}{\partial x_3} dz \quad k=1,2$$

In the case of the infinite landslide, above integral is obtained easily by integrating along the vertical direction, resulting on:

$$\bar{d}_{k3} = \frac{2m+1}{(m\eta+m+1)} \frac{\bar{v}_k}{h} \quad k=1,2 \quad (3.5.95)$$

In the case $m=2$, we have:

$$\bar{d}_{k3} = \frac{5}{(2\eta+3)} \frac{\bar{v}_k}{h} \quad k=1,2 \quad (3.5.96)$$

(iii) \bar{d}_{xx}^2 where x is the abscissa in the direction of the flow.

Following the same method as we did for Bagnold's fluid, we obtain:

$$\bar{d}_{xx}^2 = \frac{1}{2} \left\{ \frac{(m+1)(2m+1)}{m(m\eta+m+1)} \right\}^m \left(\frac{\bar{v}}{h} \right)^m \frac{1}{(1-\eta)^{m-1}} \quad (3.5.97)$$

from where we obtain the contribution of this quadratic term to the stress tensor as:

$$\bar{\sigma}_{xx}^{dyn} = \frac{1}{2} \mu_c \cos \phi_c \left\{ \frac{(m+1)(2m+1)}{m(m\eta+m+1)} \right\}^m \left(\frac{\bar{v}}{h} \right)^m \frac{1}{(1-\eta)^{m-1}} \quad (3.5.98)$$

In the case $m=2$, above expression results in:

$$\overline{\sigma_{xx}^{dyn}} = \frac{1}{2} \mu_C \cos \phi_C \left(\frac{15}{2(2\eta+3)} \right)^2 \left(\frac{\bar{v}}{h} \right)^2 \frac{1}{(1-\eta)} \quad (3.5.99)$$

which has to be transformed back to the reference system (x_1, x_2, x_3) and added to the term

$$\frac{\partial}{\partial x_j} \left(h \overline{\sigma_{ij}^*} \right)$$

3.5.7 The Herschel-Bulkley fluid

The Herschel-Bulkley fluid can be considered a particular case of the Chen's generalized viscoplastic fluid, assuming that both the friction angle and the dispersive stresses are zero. In simple shear flow,

The main results are the following:

$$\tau = s + \mu_C \sin \phi_C \left(\frac{\partial v}{\partial z} \right)^m \quad (3.5.100)$$

$$\sigma_v = \sigma_h = p$$

Setting $s = \tau_y$ and $\mu_C \sin \phi_C = K$ we obtain:

$$\tau = \tau_y + K \left(\frac{\partial v}{\partial z} \right)^m \quad (3.5.101)$$

$$\sigma_v = \sigma_h = p$$

The height of the plug is the same than in the Bingham fluid, i.e.:

$$h_p = \frac{\tau_y h}{\tau_B} \quad (3.5.102)$$

Introducing the non dimensional vertical coordinate ξ in the shear zone $\xi = \frac{z}{h_s}$ and the

relative plug height $\eta = \frac{h_p}{h}$, we obtain the velocity profile:

$$v = v_p \left\{ 1 - (1 - \xi)^{\frac{m+1}{m}} \right\} \quad (3.5.103)$$

from where:

$$v_P = \frac{m}{m+1} h_s \left(\frac{\tau_y h_s}{K h_p} \right)^{\frac{1}{m}} \quad (3.5.104)$$

and

$$\bar{v} = \frac{v_P}{2m+1} (m\eta + m + 1) \quad (3.5.105a)$$

or

$$\bar{v} = \frac{m}{(m+1)(2m+1)} \left(\frac{\tau_y}{K} \right) \left\{ \frac{(1-\eta)^{\frac{m+1}{m}}}{\eta^{\frac{1}{m}}} (m\eta + m + 1) \right\} \quad (3.5.105b)$$

As in Chen's model, we introduce the non dimensional number a

$$a = \frac{(m+1)(2m+1)}{m} \left(\frac{K}{\tau_y} \right)^{1/m} \frac{1}{h} \bar{v} \quad (3.5.106)$$

we obtain the $2m+1$ polynomial

$$(1-\eta)^{m+1} (m\eta + m + 1)^m - a\eta = 0 \quad (3.5.107)$$

The solution of this equation provides η , from where we can obtain the basal friction as

$$\tau_b = \frac{\tau_y}{\eta} \quad (3.5.108)$$

The momentum correction factor was obtained in (3.5.90):

$$\alpha = \frac{\left\{ \eta + (1-\eta) \frac{2(m+1)^2}{(3m+2)(2m+1)} \right\}}{\left\{ \eta + (1-\eta) \frac{(m+1)}{(2m+1)} \right\}^2} - 1 \quad (3.5.109)$$

3.5.8 The frictional fluid

It is interesting to notice that most of existing depth integrated codes use very simple rheological laws, the main reason being the difficulty of implementing models such as the generalized viscoplastic model of Cheng and Ling.

One simple model which can be derived from Chen and Ling is the frictional fluid, where the cohesion and all viscous terms are disregarded.

We will consider first the vertical distributions of shear stress and strength, which are, respectively:

$$\tau(z) = \rho g (h - z) \sin \theta \quad (3.5.110)$$

and

$$s(z) = p' \tan \phi \quad (3.5.111)$$

where

$$p' = g (h - z) (\rho'_d - \beta_w \rho_w) \cos \theta \quad (3.5.112)$$

It can be seen that, as both are linear, if they are equal at the bottom, they will be equal all along the depth of the landslide. This condition reads:

$$\tan \theta = \frac{(\rho'_d - \beta_w \rho_w)}{\rho} \quad (3.5.112)$$

Without further additional data it is not possible to obtain the velocity distribution. This is why depth integrated models using pure frictional models cannot include the momentum correction factor. Concerning the basal friction, it is usually approximated as:

$$\tau_b = -p' \tan \phi \frac{\bar{v}_i}{|\bar{v}|} \quad (3.5.113)$$

Again, it is not possible to know the distribution of the shear stress along the vertical. In some cases, the fluidized soil flows over a basal surface made of a different material. If the friction angle between both materials δ is smaller than the friction angle of the fluidized soil, the basal shear stress is given by:

$$\tau_b = -(\rho'_d - \beta_w \rho_w) g h \tan \phi_b \frac{\bar{v}_i}{|\bar{v}|} \quad (3.5.114)$$

where the basal friction ϕ_b is

$$\phi_b = \min(\delta, \phi) \quad (3.5.115)$$

This simplified model implements the effect of pore pressure at the basal surface, and we can see that the effect of the pore pressure is similar to decreasing the friction angle.

Frictional fluid models can be complemented using some sort of additional basal friction taken from channel flows. We can mention here the Chezy-Manning equation where the basal friction is given by:

$$\tau_i^b = -\rho \frac{gn^2 |\bar{v}|}{h^{7/3}} \bar{v}_i \quad (3.5.116)$$

In above, n is the Manning number and g is the gravity.

Other interesting model which has proven useful in the case of rock avalanches is Voellmy's fluid, as shown by Hungr (1995) and Evans et al (2001). In this case, the bed friction term is:

$$\tau_b = - \left\{ \left(\rho'_d gh \tan \phi_b - p_w^b \right) \frac{\bar{v}_i}{|\bar{v}|} + \rho g \frac{|\bar{v}|}{\zeta} \bar{v}_i \right\} \quad (3.5.108)$$

This model introduces a friction term due to the turbulent dissipation. The turbulence coefficient ζ takes into account the thickness of the basal layer where most of the tangential deformation in granular materials would take place.

In the case of frictional fluids, some researchers have assumed that the horizontal and vertical stresses can be different, by introducing a K_0 parameter as in Soil Mechanics. The main problem is how to estimate this value, as it can change as the shearing velocity increases.

3.6 REFERENCES

R.A.Bagnold, "Experiments on a gravity-free dispersion of large solid spheres in a Newtonian fluid under shear", **Proc.Royal Society A**, 225, pp.49-63, 1954

Chen, C.L. and Ling, C.H. "Granular-Flow Rheology: Role of Shear-Rate Number in Transition Regime", **J.Engng.Mech. ASCE**, 122, 5, 469-481, 1996

Evans, S.G., Hungr, O., Clague, J.J., (2001). Dynamics of the 1984 rock avalanche and associated distal debris flow on Mount Cayley, British Columbia, Canada; Implications for the landslide hazard assessment on dissected volcanoes. *Engineering Geology*, 61: 29-51

D.M.Hanes and D.L.Inman, "Observations of rapidly flowing granular fluid materials", **J.Fluid Mech. 150**, 357-380, 1985

Hungr, O. (1995): "A model for the runout analysis of rapid flow slides, debris flows and avalanches", *Can.Geotech.J.* 32, pp 610-623.

K.Hutter, B.Svendsen and D.Rickenmann, "Debris Flow modelling: A review". *Continuum Mech.Thermodyn*, 8, 1-35, 1996.

Jan, C.D., "A study on the numerical modelling of debris flows", in **Debris-Flow Hazards Mitigation:Mechanics, Prediction and Assessment, Proc.1st Int.Conference, ASCE 1997**, C-I.Chen (Ed.), pp.717-726.

Jeyapalan, J.K., Duncan, J.M., Seed, H.B., (1983). Investigation of flow failures of tailing dams. *J. Geotech. Engng.*, ASCE, 109: 172-189.

Jin, M. & Fread, D.L. One-dimensional routing of mud/debris flows using NWS FLDWAV model, in C.L.Chen (Ed.), **Debris-Flow Hazards Mitigation: Mechanics, Prediction and Assessment**, ASCE, pp. 687-696. (1997).

Johnson, A.M. "A model for grain flow and debris flow", U.S.Geological Survey Open-File Report 96-728, 1996 Hazards Mitigation:Mechanics, Prediction and Assessment, Proc.1st Int.Conference, ASCE 1997, C-I.Chen (Ed.), pp 687-696

A.M.Johnson and S.Y.Martosudarmo, "Discrimination between inertial and macro-viscous flows of fine-grained debris with a rolling-sleeve viscometer", in *Debris-Flow Hazards Mitigation:Mechanics, Prediction and Assessment, Proc.1st Int.Conference, ASCE 1997*, C-I.Chen (Ed.), pp.229-238.

Julien, P.Y. and Lan, Y. "Rheology of hyperconcentrations", **J. Hydr.Engng. ASCE**, 117, 3, 346-353, 1991

Laigle, D. and Coussot, P. (1997): Numerical modelling of mudflows. **Journal of Hydraulic Engineering, ASCE**, **123** (7): 617-623.

Malvern, L.E. (1969): **Introduction to the Mechanics of a continuous medium**. Prentice-Hall. (1969).

Pastor, M., Quecedo, M., González,E., Herreros, I., Fernández Merodo, J.A., and Mira, P., "A simple approximation to bottom friction for Bingham fluid depth integrated models", **Journal of Hydraulic Engineering ASCE**, **Vol. 130**, No. 2, pp. 149-155, 2004

G.R.MIDI, On dense granular flows, *The European Physical Journal E*, Vol. 14 No. 4, pp. 341-366 (2004)

Rickenmann, D. and Koch, T. "Comparison of debris flow modelling approaches", in **Debris-Flow Hazards Mitigation: Mechanics, Prediction and Assessment, Proc.1st Int.Conference, ASCE 1997**, C-1.Chen (Ed.), pp.576-585.

4 NUMERICAL MODELS FOR LANDSLIDE RUN OUT

4.1 INTRODUCTION

Numerical models have become a fundamental tool to obtain approximations to engineering and science problems for which there is no available analytical solution. As examples, we can mention the liquefaction failure of a earth dam under earthquake loading, the downhill propagation of a fast catastrophic landslide or the pollutant transport in the ocean.

Landslides present different failure mechanisms. In some cases, the failure mechanism consists on a clearly defined surface where shear strain concentrates. From a mathematical point of view, the inception of the shear band is characterized by a discontinuity in the strain field, which can evolve towards a discontinuity in the displacements at a later stage. Much effort has been devoted during the past years to better understand this phenomenon. From a mathematical point of view, the problem is ill posed for elastoplastic materials, and the results obtained in numerical models depend on the mesh size and alignment.

The interested reader is addressed to the text by Vardoulakis and Sulem (1995) where a detailed explanation is provided. Depending on the mechanical behaviour of the material, a local collapse can be produced, with an important increase of pore pressures and a corresponding decrease of the effective stresses, which can lead to liquefaction on the failure surface (Sassa 2000).

In other cases, the failure mechanism involves a much larger mass of soil. This is the case of the liquefaction of a sand layer induced by an earthquake. This mechanism of failure can be referred to as "diffuse", and it is characteristic of soils presenting very loose or metastable structures with a strong tendency to compact under shearing. One paramount feature is that effective stresses approach zero, and the material behaves like a viscous fluid in which buildings can sink, as it happened during the 1966 earthquake of Niigata in Japan. When this failure mode takes place in a slope, the mass of mobilized soil can propagate downhill, evolving into flow slides or mudflows.

Hutchinson (1986) proposed in 1986 a simple sliding-consolidation model to describe "slope failures involving the collapse of metastable structures", following his earlier work of (Hutchinson 1971).

It has to be mentioned here that this mode of failure can be exhibited also by non-saturated soils such as those of volcanic origin. Indeed, collapse of the material under the loading induced by an earthquake can make the pore air pressure to increase. The phenomenon is controlled by two characteristic time scales, a characteristic time for the consolidation and a characteristic time of loading. If the former is much larger than the latter, there will be not enough time for dissipation of air pore pressures, and the material will arrive to a "dry" liquefaction. Some of the catastrophic landslides caused in El Salvador by the 13th of January 2001 earthquake can be explained by this mechanism.

Once failure has been triggered in a mass of soil, it can start moving in a fluid like manner. It is important to notice here the fundamental role played by the pore pressures generated during

the initiation phase. Depending on the relative lengths of the time scales described above, the movement, once initiated, can continue even at slopes much smaller than the effective friction angle. Indeed, the generated pore pressures can explain how submarine landslides can develop and propagate DiPrisco, Matiotti and Nova (1995).

Mathematical and numerical models of flowslides can be classified on two main groups:

- Full 3D formulations where the equations of balance of mass and linear momentum are solved on a domain which changes with time. The position of the interface between the soil and the air is tracked using special techniques such as the MAC algorithm applied by Sousa and Blight (1991), or the pseudoconcentration function implemented in the model proposed by Frenette, Eyheramendy and Zimmermann (1997). The pseudoconcentration function is an indicator which can take two different values depending whether the point being considered is occupied by soil or by air. The pseudoconcentration function is advected by the velocity field, presenting the well known difficulties of the advection of a discontinuous function. In consequence, the solution can be corrupted as time advances. As an effective alternative, it is possible to use the "level set" technique, which consists on transforming the indicator function on a distance function (Quecedo and Pastor 2000). These models are expensive in terms of computer effort and therefore its use is restricted to cases in which it is necessary to know the fine structure of the flow, forces against structures, etc.
- If some assumptions are made about the vertical structure of the flow, it is possible to integrate the balance equations on depth, arriving to the so-called "depth-integrated" equations or "shallow water equations" in coastal and hydraulic engineering. The equations can be further simplified by integrating on cross sections, arriving to simple 1D models.

The depth integrated equations can be cast either in an eulerian or a lagrangian form. The second approach presents several clear advantages, such as the possibility of introducing a K_0 coefficient relating the horizontal and vertical stress components, the possibility of formulating the equations in a curvilinear coordinate system following the terrain (Savage and Hutter 1991), Hutter and Koch (1991), Hungr (1995), and Rickenmann and Koch (1997).

However, mesh based lagrangian formulations present some important difficulties in the 2D case, as how the mesh can follow the bifurcation of the flow when arriving to an obstacle, or merging after it has been passed. Because of this, most of the effort has been devoted in the past to the development of eulerian models following the approaches used in Hydraulic Engineering to model the propagation of flood waves, dam break problems, etc. (See for instance Vulliet and Hutter 1988, O'Brien, Julien and Fullerton 1993; Jin and Fread 1997).

In the past years, there has been a continuously increasing interest in the so-called Riemann solvers, where a Riemann problem is solved at the boundaries between cells or elements at every time step (See, for instance the work of Laigle and Coussot (1977), for mudflows or the more recent works of Zappou and Roberts (1999) and Toro (2001) in Hydrodynamics. The use of such specialized algorithms introduces an additional computational load, as a non-linear Riemann problem has to be solved at boundaries between cells or elements at every time step.

To circumvent this difficulty, approximate Riemann solvers have been introduced, but care must be taken to avoid entropy violating solutions.

As a simple yet effective alternative we will present in this chapter a numerical model based on a classical Taylor Galerkin algorithm, which has been modified to deal with propagation over dry regions and which is able to provide accurate enough solutions.

During the past decades, most of numerical methods of approximations used were based on grids, either structured (finite differences), or unstructured (finite elements and volumes). These methods have been extensively developed since the early 80's, and there abound excellent texts describing them, as the classical of Zienkiewicz and Taylor.

One fundamental problem found in mesh based methods is the solution of free surface flows in fluids or very large deformations in solids. The latter has been solved using lagrangian and ALE formulations, but in extreme cases it is necessary to perform remeshing. In the former, free surface problems have been solved using techniques such as the VOF (volume of fluid) or Level Set.

An interesting alternative has been found in the so-called meshless methods, which will be described next.

4.2 MESHLESS TECHNIQUE: THE SPH METHOD. APPLICATION TO DETH INTEGRATED MODELS.

4.2.1 Introduction

In the last decades, a new group of methods, characterized for not using meshes but only nodes has been developed. They have been called “meshless”, and provide an interesting and powerful alternative to more classical numerical methods such as finite differences, finite elements and finite volumes. Their name comes from the fact that they do not rely on meshes but on points to approximate functions or derivatives. As examples of these methods, it is worth mentioning the Diffuse Element Method introduced by Nayroles, Touzot and Villon (1992), the Element Free Galerkin Method of Belytschko, Lu and Gu (1994), the hp-cloud method of Duarte and Oden (1996), the Partition of Unity Method of Babuska and Melenk (1995), the Finite Point Method introduced by Oñate and Iddlesohn (1998) and, finally, the Smoothed Particle Hydrodynamics Method which will be described later in this Section.

Figure 4.2.1 provides a simplified overview of the different approaches mentioned.

	Eulerian	Lagrangian
Finite Differences	Interface tracking: Level set Consistency for material history!	Meshes: distortion Remeshing Adaptivity techniques
Finite Elements		
Finite Volume		
Meshless: SPH...	Problems with Boundary Conditions	
Discrete Elements		Granular materials

Figure 4.2.1. Comparison between alternative modelling techniques

Smoothed particle hydrodynamics is a meshless method based on discretized forms of integral approximations of functions and derivatives. The method was introduced independently by Lucy (1977) and Gingold and Monaghan (1977) and applied to astrophysical modelling, a domain where SPH presents important advantages over other methods (see also the work of Monaghan and Latanzio 1985). Goods review can be found in Benz (1990), Monaghan (1992) or in the recent texts of Liu and Liu (2003) or Li and Liu (2004).

SPH is well suited for hydrodynamics, and researchers have applied it to a variety of problems, like those described in Gingold and Monaghan (1982), Monaghan and Gingold (1983), Takeda, Miyama and Sekiya (1994), Monaghan (1994), Monaghan and Kocharyan (1995), Monaghan and Kos (1999), Monaghan, Cas, Kos, and Hallworth (1999), Bonet and S. Kulasegaram (2000), and Monaghan, Kos and Issa (2003).

Problems found in Solid Mechanics have also been solved using the SPH technique. Among the many contributions, it is worth mentioning those of Libersky and Petschek (1990), Libersky, Petschek, Carney, Hipp, Allahdadi and High (1993), Randles and Libersky(2000), Bonet and Kulasegaram (2000) and Gray, Monaghan and Swift (2001)

4.2.2 Fundamentals: integral approximations

The SPH method is based on the equality:

$$\phi(x) = \int_{\Omega} \phi(x') \delta(x'-x) dx' \quad (4.2.1)$$

where $\delta(x)$ is the Dirac delta. Traditionally, Dirac delta “function” is defined as:

$$\delta(x) = \begin{cases} \infty & x = 0 \\ 0 & |x| > 0 \end{cases} \quad (4.2.2)$$

with the additional requirement of “unity”

$$\int_{\Omega} \delta(x) dx = 1$$

Dirac delta can be defined from a sequence $W_k(x, h)$ of functions referred to as kernels, such as

$$W_k(x, h) = \frac{1}{\sqrt{2\pi h}} \exp\left(-\frac{x^2}{h^2}\right) \quad \text{where} \quad h = 1/k \quad (4.2.3)$$

where the kernel depends on a length h or an integer k . It can be shown that

$$\lim_{h \rightarrow 0} \int_{\Omega} W_k(x'-x, h) \phi(x') dx' = \int_{\Omega} \phi(x') \delta(x'-x) dx' = \phi(x) \quad (4.2.4)$$

Above expressions can be immediately generalized to 2 or 3 dimensions, by considering a scalar or vector valued function $\phi(x)$ of $x \in \Omega \subset \square^{\text{ndim}}$ where Ω is an open bounded domain.

These results are the starting point for constructing smoothed particle hydrodynamics (SPH) approximations, where regular distributions are used to approximate the value of a function. The approximation is written as:

$$\langle \phi(x) \rangle = \int_{\Omega} \phi(x') W(x'-x, h) dx' \quad (4.2.5)$$

The accuracy of SPH approximations depends on the properties of the kernel $W(x, h)$. A special class of kernels is that of functions having radial symmetry, i.e., depending only on r :

$$r = |x' - x| \quad (4.2.6)$$

It is convenient to introduce the notation:

$$\xi = \frac{|x' - x|}{h} = \frac{r}{h} \quad (4.2.7)$$

because it allows to write $W(x'-x, h)$ as $W(\xi)$ in this case. We will use in the following both notations.

The functions $W(x, h)$ used as kernels in SPH approximations are required to fulfil the following conditions:

$$(i) \lim_{h \rightarrow 0} W(x'-x, h) = \delta(x) \quad (4.2.8a)$$

$$(ii) \int_{\Omega} W(x'-x, h) dx' = 1 \quad (4.2.8b)$$

This condition, which follows also from (i) can be interpreted as well as the ability of the approximation to reproduce a constant or polynomial of degree zero (zero order consistency).

(iii) The kernel $W(x-x', h)$ is positive and has compact support:

$$W(x'-x, h) = 0 \text{ if } |x'-x| \geq kh \quad (4.2.8c)$$

where k is a positive integer which is usually taken as 2.

(iv) The kernel $W(x'-x, h)$ is a monotonically decreasing function of ξ

$$\xi = |x'-x|/h \quad (4.2.8d)$$

(v) The kernel $W(x'-x, h)$ is a symmetric function of $(x'-x)$

Figure 4.2.2 illustrates the sequence of kernels approximating the Dirac delta distribution.

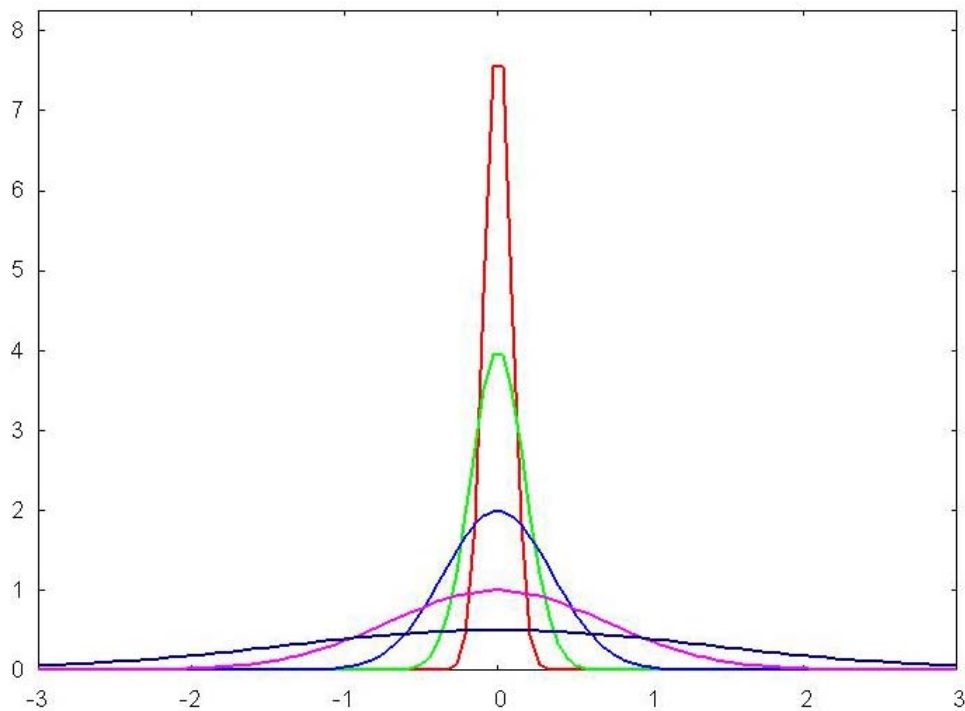


Figure 4.2.2 Kernels approximating Dirac delta

It is possible to show that, under the conditions specified above, the approximation is second order accurate, i.e.,

$$\langle \phi(x) \rangle = \phi(x) + O(h^2)$$

In the framework of SPH formulations, several kernels have been proposed in the past. Among them, it is worth mentioning the following:

(a) The Gaussian kernel proposed by Gingold and Monaghan (1977) defined as

$$W(x' - x, h) = W(\xi) = \begin{cases} \frac{1}{h^{\text{ndim}} \pi^{\text{(ndim/2)}}} \exp(-\xi^2) & \xi \leq 3 \\ 0 & \text{otherwise} \end{cases}$$

(b) The cubic spline introduced by Monaghan (Monaghan and Gingold 1983; Monaghan and Lattanzio 1985)

$$W(x'-x, h) = W(\xi) = \frac{C}{h^{\text{ndim}}} \begin{cases} \left(1 - \frac{3}{2}\xi^2 + \frac{3}{4}\xi^3\right) & \xi < 1 \\ \frac{1}{4}(2-\xi)^3 & 1 \leq \xi \leq 2 \\ 0 & 2 \leq \xi \end{cases}$$

where C is a constant which depends on the dimension of the domain:

$$C = \begin{cases} \frac{2}{3} & \text{for ndim} = 1 \\ \frac{10}{7\pi} & 2 \\ \frac{1}{\pi} & 3 \end{cases}$$

This scaling factor is chosen for the kernel to satisfy conditions (4.2.8a) to (4.2.8d).

Figure 4.2.3 depicts both kernels for the one dimensional case.

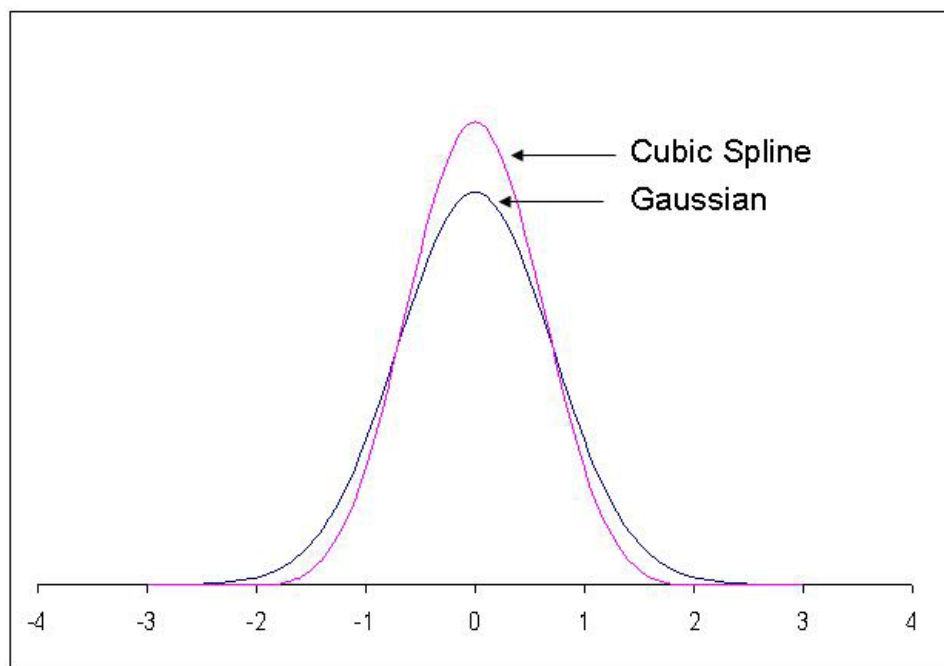


Figure 4.2.3. Kernels in 1D: (a) Gaussian (b) Cubic Spline

Concerning the integral representation of the derivatives in SPH, it is written as:

$$\langle \phi'(x) \rangle = \int_{\Omega} \phi'(x') W(x'-x, h) dx'$$

This expression is integrated by parts – in one dimensional problems –, and, taking into account that the kernel has compact support, it results

$$\langle \phi'(x) \rangle = - \int_{\Omega} \phi(x') W'(x'-x, h) dx'$$

Classical differential operators of continuum mechanics can be approximated in the same way. We list below the gradient of a scalar function, the divergence of a vector function, and the divergence of a tensor function:

$$\langle \text{grad } \phi(x) \rangle = - \int_{\Omega} \phi(x') \frac{1}{h} W' \frac{x'-x}{r} d\Omega \quad \text{with } r = |x'-x|$$

$$\langle \text{div } u(x) \rangle = - \int_{\Omega} u(x') \text{grad } W d\Omega = - \int_{\Omega} \frac{1}{h} W' \frac{u(x') \cdot (x'-x)}{r} d\Omega \quad (4.2.9)$$

$$\langle \text{div } \sigma(x) \rangle = - \int_{\Omega} \sigma \cdot \text{grad } W d\Omega = - \int_{\Omega} \frac{1}{h} W' \frac{\sigma \cdot (x'-x)}{r} d\Omega$$

4.2.3 SPH discretization in continuum mechanics

4.2.3.1 Introduction

The approximations of functions and derivatives given in the preceding Section are valid at continuum level. If the information is stored in a discrete manner, for instance, in a series of points or nodes, it is necessary to construct discrete approximations. The SPH method introduces the concept of “particles”, to which information concerning field variables and their derivatives is linked. But indeed, they are nodes, much in the same way than found in finite elements or finite differences. All operations are to be referred to nodes. We will therefore introduce the set of particles or nodes $\{x_K\}$ with $K = 1..N$. Of course, the level of approximation will depend on how the nodes are spaced and on their location. The classical finite element strategy of having more nodes in those zones where larger gradients are expected is of application here.

It was shown in (4.2.5) that the integral or continuum approximation of a function is given by:

$$\langle \phi(x) \rangle = \int_{\Omega} \phi(x') W(x'-x, h) dx'$$

As the information concerning the function is only available at a set of N nodes the integral could be evaluated using a numerical integration technique of the type:

$$\langle \phi(x_I) \rangle_h = \sum_{J=1}^N \phi(x_J) W(x_J - x_I, h) \omega_J$$

where we have used the sub index “ h ” to denote the discrete approximation, with ω_J denoting the weights of the integration formula. In order to simplify the notation, we will use introduce ϕ_I , defined as:

$$\phi_I = \langle \phi(x_I) \rangle_h = \sum_{J=1}^N \phi(x_J) W(x_J - x_I, h) \omega_J$$

If we take into account that the kernel function has local support, i.e. it is zero when $|x_J - x_I| > 2h$, the summation extends only to the set of Nh points which fulfil this condition:

$$\phi_I = \langle \phi(x_I) \rangle_h = \sum_{J=1}^{Nh} \phi(x_J) W(x_J - x_I, h) \omega_J \quad (4.2.10)$$

Figure 4.2.4 illustrates the numerical integration procedure performed.

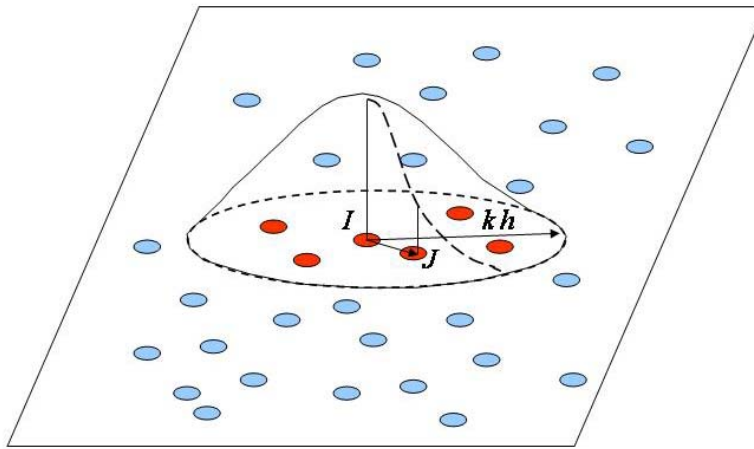


Figure 4.2.4. Nodes and numerical integration in a SPH mesh.

We will introduce the notation:

$$x_{IJ} = x_I - x_J$$

$$r_{IJ} = |x_I - x_J|$$

$$\text{grad } W_{IJ} = \frac{W'}{h} \frac{x_{IJ}}{r_{IJ}}$$

The weight ω_j can be shown to be the volume Ω_j or area associated to the node. In the context of continuum mechanics (solids and fluids), it is convenient to introduce the density ρ_j associated to node J as

$$\rho_j = m_j / \Omega_j \quad (4.2.11)$$

where m_j is the mass associated to node j , which is nothing else than the mass of the volume associated to the considered node. The nodal variable ϕ_j is then:

$$\phi_I = \sum_{J=1}^{N_h} \phi(x_J) W_{IJ} \frac{m_J}{\rho_J} \quad (4.2.12)$$

which is a form commonly used in SPH. In the case we choose the function ϕ to represent the density, we will obtain, after substituting in (4.2.12)

$$\begin{aligned} \rho_I &= \sum_{J=1}^{N_h} \rho_J W_{IJ} \frac{m_J}{\rho_J} \\ \rho_I &= \sum_{J=1}^n W_{IJ} m_J \end{aligned} \quad (4.2.13)$$

4.2.3.2 Discretization of continuum differential operators

One interesting aspect of SPH is the existence of several alternative discretized forms for the differential operators. For instance, the **gradient of a scalar function** can be approximated as:

$$\text{grad } \phi_I = \sum_{J=1}^{N_h} \frac{m_J}{\rho_J} \phi_J \text{grad } W_{IJ} \quad (\text{basic form})$$

and the three following symmetrised forms

$$\text{grad } \phi_I = \frac{1}{\rho_I} \sum_J m_J (\phi_J - \phi_I) \text{grad } W_{IJ} \quad (4.2.14a)$$

$$\text{grad } \phi_I = \rho_I \sum_J m_J \left\{ \frac{\phi_J}{\rho_J^2} + \frac{\phi_I}{\rho_I^2} \right\} \text{grad } W_{IJ} \quad (4.2.14b)$$

$$\text{grad } \phi_I = \sum_{J=1}^{N_h} \frac{m_J}{\rho_J} (\phi_I + \phi_J) \text{grad } W_{IJ} \quad (4.2.14c)$$

Sometimes it is preferred to use a variant of this form, which is

$$\text{grad } \phi_I = \sum_{J=1}^{N_h} \frac{m_J}{\rho_J} (\phi_I + \phi_J) \text{grad } W_{IJ} \quad (4.2.14d)$$

In the same way, we can obtain the **gradient of a vector field** as:

$$\text{grad } v_I = \sum_{J=1}^{N_h} \frac{m_J}{\rho_J} v_J \otimes \text{grad } W_{IJ} \quad (4.2.15a)$$

It is possible to derive symmetrised forms for the gradient of a vector field.

The first form is obtained from the identity:

$$\text{grad}(v\rho) = \rho \text{grad } v + v \otimes \text{grad } \rho \quad (4.2.15b)$$

from where we obtain

$$\text{grad } v_I = \frac{1}{\rho_I} \sum_J m_J (v_J - v_I) \otimes \text{grad } W_{IJ} \quad (4.2.15c)$$

The second symmetrised form follows from the identity:

$$\text{grad} \left(\frac{v}{\rho} \right) = \frac{1}{\rho} \text{grad } v - \frac{v}{\rho^2} \otimes \text{grad } \rho \quad (4.2.15d)$$

from where we arrive to:

$$\text{grad } v_I = \rho_I \sum_J m_J \left\{ \frac{v_J}{\rho_J^2} + \frac{v_I}{\rho_I^2} \right\} \otimes \text{grad } W_{IJ} \quad (4.2.15e)$$

The third symmetrised form is obtained in the same way presented above, resulting on:

$$\text{grad } v_I = \sum_{J=1}^{N_h} \frac{m_J}{\rho_J} (v_J - v_I) \otimes \text{grad } W_{IJ} \quad (4.2.15f)$$

Concerning the **divergence of a vector field**, its SPH approximations are the following:

$$\text{div } v_I = \sum_J \frac{m_J}{\rho_J} u_{J \cdot} \text{grad } W_{IJ} \quad (4.2.16a)$$

As we have done for the gradient of a scalar and a vector field, it is possible to use alternative symmetrised forms.

The first symmetrised form is obtained using the identities:

$$\begin{aligned}\operatorname{div}(\rho v) &= \operatorname{grad} \rho \cdot v + \rho \operatorname{div} v \\ \rho \operatorname{div} v &= \operatorname{div}(\rho v) - \operatorname{grad} \rho \cdot v \\ \operatorname{div} v &= \frac{1}{\rho} (\operatorname{div}(\rho v) - \operatorname{grad} \rho \cdot v)\end{aligned}$$

From here, we discretize the latter, obtaining:

$$\operatorname{div} v_I = \frac{1}{\rho_I} \sum_J (\rho_J v_J \operatorname{grad} W_{IJ} - v_I \rho_J \operatorname{grad} W_{IJ}) \frac{m_J}{\rho_J}$$

and

$$\operatorname{div} v_I = -\frac{1}{\rho_I} \sum_J v_{IJ} \operatorname{grad} W_{IJ} m_J \quad (4.2.16b)$$

where we have introduced

$$v_{IJ} = v_I - v_J$$

The second symmetrised form is obtained from the identities:

$$\operatorname{div} \left(\frac{v}{\rho} \right) = \frac{1}{\rho} \operatorname{div} v - \frac{1}{\rho^2} \operatorname{grad} \rho \cdot v$$

and

$$\operatorname{div} v = \rho \left(\operatorname{div} \left(\frac{v}{\rho} \right) + \frac{1}{\rho^2} \operatorname{grad} \rho \cdot v \right)$$

We obtain, after discretizing:

$$\operatorname{div} v_I = \rho_I \sum_J m_J \left(\frac{v_J}{\rho_J^2} + \frac{v_I}{\rho_I^2} \right) \cdot \operatorname{grad} W_{IJ} \quad (4.2.16c)$$

which is the second symmetrised form.

The third symmetrised form is obtained by subtracting from

$$\operatorname{div} v_I = \sum_J \frac{m_J}{\rho_J} u_J \cdot \operatorname{grad} W_{IJ}$$

the discrete form of the divergence of a unit vector field, which is zero:

$$0 = \text{div} 1 = \sum_J \frac{m_J}{\rho_J} 1 \cdot \text{grad} W_{IJ}$$

resulting on:

$$\text{div} v_I - 0 = \sum_J \frac{m_J}{\rho_J} v_J \cdot \text{grad} W_{IJ} - \sum_J \frac{m_J}{\rho_J} v_I \cdot \text{grad} W_{IJ}$$

and, finally,

$$\text{div} v_I = - \sum_J \frac{m_J}{\rho_J} v_{IJ} \cdot \text{grad} W_{IJ} \quad (4.2.16d)$$

4.2.3.3 SPH Discretization of balance laws

Balance of mass

The Lagrangian form of the mass balance equation is given by:

$$\frac{D\rho}{Dt} + \rho \text{div} v = 0$$

First of all, we will obtain the integral form of the equation:

$$\left\langle \frac{D\rho}{Dt} + \rho \text{div} v \right\rangle = 0$$

i.e.,

$$\int_{\Omega} W \left(\frac{D\rho}{Dt} + \rho \text{div} v \right) = 0$$

We will make use of the following properties of the approximation:

$$\begin{aligned} \left\langle \frac{D\rho}{Dt} + \rho \text{div} v \right\rangle &= \left\langle \frac{D\rho}{Dt} \right\rangle + \langle \rho \text{div} v \rangle \\ \left\langle \frac{D\rho}{Dt} \right\rangle &= \frac{D}{Dt} \langle \rho \rangle \\ \langle \rho \text{div} v \rangle &= \langle \rho \rangle \langle \text{div} v \rangle \end{aligned} \quad (4.2.17)$$

The integral approximation of the balance of mass equation is written, therefore, as

$$\frac{D}{Dt}\langle\rho\rangle+\langle\rho\rangle\langle\text{div }v\rangle=0 \quad (4.2.18)$$

As there are several alternatives to discretize $\langle\text{div }v\rangle$, there will be the following discretized forms of the equation:

(a) Basic form

$$\frac{D\rho_I}{Dt}=-\rho_I\sum_J\frac{m_J}{\rho_J}v_J\text{grad }W_{IJ} \quad (4.2.19a)$$

(b) First symmetrized form

$$\frac{D\rho_I}{Dt}=\sum_Jm_Jv_{IJ}\text{grad }W_{IJ} \quad (4.2.19b)$$

(c) Second symmetrized form

$$\frac{D\rho_I}{Dt}=-\rho_I^2\sum_Jm_J\left(\frac{v_I}{\rho_I^2}+\frac{v_J}{\rho_J^2}\right)\text{grad }W_{IJ} \quad (4.2.19c)$$

(d) Third symmetrized form

$$\frac{D\rho_I}{Dt}=\rho_I\sum_J\frac{m_J}{\rho_J}v_{IJ}\text{grad }W_{IJ} \quad (4.2.19d)$$

Balance of linear momentum

The balance of momentum equation is:

$$\rho\frac{Dv}{Dt}=\rho b+\text{div } \sigma$$

This form is more frequently found in Solid Mechanics, while in Fluid Dynamics the stress tensor is decomposed into a hydrostatic and a deviatoric component as:

$$\sigma=-pI+s$$

where

$$p = -\frac{1}{3} \text{tr}(\sigma)$$

The balance equation is then written as:

$$\rho \frac{Dv}{Dt} = \rho b + \text{div } s - \text{grad } p \quad (4.2.20)$$

We will follow the same procedure than in the previous Section. First, we will obtain the integral approximation of eqn. (4.2.20), which is:

$$\langle \rho \rangle \frac{D}{Dt} \langle v \rangle = -\langle \text{grad } p \rangle + \langle \text{div } s \rangle + \langle \rho \rangle \cdot \langle b \rangle \quad (4.2.21)$$

where we have used the properties of the integral approximations:

$$\begin{aligned} \left\langle \rho \frac{Dv}{Dt} \right\rangle &= \langle \rho \rangle \left\langle \frac{Dv}{Dt} \right\rangle = \langle \rho \rangle \frac{D}{Dt} \langle v \rangle \\ \langle -\text{grad } p + \text{div } s + \rho b \rangle &= -\langle \text{grad } p \rangle + \langle \text{div } s \rangle + \langle \rho \rangle \cdot \langle b \rangle \end{aligned} \quad (4.2.22)$$

Again, we have several alternatives to discretize the gradient and the divergence operators. If we use the same for both, for the sake of consistency, we find:

(a) Basic form

$$\rho_I \frac{Dv_I}{Dt} = -\sum_J \frac{m_J}{\rho_J} p_J \text{grad } W_{IJ} + \sum_J \frac{m_J}{\rho_J} s_J \text{grad } W_{IJ} + b_I \quad (4.2.23a)$$

(b) First symmetrized form

$$\rho_I \frac{Dv_I}{Dt} = -\frac{1}{\rho_I} \sum_J m_J (p_J - p_I) \text{grad } W_{IJ} + \frac{1}{\rho_I} \sum_J m_J (s_J - s_I) \text{grad } W_{IJ} + b_I \quad (4.2.23b)$$

(c) Second symmetrized form

$$\rho_I \frac{Dv_I}{Dt} = -\sum_J m_J \left(\frac{p_I}{\rho_I^2} + \frac{p_J}{\rho_J^2} \right) \text{grad } W_{IJ} + \sum_J m_J \left(\frac{s_I}{\rho_I^2} + \frac{s_J}{\rho_J^2} \right) \text{grad } W_{IJ} + b_I \quad (4.2.23c)$$

(d) Third symmetrized form

$$\rho_I \frac{Dv_I}{Dt} = - \sum_J m_J \left(\frac{p_I + p_J}{\rho_I \rho_J} \right) \text{grad } W_{IJ} + \sum_J m_J \left(\frac{s_I + s_J}{\rho_I \rho_J} \right) \text{grad } W_{IJ} + b_I \quad (4.2.23d)$$

4.2.4 SPH discretization of depth integrated equations

4.2.4.1 Introduction. Recall of the depth integrated equations for fast landslides

Many fast, catastrophic landslides have average depths which are small in comparison with their length or width. In this case, it is possible to simplify the 3D propagation-consolidation models by integrating its equations along the vertical axis. The resulting 2D depth integrated model presents an excellent combination of accuracy and simplicity providing important information such as velocity of propagation, time to reach a particular place, depth of the flow at a certain location, etc. Most of the depth integrated models available in the literature do not take into account basal pore pressure, although they play a paramount role. The purpose of this Section is to present the SPH discretization procedure of the depth integrated model which takes into account pore pressure dissipation during the propagation phase.

The depth integrated equations can be cast in either an eulerian or a lagrangian framework. The eulerian forms are the following:

(a1) Balance of mass

$\frac{\partial h}{\partial t} + \frac{\partial}{\partial x_j} (\bar{v}_j h) = e_R$	(4.2.24)
---	----------

(b1) Balance of linear momentum

$\frac{\partial}{\partial t} (h \bar{v}_i) + (1 + \alpha) \frac{\partial}{\partial x_j} (h \bar{v}_i \bar{v}_j) = b_i h + \frac{1}{\rho} \frac{\partial}{\partial x_j} (h \bar{\sigma}_{ij}) + \frac{1}{\rho} N^A t_i^A + \frac{1}{\rho} N^B t_i^B$	(4.2.25)
---	----------

or, introducing the decomposition:

$$\sigma_{ij} = -\bar{p} \delta_{ij} + \sigma_{ij}^*$$

with

$$\bar{p} = \frac{1}{2} \rho b_3 h \quad \sigma_{ij}^* = \bar{\sigma}_{ij} + \bar{p} \delta_{ij}$$

$\frac{\partial}{\partial t}(h\bar{v}_i) + \frac{\partial}{\partial x_j} \left(h\bar{v}_i\bar{v}_j - \frac{1}{2}b_3h^2\delta_{ij} \right) =$ $\alpha \frac{\partial}{\partial x_j} (h\bar{v}_i\bar{v}_j) + \frac{1}{\rho} \frac{\partial}{\partial x_j} (h\bar{\sigma}_{ij}^*) + b_i h + \frac{1}{\rho} N^A t_i^A + \frac{1}{\rho} N^B t_i^B$	(4.2.26)
--	----------

(c1) Vertical consolidation

$\frac{\partial}{\partial t}(P_1 h) + \frac{\partial}{\partial x_j} (\bar{v}_j P_1 h) + \frac{\pi}{2} C.T. = -\frac{\pi^2}{4h} c_v P_1$	(4.2.27)
---	----------

The quasi-lagrangian forms are:

(a2) Balance of mass

$\frac{d\bar{h}}{dt} + h \frac{\partial \bar{v}_j}{\partial x_j} = 0$	4.2.28)
---	---------

(b2) Balance of linear momentum

$h \frac{d\bar{v}_i}{dt} - \frac{\partial}{\partial x_i} \left(\frac{1}{2} b_3 h^2 \right) = -e_R \bar{v}_i - \alpha \frac{\partial}{\partial x_j} (h\bar{v}_i\bar{v}_j) + \frac{1}{\rho} \frac{\partial}{\partial x_j} (h\bar{\sigma}_{ij}^*) + b_i h + \frac{1}{\rho} N^A t_i^A + \frac{1}{\rho} N^B t_i^B$	(4.2.29)
--	----------

(b3) Vertical consolidation

$\frac{d\bar{P}_1}{dt} + \frac{1}{h} P_1 e_R + \frac{\pi}{2h} C.T. = \frac{\pi^2}{4h^2} c_v P_1$	(4.2.30)
--	----------

The eulerian form is often written in a more compact manner as:

$$\frac{\partial \phi}{\partial t} + \frac{\partial F_1}{\partial x_1} + \frac{\partial F_2}{\partial x_2} = D + S \quad (4.2.31)$$

where we have introduced:

- (i) A vector of unknowns ϕ
- (ii) The fluxes F_1 and F_2 following axes x_1 and x_2

- (iii) The diffusive terms D
(iv) The source terms S

which are defined as:

$$\phi = \begin{pmatrix} h \\ h\bar{v}_1 \\ h\bar{v}_2 \\ hP_1 \end{pmatrix} \quad F_1 = \begin{pmatrix} h\bar{v}_1 \\ h\bar{v}_1^2 + \frac{1}{2}b_3h^2 \\ h\bar{v}_1\bar{v}_2 \\ h\bar{v}_1P_1 \end{pmatrix} \quad F_2 = \begin{pmatrix} h\bar{v}_2 \\ h\bar{v}_1\bar{v}_2 \\ h\bar{v}_2^2 + \frac{1}{2}b_3h^2 \\ h\bar{v}_1P_1 \end{pmatrix} \quad (4.2.32)$$

$$D = \begin{pmatrix} 0 \\ \frac{1}{\rho} \frac{\partial}{\partial x_j} (h\bar{\sigma}_{1j}^*) \\ \frac{1}{\rho} \frac{\partial}{\partial x_j} (h\bar{\sigma}_{2j}^*) \\ 0 \end{pmatrix} \quad S = \begin{pmatrix} e_R \\ b_1h + \frac{1}{\rho} |N^A| t_1^A + \frac{1}{\rho} |N^B| t_1^B \\ b_2h + \frac{1}{\rho} |N^A| t_2^A + \frac{1}{\rho} |N^B| t_2^B \\ -\frac{\pi^2}{4h} c_v P_1 \end{pmatrix} + \begin{pmatrix} 0 \\ -\alpha \frac{\partial}{\partial x_j} (h\bar{v}_1\bar{v}_j) \\ -\alpha \frac{\partial}{\partial x_j} (h\bar{v}_2\bar{v}_j) \\ -\frac{\pi}{2} C.T. \end{pmatrix} \quad (4.2.33)$$

It is possible to use either or the eulerian or the quasi lagrangian approximations with SPH models, but the latter presents clear advantages over the former.

4.2.4.2 SPH Discretization

We will introduce a set of nodes $\{x_K\}$ with $K = 1..N$ and the nodal variables

$$\begin{aligned} h_I & \quad \text{height of the landslide at node } I \\ \bar{v}_I & \quad \text{depth averaged, 2D velocity} \\ t_I^b & \quad \text{surface force vector at the bottom} \\ \bar{\sigma}_I^* & \quad \text{depth averaged modified stress tensor} \\ P_{1I} & \quad \text{Pore pressure at the basal surface} \end{aligned} \quad (4.2.34)$$

If the 2D area associated to node I is Ω_I , we will introduce for convenience:

- (i) a fictitious mass m_I moving with this node:

$$m_I = \Omega_I h_I \quad (4.2.35)$$

(ii) and \bar{p}_I , an averaged pressure term, given by:

$$\bar{p}_I = \frac{1}{2} b_3 h_I^2$$

It is important to note that m_I has no physical meaning, as when node I moves, the material contained in a column of base Ω_I has entered it or will leave it as the column moves with an averaged velocity which is not the same for all particles in it.

The SPH approximation of the balance of mass equation is built from

$$\left\langle \frac{d\bar{h}}{dt} + h \frac{\partial \bar{v}_j}{\partial x_j} \right\rangle = 0 \quad (4.2.36)$$

from which:

$$\frac{d\bar{h}}{dt} \langle h \rangle + \langle h \rangle \left\langle \frac{\partial \bar{v}_j}{\partial x_j} \right\rangle = 0 \quad j = 1, 2 \quad (4.2.37)$$

The equation is written at node I as:

$$\frac{d\bar{h}}{dt} h_I + h_I \left\langle \frac{\partial \bar{v}_j}{\partial x_j} \right\rangle_I = 0 \quad j = 1, 2$$

where the divergence term is given by:

$$\text{div } v_I = - \sum_J \Omega_J v_J \text{ grad } W_{IJ} \quad (4.2.38)$$

or

$$\text{div } v_I = - \sum_J \frac{m_J}{h_J} v_J \text{ grad } W_{IJ} \quad (4.2.39)$$

Of course, we could have used any alternative symmetrized form.

The discretized balance of mass equation is written as

$$\frac{\bar{d}h_I}{dt} = -h_I \sum_J \frac{m_J}{h_J} v_J \text{grad } W_{IJ} \quad (\text{Basic form})$$

$$\frac{\bar{d}h_I}{dt} = \sum_J m_J v_{IJ} \text{grad } W_{IJ} \quad (\text{1st form}) \quad (4.2.40)$$

$$\frac{\bar{d}h_I}{dt} = h_I \sum_J \frac{m_J}{h_J} v_{IJ} \text{grad } W_{IJ} \quad (\text{3rd form})$$

where we have introduced v_{IJ}

$$v_{IJ} = v_I - v_J$$

Alternatively, the height can be obtained once the position of the nodes is known as:

$$\begin{aligned} h_I &= \langle h(x_I) \rangle \\ &= \sum_J h_J \Omega_J W_{IJ} \\ &= \sum_J m_J W_{IJ} \end{aligned} \quad (4.2.41)$$

The height can be normalized, which allows improving the approximation close to the boundary nodes:

$$h_I = \frac{\sum_J m_J W_{IJ}}{\sum_J \left(\frac{m_J}{h_J} \right) W_{IJ}} \quad (4.2.42)$$

Next, we will discretize the simplified form of the balance of linear momentum equation

$$h \frac{\bar{d}}{dt} \bar{v} = \text{grad} \left(\frac{1}{2} b_3 h^2 \right) + \frac{1}{\rho} \text{div} (h \bar{\sigma}_{ij}^*) + bh + \frac{1}{\rho} |N^B| t^B \quad (4.2.43)$$

or, introducing the averaged pressure

$$h \frac{\bar{d}}{dt} \bar{v} = -\frac{1}{\rho} \text{grad } p + \frac{1}{\rho} \text{div} (h \bar{\sigma}_{ij}^*) + bh + \frac{1}{\rho} |N^B| t^B \quad (4.2.44)$$

where we have neglected the terms corresponding to surface forces at the surface of the landslide, erosion and the correction factor α .

The left hand side results on:

$$h_I \frac{\bar{d}}{dt} \bar{v}_I \quad (4.2.45)$$

Depending on the symmetrized form chosen to discretize the gradient of pressure and the divergence of the stress tensor, we obtain the following discretized forms of the balance of momentum equation:

$$\frac{\bar{d}}{dt} \bar{v}_I = - \sum_J m_J \frac{p_I + p_J}{h_I h_J} \text{grad } W_{IJ} + \frac{1}{\rho} \sum_J m_J \frac{\sigma_I + \sigma_J}{h_I h_J} \text{grad } W_{IJ} + b + \frac{1}{\rho h_I} \left| N^B \right| t_I^B \quad (4.2.46)$$

$$\begin{aligned} \frac{\bar{d}}{dt} \bar{v}_I = & - \sum_J m_J \left(\frac{p_I}{h_I^2} + \frac{p_J}{h_J^2} \right) \text{grad } W_{IJ} \\ & + \frac{1}{\rho} \sum_J m_J \left(\frac{\sigma_I}{h_I^2} + \frac{\sigma_J}{h_J^2} \right) \text{grad } W_{IJ} + b + \frac{1}{\rho h_I} \left| N^B \right| t_I^B \end{aligned} \quad (4.2.47)$$

Finally, the SPH discretized form of the basal pore pressure dissipation is:

$$\frac{\bar{d}}{dt} P_{1I} = - \frac{\pi^2 c_v}{4h_I} P_{1I} \quad (4.2.48)$$

So far, we have discretized the balance of mass, balance of momentum and pore pressure dissipation equations. The resulting equations are ODEs which can be integrated in time using a scheme such as Leap Frog or Runge Kutta (2nd or 4th order).

We will describe here the second order Runge Kutta which provides a reasonable compromise between computational effort and accuracy.

We will assume that nodal variables are known at time step n , and perform a first time step:

$$\begin{aligned} h_I^{n+1/2} &= h_I^n + \frac{\Delta t}{2} \frac{\bar{d}}{dt} h_I \Big|_n \\ v_I^{n+1/2} &= v_I^n + \frac{\Delta t}{2} \frac{\bar{d}}{dt} v_I \Big|_n \\ P_{1I}^{n+1/2} &= P_{1I}^n + \frac{\Delta t}{2} \frac{\bar{d}}{dt} P_{1I} \Big|_n \end{aligned} \quad (4.2.49)$$

Once the variables are known at time $n + \frac{1}{2}$, we can obtain the value of the derivatives at this stage, and perform the second step:

$$\begin{aligned}
 h_I^{n+1} &= h_I^n + \frac{\Delta t}{2} \frac{\bar{d}}{dt} h_I \Big|^{n+1/2} \\
 v_I^{n+1} &= v_I^n + \frac{\Delta t}{2} \frac{\bar{d}}{dt} v_I \Big|^{n+1/2} \\
 P_{1I}^{n+1} &= P_{1I}^n + \frac{\Delta t}{2} \frac{\bar{d}}{dt} P_{1I} \Big|^{n+1/2}
 \end{aligned}
 \tag{4.2.50}$$

4.2.5 Examples and applications

We will include here some applications of SPH codes to run out analysis of landslides.

4.2.5.1. Cases with available analytical solution

We will devote this Section to present a short series of benchmarks which illustrate the predictive capacity of the proposed models. As any numerical model, a first step is to ensure that the model is able to provide accurate results for cases having an analytical solution. This is the case of the 1D dam break problem, where a vertical dam retaining the impounded water suddenly collapses. The solution depends on whether there is water in the domain where the water propagates (wet bottom) or not (dry bottom). Both cases are sketched in figure 4.2.5.

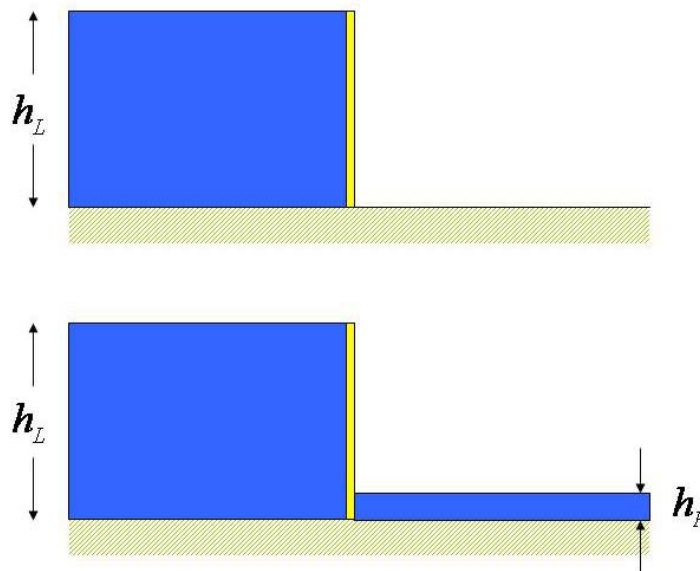


Figure 4.2.5 . 1D Dam break problem over (a) Dry bed (b) Wet bed

We will begin considering the “dry bottom” case. The analytical solution is found in the classical text of Stoker (1957) or in the more modern text by Guinot (2003).

The analytical solution is given in Figure 4.2.6 for $t = 0., 0.2, 0.4$ and $0.5 s$, and it consists on a rarefaction wave which propagates leftwards. In this figure we provide the results of the model, and we can observe that the agreement is good. More precise details are given in Figure 4.2.7, where we have plotted the profiles of water height and depth integrated velocity for $t = 0.5 s$. The initial height on the left side is $h_L = 10m$

Regarding the second case, propagation over a wet bed, the analytical solution is given in figure 4.2.8. (left), and consists of a rarefaction wave and a shock. In the case considered here, we have chosen a height on the left $h_L = 10m$, the water depth on the wet bed being $h_R = 1m$. We provide in this figure a comparison between the analytical and the computed results. Again, we found a good agreement, the rarefaction and the shock being captured well. In figure 4.2.9 we provide the profiles of water height and averaged velocity at time $t = 0.4 s$

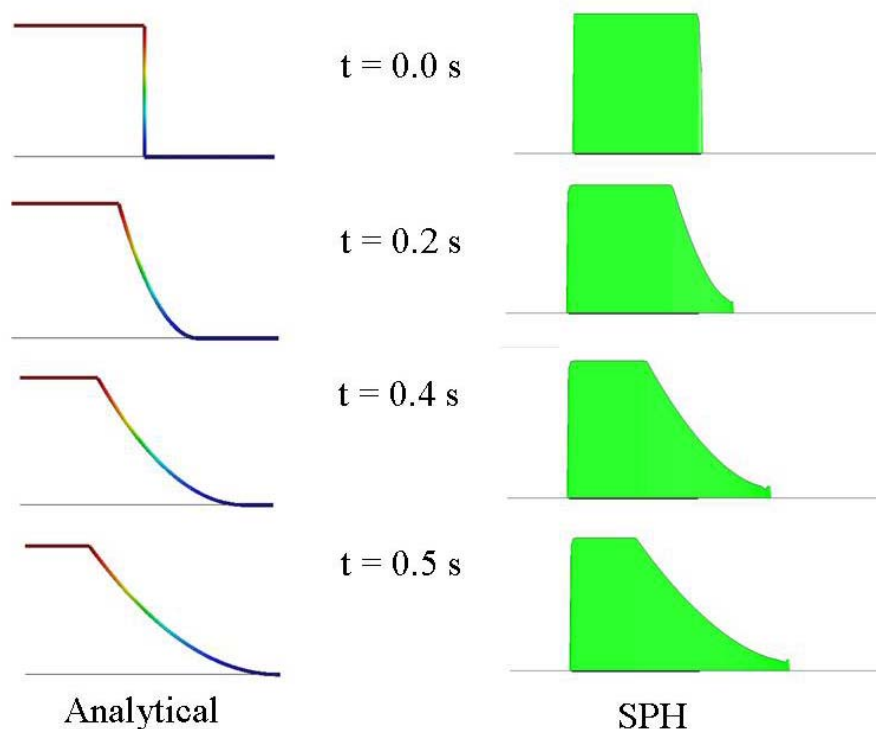


Figure 4.2.6. 1D Dam break problem: dry bed. Analytical (left) and computed results (right)

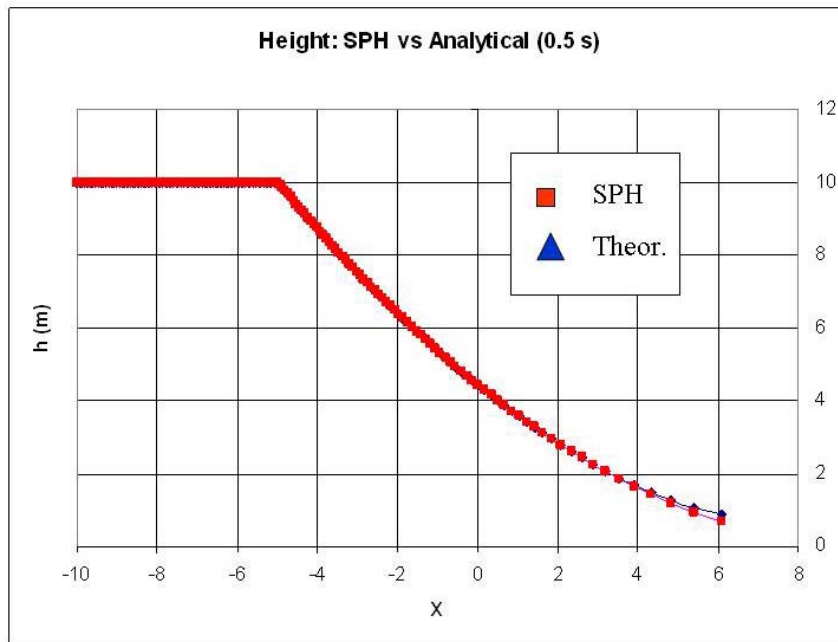


Figure 4.2.7a. 1D Dam break problem: Height of water at time $t = 0.5 s$

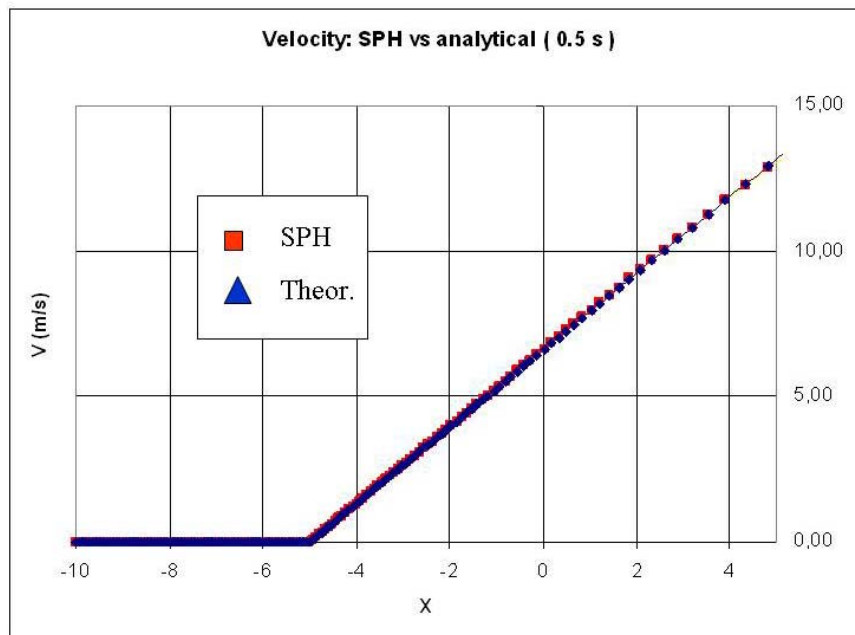


Figure 4.2.7b. 1D Dam break problem: Averaged velocity at time $t = 0.5 s$

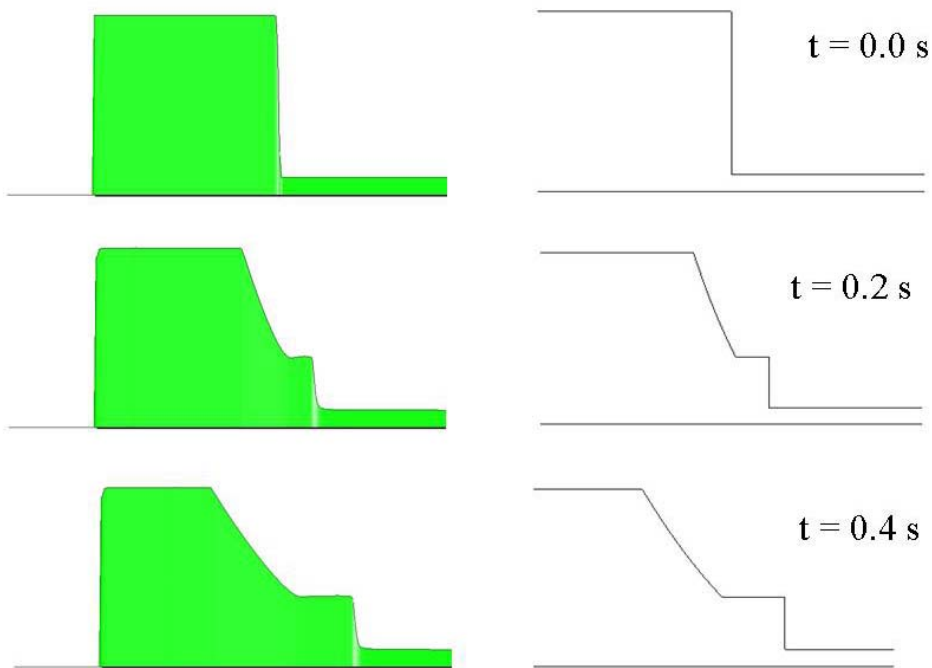


Figure 4.2.8. 1D Dam break problem: wet bed. Analytical (left) and computed results (right)

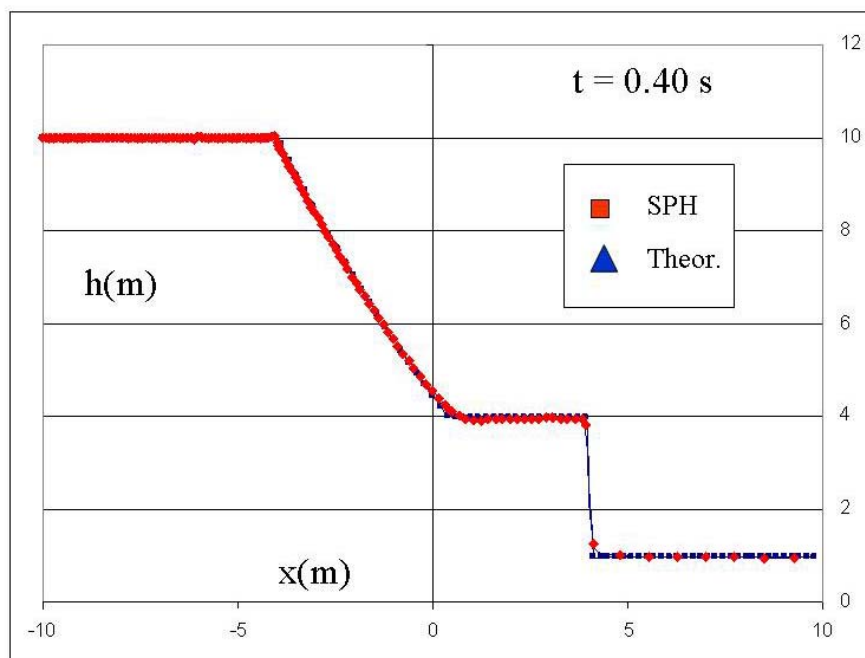


Figure 4.2.9(a). 1D Dam break problem over wet bed: Height of water at time $t = 0.4$ s

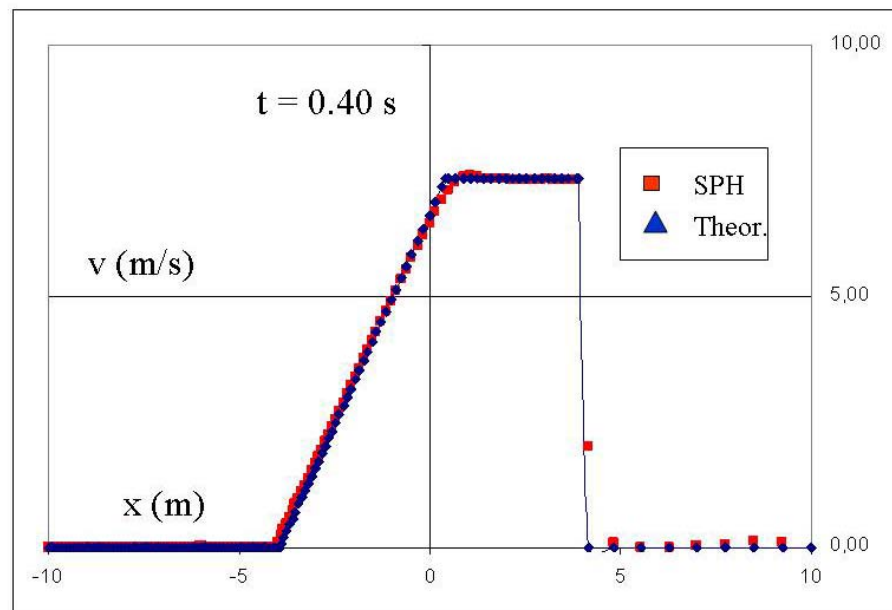


Figure 4.2.9(b). 1D Dam break problem over wet bed: Height of water at time $t = 0.4 s$

4.2.5.2. Laboratory small scale experiments

The results presented so far are tests which are used to assess the validity of the discretization technique chosen. In order to provide more insight on the performance of the method, we have chosen a laboratory test concerning a granular avalanche. The experiments were done at Ecole Polytechnique Fédérale de Lausanne by Dr. Irene Manzella (Manzella, 2008), who has provided all necessary information. The authors of this report acknowledge her assistance.

The granular material is fine Hostun sand, with an estimated angle of friction of 34° . The base material is forex, with a basal friction angle of 32° . The total volume of sand is 301 cm^3 . We provide in figure 4.2.10 a perspective of the experimental device, where the initial position of the sand can be seen.

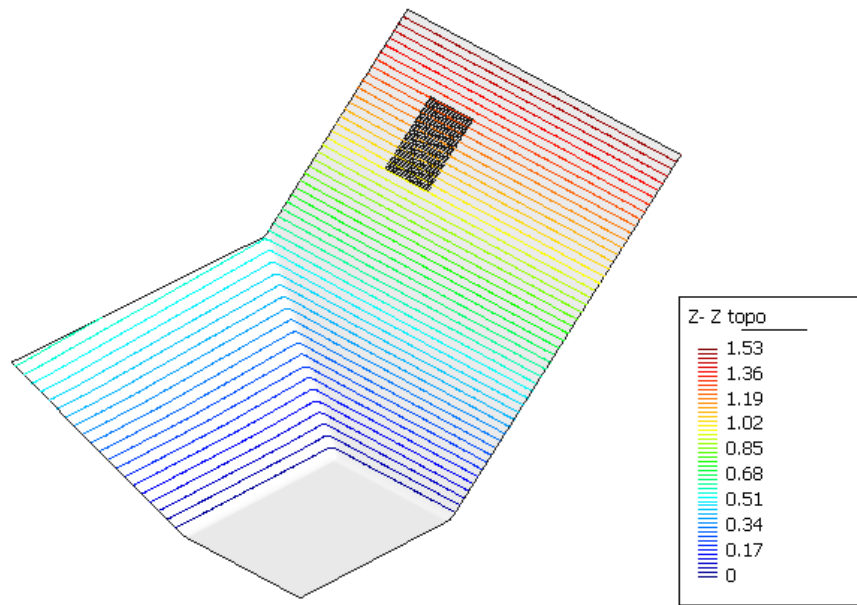


Figure 4.2.10. Schematic view of the Lausanne experiment arrangement

We depict in figure 4.2.11 the position of the nodes at different times obtained with the SPH depth integrated code.

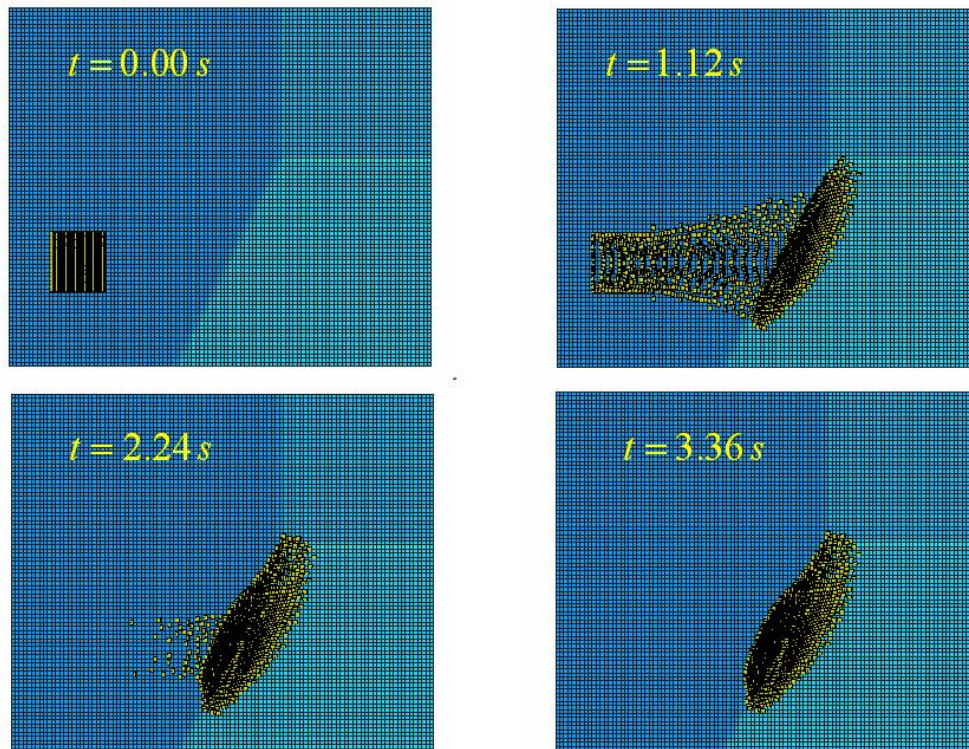


Figure 4.2.11. Position of nodes at times 0., 1.12, 2.24 and 3.36 s.

Finally, figures 4.2.12 and 4.2.13 provide a comparison between the experiments and the model predictions. This case has been presented in Pastor et al (2009)

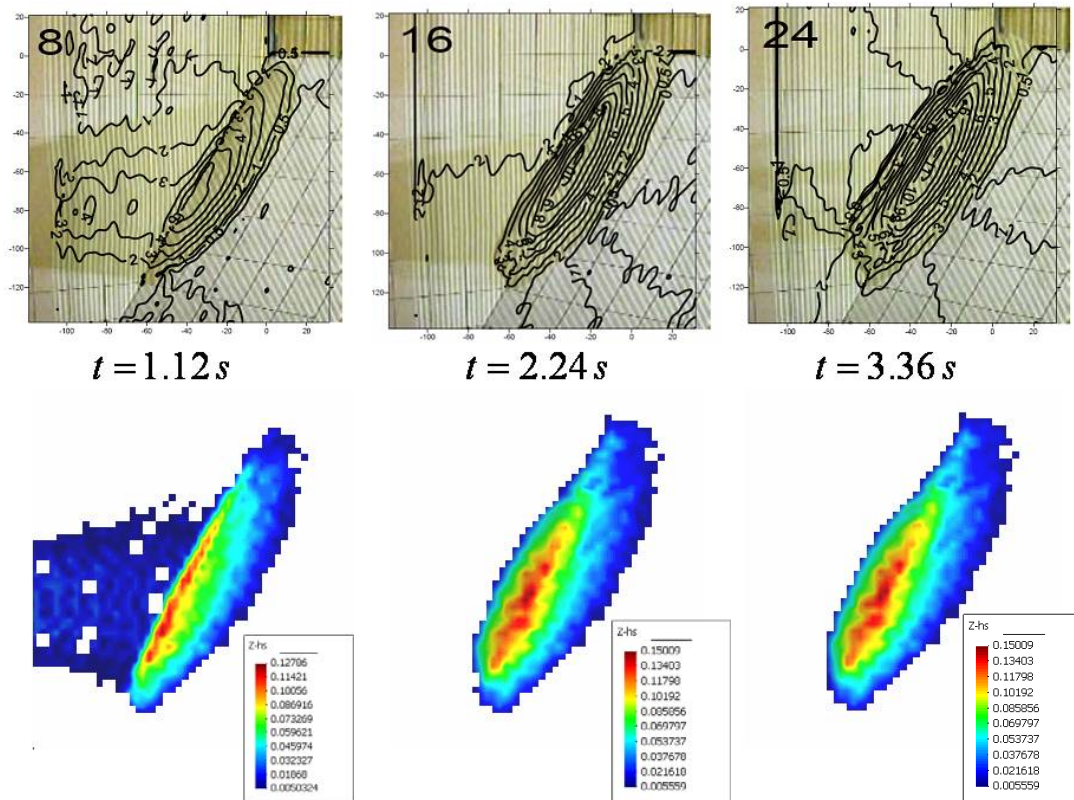


Figure 4.2.12 Comparison between experimental and laboratory results.

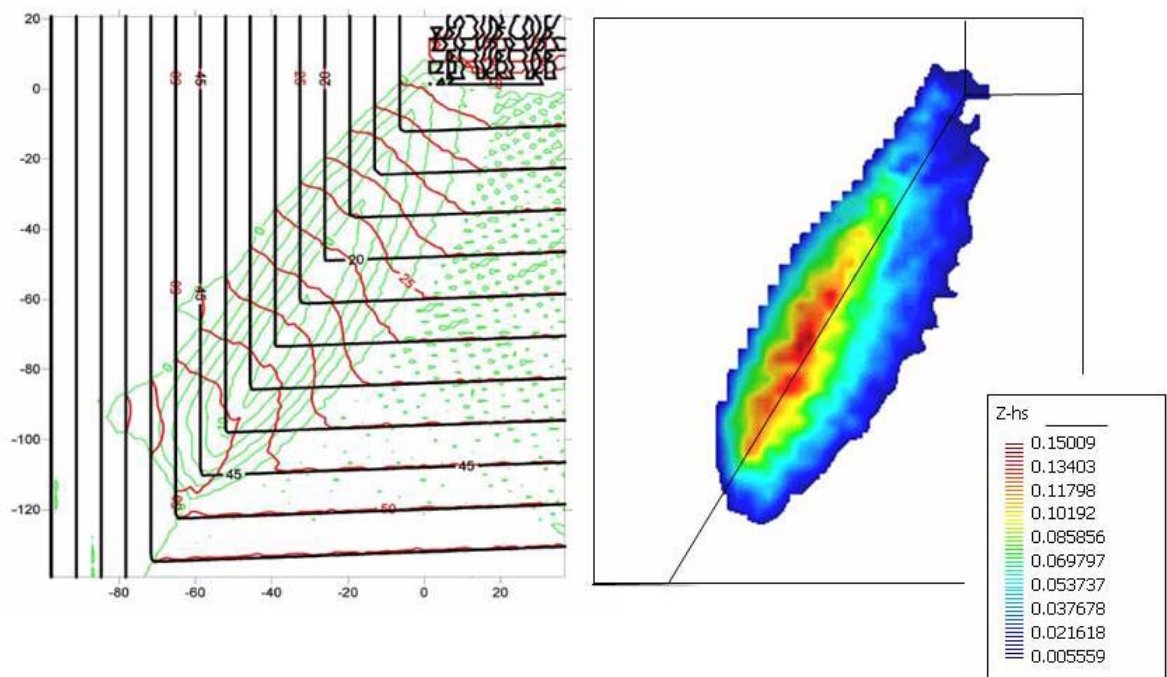


Figure 4.2.13. Final state: experimental results and model predictions

4.2.5.3. The Frank Slide (1903)

This example is based on the information found both in the package provided by Hong Kong Geotechnical Office, whose help is gratefully acknowledged. Frank slide happened in Canada in 1903. It is the event causing a larger number of victims in Canadian history. It consisted of a rock avalanche involving approximately 36 million of cubic meters of fragmented limestone which detached from the ridge of Turtle Mountain. The front extension was 700 m, and it travelled downhill, forming a deposit with an average thickness of 18 m. Concerning velocity of propagation, there is no available information, but McConnell and Brock (1904), who reported the event, estimated a propagation time less than 100 seconds, according to witnesses. The Frank slide has been described extensively by Cruden and Hungr (1986).

Modellers were provided with (i) a digital terrain model describing the situation before landslide took place, based on historic photographs and maps, and (ii) a full topographical description of the sliding mass. The grid spacing was 20 m.

The model used in the simulation is a depth integrated SPH code, which has been described in Pastor et al (2009). The rheological model used has been a dilatant viscoplastic frictional fluid with $\tan \phi = 0.218$ and $\mu_{CF} = 0.15 \cdot 10^{-3} \text{ Pa}\cdot\text{s}^2$. These values have been obtained from back analysis.

The analysis is an approximation, as in addition of using a depth integrated model, inverse segregation and fragmentation happened, which have not be taken into account in the analysis.

Concerning the results of the computations, (i) The final position agrees well, (ii) the width and length of the deposit are 1300 and 2000 m, to be compared to the measured values of 1700 and 2000 m. reported. Concerning the depth, we have obtained depths ranging from 0 to 28 m, which compare well with those reported. Computed propagation time is 80 s., of the order of magnitude reported by eye witnesses.

We provide in figure 4.2.14 a topographical map showing the landslide path and the position of the sliding mass, together with the computed final position of the nodes. Figure 4.2.15 provides the contours of depth in the deposit.

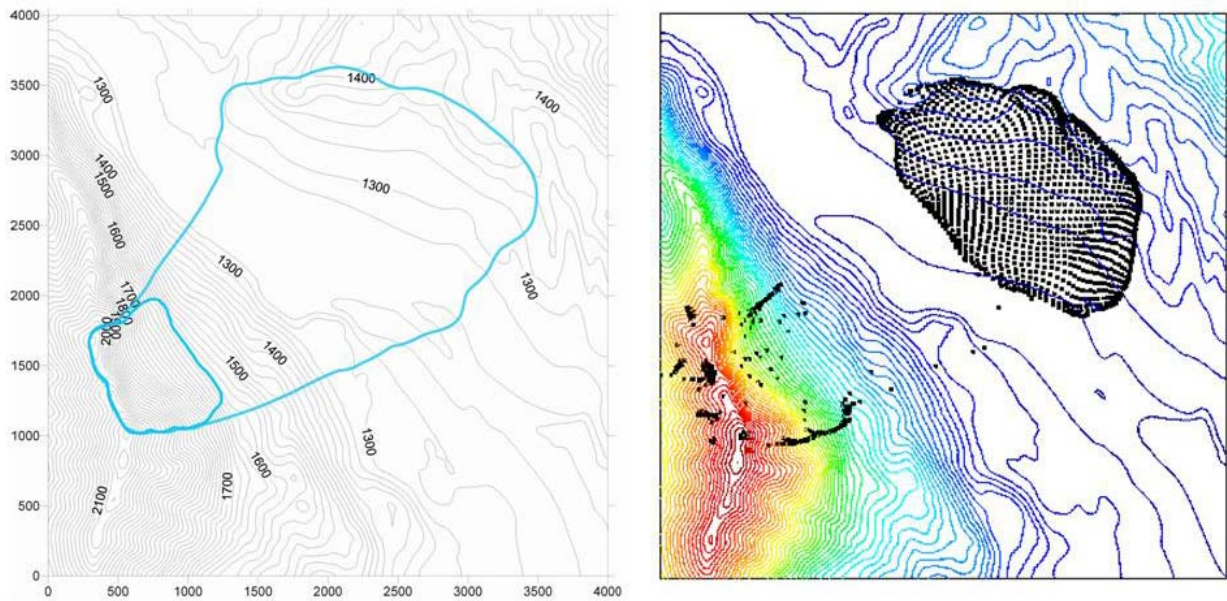


Figure 4.2.14. Frank Slide: Topography and landslide track (left), and final position of the SPH nodes (right)

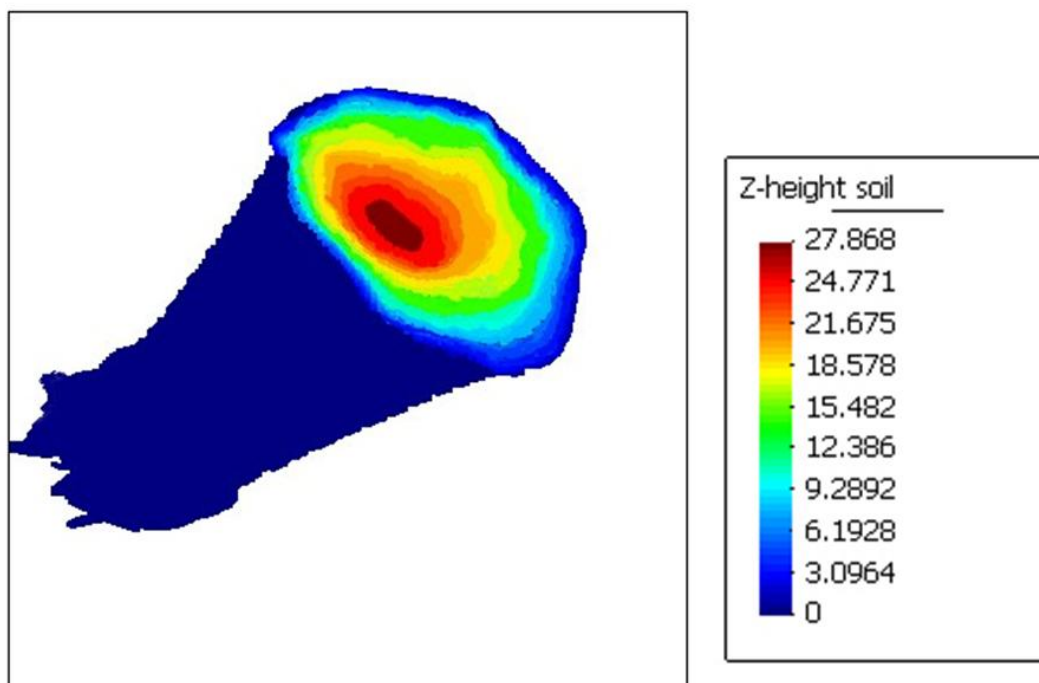


Figure 4.2.15. Frank Slide: Track of the rockslide (dark blue) and deposit depths

In conclusion, the performance of the model is based on

- (i) position of deposit and its track
- (ii) average depth of the deposit
- (iii) duration of the slide

4.2.5.4 The 2000 Tsing Shan debris flow

The second example we will consider is the Tsing Shan debris flow which happened in Hong Kong in on the 14th April 2000. As in the previous case, the analysis based on the information found both in the package provided by Hong Kong Geotechnical Office and the report by King (2001). This debris flow took place following rains which triggered more than 50 landslides in the area. The accumulated rainfall was 160 mm. The terrain was vegetated, and consisted of colluvial boulders. One important feature of this event is the strong erosion which made the initial mass to increase from 150 to 1600 cubic meters. Figure 4.2.16, taken from King provides two general views of the debris flow. One important aspect is the bifurcation of the flow which can be observed in the pictures.



Figure 4.2.16 General view of the 2000 Tsing Shan debris flow. (King 2001)

In order to model it, we have used the proposed model, with $\tan \phi = 0.18$, zero cohesion and $\mu_{CF} = 0.00133 \text{ Pa}\cdot\text{s}^2$. We have chosen the Hungr's erosion model, using an erosion coefficient of 0.0082 m^{-1} . The results of the simulation are given in Figure 4.2.17 which provides information regarding both the position and depths of the final deposit and the track. One peculiarity of this debris flow is the bifurcation in two branches, which is a feature difficult to capture in simulations. The computed path depicted in figure 11 shows the branching. In figure 4.2.17, it can be seen that the deepest deposit was formed at the end of the lower south branch, with a maximum depth of 1.8 m. Regarding velocities, there is no

available information. The model predicts a time of propagation close to 120 s. Considering that the runout was 900 m in the lowest branch, the average velocity is close to 30 km/h. The report provides a total mass deposited in the south branch of 500 cubic meters, while the computation provides a value of 525 cubic meters. Concerning the total volume of eroded soil, the report estimates it as 1600 cubic meters, while the computations provide a value of 1550.

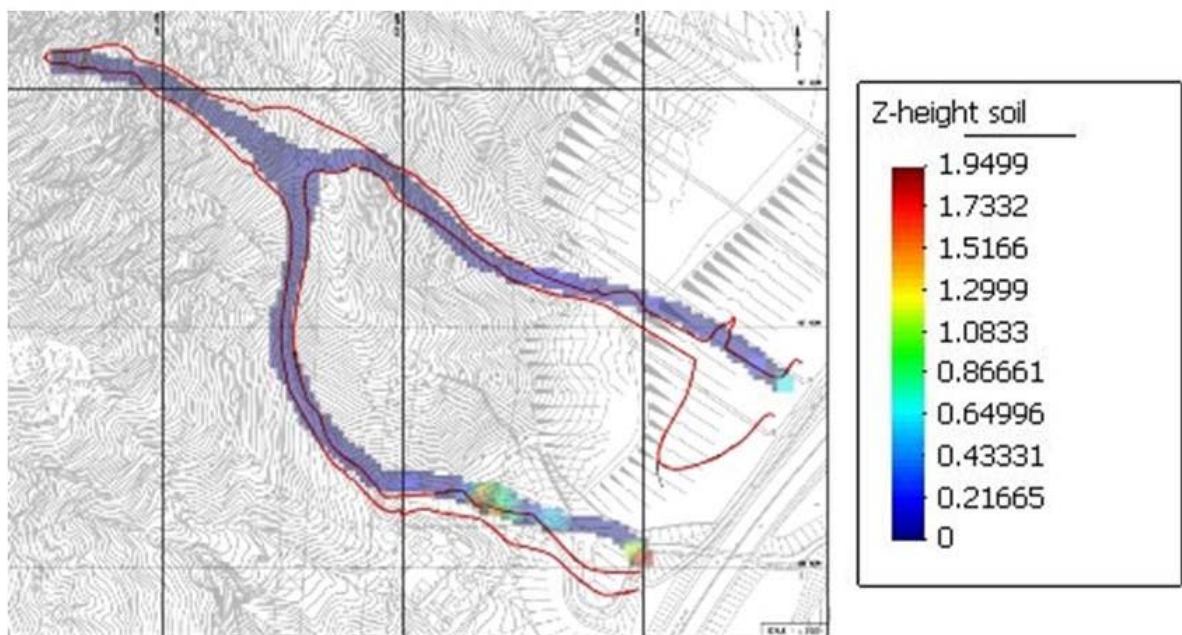


Figure 4.2.17 Tsing Shan debris flow: Model predictions vs. field observations

4.2.6 References

I.Babuska and J.Melenk, **The partition of unity element method**, Tech.Rep. BN-1185, Inst.Phys.science and Techn., Univ. Maryland, Maryland USA 1995

T.Belytschko, Y.Y. Lu and L.Gu, “Element-free Galerkin methods”, **Int.J.Num.Meth.Eng.** 37, 229-256, 1994

W. Benz, “Smooth particle hydrodynamics: a review”, in **The Numerical Modelling of Nonlinear Stellar Pulsations**, pp. 269-288, J.R. Buchler (Ed), Kluwer Academic Publishers, 1990

J. Bonet and S. Kulasegaram, "Correction and stabilization of smooth particle hydrodynamics methods with applications in metal forming simulations", **Int. J. Numer. Meth. Engng.**, 47, 1189-1214, 2000.

Cruden, D.M. and Hungr, O., The debris of the Frank Slide and theories of rockslide-avalanche mobility. **Canadian Journal of Earth Sciences**, 23 (1986) 425-432

C.di Prisco, R.Matiotti and R.Nova, "Theoretical investigation of the undrained stability of shallow submerged slopes", **Géotechnique** 45, No.3, pp. 479-496, 1995

C.A.Duarte and J.T.Oden, "An h-p adaptive method using clouds", **Comp.Meth.Appl.Mech.Eng.** 139, 237-262, 1996

R.Frenette, D.Eyheramendy and T.Zimmermann, "Numerical Modelling of dam-break type problems for Navier-Stokes and Granular Flows", in C.L.Chen (Ed.), **Debris-Flow Hazards Mitigation: Mechanics, Prediction and Assessment**, ASCE , pp. 586-595, 1997

R.A. Gingold and J.J. Monaghan, Kernel estimates as a basis for general particle methods in hydrodynamics, **J. Comput. Phys.** 46 (1982) 429.

J.P. Gray and J.J. Monaghan and R.P. Swift, SPH elastic dynamics, **Comput. Methods Appl.Mech. Engrg.**, 190, 6641-6662, (2001).

Guinot, V. (2003). **Godunov-type schemes. An introduction for engineers**, Elsevier

O.Hungr, "A model for the runout analysis of rapid flow slides, debris flows and avalanches", **Can.Geotech.J.** 32, pp 610-623, 1995

J.N.Hutchinson, "A sliding-consolidation model for flow slides", **Can.Geotech.J.**, 23, 115-126, 1986

J.N.Hutchinson, "Undrained loading, a fundamental mechanism of mudflows and other mass movements", **Géotechnique** 21, No.4, 353-358, 1971

K.Hutter and T.Koch, "Motion of a granular avalanche in an exponentially curved chute: experiments and theoretical predictions", **Phil.Trans.R.Soc.London**, A 334, pp 93-138, 1991

M.Jin and D.L.Fread, One-dimensional routing of mud/debris flows using NWS FLDWAV model, in C.L.Chen (Ed.), **Debris-Flow Hazards Mitigation: Mechanics, Prediction and Assessment**, ASCE , pp. 687-696, 1997

J.P.King, The 2000 Tsing Shan Debris Flow, Report LSR 3/2001, Planning Division, Geotechnical Engineering Office, Civil Engineering and Development Department, The Government of the Hong Kong Special Administrative Region (2001)

D.Laigle and P.Coussot, "Numerical Modelling of Mudflows", **J.Hydr.Engng.** ASCE, Vol.123, pp. 617-623, 1997

D.Laigle, "A two-dimensional model for the study of debris-flow spreading on a torrent debris fan", in C.L.Chen (Ed.), **Debris-Flow Hazards Mitigation: Mechanics, Prediction and Assessment**, ASCE , pp. 123-132, 1997

S.Li and W.K.Liu, **Meshfree particle method**, Springer Verlag, 2004 ISBN 3-540-22256-1

L.D. Libersky and A.G.Petschek, "Smooth particle hydrodynamics with strength of materials". **Advances in the Free Lagrange Method, Lecture Notes in Physics**, Vol. 395, pp. 248-257, 1990.

L.D. Libersky, A.G.Petschek, A.G., Carney, T.C., Hipp, J.R., Allahdadi and F.A. High, "Strain Lagrangian Hydrodynamics: A Three-Dimensional SPH Code for Dynamic Material Response". **J. Comp. Phys**, Vol. 109, 67-75, 1993.

G.R.Liu and M.B.Liu, Smoothed Particle Hydrodynamics: a meshfree particle method, **World Scientific**, 2003 ISBN 981-238-456-1

L.B. Lucy, "A numerical approach to the testing of fusion process", **Astronomical Journal**, Vol. 82, pp. 1013-1024, 1977.

Manzella, I. 2008. Dry Rock Avalanche Propagation: Unconstrained Flow Experiments with Granular Materials and Small Bricks. Ph.D. thesis n°4032, Ecole Polytechnique Fédérale de Lausanne, CH

McConnell, R.G., and Brock, R.W., The great landslide at Frank, Alberta, in Annual Report for the year 1902–1903: Department of the Interior, Government of Canada Sessional Paper 25 (1904), p. 1–17

J. J. Monaghan, "Smoothed particle hydrodynamics", **Ann. Rev. Astron. Astrophys.**, 30, 543-574, 1992

J.J. Monaghan, Simulating free surface flows with SPH, **J. Comput. Phys.** 110, 399-406, 1994..

J.J.Monaghan and R.A.Gingold, "Shock simulation by the particle method SPH", **J.Comp.Phys.** 52, pp. 374-389, 1983

J.J. Monaghan and A. Kocharyan, "SPH simulation of multi-phase flow", **Comput. Phys. Commun.** 87, 225-235, 1995

J.J.Monaghan and A.Kos, "Solitary waves on a Cretan beach." J. Waterways., Port, Coastal, Ocean Eng. ASCE, 125, 145–154, 1999

J.J.Monaghan and J.C.Latanzio, A refined particle method for astrophysical problems, **Astronomy and Astrophysics** 149, pp.135-143, 1985

Monaghan, J. J., Cas, R. F., Kos, A., and Hallworth, M., "Gravity currents descending a ramp in a stratified tank", **J. Fluid Mech.**, 379, 36–39, 1999

J. J. Monaghan; A. Kos and N. Issa, "Fluid Motion Generated by Impact", **Journal of Waterway, Port, Coastal, and Ocean Engineering** ASCE 129, 250–259, 2003

B.Nayroles, G.Touzot and P.Villon, "Generalizing the finite element method: diffuse approximation and diffuse elements", **Comp. Mech.** 10, 307-318, 1992

J.S.O'Brien, P.Y.Julien and W.T.Fullerton, "Two-dimensional water flow and mudflow simulation", **J.Hydr.Engng.** ASCE, Vol.119, pp. 244-261, 1993

E.Oñate and S. Idelsohn, "A mesh free finite point method for advective-diffusive transport and fluid flow problems", **Comp.Mech.** 21, 283-292, 1998

M. Quecedo and M. Pastor, "Application of the Level Set Method to the Finite Element Solution of Two-Phase Flows", *Int.J. Num.Meth.Engng*, Volume 50 Issue 3, Pages 645 – 663, 2001

P.W. Randles and L.D. Libersky, Normalized SPH with stress points, *Int. J. Numer. Meth. Engng.*, 48, 1445-1462, (2000).

D.Rickenmann and T.Koch, "Comparison of debris flow modelling approaches", in C.L.Chen (Ed.), **Debris-Flow Hazards Mitigation: Mechanics, Prediction and Assessment**, ASCE , pp. 576-585, 1997.

S.B.Savage and K.Hutter, "The dynamics of avalanches of granular materials from initiation to runout. Part I: Analysis", **Acta Mechanica** 86, pp 201-223, 1991.

J.Sousa and B.Blight, "Continuum simulation of flow failures", **Géotechnique** 41, 4, pp. 515-538, 1991d free surface NS SMAC.

Stoker, J.J. (1957). *Water waves*, Interscience, New York.

Pastor M., Haddad B., Sorbino G., Cuomo S., Drempetic V. A depth integrated coupled SPH model for flow-like landslides and related phenomena. **Int.J.Num.Anal.Meth.Geomechanics** 33, 2, 143-172, 2009. ISSN 0363-9061, DOI: 10.1002/nag.705.

K.Sassa, "Mechanism of flows in granular soils", pp. 1671-1702, in *GeoEng2000, Int.Conf.on Geotechnical and Geological Engineering*, Melbourne, 19-24 Nov.2000, Technomic publishing Co. Inc. Lancaster.Basel

H.T. Takeda, S.M. Miyama and M.Sekiya, "Numerical simulation of viscous flow by smooth particle hydrodynamics", **Progress of Theoretical Physics**, Vol 92, 939-960, 1994

E.F.Toro, **Shock-Capturing Methods for Free-Surface Shallow Flows**, Sons, New York, 2001

I.Vardoulakis and J.Sulem, **Bifurcation Analysis in Geomechanics**, Blakie academic & professional, 1995

L.Vulliet and K.Hutter, "Continuum model for natural slopes in slow movement", **Géotechnique** 38, pp. 199-217, 1988

C.Zoppou and S.Roberts, "Catastrophic collapse of water supply reservoirs in urban areas", **J.Hydr.Engng.** ASCE, Vol.125, pp. 686-695, 1997

4.3 MESHLESS TECHNIQUE: THE EFGM METHOD TO MODEL RUN OUT BY INTEGRATED MODELS

4.3.1 Introduction

The purpose of this section is to present another meshless or meshfree technique (namely the Element-Free Galerkin method or EFGM), to model the run-out of fast landslides. The mathematical models used to describe the propagation phase of a catastrophic landslide have been already presented in the previous sections. In Safeland, we propose to implement a 2D EFGM depth integrated approach, comparing the performances obtained by considering a Eulerian formulation for the governing equations and various boundary condition considerations, with the different numerical approaches implemented in the project (essentially SPH, FEM, FDM).

The EFGM is a meshfree method based on moving least square approximation and following the Partition of Unity principle as defined by Babuška & Melenk (1995, 1997). It was first proposed by Belytschko and co-workers (Belytschko *et al.*, 1994) and has so far, mainly been applied to Solid Mechanics modelling (e.g. see an overview in Belytschko *et al.*, 1996).

4.3.2 Description of the EFG method

In meshfree methods, a field u can be approximated by the quantity $u^h(\underline{x}, t)$ derived at spatial location \underline{x} and at time t , on a set of nodes $I = 1, \dots, N$ as:

$$u^h(\underline{x}, t) = \sum_{I=1}^N \varphi_I(\underline{x}) d_I(t) \quad (4.3.1)$$

where $\varphi_I(\underline{x})$ is the shape function at node I and $d_I(t)$, the corresponding nodal contribution.

The set of functions $F_N = \{\varphi_I\}_{I=1}^N$ constitutes a partition of unity associated to the open $B_N = \bigcup_{I=1}^N \Omega_I$, with Ω_I , a compact support representing the domain of influence of node I , i.e. the area (or volume) around node I contributing to the approximation, if the following conditions are verified:

$$\forall I, \varphi_I \in C^s(\Omega_I), s \in \square \quad (4.3.2)$$

$$\forall \underline{x}, \sum_{I=1}^N \varphi_I(\underline{x}) = 1 \quad (4.3.3)$$

Condition (4.3.3) corresponds to the Partition of Unity condition and can be seen as the consistency of order zero.

In the framework of Moving Least Square (MLS) methods such as EFGM, the shape function φ_I is built by using a symmetric monotonous decreasing weight function $W_I(\underline{x})$ defined on Ω_I , such that:

$$W_I(\underline{x}) \begin{cases} > 0 & \text{if } \underline{x} \in \Omega_I \\ = 0 & \text{if } \underline{x} \notin \Omega_I \end{cases} \quad (4.3.4)$$

This condition is crucial as it allows a global approximation on the domain through a local representation.

The weight function W_I is generally chosen as radial, (i.e. a circle in 2-D and a sphere in 3-D) and can be written as:

$$W_I(\underline{x}) = W(\|\underline{x} - \underline{x}_I\|, h_I) = W(r) \quad \text{with } r = \|\underline{x} - \underline{x}_I\|_2 / h_I \quad (4.3.5)$$

where $\|\underline{x} - \underline{x}_I\|_2$ is the Euclidian distance between the evaluation point \underline{x} and node I and h_I , the radius of the influence domain Ω_I .

In the MLS approximation, $u^h(\underline{x})$ is expressed as :

$$u^h(\underline{x}) = \underline{p}^T(\underline{x}) \cdot \underline{\alpha}(\underline{x}) \quad (4.3.6)$$

with $\underline{p}^T(\underline{x}) = \{p_i(\underline{x})\}_{i=1}^m$, the *primary basis* vector of the approximation, generally a polynomial basis of order \tilde{m} , i.e. a vector of m monomial functions $p_i(\underline{x})$ defined in 2-D as:

$$\begin{cases} p_i(x) = x^k y^{j-k} & 0 \leq j+k \leq \tilde{m}, 0 \leq i \leq \frac{1}{2}(j+1)(j+2) \\ m = \frac{1}{2}(\tilde{m}+1)(\tilde{m}+2) \end{cases} \quad (4.3.7)$$

The vector of coefficients $\underline{\alpha}$ is obtained by minimizing the following quantity:

$$J(\underline{\alpha})\Big|_{\underline{x}} = \sum_I W_I(\underline{x}) \left[\underline{p}^T(\underline{x}_I) \cdot \underline{\alpha}(\underline{x}) - d_I \right]^2 \quad (4.3.8a)$$

which means to calculate:

$$\frac{\partial J(\underline{\alpha})}{\partial \underline{\alpha}} \Big|_{\underline{x}} = 0 \quad (4.3.8b)$$

This leads to the expression of shape function $\varphi_I(\underline{x})$ as:

$$\varphi_I(\underline{x}) = C_I(\underline{x}) W_I(\underline{x}) \quad (4.3.9)$$

with:

$$C_I(\underline{x}) = \underline{p}^T(\underline{x}) \cdot \mathbf{M}^{-1}(\underline{x}) \cdot \underline{p}(\underline{x}_I) \quad (4.3.10)$$

and \mathbf{M} , the moment matrix defined by:

$$\mathbf{M}(\underline{x}) = \sum_{I=1}^N W_I(\underline{x}) \underline{p}(\underline{x}_I) \cdot \underline{p}^T(\underline{x}_I) \quad (4.3.11a)$$

The necessary condition for the inverse of matrix \mathbf{M} to exist is the following:

$$\forall \underline{x}, N_{\underline{x}} \geq m \quad (4.3.11b)$$

with $N_{\underline{x}}$, the number of nodes whose influence domain includes \underline{x} . Another important condition is to verify that the spatial arrangement of neighbouring nodes is not singular, i.e. allows deriving the primary basis terms.

Remark:

Due to the consistency condition, shape function $\varphi_I(\underline{x})$ is able to reproduce polynomial of degree \tilde{m} :

$$\forall \underline{x} \in \overline{\Omega}, \sum_{I=1}^N \varphi_I(\underline{x}) p_j(\underline{x}_I) = p_j(\underline{x}) \quad 1 \leq j \leq m \quad (4.3.12)$$

In the following, we indicate some usual radial weight functions (see Fig. 4.3.1).

Cubic spline functions:

Spline1 :

$$W(r) = \begin{cases} 1 - 6r^2 + 6r^3 & \text{if } r \leq \frac{1}{2} \\ 2(1-r)^3 & \text{if } \frac{1}{2} < r \leq 1 \end{cases} \quad (4.3.13)$$

Spline2 :

$$W(r) = \begin{cases} \frac{2}{3} - 4r^2 + 4r^3 & \text{if } r \leq \frac{1}{2} \\ \frac{4}{3}(1-r)^3 & \text{if } \frac{1}{2} < r \leq 1 \end{cases} \quad (4.3.14)$$

Exponential or Gauss functions:

Gauss1 :

$$W(r) = e^{-(r/c_I)^{2k}}, k \geq 1, c_I > 0 \quad (4.3.15)$$

Gauss2 :

$$W(r) = \frac{e^{-(rh_{max})^{2k}} - e^{-(h_{max})^{2k}}}{1 - e^{-(h_{max})^{2k}}} \quad \text{with } h_I = c_I h_{max} \quad (4.3.16)$$

where h_{max} represents the maximum radius value for all influence domains and coefficient c_I , the minimal distance from node I to have a non singular moment matrix. In practice, c_I is set equal to the distance of node I to its second or third closer neighbouring node.

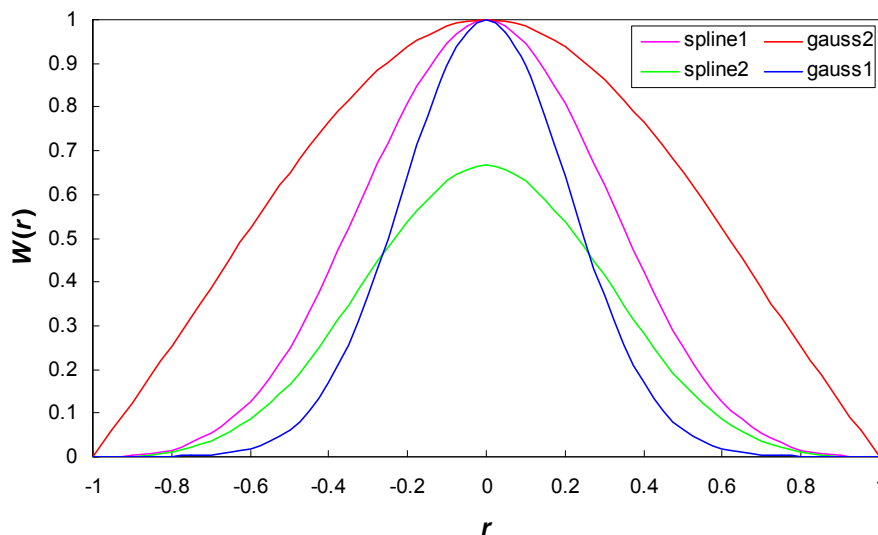


Figure 4.3.1 Usual radial weight functions with $h_I = 1$ and $c_I = 0.3, k = 1$ (Gauss)

An example of simple shape function is proposed by Shepard (1968), obtained by considering a constant primary basis ($\tilde{m} = 0$):

$$\varphi_I(\underline{x}) = \frac{W_I(\underline{x})}{\sum_{J=1}^N W_J(\underline{x})} \quad (4.3.17)$$

Contrary to FEM, shape function $\varphi_I(\underline{x})$ is non interpolant. Hence, the approximated field value $u_I(t) = u^h(\underline{x}_I, t)$ and nodal contribution $d_I(t)$ are not equal: $\forall I, u_I \neq d_I$. A special treatment is thus required for essential (Dirichlet) boundary conditions.

Among the various techniques that have been proposed, it is worth presenting the following:

- use of singular weight functions;
- coupling with finite elements on the boundary.

Singular weight functions:

This technique consists in using discontinuous or singular weight functions $\tilde{W}_I(\underline{x})$ for nodes located on the essential boundary, such that: $\forall I, \tilde{W}_I(\underline{x}) \xrightarrow[\underline{x} \rightarrow \underline{x}_I]{} +\infty$, in order to obtain interpolant shape functions.

An simple example of such a function is proposed by Laouar (1996).

We prefer to use the modified weight functions proposed by Breitkopf and co-workers (Breitkopf *et al.*, 2000), obtained by normalizing with a Shepard-type interpolation (see Fig. 4.3.2):

$$\tilde{W}_I(\underline{x}) = \frac{W_I(\underline{x})}{W_I(\underline{x}) + [1 - W_I(\underline{x})] \sum_{J \neq I} \frac{W_J(\underline{x})}{[1 - W_J(\underline{x})]}} \quad (4.3.18)$$

These weight functions (4.3.20) are continuous on their support and verify also:

$$\left\{ \begin{array}{l} \tilde{W}_I(\underline{x}) \in [0, 1] \\ \sum_{I=1}^N \tilde{W}_I(\underline{x}) = 1 \\ \forall I, \tilde{W}_I(\underline{x}_J) = \delta_{IJ} \end{array} \right. \quad (4.3.19)$$

This technique is interesting as the modified weight functions can be used on the whole domain and not only for the boundary nodes, leading to an interpolant approximation.

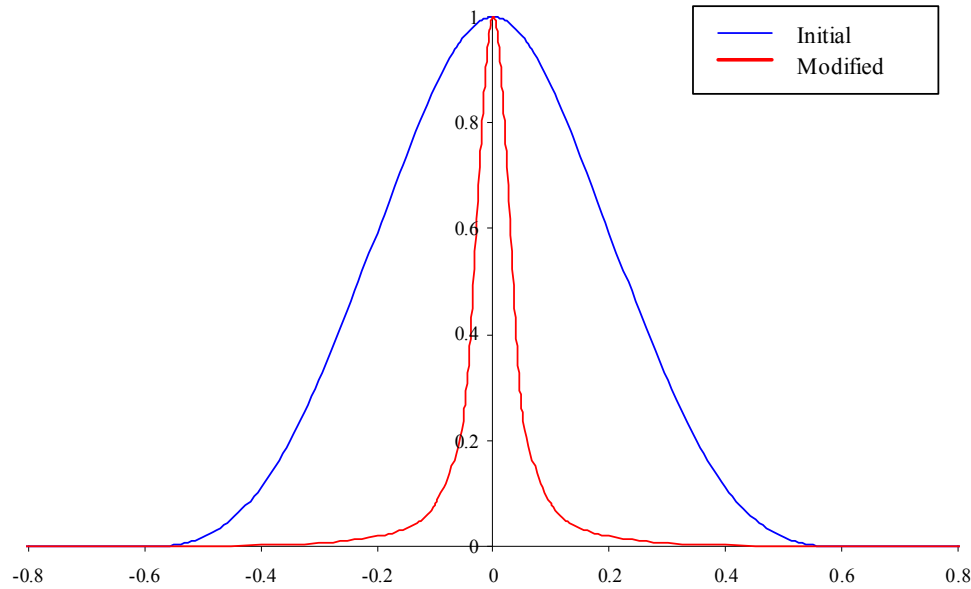


Figure 4.3.2 Comparison of initial and modified weight functions, as proposed by Breitkopf *et al.*(2000)

Coupling with finite elements on the boundary:

This technique, which has been proposed by Belytschko and co-workers (Belytschko *et al.*, 1995, 1996; Krongauz & Belytschko, 1996), consists in introducing interface elements (Ω_I) between meshfree (Ω_M) and FEM (Ω_F) sub-domains (see Fig. 4.3.3).

Then, $u^h(\underline{x}, t)$ is evaluated on the interface element Ω_I^e , by a combined approximation:

$$\begin{aligned} \forall \underline{x} \in \Omega_I^e, u^h(\underline{x}, t) &= [1 - R(\underline{x})] \sum_{I=1}^{N_F} N_I(\underline{x}) d_I(t) + R(\underline{x}) \sum_{I=1}^N \varphi_I(\underline{x}) d_I(t) \\ &= \sum_{I=1}^N \tilde{N}_I(\underline{x}) d_I(t) \end{aligned} \quad (4.3.20)$$

N_F and $N_I(\underline{x})$ are respectively the number of nodes and shape function for the finite-element at the interface Ω_I^e . N is the number of meshfree and/or FEM nodes used to build the meshfree shape functions, i.e. whose domains of influence contain the evaluation point \underline{x} .

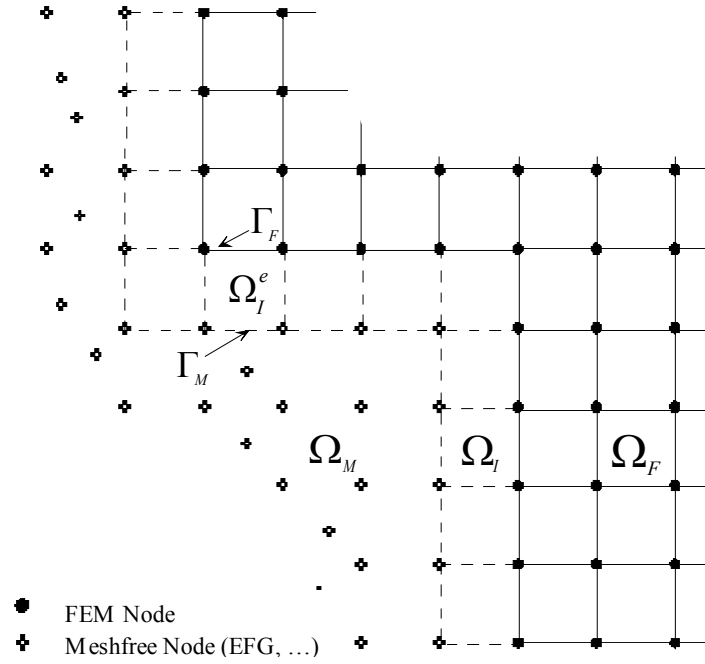


Figure 4.3.3 Coupling of EGM-FEM domains (Γ_M represents the boundary between Ω_M and Ω_I , and Γ_F , the one between Ω_I and Ω_F)

The blending shape function $\tilde{N}_I(\underline{x})$ is expressed on Ω_I^e , as follows:

$$\tilde{N}_I(\underline{x}) = \begin{cases} [1 - \bar{R}(\underline{x})] N_I(\underline{x}) + \bar{R}(\underline{x}) \phi_I(\underline{x}) & \underline{x}_I \in \Omega_I^e \\ \bar{R}(\underline{x}) \phi_I(\underline{x}) & \underline{x}_I \notin \Omega_I^e \end{cases} \quad (4.3.21)$$

with $\bar{R}(\underline{x})$, a transition function, such that $\bar{R}(\underline{x}) = 1$ for \underline{x} in Γ_M and zero elsewhere, defined as:

$$\tilde{R}(\underline{x}) = R^2(\underline{x}) [3 - 2R(\underline{x})] \quad (4.3.22a)$$

and:

$$R(\underline{x}) = \sum_{\substack{J \\ \underline{x}_J \in \Gamma_M}} N_J(\underline{x}) \quad (4.3.22b)$$

In this case, partial derivative $\partial_i \tilde{N}_I$ of \tilde{N}_I at point \underline{x} along i^{th} direction is written as:

$$\partial_i \tilde{N}_I = \begin{cases} -\partial_i \bar{R} N_I + [1 - R] \partial_i N_I + \partial_i \bar{R} \phi_I + \bar{R} \partial_i \phi_I & \underline{x}_I \in \Omega_I^e \\ \partial_i \bar{R} \phi_I + \bar{R} \partial_i \phi_I & \underline{x}_I \notin \Omega_I^e \end{cases} \quad (4.3.23)$$

with:

$$\partial_i \tilde{R} = 6R [1 - R] \partial_i R \quad (4.3.24a)$$

and:

$$\partial_i R = \sum_{\substack{J \\ \underline{x}_J \in \Gamma_M}} \partial_i N_J \quad (4.3.24b)$$

In order to set essential boundary conditions, Belytschko and co-workers propose to use the coupled EFGM-FEM methodology, by considering integration cells or interface elements of the same order as the finite elements on the boundary (for instance in 2-D, 4-node quadrangular elements for interface and boundaries). In our case, we have chosen to implement different orders, e.g. 4-node quadrangular interface elements and 2-node line (FEM) elements on the boundary (see Fig. 4.3.4).

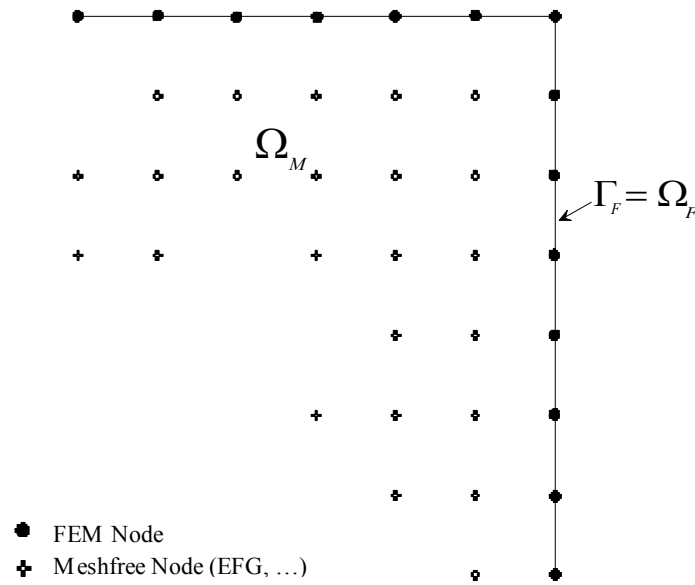


Figure 4.3.4 Coupling of EGM-FEM domains by using line finite-elements on the essential boundaries

Fast evaluation of partial derivatives

If we write shape function $\varphi_I(\underline{x})$ as:

$$\varphi_I(\underline{x}) = \underline{p}^T(\underline{x}) \cdot \mathbf{M}^{-1}(\underline{x}) \cdot \underline{b}_I(\underline{x}) \quad (4.3.25)$$

with:

$$\underline{b}_I(\underline{x}) = W_I(\underline{x}) \underline{p}(\underline{x}_I) \quad (4.3.26)$$

Then, the partial derivative $\partial_i \varphi_I$ of φ_I along the i^{th} direction, is expressed as:

$$\begin{aligned} \partial_i \varphi_I(\underline{x}) &= \partial_i \underline{p}^T(\underline{x}) \cdot \mathbf{M}^{-1}(\underline{x}) \cdot \underline{b}_I(\underline{x}) + \underline{p}^T(\underline{x}) \cdot \partial_i \mathbf{M}^{-1}(\underline{x}) \cdot \underline{b}_I(\underline{x}) \\ &\quad + \underline{p}^T(\underline{x}) \cdot \mathbf{M}^{-1}(\underline{x}) \cdot \partial_i \underline{b}_I \end{aligned} \quad (4.3.27)$$

with:

$$\partial_i \mathbf{M}^{-1} = -\mathbf{M}^{-1} \cdot \partial_i \mathbf{M} \cdot \mathbf{M}^{-1} \quad (4.3.28)$$

This evaluation appears to be of high computational cost and different techniques have been proposed to reduce it. An efficient technique consists in using the linear consistency property of the MLS approximation (Belytschko et al., 1996).

If we express shape functions as :

$$\varphi_I(\underline{x}) = \underline{V}^T(\underline{x}) \cdot \underline{b}_I(\underline{x}) \quad (4.3.29)$$

where:

$$\underline{V}(\underline{x}) = \mathbf{M}^{-1}(\underline{x}) \cdot \underline{p}(\underline{x}) \quad (4.3.30)$$

Then solving eq. (4.8.8b) is equivalent to solving the following system:

$$\mathbf{M}(\underline{x}) \cdot \underline{V}(\underline{x}) = \underline{p}(\underline{x}) \quad (4.3.31)$$

Moreover, solving system (4.3.33) using the LU decomposition of \mathbf{M} instead of computing \mathbf{M}^{-1} , leads to determine the unknown vector \underline{V} by solving the following system:

$$\begin{cases} \mathbf{L} \cdot \underline{Y} = \underline{p} \\ \mathbf{U} \cdot \underline{V} = \underline{Y} \end{cases} \quad (4.3.32)$$

The same LU decomposition of \mathbf{M} can be used to calculate the partial derivatives $\partial_i \underline{V}(\underline{x})$ of \underline{V} :

$$\mathbf{M} \cdot \partial_i \underline{V} = \partial_i \underline{p} - \partial_i \mathbf{M} \cdot \underline{V} \quad (4.3.33)$$

Finally, the partial derivatives of φ_I are obtained by:

$$\partial_i \varphi_I = \partial_i \underline{V}^T \cdot \underline{b}_I + \underline{V}^T \cdot \partial_i \underline{b}_I \quad (4.3.34)$$

4.3.3 EFGM discretization of depth integrated equations

The Eulerian form (a1) to (c1) of the governing equations are considered for analysis:

(a1) Balance of mass

$$\partial_t h + \partial_{x_j} (\bar{v}_j h) = e_R \quad (4.3.35)$$

(b1) Balance of linear momentum

$$\begin{aligned} \forall i, \partial_t (h\bar{v}_i) + \partial_{x_j} \left(h\bar{v}_i\bar{v}_j - \frac{1}{2}b_3h^2\delta_{ij} \right) = -\alpha \partial_{x_j} (h\bar{v}_i\bar{v}_j) + b_3h\partial_{x_i}Z \\ + \frac{1}{\rho} \partial_{x_j} (h\bar{\sigma}_{ij}^*) + S_{fi} \end{aligned} \quad (4.3.36)$$

S_{fi} represents the friction terms along the i^{th} direction and depends of the fluid rheology assumed for analysis (e.g. Darcy-Weisbach friction terms at the basal surface, etc.). In Safeland, it will be written as:

$$S_{fi} = \frac{1}{\rho} |N^B| t_i^B \quad (4.3.37)$$

where the forces at the top of the slide have been neglected.

(c1) Vertical consolidation

$$\partial_t (P_1h) + \partial_{x_j} (\bar{v}_jP_1h) + \frac{\pi}{2} C.T. = -\frac{\pi^2}{4h} c_v P_1 \quad (4.3.38)$$

with $P_1 = \frac{\pi}{2} \bar{p}_w$ and \bar{p}_w being the depth-averaged pore pressure.

Writing the above equations in a more compact form leads to:

$$\partial_t \phi + \text{div}F = D + S \quad (4.3.39)$$

with the vectors of unknowns ϕ , flux F , diffusive terms D and source terms S defined as:

$$\phi = \begin{pmatrix} h \\ h\bar{v}_1 \\ h\bar{v}_2 \\ hP_1 \end{pmatrix} \quad F_1 = \begin{pmatrix} h\bar{v}_1 \\ h\bar{v}_1^2 - \frac{1}{2}b_3h^2 \\ h\bar{v}_1\bar{v}_2 \\ h\bar{v}_1P_1 \end{pmatrix} \quad F_2 = \begin{pmatrix} h\bar{v}_2 \\ h\bar{v}_1\bar{v}_2 \\ h\bar{v}_2^2 - \frac{1}{2}b_3h^2 \\ h\bar{v}_2P_1 \end{pmatrix} \quad (4.3.40a)$$

$$D = \frac{1}{\rho} \begin{pmatrix} 0 \\ \partial_{x_j} (h\bar{\sigma}_{1j}^*) \\ \partial_{x_j} (h\bar{\sigma}_{2j}^*) \\ 0 \end{pmatrix} \quad S = \frac{1}{\rho} \begin{pmatrix} e_R \\ \rho b_3 h \partial_{x_1} Z + |N^B| t_1^B \\ \rho b_3 h \partial_{x_2} Z + |N^B| t_2^B \\ -\rho \frac{\pi^2}{4h} c_v P_1 \end{pmatrix} + \begin{pmatrix} 0 \\ -\alpha \partial_{x_j} (h\bar{v}_1\bar{v}_j) \\ -\alpha \partial_{x_j} (h\bar{v}_2\bar{v}_j) \\ -\frac{\pi}{2} C.T. \end{pmatrix} \quad (4.3.40b)$$

As in the SPH method, the same nodal variables will be considered on the set of nodes chosen for the meshfree approximation. Then, the spatial discretization of equation (4.3.41) is performed using the EFG methodology described in this section and the two-step Taylor–

Galerkin algorithm (described in the FEM technique section of this deliverable) is used for time integration.

4.3.4 References

Babuška, I. & Melenk, J. M. (1995), The partition of unity element method, Technical Report BN-1185, Institute for Physical Science and Technology, University of Maryland, Maryland USA.

Babuška, I. & Melenk, J. M. (1997), ‘The Partition of Unity Method’, **Int. J. Num. Meth. Engng.**, 40: 727-758.

Beissel, S. & Belytschko, T. (1996), ‘Nodal integration of the Element-free Galerkin method’, **Computer Meth. Applied Mech. Engng.**, 139: 49-74, 1996.

Belytschko, T., Lu, Y.Y. and Gu, L. (1994), ‘Element-free Galerkin methods’, **Int. J. Num. Meth. Eng.**, 37: 229-256.

Belytschko, T., Organ, D., Krongauz, Y. (1995), ‘A coupled finite element-element-free Galerkin method’, **Computational Mech.**, 17:186-195.

Belytschko, T., Krongauz, Y., Organ, D., Fleming, M., Krysl, P. (1996), ‘Meshless methods: an overview and recent developments’, **Computer Meth. Applied Mech. Engng.**, 139: 3-48.

Breitkopf, P., Rassinoux, A., Touzot, G., Villon, P. (2000), ‘Explicit form and efficient computation of MLS shape functions and their derivatives’, **Int. J. Num. Meth. Engng.**, 48: 451-466.

Duarte, C. A. & Oden, J. T. (1996), An h-p adaptive method using clouds, **Computer Meth. Applied Mech. Engng.**, 139: 237-262.

Krongauz, Y. & Belytschko, T. (1996), Enforcement of essential boundary conditions in meshless approximations using finite elements, **Computer Meth. Applied Mech. Engng.**, 131: 133-145.

Laouar, T. (1996), Contribution à l’étude de l’approximation diffuse : auto - adaptativité en éléments diffus, *Thèse de Doctorat*, Université de Technologie de Compiègne, France (in French).

4.4 FINITE ELEMENT MODELLING OF RUN OUT OF FAST LANDSLIDES

4.4.1 Introduction

We have presented in the Chapter devoted to describe the mathematical models which describe the propagation phase of a catastrophic landslide the depth integrated equations. While SPH formulations are more suited to the “quasi-lagrangian” formulation, eulerian formulations are best for finite elements. We will recall here the main equations written in an eulerian framework.

(a1) Balance of mass

$\frac{\partial h}{\partial t} + \frac{\partial}{\partial x_j} (\bar{v}_j h) = e_R$	(4.4.1)
---	---------

(b1) Balance of linear momentum

$\frac{\partial}{\partial t} (h \bar{v}_i) + (1 + \alpha) \frac{\partial}{\partial x_j} (h \bar{v}_i \bar{v}_j) = b_i h + \frac{1}{\rho} \frac{\partial}{\partial x_j} (h \bar{\sigma}_{ij}) + \frac{1}{\rho} N^A t_i^A + \frac{1}{\rho} N^B t_i^B$	(4.4.2)
---	---------

or, introducing the decomposition:

$$\sigma_{ij} = -\bar{p} \delta_{ij} + \sigma_{ij}^*$$

with

$$\bar{p} = \frac{1}{2} \rho b_3 h \quad \bar{\sigma}_{ij}^* = \bar{\sigma}_{ij} + \bar{p} \delta_{ij}$$

$\frac{\partial}{\partial t} (h \bar{v}_i) + \frac{\partial}{\partial x_j} \left(h \bar{v}_i \bar{v}_j - \frac{1}{2} b_3 h^2 \delta_{ij} \right) =$ $\alpha \frac{\partial}{\partial x_j} (h \bar{v}_i \bar{v}_j) + \frac{1}{\rho} \frac{\partial}{\partial x_j} (h \bar{\sigma}_{ij}^*) + b_i h + \frac{1}{\rho} N^A t_i^A + \frac{1}{\rho} N^B t_i^B$	(4.4.3)
--	---------

(c1) Vertical consolidation

$\frac{\partial}{\partial t} (P_1 h) + \frac{\partial}{\partial x_j} (\bar{v}_j P_1 h) + \frac{\pi}{2} C.T. = -\frac{\pi^2}{4h} c_v P_1$	(4.4.4)
--	---------

This eulerian form is often written in a more compact manner as:

$$\frac{\partial \phi}{\partial t} + \frac{\partial F_1}{\partial x_1} + \frac{\partial F_2}{\partial x_2} = D + S \quad (4.4.5)$$

where we have introduced:

- (i) A vector of unknowns ϕ
- (ii) The fluxes F_1 and F_2 following axes x_1 and x_2
- (iii) The diffusive terms D
- (iv) The source terms S

which are defined as:

$$\phi = \begin{pmatrix} h \\ h\bar{v}_1 \\ h\bar{v}_2 \\ hP_1 \end{pmatrix} \quad F_1 = \begin{pmatrix} h\bar{v}_1 \\ h\bar{v}_1^2 + \frac{1}{2}b_3h^2 \\ h\bar{v}_1\bar{v}_2 \\ h\bar{v}_1P_1 \end{pmatrix} \quad F_2 = \begin{pmatrix} h\bar{v}_2 \\ h\bar{v}_1\bar{v}_2 \\ h\bar{v}_2^2 + \frac{1}{2}b_3h^2 \\ h\bar{v}_1P_1 \end{pmatrix} \quad (4.4.6)$$

and

$$D = \begin{pmatrix} 0 \\ \frac{1}{\rho} \frac{\partial}{\partial x_j} (h\bar{\sigma}_{1j}^*) \\ \frac{1}{\rho} \frac{\partial}{\partial x_j} (h\bar{\sigma}_{2j}^*) \\ 0 \end{pmatrix} \quad S = \begin{pmatrix} e_R \\ b_1h + \frac{1}{\rho} |N^A| t_1^A + \frac{1}{\rho} |N^B| t_1^B \\ b_2h + \frac{1}{\rho} |N^A| t_2^A + \frac{1}{\rho} |N^B| t_2^B \\ -\frac{\pi^2}{4h} c_v P_1 \end{pmatrix} + \begin{pmatrix} 0 \\ -\alpha \frac{\partial}{\partial x_j} (h\bar{v}_1\bar{v}_j) \\ -\alpha \frac{\partial}{\partial x_j} (h\bar{v}_2\bar{v}_j) \\ -\frac{\pi}{2} C.T. \end{pmatrix} \quad (4.4.7)$$

This Section is devoted to present the finite element solution of (4.4.6), which is a system of first order hyperbolic PDEs. This type of equations present a fundamental difficulty, as the classical Galerkin method used for parabolic or elliptic problems such as the transient or steady state heat conduction equation result on severe oscillations. This problem is due to the existence of convective terms in the equation, i.e., the fluxes F_1 and F_2 following axes x_1 and x_2 .

First of all, we will study the simplest equation with convective terms in order to gain insight in the mentioned instability and the alternative ways to circumvent it.

4.4.2 Model equation: the 1D convective transport

Let us consider the transport of a specie having a concentration ϕ by a steady, uniform current of velocity v (Fig. 4.4.1).

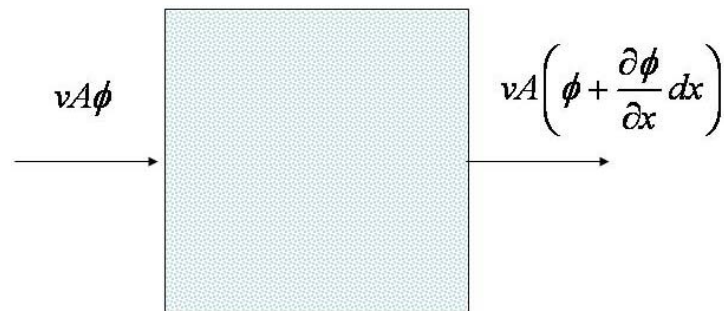


Figure 4.4.1 Convection of a specie by an uniform current

The equation of balance of mass for the specie being convected is

$$A dx \frac{\partial \phi}{\partial t} = vA\phi - vA \left(\phi + \frac{\partial \phi}{\partial x} dx \right)$$

from where we obtain

$$\frac{\partial \phi}{\partial t} + v \frac{\partial \phi}{\partial x} = 0 \tag{4.4.8}$$

This Partial Differential Equation has to be complemented by suitable initial and boundary conditions:

$$\phi(x, t = 0) = f_0(x) \tag{4.4.9a}$$

$$\phi(x = 0, t) = g(t) \tag{4.4.9b}$$

It is important to notice that the boundary condition is only given at the part of the domain where the current enters the domain, or, better, where the information concerning the concentration enters the domain. This is an important difference with parabolic or elliptic problems, where we should have provided information in both sides of the channel.

The general solution of the problem is of the type:

$$\phi(x, t) = \phi(x - vt) \quad (4.4.10)$$

which is a “wave” propagating to the right with the velocity of the current. This can be easily checked by substituting in the PDE and verifying it is satisfied.

4.4.3 Finite elements that work: the Taylor Galerkin scheme.

The Taylor Galerkin algorithm is obtained following the same procedure than in the Lax Wendroff scheme, the only difference being that the space discretization is performed using the Galerkin method.

The Taylor Galerkin method was introduced independently by Donea (1983) and Lohner, Morgan and Zienkiewicz (1984), and applied to fluid dynamics problems by Peraire (1986), Peraire, Zienkiewicz and Morgan (1987), Donea, Quartapelle and Selmin (1992) and Quecedo and Pastor (2002). The interested reader can find a detailed description in the text by O.C.Zienkiewicz and R.L.Taylor (2000).

This Section is devoted to present this simple yet accurate algorithm, starting from the very simple case of the convective transport equation in 1D, following with its implementation for quasi-linear equations and systems, where we will introduce the two-step variant of the Taylor Galerkin method. Finally, we will analyze the discretization of source and diffusive terms.

4.4.3.1 The Taylor Galerkin algorithm for the 1D convective transport equation

We will start with the 1D convective transport equation

$$\frac{\partial \phi}{\partial t} + v \frac{\partial \phi}{\partial x} = 0$$

and the Taylor series expansion

$$\phi^{n+1} = \phi^n - v \Delta t \left. \frac{\partial \phi}{\partial x} \right|^n + \frac{1}{2} v^2 \Delta t^2 \left. \frac{\partial^2 \phi}{\partial x^2} \right|^n \quad (4.4.11)$$

Next, we will introduce the finite element approximation:

$$\phi(x, t) \approx \hat{\phi}(x, t) = \sum_{j=1}^5 N_j(x) \hat{\Phi}_j(t) \quad (4.4.12a)$$

or,

$$\hat{\phi}(x, t) = N \cdot \hat{\Phi}$$

where we have introduced the global shape functions $N_j(x)$ $j = 1, \dots, 5$, and nodal variables $\hat{\Phi}_j(t)$ $j = 1, \dots, 5$.

If we substitute the approximation (4.4.12a) in (4.4.11), multiply both sides by $N_i(x)$ and integrate in our domain, we obtain:

$$\int_{\Omega} N_i \hat{\phi}^{n+1} d\Omega = \int_{\Omega} N_i \hat{\phi}^n d\Omega - v \Delta t \int_{\Omega} N_i \left. \frac{\partial \hat{\phi}}{\partial x} \right|^n d\Omega + v^2 \frac{\Delta t^2}{2} \int_{\Omega} N_i \left. \frac{\partial^2 \hat{\phi}}{\partial x^2} \right|^n d\Omega \quad (4.4.13)$$

We will study each term separately:

$$\int_{\Omega} N_i \hat{\phi}^{n+1} d\Omega = \left(\int_{\Omega} N_i N_j d\Omega \right) \hat{\Phi}_j^{n+1} = M \hat{\Phi}_j^{n+1} \quad (4.4.14)$$

$$\int_{\Omega} N_i \hat{\phi}^n d\Omega = \left(\int_{\Omega} N_i N_j d\Omega \right) \hat{\Phi}_j^n = M \hat{\Phi}_j^n$$

where M is the mass matrix.

$$\int_{\Omega} N_i \left. \frac{\partial \hat{\phi}}{\partial x} \right|^n d\Omega = \left(\int_{\Omega} N_i \frac{\partial N_j}{\partial x} d\Omega \right) \hat{\Phi}_j^n = H \hat{\Phi}_j^n$$

where we have introduced the discrete convective operator matrix H as:

$$H_{ij} = \int_{\Omega} N_i \frac{\partial N_j}{\partial x} d\Omega$$

Finally, the term involving second derivatives of $\hat{\phi}$ cannot be obtained as the approximation is continuous of class C^0 , with discontinuous first derivatives and second derivatives not defined at nodes between elements. We will integrate by parts this term to get:

$$\int_{\Omega} N_i \left. \frac{\partial^2 \hat{\phi}}{\partial x^2} \right|^n d\Omega = - \int_{\Omega} \frac{\partial N_i}{\partial x} \left. \frac{\partial \hat{\phi}}{\partial x} \right|^n d\Omega + \int_{\partial\Omega} N_i \left. \frac{\partial \hat{\phi}}{\partial n} \right|^n d\Gamma$$

where $\partial\Omega$ is the boundary of the domain (in 1D problems the two points limiting the interval) and n the unit normal to the boundary.

This expression can be further elaborated, arriving to:

$$\begin{aligned}
 & - \left(\int_{\Omega} \frac{\partial N_i}{\partial x} \frac{\partial N_j}{\partial x} d\Omega \right) \hat{\Phi}_j^n + \int_{\partial\Omega} N_i \frac{\partial \hat{\phi}}{\partial n} \Big| d\Gamma \\
 & = -K_{ij} \hat{\Phi}_j^n + \int_{\partial\Omega} N_i \frac{\partial \hat{\phi}}{\partial n} \Big| d\Gamma
 \end{aligned} \tag{4.4.15}$$

where K is a matrix which is usually referred to as “stiffness matrix” in structural analysis. Therefore, after collecting all the terms we obtain:

$$M \hat{\Phi}^{n+1} = M \hat{\Phi}^n - v \Delta t H \hat{\Phi}^n - v^2 \frac{\Delta t^2}{2} K \hat{\Phi}^n + f^n$$

where f^n is the vector arising from the integral along the boundary.

This equation can be cast as:

$$M \Delta \hat{\Phi}^{n+1} = rhs^n \tag{4.4.16}$$

where the vector of unknowns is:

$$\Delta \hat{\Phi}^n = \hat{\Phi}^{n+1} - \hat{\Phi}^n$$

The algorithm is explicit, as the coefficient matrix is the mass matrix, and it can be solved using an iterative scheme of Jacobi type:

$$\Delta \hat{\Phi}^n \Big|^{(k+1)} = M_L^{-1} \left(rhs^n - M \Delta \hat{\Phi}^n \Big|^{(k)} \right) \tag{4.4.17}$$

which usually converges within 3 to 5 iterations.

4.4.3.2 The 1 step Taylor Galerkin algorithm.

First order hyperbolic equations can be cast in an alternative form called conservative or conservation form. In the case of the convective transport equation, we introduce the flux F as:

$$F(x, t) = v \phi(x, t)$$

and the equation can be written as:

$$\frac{\partial \phi}{\partial t} + \frac{\partial F}{\partial x} = 0 \quad (4.4.18)$$

Another example is the Burger's equation, which is the simplest equation incorporating a convective term similar to those found in the eulerian balance of momentum equations of fluid dynamics:

$$\frac{\partial \phi}{\partial t} + \phi \frac{\partial \phi}{\partial x} = 0 \quad (4.4.19)$$

where we can define the flux as:

$$F = \frac{1}{2} \phi^2 \quad (4.4.20)$$

This equation is an example of quasi linear hyperbolic PDEs.

To derive the Taylor Galerkin algorithm for a quasi linear equation written in conservation form, we use the Taylor series expansion:

$$\phi^{n+1} = \phi^n + \Delta t \left. \frac{\partial \phi}{\partial t} \right|^n + \frac{1}{2} \Delta t^2 \left. \frac{\partial^2 \phi}{\partial t^2} \right|^n \quad (4.4.21)$$

From here, and using the PDE written in conservation form we obtain:

$$\frac{\partial \phi}{\partial t} = - \frac{\partial F}{\partial x}$$

and

$$\frac{\partial^2 \phi}{\partial t^2} = \frac{\partial}{\partial t} \left(- \frac{\partial F}{\partial x} \right) = - \frac{\partial}{\partial x} \left(\frac{\partial F}{\partial t} \right)$$

We will write the time derivative of the flux as:

$$\frac{\partial F}{\partial t} = \frac{\partial F}{\partial \phi} \frac{\partial \phi}{\partial t} = -A \frac{\partial F}{\partial x} \quad (4.4.22)$$

where

$$A = \frac{\partial F}{\partial \phi}$$

From here, we obtain:

$$\phi^{n+1} = \phi^n - \Delta t \left. \frac{\partial F}{\partial x} \right|^n + \frac{1}{2} \Delta t^2 \left. \frac{\partial}{\partial x} \left(A \frac{\partial F}{\partial x} \right) \right|^n \quad (4.4.23)$$

which is the one step Taylor Galerkin algorithm for quasi linear equations.

In the case of a one dimensional system of 1st order PDEs, the unknowns and fluxes would be vectors of a certain dimension. The system could be written in a compact manner as:

$$\frac{\partial \phi}{\partial t} + \frac{\partial F}{\partial x} = 0 \quad (4.4.24)$$

and the Taylor Galerkin algorithm would be (4.4.23), the only difference being now that A is a matrix.

Space Discretization of (3.4.10) is performed through the method of Galerkin. First, we substitute the finite element approximation of the unknowns in (3.4.10), and then the equation is multiplied by the shape functions and integrated in the domain:

$$\int_{\Omega} N_i \hat{\phi}^{n+1} d\Omega = \int_{\Omega} N_i \hat{\phi}^n d\Omega - \Delta t \int_{\Omega} N_i \left. \frac{\partial F}{\partial x} \right|^n d\Omega + \frac{1}{2} \Delta t^2 \int_{\Omega} N_i \left. \frac{\partial}{\partial x} \left(A \frac{\partial F}{\partial x} \right) \right|^n d\Omega \quad (4.4.25)$$

The third term is obtained easily if we are using linear elements. The flux is obtained at nodes and interpolated using the shape functions as:

$$F = N_j \hat{F}_j$$

The partial derivative is constant within elements. The contribution of a particular element (e) to the integral is then obtained as:

$$\int_{\Omega_e} N_i \left. \frac{\partial F}{\partial x} \right|^n d\Omega_e = \overline{\left. \frac{\partial F}{\partial x} \right|^n} \int_{\Omega_e} N_i d\Omega \quad (4.4.26)$$

where the overbar refers to the constant value at the element. In the case of 1D linear elements considered here, the integral of a shape function over an element is:

$$\int_{\Omega} N_i d\Omega = \frac{1}{2} l_e$$

where l_e is the length of the element.

Concerning the term involving second order derivatives, it is integrated by parts (in 2 and 3D problems we will use the Gauss theorem):

$$\int_{\Omega} N_i \frac{\partial}{\partial x} \left(A \frac{\partial F}{\partial x} \right)^n d\Omega = - \int_{\Omega} \frac{\partial N_i}{\partial x} A \frac{\partial F}{\partial x} \Big| ^n d\Omega + \int_{\partial\Omega} N_i A \frac{\partial F}{\partial n} \Big| ^n d\Gamma \quad (4.4.27)$$

The integral in the domain is easily obtained, as both partial derivatives are constant within each element. Depending on the nature of A the integral could be directly computed or we will have to use numerical integration techniques. In the case of Burgers equation, $A = \phi$, and the integral is obtained as the product of the element length by the partial derivatives (constant) in the element by the average of ϕ in the element.

4.4.3.3 The two step Taylor Galerkin algorithm

In the preceding Section we have presented a one step Taylor Galerkin algorithm for systems of quasi linear first order PDEs. The algorithm involves products of a jacobian matrix A by a vector, which introduces an important computational load.

The two step Taylor Galerkin method is an improvement which circumvents this problem. It was introduced by Lohner, Morgan and Zienkiewicz in 1984. It consists on two steps:

In the **first step**, the solution is advanced in time $\Delta t / 2$:

$$\phi^{n+\frac{1}{2}} = \phi^n - \frac{\Delta t}{2} \frac{\partial F}{\partial x} \Big| ^n \quad (4.4.28a)$$

It is important to notice that the flux derivative is obtained at elements and not at nodes. Therefore, this expression is reformulated using element averaged values as:

$$\bar{\phi}^{n+\frac{1}{2}} = \bar{\phi}^n - \frac{\Delta t}{2} \frac{\partial F}{\partial x} \Big| ^n \quad (4.4.28b)$$

Once the values of the unknowns at the elements are known, we can obtain the fluxes $\bar{F}^{n+\frac{1}{2}}$ at time $n + \frac{1}{2}$ as they are functions of the unknowns.

In the **second step**, we obtain the values of the unknowns at time $n + 1$ as:

$$\phi^{n+1} = \phi^n - \Delta t \frac{\partial F}{\partial x} \Big| ^{n+\frac{1}{2}} \quad (4.4.29)$$

We will use Galerkin method to obtain:

$$\int_{\Omega} N_i \hat{\phi}^{n+1} d\Omega = \int_{\Omega} N_i \hat{\phi}^n d\Omega - \Delta t \int_{\Omega} N_i \left. \frac{\partial F}{\partial x} \right|^{n+\frac{1}{2}} d\Omega \quad (4.4.30)$$

The first two terms are:

$$\int_{\Omega} N_i \hat{\phi}^n d\Omega = M_{ij} \hat{\Phi}_j^n$$

$$\int_{\Omega} N_i \hat{\phi}^{n+1} d\Omega = M_{ij} \hat{\Phi}_j^{n+1}$$

The last term is obtained using integration by parts or Gauss theorem, as the fluxes at time $n + \frac{1}{2}$ are known at element level and not at nodes:

$$\int_{\Omega} N_i \left. \frac{\partial F}{\partial x} \right|^{n+\frac{1}{2}} d\Omega = - \int_{\Omega} \frac{\partial N_i}{\partial x} \bar{F} \Big|^{n+\frac{1}{2}} d\Omega + \int_{\Omega} N_i \left. \frac{\partial \bar{F}}{\partial n} \right|^{n+\frac{1}{2}} d\Omega \quad (4.4.31)$$

The second step can be written as:

$$M \Delta \hat{\Phi}^n = r.h.s \Big|^{n+\frac{1}{2}}$$

which can be solved in the iterative manner described in (4.4.17)

4.4.3.4 Diffusive and source terms.

The two step algorithm can be extended easily to the general case involving diffusive and source terms. Let us consider the equation:

$$\frac{\partial \phi}{\partial t} + \frac{\partial F}{\partial x} = S + D \quad (4.4.32)$$

where S is the source and D the diffusive term:

$$D = \frac{\partial}{\partial x} \left(k \frac{\partial \phi}{\partial x} \right) \quad (4.4.33)$$

The first step is:

$$\phi^{n+\frac{1}{2}} = \phi^n + \frac{\Delta t}{2} \left(S - \left. \frac{\partial F}{\partial x} \right|^n \right) \quad (4.4.34)$$

where we have not included the diffusive terms.

The second step is:

$$\phi^{n+1} = \phi^n + \Delta t \left(S + D + \frac{\partial F}{\partial x} \Big|^{n+\frac{1}{2}} \right) \quad (4.4.35)$$

We find here two additional terms, source and diffusive, to be discretized. Concerning the former, its contribution is:

$$\int_{\Omega} N_i \bar{S}^{n+\frac{1}{2}} d\Omega \quad (4.4.36)$$

This term can be approximated using the value of the source term at the element.

The diffusive term is approximated by its value at time t_n :

$$\int_{\Omega} N_i \frac{\partial}{\partial x} \left(k \frac{\partial \phi}{\partial x} \right)^n d\Omega$$

We will integrate it by parts, obtaining:

$$-\int_{\Omega} \frac{\partial N_i}{\partial x} k \frac{\partial \hat{\phi}}{\partial x} d\Omega + \int_{\Omega} N_i k \frac{\partial \hat{\phi}}{\partial n} d\Omega$$

which can be written as:

$$-K_{ij} \hat{\Phi}_j^n + f_{Di} \quad (4.4.37)$$

The algorithm described above performs well provided that the intensity of the source term is not very high. Otherwise, we will have to introduce special splitting algorithms to deal with this term. This situation happens quite frequently in the analysis of fast catastrophic landslides, where source terms are due to the slope of the terrain and the basal friction.

4.4.3.5 A 4th order Runge Kutta splitting method for strong sources.

The system of hyperbolic equations (6) will be discretized using a splitting operator technique in which each of the two operators, convective transport and sources, will be treated separately. Therefore, we will consider two problems:

(i) A pure convection problem of the type

$$\left. \begin{aligned} \frac{\partial \phi}{\partial t} + A \frac{\partial \phi}{\partial x} &= 0 \\ \phi(x, t^n) &= \phi^n(x) \end{aligned} \right\} \Rightarrow \phi^{\text{adv}} \quad (4.4.38)$$

(ii) The source problem, which is a ordinary differential equation:

$$\begin{aligned} \frac{d\phi}{dt} &= S(\phi, t) \\ \phi(x, t^n) &= \phi^{\text{adv}} \end{aligned} \quad (4.4.39)$$

Above decomposition can be written in a compact manner as:

$$\phi^{n+1} = S(\Delta t) \text{Adv}(\Delta t) \phi^n \quad (4.4.40)$$

where S and Adv are the differential operators for the source and convective transport parts.

The second part of the splitting concerns the source term. The solution which we will obtain is:

$$\phi_i^{n+1} = \phi_i^{\text{adv}} + \Delta t G(\phi_i^s) \quad (4.4.41)$$

Runge-Kutta algorithms provide a high accuracy in the evaluation of ODEs. A detailed description is provided by Hirsch (1984). The general form of a RK algorithm is

$$\begin{aligned} \phi^1 &= \phi^n \\ \phi^2 &= \phi^n + \Delta t \alpha_2 H(\phi^1) \\ \phi^3 &= \phi^n + \Delta t \alpha_3 H(\phi^2) \\ &\dots\dots\dots \\ \phi^k &= \phi^n + \Delta t \alpha_k H(\phi^{k-1}) \\ \phi^{n+1} &= \phi^n + \Delta t \sum_{k=1}^k \beta_k H(\phi^k) \end{aligned} \quad (4.4.42)$$

where the consistency condition $\sum_{k=1}^k \beta_k = 1$ has to be fulfilled.

Here we have chosen a 4th order RK algorithm, as it provides an excellent combination of accuracy and computational effort. The coefficients are given by:

$$\begin{aligned} \alpha_2 &= \frac{1}{2}; & \alpha_3 &= \frac{1}{2}; & \alpha_4 &= 1; \\ \beta_1 &= \frac{1}{6}; & \beta_2 &= \beta_3 = \frac{1}{3}; & \beta_4 &= \frac{1}{6}; \end{aligned} \tag{4.4.43}$$

from where we obtain

$$\begin{aligned} \phi^1 &= \phi^n \\ \phi^2 &= \phi^n + \frac{1}{2} \Delta t H(\phi^1) \\ \phi^3 &= \phi^n + \frac{1}{2} \Delta t H(\phi^2) \\ \phi^4 &= \phi^n + \frac{1}{2} \Delta t H(\phi^3) \\ \phi^{n+1} &= \phi^n + \frac{\Delta t}{6} [H(\phi^1) + 2H(\phi^2) + 2H(\phi^3) + H(\phi^4)] \end{aligned} \tag{4.4.44}$$

4.4.4 Examples and applications

We will include here some applications of FEM eulerian codes to run out analysis of landslides. The first example is that of the dam break problem, for which it exists an analytical solution.

Then we have selected two well documented cases involving a Bingham fluid, which is the failure of a tailings dam in Texas. Even if it is not a proper mudflow, the material is very similar to those encountered there, hence the interest of the modelization.

Finally, we include the case of a flow slide involving pore pressure dissipation in Cougar Hill, which has been described in the literature.

4.4.4.1. Cases with available analytical solution

We will devote this Section to present a short series of benchmarks which illustrate the predictive ability of FEM models. The first example is the dam break problem, for which an analytical solution exists in the cases of dry and wet bed. See for instance the texts by Stoker (1957) and Guinot (2003).

This is the case of the 1D dam break problem, where a vertical dam retaining the impounded water suddenly collapses. The solution depends on whether there is water in the domain

where the water propagates (wet bottom) or not (dry bottom). Both cases are were sketched in figure 4.2.5. which will be repeated here for completeness (Fig.4.4.2).

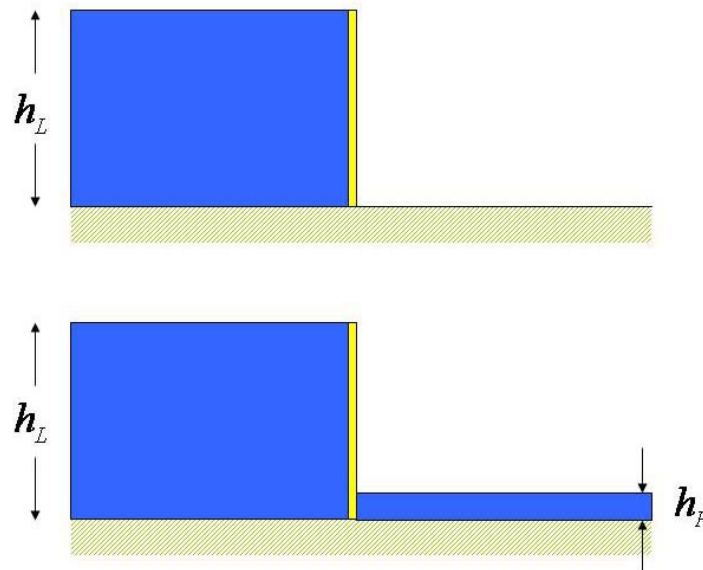


Figure 4.4.2 . 1D Dam break problem over (a) Dry bed (b) Wet bed

We will begin considering the “dry bottom” case. The analytical solution is found in the classical text of Stoker (1957) or in the more modern text by Guinot (2003). The comparison between the analytical solution (broken line) and the computed results are depicted in figures 4.4.3. and 4.4.4 for both the dry and the wet bed cases.

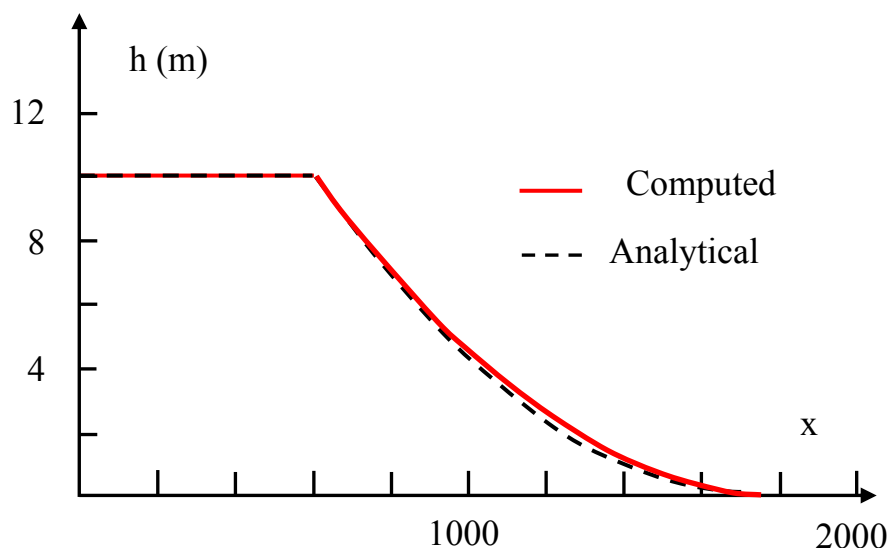


Figure 4.4.3 Analytical solution vs computed results for the dam break problem over dry bed (height of water 10 m).

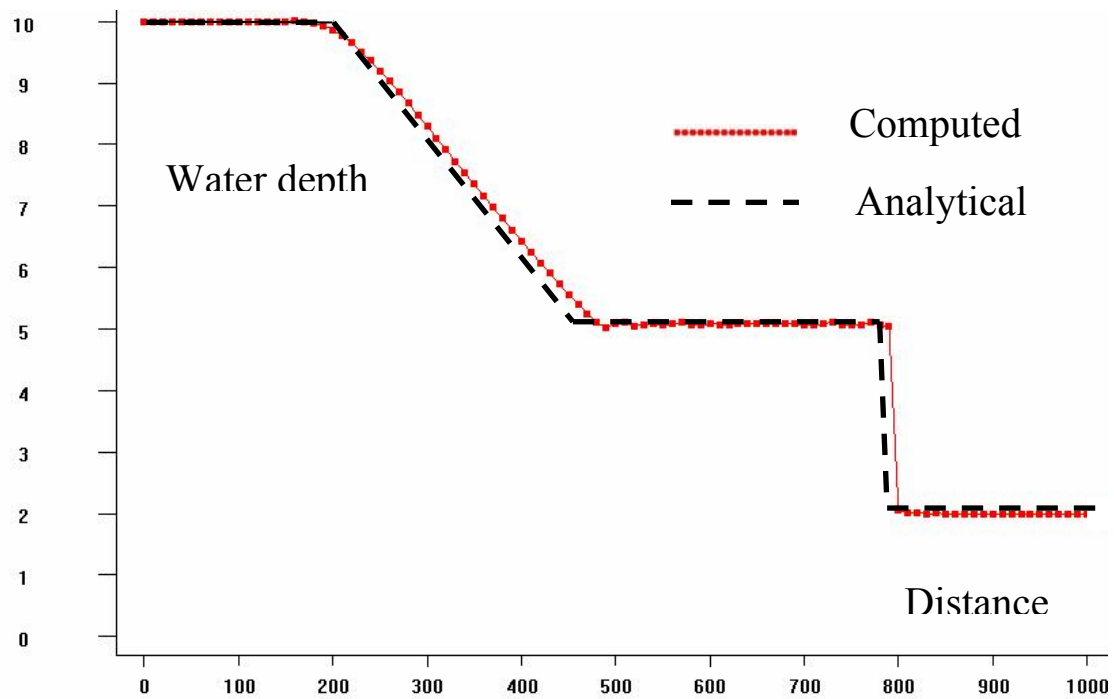


Figure 4.4.4 Analytical solution vs computed results for the dam break problem over wet bed (heights of water 10 m and 2 m)

4.4.4.2. Gypsum Tailings impoundment

Jeyapalan, Duncan and Seed (1983) report the flow of liquefied tailings from Gypsum Tailings Impoundment in East Texas which took place in 1966. The impoundment was rectangular, and had reached a height of 11 m. by the time failure took place. The slide was caused by seepage at the toe of the slope, and affected a length of 140 m. of the dyke, extending 110 m. into the impoundment lagoon. The released material travelled 300 m. before stopping, with an average velocity of 2.5 to 5 m/s. A section of the flow by a vertical plane perpendicular to the dyke at the centre of the breach is given in Fig.4.4.4

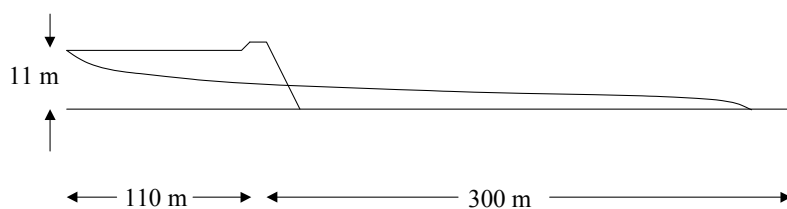


Figure 4.4.4 Central section of the failure at Gypsum Tailings impoundment

Properties of the tailings have been taken from Jeyapalan et al (1983) who assumed that the behaviour of the flowing material could be described by a Bingham model. The tailings were classified as "non-plastic silts", with $D_{50} \approx 0.07$ mm, a uniformity coefficient close to 3, density of particles 2450 Kg/cm^2 and an average water content of 30%. The yield stress was determined from simple slope stability analysis as $\tau_y = 10^3$ Pa, and the viscosity was taken as $\mu = 50$ Pa.s. Finally, density of the tailings was assumed to be $\rho = 1400$ Kg/m³.

The finite element mesh used in the analysis is shown in Fig.4.4.5. We have modelled the 350 m. length dyke, removing the 140 m. long section which failed. Therefore, the model assumes that collapse of the dyke takes place instantaneously. The plain onto which the tailings flow has been limited for computational reasons, imposing absorbing conditions at the artificial boundaries.

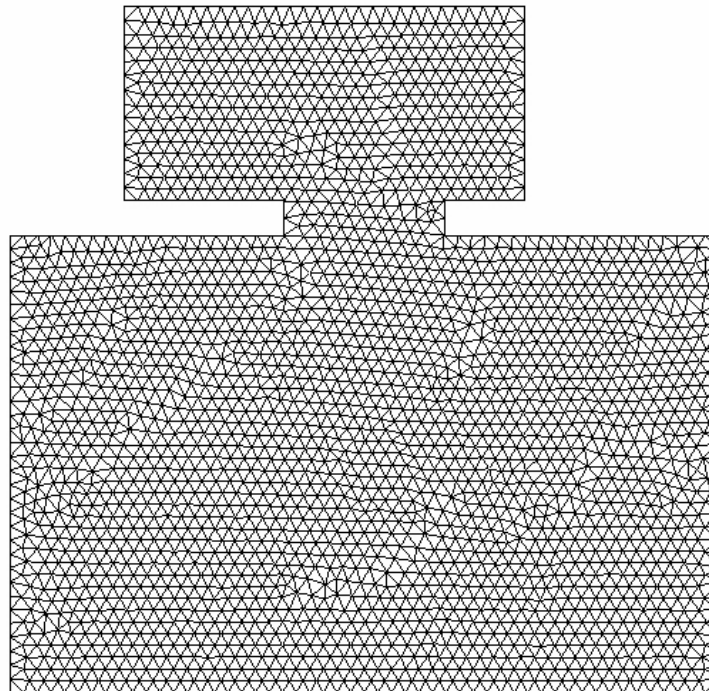


Figure 4.4.5. Finite element mesh used in the analysis

Figure 4.4.6. shows the contours of tailings depth on the plane at times 0., 30, 60, 90 and 120 s. The vertical scale has been enlarged by a factor of ten in order to better describe the properties of the flowslide. It is interesting to see the development of a transient jump at $t = 30s$ which propagates backwards. This jump is also seen in Fig. Figure 4.4.7., where free surface profiles along the vertical plane passing by the centerline of the breach are given.

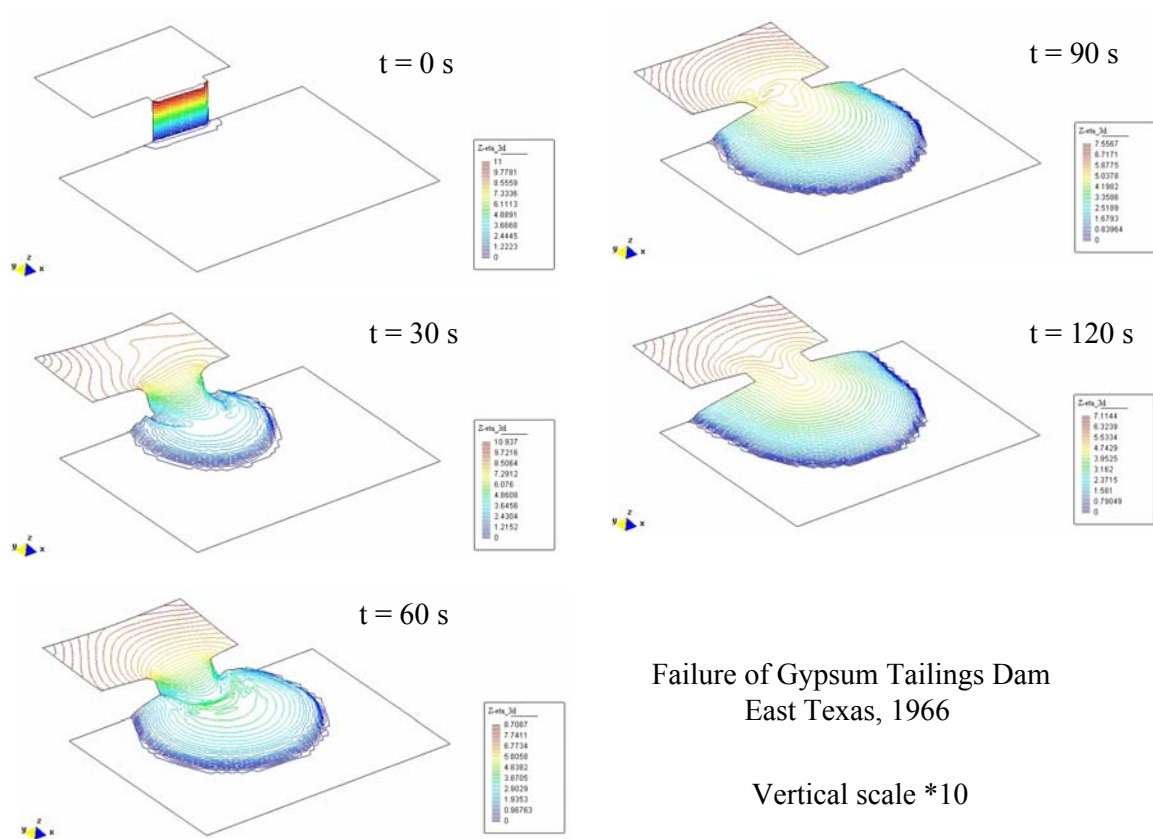


Figure 4.4.6 Run out of Gypsum tailings dam failure

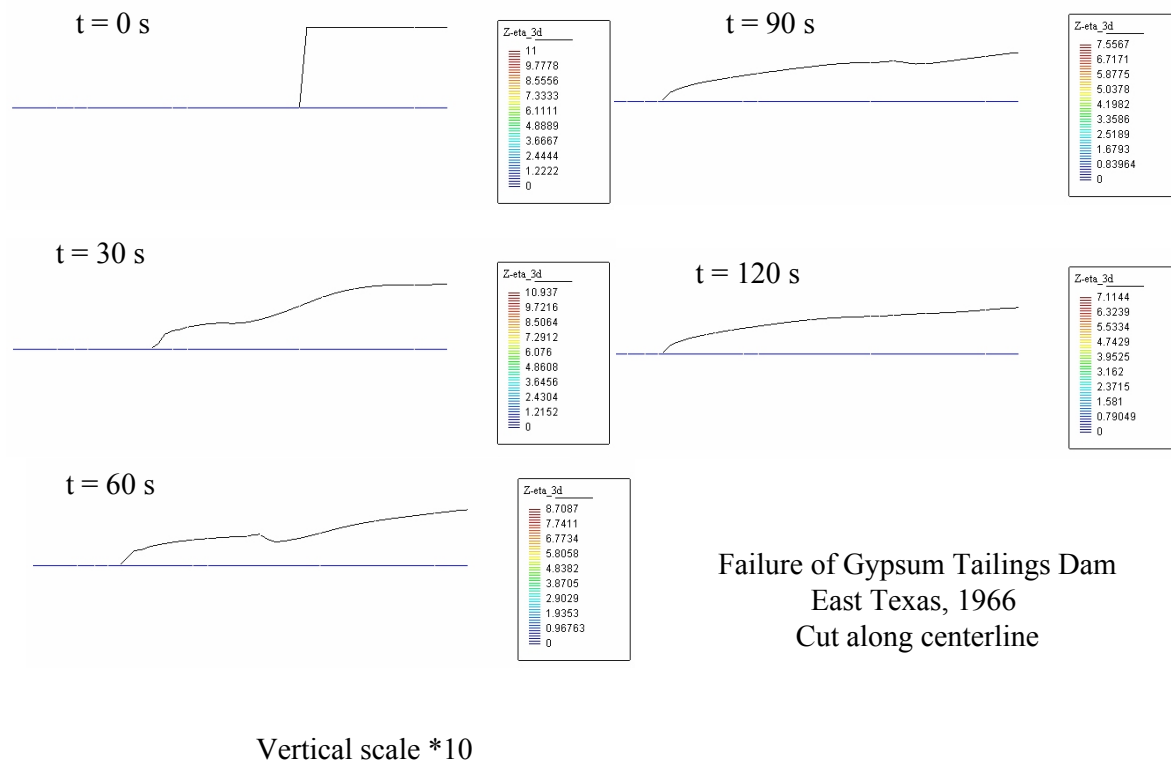


Figure 4.4.7 Gypsum tailings dam failure: profiles along central section

The results agree well with observed values of inundation distance (300 m), freezing time ($60\text{--}120\text{ s}$) and mean velocity ($2.5\text{--}5.0\text{ m/s}$). However, the flowslide progressed back into the pond about 110 m , while in the simulation reaches a longer distance.

4.4.4.3. Flowslides in Rocky Mountains

Three interesting cases of flowslides of coal mine waste dumps in Western Canadian Rocky Mountains have been recently reported by Dawson, Morgenstern and Stokes (1988). These cases were selected by the authors between about 50 flowslides documented in British Columbia during the period 1972-1997. Runout distances up to 3500 m were reported, with a maximum frequency of 500 to 100 m . in the histogram representing number of flowslide events against runout distances.

In this text, we have selected the case of Fording Greenhills, where in May 1992 the Cougar 7 dump failed. The mobilized mass of debris consisted on approximately $200,000\text{ m}^3$, which slid off the 100 m high dump travelling a distance of 700 m before coming to rest.

This dump was constructed by end tipping between February and May 1991. During spring, there were heavy rains, but the dump remained stable for the next year. During March and

April, an access road was built below the toe and without interfering with it. In the days preceding the flowslide, warm weather could have caused melting of the snow cover with an effect similar to that of rain. Just prior to failure, both cracks on the dump face and seepage zones were noticed.

The debris were mainly sandy gravel, and the foundation beneath the dump and the runout debris consisted on a sand and gravel colluvium layer with a depth varying between 0.3 and 0.5 m beneath the dump. Wet fine grained layers were found at the foundation contact, near the crest, and in the debris.

According to the post failure analysis carried out by Dawson and co workers, these layers played a paramount role in both the initiation and the propagation phases. The collapse model proposed by them is based on the existence of layers of finer sandy gravel materials of low permeability deposited parallel to the dump face. Triggering mechanism could have consisted on: (i) a redistribution of effective stresses caused by pore pressure changes, and (ii) liquefaction of these layers under quasi undrained conditions. The flowslide could have ride over these layers of liquefied materials.

We have based the analysis of this flowslide on the geotechnical properties obtained by Dawson and co-workers, and we have chosen accordingly a density of 1900 kg/m^3 and an effective friction angle $\phi = 37^\circ$.

The mobilized mass has been taken from Fig.6 in Dawson et al (1988), and the consolidation time has been chosen from back analysis equal to 68 s.

We have performed a 1D simulation. The results can be seen in fig. 4.4.8, where we have plot at different instants the profiles of the flowslide. The results agree well with the observed values, with the exception of the hump which was observed at mid slope in the field, which has not been reproduced correctly by the model.

The two dimensional model of Greenhills Cougar 7 dump is given in Fig. 4.4.8. The terrain model has been obtained from the data given in Dawson et al (1988), and the results of the simulation are given in Figs. 4.4.9 a to c, where it can be seen: (i) perspectives of the flowslide extension, (ii) isolines of debris depth and (iii) sections along vertical plane AA' .

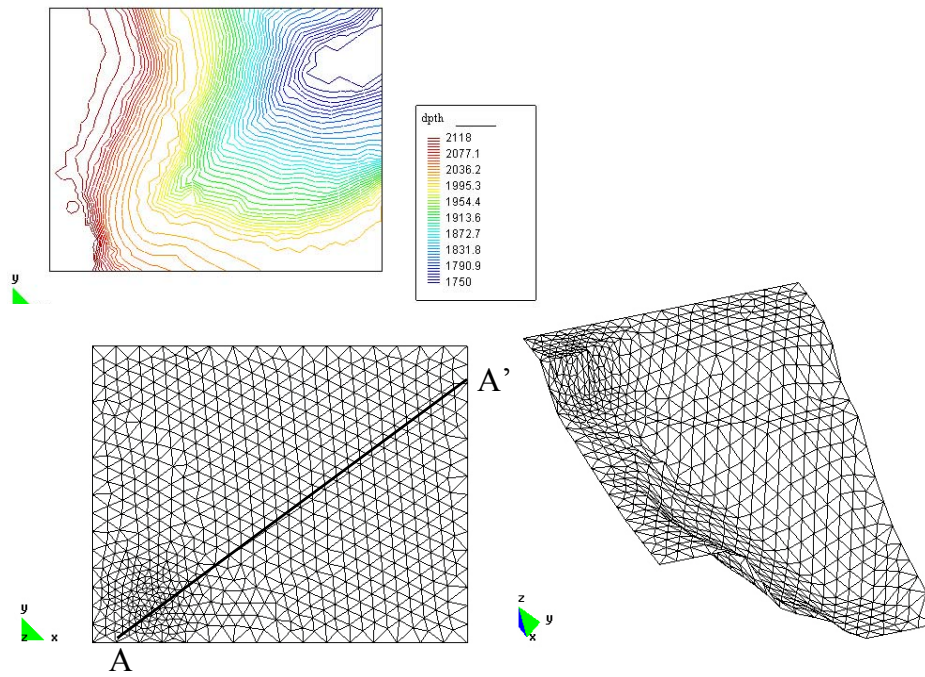


Figure 4.4.8 Cougar Hill flowslide layout.

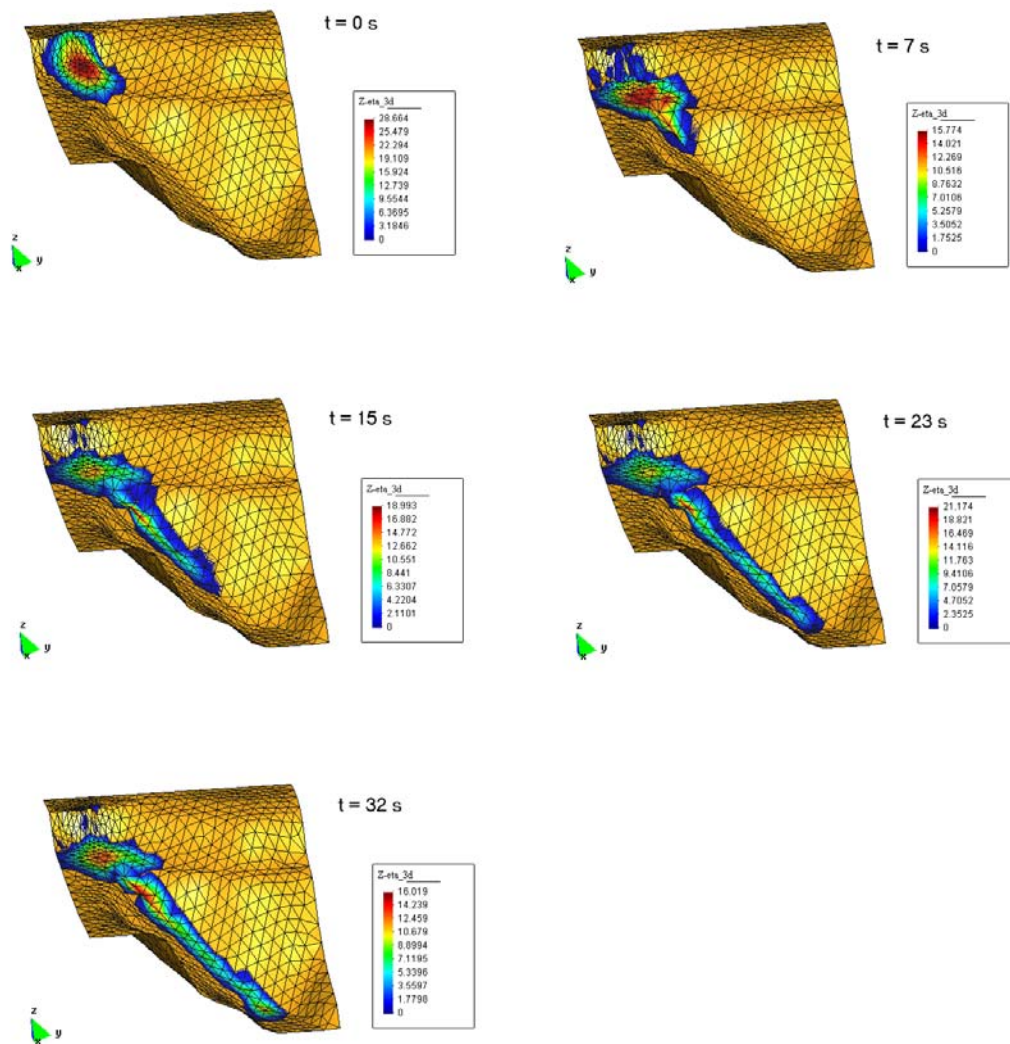


Figure 4.4.9 (a) Flowslide propagation

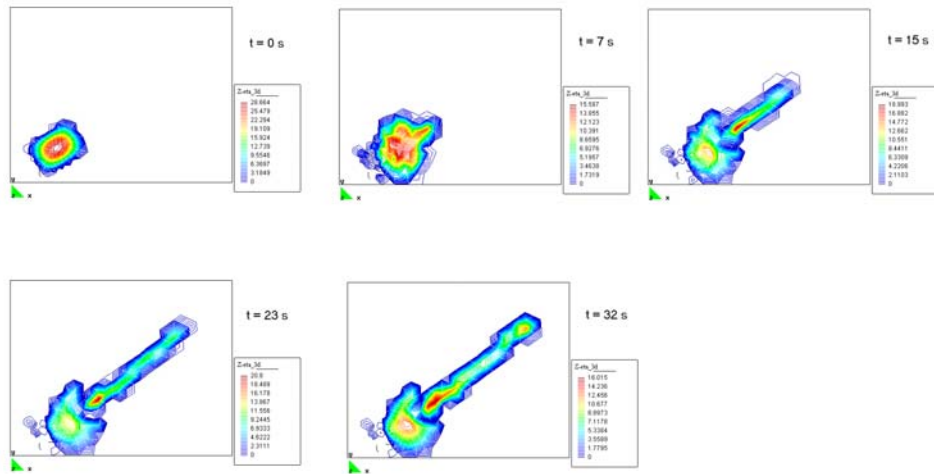


Figure 4.4.9(b) Cougar Hill flowslide: depth isolines.

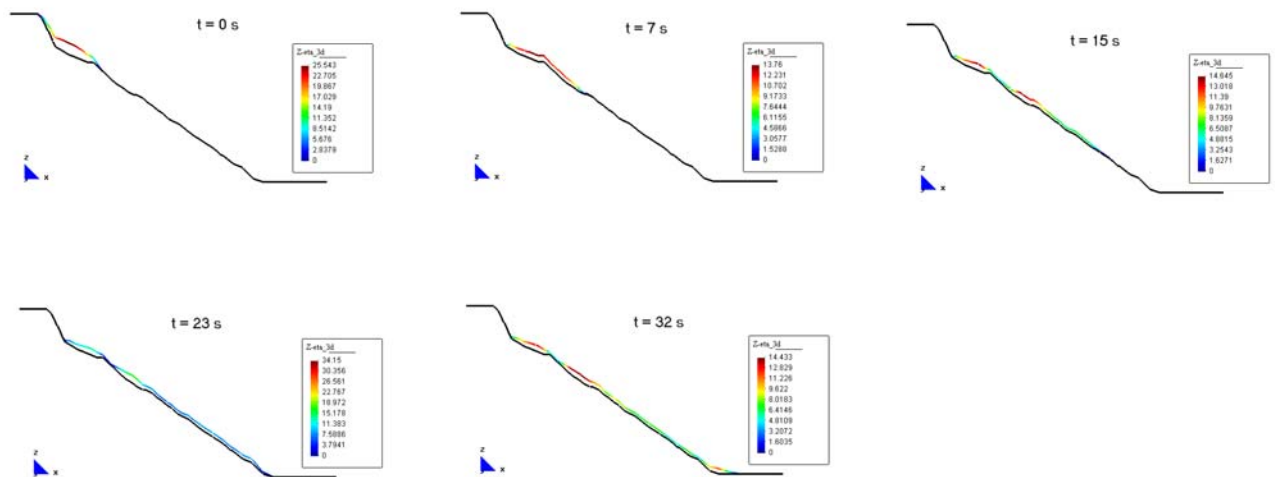


Figure 4.4.9 (c) Vertical profiles

4.4.5 References

R.F.Dawson, N.R.Morgenstern and A.W.Stokes, "Liquefaction flowslides in Rocky Mountain coal mine waste dumps", **Can.Geotech.J.**, **35**, 328-343, 1998

J. Donea. "A Taylor- Galerkin Method for Convective Transport Problems", **Int. J.Num. Meth. Engng.** **20**, pp 101-109, 1983.

J. Donea, S. Giuliani, H. Laval and L. Quartapelle, "Time-accurate solution of advection-diffusion problems by finite elements", **Comp. Meth. Appl.Mech. Engng.**, **45**, 123-145 (1984)

J.Donea, L.Quartapelle and V.Selmin, "An analysis of Time Discretization in the Finite Element Solution of Hyperbolic Problems", **J.Comp.Phys.** **70**, 463-499 (1987)

J.Donea and L.Quartapelle and V.Selmin, "An introduction to finite element methods for transient advection problems", **Comp.Meth.Appl.Mech.Engng.** **95**, 169-203 (1992)

Guinot, V. (2003). **Godunov-type schemes. An introduction for engineers**, Elsevier

C.Hirsch, **Numerical Computation of Internal and External Flows**, Vol II, John Wiley and Sons, 1988

J.K.Jeyapalan, J.M.Duncan and H.B.Seed, "Investigation of flow failures of tailing dams", **J.Geotech.Engng.ASCE** **109**, pp 172-189, 1983

R. Löhner, K. Morgan, O.C. Zienkiewicz. "The solution of non-linear hyperbolic equation systems by the finite element method". **Int. J. Num. Meth. Fluids**, **4**, pp 1043- 1063, 1984

J.Peraire .(1986): **A finite element method for convection dominated flows**. Ph.D. thesis. University of Wales, Swansea

J.Peraire, O.C.Zienkiewicz and K.Morgan, Shallow water problems. A general explicit formulation. **Int.J.Num.Meth.Engng.** **22**, 547-574, 1986

M.Quecedo and M.Pastor, A reappraisal of Taylor-Galerkin algorithm for drying-wetting areas in shallow water computations, **Int.J.Num.Meth.Fluids** **38**, 515-531. (2002)

Stoker, J.J. (1957). **Water waves**, Interscience, New York

O.C. Zienkiewicz and R. L. Taylor, **The Finite Element Method**, 5th Edition , Butterworth-Heinmann (2000).

4.5 GRANULAR FLOWS ON ERODIBLE AND NON ERODIBLE SURFACES

G. B. Crosta,¹ S. Imposimato,² D. Roddeman,²

(1) Dipartimento Scienze Geologiche e Geotecnologie, Piazza della Scienza 4, 20126
Milano, Italy (giovannibattista.crosta@unimib.it),

(2) FEAT, The Netherlands, www.feat.nl

4.5.1 Introduction

The physical behavior of flowing dense granular media is of interest in many diverse areas and it is particularly remarkable for the understanding of the propagation and the prediction of the runout of geophysical mass flows (rock and debris avalanches, landslides, pyroclastic flows) on a very wide range of length and volume scales. Rock and debris avalanches, for example, can travel extremely long distances along flat or almost flat surfaces, and represent a class of exceptionally dangerous geomorphological processes. These types of geophysical flows involve multiple types of physics on multiple scales with significant convective transport and are characterized as large scale and transient, with complex free-surface behaviour upon geometrically complex topography [Cleary and Prakash, 2003]. Numerical simulations of natural mass flows over complex terrains are currently used and developed to assess hazard and risk in exposed areas [Iverson and Denlinger, 2001, Denlinger and Iverson, 2001, 2004, Mangeney et al., 2000, 2005; Hungr, 1995, Chen and Lee, 2000, Chen et al., 2006, Crosta et al; 2003, 2005, 2006, 2009; Pastor et al., 2002; Ancey, 2007; Pudasaini and Hutter, 2007; Bui et al., 2008]. The most commonly adopted approach includes the use of depth-averaged shallow water equations and empirical strength laws where parameters are usually obtained by back-analyses of occurred events or by calibration. This is the result of the extreme complexity of such phenomena and the still incomplete knowledge of the governing laws controlling the behaviour of these materials under dynamic conditions. Savage and Hutter (1989) integrated the Saint Venant 's equations with a Lagrangian scheme to describe the flow of a granular mass in two and three dimensions [Hutter et al., 1993, Greve et al., 1993, 1994], characterized by different rheological constitutive laws. The depth-integrated model of Savage and Hutter has been improved and generalized, and a set of different mathematical model has been presented to considered the behaviour of the materials, the eventual presence and effect of water, and of an erodible basal layer (Pitman et al., 2003). Laboratory tests, under simple and controlled conditions, are an extremely useful tool for the understanding of the mechanics of granular flows and their geomorphologic equivalents. Laboratory tests have been performed along channels with longitudinally and transversally straight and curved channels, or along more complex topographies by releasing different types of granular material with different methods. The collapse of a granular step or column is

of great interest in this contest and has been recognized as an important phenomenon useful for studying transient granular flow conditions. This type of process is similar to the well known dam break problem in fluid mechanics [Ritter, 1892; Hogg, 2006; Ancey *et al.*, 2008] but involves a granular material. A series of very well detailed experiments is available in the literature [Lajeunesse *et al.* 2004, 2005; Lube *et al.* 2004, 2005, 2007; Siavoshi and Kudrolli 2005; Balmforth and Kerswell 2005] and they can constitute a basis for model testing and validation. They have been performed with different granular materials and under different boundary conditions.

These tests have been compared both with qualitative and theoretical models, aimed at finding some general scaling laws or at testing some two dimensional depth averaged shallow water and particle mechanics models.

On the other hand, landslides frequently occur along surfaces mantled by a shallow layer (erosion-limited or supply-limited conditions) or thick deposits (transport-limited or supply-unlimited conditions), made of erodible materials. As a consequence, material entrainment, the consequent increase in volume and change in behavior and mobility of the flowing material are possible and can strongly influence the spreading [Hungr and Evans, 2004; Crosta *et al.*, 2006; Mangeney *et al.*, 2007; Crosta *et al.*, 2008a, b]. The eroded material, both at the front and along the lateral margin, can be pushed forward, accreted to the main flow front or entrained and mixed within the moving mass. Furthermore, the thickness of the erodible layer, its physical mechanical characteristics [e.g. Borzsonyi *et al.*, 2005, 2008], inclination [Savage, 1979; Pouliquen, 1999, Borzsonyi *et al.*, 2005, 2008; Mangeney *et al.*, in press] and other boundary conditions [Pouliquen and Forterre, 2002; Girolami *et al.*, 2008; Crosta *et al.*, 2009] can play a major role on entrainment and on the runout, inducing a deceleration or an acceleration of the flowing mass.

Field evidence has been presented for rock and debris avalanches under different geological and environmental conditions, and entrained volumes have been quantified [e.g. McDougall, 2006: shallow flows/debris avalanches in pyroclastic deposits, erosion rate of 0.01 – 0.1 m⁻¹; Nomash river rock slide, erosion rate 1.9 *10⁻³ m⁻¹; Zymoetz River: 500,000 m³ at an erosion rate of 3.3*10⁻⁴ m⁻¹; Hungr and Evans, 2004, suggest total entrainment values up to 10 times the original failure volume; Crosta *et al.*, 2004, for the Val Pola rock avalanche report an entrainment of about 8 Mm³ or 20% of the initial volume; Chen *et al.*, 2006 estimate an increase in volume of more than 10 times for shallow debris avalanches along alpine slopes].

In other cases, rock slide/avalanche processes along steep rocky cliffs triggered large slumping/entrainment within the talus slopes. This has been observed for example [Crosta, 1992] for a case study where a $0.15\text{-}0.2 \cdot 10^6 \text{ m}^3$ rock slide/avalanche, triggered/entrained $0.25 \cdot 10^6 \text{ m}^3$ of prevalently dry material while moving along a 35° inclined scree slope deposit (Figure 4.5.1). A 300 m long and 100-150 m wide scar, up to 15-20 m in depth, remained along the scree slope.

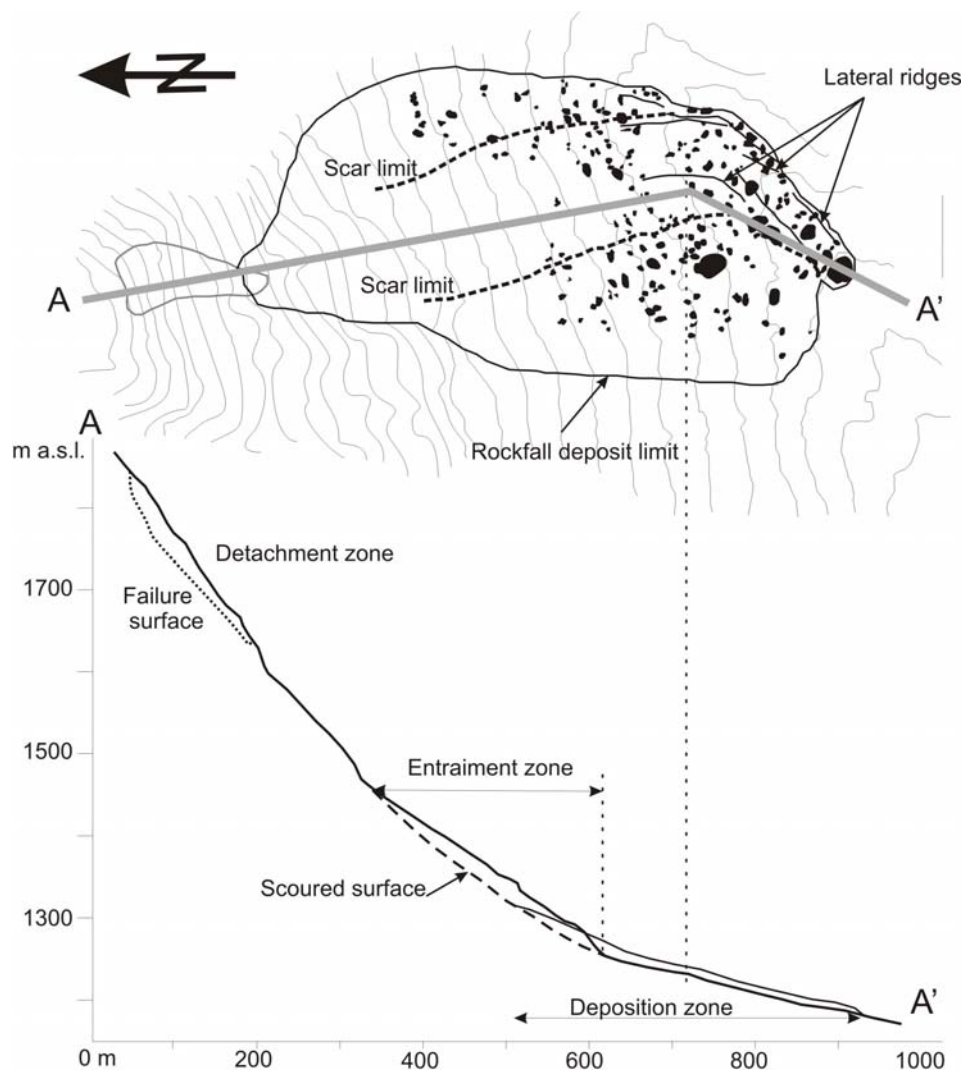


Figure 4.5.1 - The 1991 Sasso Bisolo rock fall-avalanche ($0.15\text{-}0.2 \cdot 10^6 \text{ m}^3$) which caused the erosion of $0.25 \cdot 10^6 \text{ m}^3$ of debris by slumping/entrainment [Crosta, 1992] along a 35° scree slope. The scoured sector was 300 m long and 100-150 m wide, and up to 15-20 m deep. A) plan view; B) Profile along the A-A' section with the detachment zone, the eroded sector and the geometry of final deposit.

Similar processes have been observed for snow avalanches [Gardner, 1983] moving along snow free or snow covered slopes [Issler, 1998; Sovilla and Bartelt, 2002; Gauer and Issler, 2004; Eglit and Demidov, 2005; Sovilla et al., 2007; Sailer et al., 2008] with different meaning and behaviour when considering powder or flowing wet snow avalanches. For powder snow avalanches entrainment plays a major role in counterbalancing cloud dilution resulting from air entrapment [Ancey et al., 2004], with respect to wet snow avalanches for which contrasting or minor evidences are available concerning the role of snow erosion.

McDougall and Hungr [2005] present an empirical erosion model applied to DAN-3D, where the erosion velocity is related to the growth rate. The bed-normal depth eroded per unit flow depth and unit displacement is introduced in the form of an erosion or growth rate parameter, E_s , assumed independent of flow velocity. This empirical approach is a possible base for more complicated models incorporating potential dependence on flow velocity, slope angle, path curvature, surface roughness, strength and drainage properties of the material. The volume of material, ΔV_i , entrained by a single particle i during a time step is expressed as:

$$\Delta V_i = E_s V_i \Delta s_i \quad (4.5.1)$$

where V_i is the volume of particle i , in the SPH formulation, at the beginning of the time step and Δs_i is the distance travelled by the particle during the time step. The volume of entrained material grows both with the volume and with the velocity of the particle being the velocity proportional to the travelled distance. Chen et al. [2006] suggest for preliminary estimates the relationship:

$$E \cong \alpha \frac{V_{eroded}}{A_{affected} d_{com}} \quad (4.5.2)$$

where V_{eroded} is the total eroded volume, $A_{affected}$ is the total erosion-affected area, d_{com} is the travel distance of the centre of mass, and α is a correction coefficient to account for the system non-linearity.

Erosion has been analysed without introducing a semi-empirical law by Crosta et al. [2006] through a series of 2D FEM simulations. In these simulations the case of entrainment and bulldozing of an elasto-plastic material placed along a synthetic profile has been examined (Figure 4.5.2).

Aim of this report is to present the results of a series of simulations performed considering the collapse of granular columns with variable aspect ratios, channel inclination and properties

for an elasto-plastic continuous material with a Mohr Coulomb yield rule. Spreading of the mass has been modelled on horizontal and inclined slopes with or without the presence of an erodible layer that can affect the spreading behaviour of the released mass.

The obtained results are compared with those from experimental and numerical data published in the literature. Results are discussed , and the effects of assuming a continuous approach and frictional elasto-plastic behavior are presented.

The applicability of this modeling approach to more general conditions, where an erodible layer forms/coversthe horizontal spreading surface over which the flow spreads, is verified. Results of some physical and numerical tests are compared and, finally, back analysis of a well documented rock avalanche moving on a thick mattress of alluvial deposits is presented [see also Crosta et al., 2008, 2009].

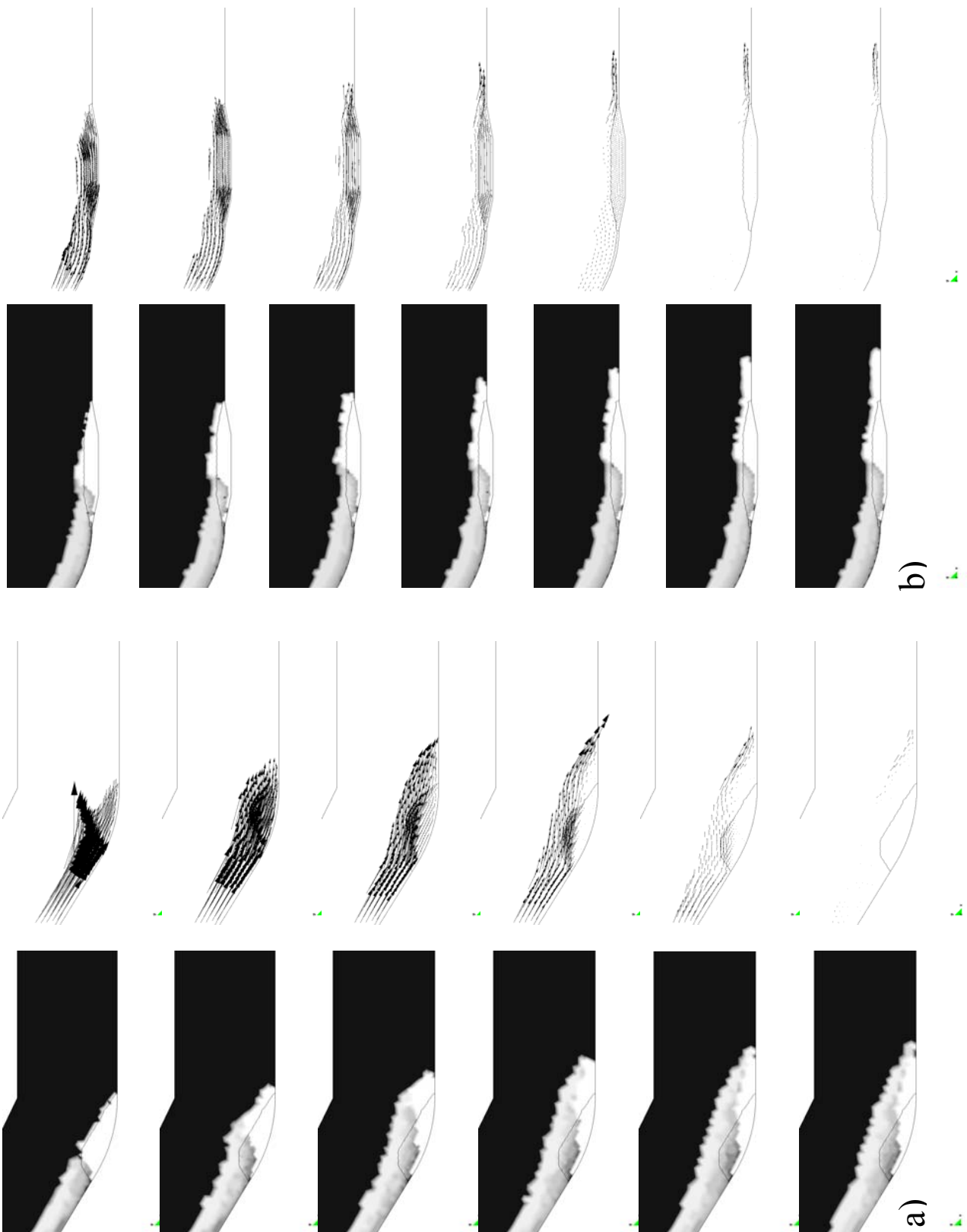


Figure 4.5.2 - 2D FEM simulations of entrainment and bulldozing of material placed along a synthetic profile. Mass distribution and velocity vectors are shown for case of flowing material a) against a deformable obstacle placed at the toe of the sloping sector of the profile; and b) on a weak sediment layer filling a trough and rising above the horizontal profile [after Crosta et al., 2006].

4.5.2 Granular Step Collapse

As mentioned above, various well detailed granular step collapse experiments are available in the literature. They have been performed on different materials [Lajeunesse *et al.* 2004, 2005; Lube *et al.* 2004, 2005; Lube, 2006; Siavoshi and Kudrolli 2005; Balmforth and Kerswell 2005]: grit, glass beads (ballotini), polystyrene balls, sand, salt grains, cous-cous grains, rice and sugar, and adopting different geometries: vertical columns or 2D steps in narrow or wide slots (i.e. rectangular channel), under unidirectional or symmetrical spreading conditions (see Figure 4.5.3 for typical experimental geometries). These experiments were focused on the dependency of the geometry of the deposit on the initial geometry of the collapsing column, and on the definition of scaling laws for the runout.

More experiments have been performed by releasing material on inclined channels/slopes from a reservoir with partial (controlled flow rate) or complete instantaneous opening [see for example, Lube, 2006; Pouliquen *et al.*, 2006; Pouliquen and Forterre, 2002, 2008; Mangeney *et al.*, 2007].

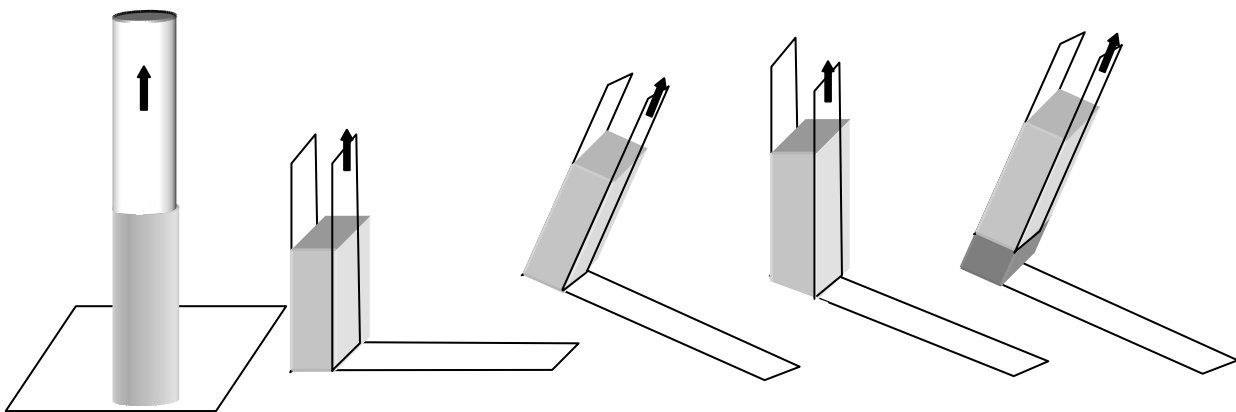


Figure 4.5.3 - Example of some of the experimental setups adopted in different studies: a) cylindrical column, axisymmetric condition [Iverson and Denlinger, 2001; Lajeunesse, 2005; Lube 2005, 2006]; b) two dimensional setting in a rectangular horizontal channel [Lube, 2006; Lajeunesse, 2005; Crosta *et al.*, 2009]; c) two dimensional setting in a rectangular inclined channel [Mangeney, *in press*]; (d) two dimensional setting in a rectangular inclined channel [Lube, 2006]; (e) flow on a pile in a narrow channel [Pouliquen and Forterre, 2002]

The experimental setting strongly influences the final results. Here in the following we will examine before the collapse and spreading along an horizontal channel and successively we will examine the case of an inclined channel. The main controlling factors are: the column or step geometry, described in terms of aspect ratio, a , between initial height, H_{ini} , and width, L_{ini} (see Figure 4.5.4); the adoption of axi-symmetric or 2D unidirectional or bidirectional channeled plane strain conditions; the material properties; the use of a smooth or rough basal surface; the mechanism adopted for releasing material, and the width of the slot in 2D tests. Eventually, the presence of erodible material along the channel could influence the evolution.

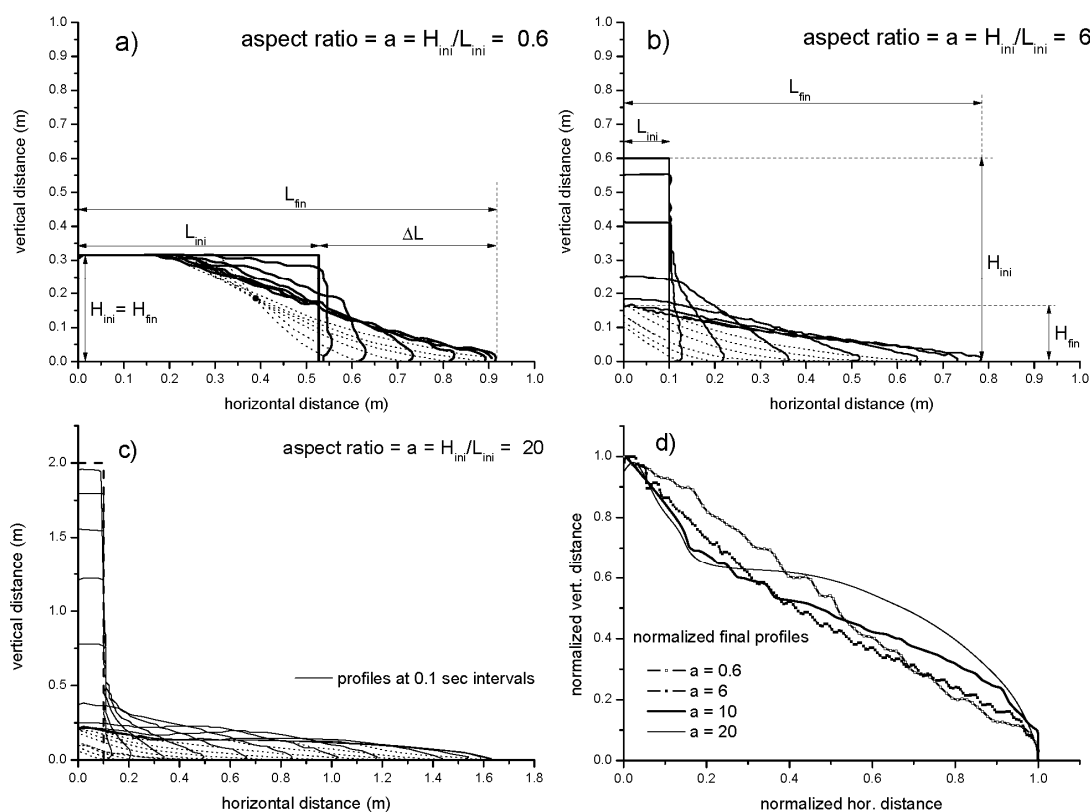


Figure 4.5.4 – Geometrical elements for the description of the granular dam break. In figures a) and b) are shown the evolution of the profile (continuous lines) and migration of the interface (dotted lines), between static and moving material, for the collapse of a 2D granular step ($a = 0.6$ and $a = 6$) as from numerical model. Profiles are traced at successive time steps ($\Delta t = 0.1$ s). c) profile evolution for an initial aspect ratio $a = 20$ at successive time steps ($\Delta t = 0.1$ s). d) Normalized profiles for the final deposit of granular steps with different aspect ratios: $a = 0.6$, $a = 6$, $a = 10$, $a = 20$. Change of mass between initial and final profiles was 2.6%, 3% and 2.8 % for a), b) and c), respectively.

Horizontal channel

The available data are of great interest for model calibration and verification especially considering the type of phenomena we are interested in. *Lajeunesse et al.* [2004] and *Lube et al.* [2004] concurrently observed that flow duration and velocity, the final extent and the amount of dissipated energy can be scaled quantitatively and with no dependence on particle properties (i.e. size, shape, roundness), substrate properties and released mass. The scaling laws for the normalized runout distance are incompatible with a simple basal friction model. Normalized runout length ($\Delta L/L_{ini}$) is linked to the aspect ratio, a , by a linear relationship for small a values [$a < 3$, *Lajeunesse et al.*, 2005; $a < 2.8$, *Lube et al.*, 2005]. For larger a values, a simple power law relationship is found, where the exponent value depends on geometrical features [$2/3$, *Lajeunesse et al.*, 2005; *Lube et al.*, 2005, and 0.9 , *Balmforth and Kerswell* 2005 for a rectangular channel], and the proportionality constant on the internal friction angle of the material [*Lajeunesse et al.*, 2005; *Balmforth and Kerswell* 2005]. We can resume the empirical relationships for the normalized runout distance ($\Delta L/L_{ini}$) and the normalized final height (H_{fin}/L_{ini}) as proposed by *Lajeunesse et al.* [2005]:

$$\frac{\Delta L}{L} \cong \begin{cases} a & a \leq 3 \\ a^{2/3} & a \geq 3 \end{cases} \quad (4.5.3a)$$

$$\frac{H_{fin}}{L_{ini}} \cong \begin{cases} a & a \leq 0.7 \\ a^{1/3} & a \geq 0.7 \end{cases} \quad (4.5.3b)$$

and by *Lube et al.* [2005]:

$$\frac{\Delta L}{L} \cong \begin{cases} \lambda a & a < 1.8 \\ 1.9a^{2/3} & a > 2.8 \end{cases} \quad (4.5.4a)$$

$$\frac{H_{fin}}{L_{ini}} \cong \begin{cases} a & a \leq 1.15 \\ ka^{2/5} & a \geq 1.15 \end{cases} \quad (4.5.4b)$$

with $\lambda = 1.2$ for symmetric 2D tests with different granular materials characterized by angle of repose ranging between 29.5 and 35 degrees.

Balmforth and Kerswell [2005] propose the following relations for 2 dimensional channeled tests with different gaps (narrow: 1 cm, and large: 20 cm) between the two vertical walls confining the column collapse:

$$\frac{\Delta L}{L} \cong \begin{cases} \lambda a^{0.65 \pm 0.05} & \text{narrow gap} \\ \lambda a^{0.9 \pm 0.1} & \text{large gap} \end{cases} \quad (4.5.5a)$$

$$\frac{H_{fin}}{L_{ini}} \cong \begin{cases} a^{0.4} & \text{narrow gap} \\ a^{0.5} & \text{large gap} \end{cases} \quad (4.5.5b)$$

with the numerical constant of proportionality, λ , clearly showing a material dependence.

These relationships suggest that the available energy to sustain spreading should depend on a . Nevertheless, as stated by *Staron and Hinch* [2005], the origin of the exponent is under discussion and no model offers a comprehensive explanation of the collapse dynamics. *Lacaze et al.* [2008] obtained similar coefficients by running tests with a low value for the ratio of the channel wall spacing to the particle diameter, and by considering the effect of sidewall friction.

The flow of the material is characterized by a highly unsteady motion with large changes of the free surface with time. The initial vertical fall phase increases with the aspect ratio, followed by a strong elongation and continuous migration of the interface between static and flowing regions towards the free surface [*Lube et al.*, 2007]. The initial free fall collapse involves the entire column and is purely vertical when the initial height is larger than 2.5 - 2.8 times the initial width of the column [*Lajeunesse et al.*, 2005; *Lube et al.*, 2005, 2007; *Staron and Hinch*, 2005]. Furthermore, *Staron and Hinch* [2005] suggest that the general shape of the final deposit profile depends on the initial aspect ratio.

These tests have been compared both with qualitative and theoretical models, aimed at finding some general scaling laws or at testing some two dimensional depth averaged shallow water models [*Mangeney et al.*, 2004, *Balmforth and Kerswell*, 2005; *Kerswell*, 2005; *Larrieu et al.*, 2006; *Doyle et al.*, 2007]. In this case, simplifications have been introduced by assuming a vertically averaged continuum description, a simple friction law along the basal surface and a Rankine coefficient. One of the consequences of adopting these depth averaged approaches consists in the inability to capture the initial vertical fall typical of collapse of columns characterized by a high value of the aspect ratio. However, in the model proposed by *Larrieu et al.* [2006] and modified by *Doyle et al* [2007] the original depth averaged approach has been modified in such way that free fall collapse of a granular column can be modeled to more accuracy by introducing a “raining” mass source term. *Larrieu et al.* [2006] assume that all the vertical kinetic energy of the initial free-fall is lost on impact on the lower column

boundary. *Doyle et al.* [2007] introduce an empirical sedimentation term with topography. Erosion and deposition have been discussed and introduced in continuum descriptions by various researches. These authors recognised that the flow depth is a priori unknown, such that it actually is a solution variable, and that the interface between flowing and static material can be time dependent [see *Bouchaud et al.*, 1994; *Douady et al.*, 1999; *Pitman et al.*, 2003; *Gray*, 2001, *Doyle et al.*, 2007, *Bouchut et al.*, 2008; *Tai and Kuo*, 2008a, 2008b, for a thorough discussion].

Other authors have used particle mechanics models or discrete element models to simulate these experiments [*Staron and Hinch* 2005, *Zenit*, 2005; *Lacaze et al.*, 2008] by assuming friction, and rigid collisions between grains. Discrete element models allow to simulate each individual particle forming the moving mass.

These authors confirmed the general form of the scaling relationships, as shown by *Staron and Hinch* [2005]:

$$\frac{\Delta L}{L} \cong \begin{cases} 2.5a & a \leq 2 \\ 3.25a^{0.7} & a \geq 2 \end{cases} \quad (4.5.6a)$$

$$\frac{H_{fin}}{L_{ini}} \cong \begin{cases} 1.6a^{0.35} & a \leq 10 \\ 1.45 & a \geq 10 \end{cases} \quad (4.5.6b)$$

who suggest independence on type, size and number of particles, as well as on inter-grain friction.

The problem with these models lies with the number of usable particles and the definition of the mechanical properties to describe the particle interaction by some parameters which do not have an immediate measurable physical mechanical equivalent (eg. restitution and damping coefficients). Numerical models can help in the understanding of the influence of the experimental configuration, the dependence on lateral confinement (channel or axisymmetric), the mechanisms controlling the flow initiation, and the general flow evolution in time and space.

Inclined channel

The dynamics of the collapse and of the spreading along an horizontal surface is controlled by the balance between different factors: the pressure gradient, friction and inertia, whereas for flows along inclined planes, the balance is mainly between gravity and friction. As for the case of horizontal channel, a set of experiments and analyses have been completed for the case of inclined channels both with and without an erodible layer of material placed along the channel bottom [Pouliquen and Forterre, 2002; MiDi GDR, 2004; Jop et al., 2005; Lube, 2006; Hogg, 2007; Pudasaini and Hutter, 2007; Mangeney et al., in press]. From numerical observations Mangeney et al [2007] observed that entrainment of material, initially under static conditions along an inclined plane, significantly increases the mobility of granular material. Below a certain thickness of the static layer the flow decelerates and eventually stops, whereas runout increases when deeper layers cover the plane surface.

The case of a vertical sand column collapse along a rough inclined channel is presented and discussed by Lube [2006]. This dataset shows the influence of the aspect ratio and channel inclination on the general flow behavior. Lube distinguishes two different flow regimes controlled by the value of the aspect ratio. For the case $a > 2.8$ and a slope angle lower than 20° the deposit is characterised by a self-similar form.

The runout distance follows different relationships as a function of the column aspect ratio and the channel slope:

$$\Delta L = k_L(\theta)H_{ini} \quad a < 2.8 \quad (4.5.7a)$$

$$\frac{\Delta L}{L_{ini}} = \begin{cases} k_H(\theta)a^{2/3} & a > 2.8 \quad \theta \leq 20^\circ \\ 4.6a^{0.84} & a > 2.8 \quad \theta \leq 25^\circ \end{cases} \quad (4.5.7b)$$

To represent the influence of the channel inclination on the final runout, Lube plots $(\Delta L/(L_{ini}a^{2/3}))$ against the inclination θ and gives the following empirical relationship:

$$\frac{\Delta L}{L_{ini}a^{2/3}} = k_H(0) + 21.7a^2 = 2.17 + 21.7a^2 \quad a > 2.8 \quad (4.5.8)$$

Releasing of a granular mass with constant discharge results in a uniform flow and the deposition of a uniform thin layer which thickness represents the minimum thickness for flow to take place at a given inclination. This approach is applicable only for inclinations higher than a threshold value, for which flow stops almost immediately, and lower than a second

threshold value for which the flow does not generate a deposit [Pouliquen and Forterre, 2002; Borzsonyi et al., 2008; Mangeney et al., in press]. Borzsonyi et al. [2008] propose a relationship for the determination of the value of the minimum thickness for flow and observe that this is inversely related to the difference: $\tan(\text{slope}) - \tan(\text{internal friction angle of the material})$.

The main observations and results for these studies are the followings and are well described in Mangeney et al. [in press]: erosion controls the behaviour of the flow in terms of its dynamics and total runout, especially when channel slope is close to the value of angle of repose of the material; erosion is controlled by the inclination and in particular it starts for slope values larger than half the value of the angle of repose and beyond this threshold it depends almost linearly by thickness of static layer [Mangeney et al., in press]; blunted flow fronts are observed especially when inclination is high and it does not seem to be influenced by thickness of the static layer; waves are present both at the flow surface and along the static/moving material interface.

4.5.2.1 Modeling Approach

Sliding and flowing rock and soil masses, and dense granular flows show very large displacements and deformations. If a traditional Lagrangian finite element method would be used, the finite element (FE) mesh would be subjected to these large displacements and deformations, rapidly leading to a highly distorted mesh. As a consequence, the calculated results would become inaccurate. We use a particular type of combined Eulerian-Lagrangian method [Roddeman, 2008; Crosta et al., 2003, 2004, 2008] which does not distort the FE mesh and guarantees accurate calculation results.

The flow of landslide material is governed by:

$$\rho \dot{v}_i = \frac{\partial \sigma_{ij}}{\partial x_j} + g_i \quad (4.5.9)$$

where ρ is the density of the material, v_i is the velocity in i -direction (i is 1, 2 or 3), σ_{ij} denotes the stress tensor, x_j is the j -th space coordinate (i.e. j equals to 1, 2, or 3) and g_i represents the gravity force in i -direction ($g_1 = g_2 = 0, g_3 = -9.81$).

If we examine the material stresses $\sigma_{\text{effective}} = \sigma_{\text{effective},ij}$, the effective stress changes due to material stiffness result in a fixed frame from two different contributions [Hunter, 1983]. The first contribution of the effective stress changes, in a fixed frame, results from rigid body rotations of the material. These rotations induce changes of the effective stress tensor components relative to a fixed frame. Nevertheless, these rigid body rotations from an arbitrary deformation field are not uniquely defined, consequently a choice has to be made about how to model this contribution. We applied an incrementally objective Lagrangian model, based on a polar decomposition of the incremental deformation tensor [Roddeman, 2002]. Mathematically, we can write: $\Delta F = \Delta R \cdot \Delta U$ where ΔF is the deformation tensor with deformation referring to the previous time step, ΔR is the rotation tensor and ΔU denotes the stretch tensor. Using the rotation tensor ΔR , the rigid body stress change is:

$$\Delta \sigma_{\text{effective}} = \Delta R \sigma_{\text{effective}} \Delta R^T \quad (4.5.10)$$

The second contribution comes from straining of the material. The incremental stretch tensor ΔU is used to determine the incremental strain tensor, ΔE :

$$\Delta E = 0.5(\Delta U + \Delta U^T) - I \quad (4.5.11)$$

with I is the identity tensor. In order to calculate the stresses from straining of the material an elasto-plastic model is adopted. We use the well known elastic isotropic stiffness tensor C [Chen and Han, 1988] for the elastic part:

$$\Delta \sigma_{\text{effective}} = C(\Delta E - \Delta E_{\text{plastic}}) \quad (4.5.12)$$

where the fourth order tensor C solely depends on Young's modulus and Poisson's ratio for an isotropic material. We use a Mohr-Coulomb model for the plastic part, so that the plastic strains $\Delta E_{\text{plastic}}$ are determined such that the yield function f :

$$f = 0.5(\sigma_{\text{effective},1} - \sigma_{\text{effective},3}) + 0.5(\sigma_{\text{effective},1} - \sigma_{\text{effective},3}) \sin \phi - c \cos \phi \leq 0 \quad (4.5.13)$$

cannot take positive values in elasto-plasticity. Here c is the cohesion, ϕ is the material friction angle, $\sigma_{\text{effective},1}$ is the maximum principal stress, and $\sigma_{\text{effective},3}$ is the smallest principal stress. We assume zero dilatancy so a flow rule with a dilatancy angle equals to zero. The rotation and stretching increments of the stresses, obtained through the above described steps (eqs. 4.5.8 to 4.5.10), are added to the stresses of the previous time point to give the new effective stresses, σ_{ij} , at the current time.

Even if water has not been included in the calculations for this manuscript, this approach can be extended to include the effect of pore water, and we include here the adopted equations to provide a more complete overview of the model. The total stress in a calculation with groundwater flow is the sum of the effective stresses and pore water pressure:

$$\sigma_{ij} = \sigma_{\text{effective},ij} + p\delta_{ij} \quad (4.5.14)$$

where p is the water pore pressure and δ_{ij} equals 1 if $i = j$ and 0 otherwise. The water pore pressure is obtained from the hydraulic head h as:

$$p = h - \rho_w g_3 x_3 \quad (4.5.15)$$

where ρ_w is the water density. The evolution of the hydraulic head is governed by the water storage equation

$$C\dot{h} = \left(k_i^p \frac{\partial^2 h}{\partial x_i^2} + k_2^p \frac{\partial^2 h}{\partial x_2^2} + k_3^p \frac{\partial^2 h}{\partial x_3^2} \right) + \frac{\partial v_i}{\partial x_i} \quad (4.5.16)$$

with C the water capacity, k_i^p the permeability in x_i direction and $\frac{\partial v_i}{\partial x_i}$ represents pressure changes due to compression of the soil skeleton. With this set of equations we can describe the large deformations and sliding of landslide material, filled or not filled with groundwater. In this approach, we neglect nonlinear soil behaviour, cracking phenomena and partial groundwater saturation that can be modelled, for example, with hypo-plasticity laws, damage

laws and smeared cracking concepts, and partially saturated soil models, respectively. However, the presented equations include the most important aspects like large deformations, shear stress limit by a standard Mohr-Coulomb law, and groundwater pressures in saturated soil zones. For the case of sliding along a rigid (non erodible) surface, we set zero velocity of the material, and a reduction in the cohesion and friction angle of the plastic law in order to model reduced friction between the material and the sliding surface.

Our numerical model uses isoparametric finite elements for space discretisation. We typically apply three-noded triangles in 2D, and eight-noded hexahedrals in 3D. For the present calculations we used about 40.000 to 150.000 triangular three-node elements to discretize the 2D space with a mean element size ranging between 0.004 m and 0.01 m.

For time discretization, we apply implicit Euler time steps, with automatic time step adjustment to keep control on out-of-balance forces at the nodes of the finite elements. Since we disconnect material displacements from the finite element mesh, state variables are transported through the mesh by a Streamline Upwind Petrov Galerkin method. The velocities at each time step are calculated such that inertia and internal stress contributions make equilibrium at the finite element nodes.

The initial equilibrium stress state is reached through quasi-static time stepping so that no inertial effect is introduced. The gravity is incrementally applied in successive time steps. The initial movement or occurrence of the landslide can be triggered by either lowering cohesion in time [Crosta *et al.*, 2003, 2004, 2008], or imposing a base acceleration diagram to simulate seismic triggering, or in this specific case by deleting instantaneously a retaining wall. The computation does not require a predefined failure surface and it continues until complete stopping of the mass.

We solve our dynamic equilibrium equations for the complete inner area of the column, without a priori applying any specific controlling term as, by example, a plug flow velocity profile [Larrieu *et al.*, 2006]. In our approach, the flow depth simply follows from the solution of the velocities of the nodes of the isoparametric finite elements at the upper edge of the flowing mass. So, differently from the previously cited contributions [Bouchaud *et al.*, 1994; Douady *et al.*, 1999; Pitman *et al.*, 2003; Gray, 2001, Doyle *et al.*, 2007, Bouchut *et al.*, 2008; Tai and Kuo, 2008a, 2008b], the depth of the slide is not a priori fixed but is an intrinsic part of the complete set of equations. However, our approach differs from those cited above because we compute velocities also for the internal part of the flowing mass by solving the

dynamic equilibrium equations for all the isoparametric finite elements. This is the major difference with the depth averaged approach which averages conservation laws over the flow depth. As a consequence, in the proposed approach we do not include any controlling condition for onset or evolution of erosion and deposition. These processes follow directly by the governing dynamic equilibrium equations applied on different materials in different zones. The solution of these equations gives velocities at the nodal points of the isoparametric finite elements, and thus for the rezoning of the different materials to erosion and deposition.

The developed code has been applied to model a series of different case studies involving flow of debris material in different conditions (e.g. steep slopes, ice covered surfaces, erodible materials of different thickness) [Crosta *et al.*, 2003, 2004, 2008a, b].

We performed a series of simulations by considering different aspect ratios, ranging between 0.6 and 20, assuming an elasto-plastic material and a Mohr-Coulomb yield rule. Adopted values for the internal friction angle, ϕ , range between 20° and 40° whereas friction angle along the horizontal plane ϕ_b was generally set equal to the adopted internal friction angle [see Table 1]. These values are similar to those typical for materials used for the experiments by Lube *et al.* [2004, 2005; coarse and fine sand, 31° and 29.5° respectively, rice, 32° , sugar, 35°], by Lajeunesse *et al.* [2004, 2005, glass ballotini, 1.15 and 3 mm; $\phi_{\text{repose}} = 22^\circ$, $\phi_{\text{avalanching}} = 27.4^\circ$, $\phi_b = 11^\circ$ and 12°], and by Balmforth and Kerswell [2005; 0.8 and 3 mm; $\phi = 36^\circ$ and 22° , respectively, $\phi_b = 14.75^\circ$ and 15°]. A slight cohesion ($c = 1$ Pa) has been maintained to avoid numerical problems that could arise for extremely low stress levels.

4.5.2.2 Results

We present here the results of the simulations by comparing them with experimental data. Figures 4.5.4a, 4.5.4b and 4.5.1c show the development of the flow since the initial failure along an inclined failure zone for three different aspect ratios ($a=0.6, 6$ and 20). For low values (Figure 4.5.4a) only the edges of the step are in motion whereas for large values the upper part of the column descends vertically maintaining its initial shape (Figures 4.5.4b and 4.5.4c) with a free fall behavior. Only the more external and lower half of the material starts moving outward with a horizontal component. In this initial phase the model correctly identifies the geometry of the failure zone as verified by experiment results and by the classical Rankine theory (see Figure 4.5.5).

The results show the progressive increase in size of the static layer, the rotational failure mechanism and the progressive thinning of the moving mass. Migration of the interface between static and moving material develops differently with aspect ratio. For low aspect ratios a point exists above and below which erosion and deposition occur, respectively. For high aspect ratios (Figures 4.5.4b and 4.5.4c), deposition is always observed along the interface. As a consequence a continuous vertical and horizontal migration of the interface is observed with time together with a thinning of the moving mass. In all the cases the interface ends up asymptotically at the flow front minimizing the contact area between the horizontal surface and the moving material.

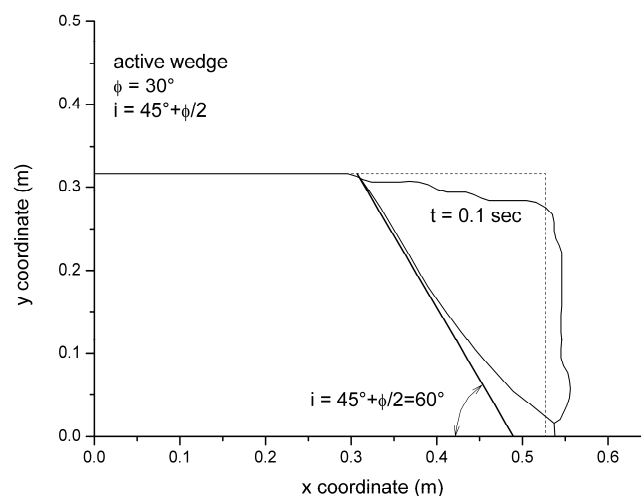


Figure 4.5.5 - Comparison between the theoretical failure plane, according to the Coulomb-Rankine theory, and the failure zone from the numerical model at 0.1 sec.

To verify how well the adopted numerical scheme is conserving mass, we computed the change between the initial and final mass of the material. For example, for simulations performed using an aspect ratio value of 0.6 and friction angles of 25, 30 and 40 degrees, we found changes equal to 1.18, 1.89 and 2.2 %, respectively. In all the simulations we observed a change in mass lower than 3.6 % (see also Figures 4.5.4 and 4.5.6).

The effect of mesh resolution on the accuracy of the numerical scheme has been assessed by running simulations with the same material geometry and a different element size. By quadrupling the number of elements, passing from an average element size of about 0.012 m to 0.005 m we observed a change of about 3 % and 5 % in the runout length and maximum final height, respectively.

The effect of internal friction angle on the computed runout distance and deposit geometry for a specific aspect ratio ($a = 10$) is represented in Figure 4.5.6a. Scaling laws include this dependence on internal friction angle through the coefficient in the power law relationship, in agreement with results by *Lajeunesse et al.*, [2005] and *Balmforth and Kerswell* [2005], and in contrast with *Lube et al.* [2005]. On the contrary, both the runout and the deposit profiles are only slightly influenced by the basal friction angle, as suggested by Figure 4.5.6b [see for example results in Table 1 for $a = 3.2$]. The secondary role played by the basal friction angle on the final runout is suggested by the small contact zone between moving material and channel bottom (see Figure 4.5.7).

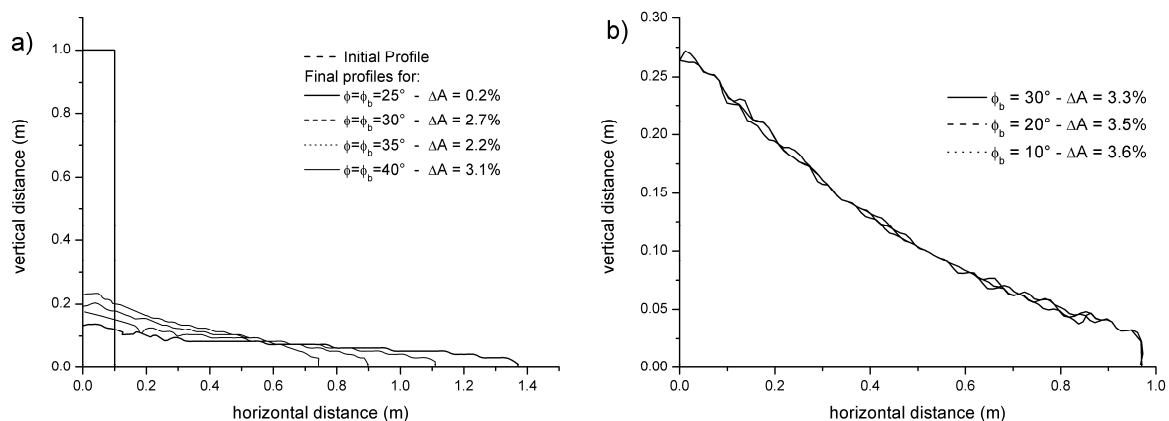


Figure 4.5.6 – a) Influence of the internal friction angle (ϕ) on the final profile and total runout for a granular column with $a = 10$.; b) influence of the basal friction angle, ϕ_b , on the final profile for a column with $a = 3.2$ and internal friction angle of 30 degrees. Measured changes between initial and final area occupied by the material are shown in the legends for each test.

a	H _i	L _i	Internal Friction Angle	Basal Friction Angle	Bottom layer thickness	H _{fin}	L _{fin}	DL = L _{fin} - L _{ini}	t _{fin}	τ _c = (H _{ini} /g) ^{0.5}	t _{fin} /τ _c	t _{fin} /(L _i /g) ^{0.5}
	m	m	°	°	m	m	m	m	sec	sec		
0.6	0.32	0.53	25	25	-	0.32	1.02	0.49	1.05	0.179	5.850	4.530
0.6	0.32	0.53	30	30	-	0.32	0.89	0.36	0.67	0.179	3.733	2.891
0.6	0.32	0.53	40	40	-	0.30	0.78	0.26	0.70	0.179	3.900	3.020
1.0	0.32	0.32	25	25	-	0.26	0.90	0.58	0.90	0.179	5.015	5.015
1.0	0.32	0.32	30	30	-	0.28	0.73	0.41	0.71	0.179	3.956	3.956
1.0	0.32	0.32	40	40	-	0.31	0.60	0.28	0.94	0.179	5.237	5.237
1.4	0.50	0.35	30	30	-	0.33	1.14	0.78	0.90	0.226	3.987	4.738
3.2	0.60	0.19	20	20	-	0.19	1.52	1.33	1.09	0.247	4.407	7.874
3.2	0.60	0.19	25	25	-	0.22	1.20	1.01	0.90	0.247	3.639	6.501
3.2	0.60	0.19	30	10	-	0.26	0.97	0.78	0.83	0.247	3.356	5.996
3.2	0.60	0.19	30	20	-	0.26	0.97	0.78	0.83	0.247	3.356	5.996
3.2	0.60	0.19	30	30	-	0.26	0.97	0.78	0.85	0.247	3.437	6.140
3.2	0.60	0.19	40	40	-	0.30	0.70	0.51	0.70	0.247	2.830	5.057
4.0	0.60	0.15	25	25	-	0.19	1.11	0.96	0.97	0.247	3.922	7.844
4.0	0.60	0.15	30	30	-	0.22	0.89	0.74	0.86	0.247	3.477	6.955
4.0	0.60	0.15	40	40	-	0.26	0.65	0.50	0.73	0.247	2.952	5.904
5.0	0.75	0.15	30	30	-	0.23	1.06	0.91	0.91	0.277	3.291	7.359
6.0	0.60	0.10	30	30	-	0.17	0.82	0.72	0.83	0.247	3.356	8.221
7.0	0.70	0.10	30	30	-	0.16	0.88	0.78	0.88	0.267	3.294	8.716
8.0	0.80	0.10	30	30	-	0.17	0.98	0.88	0.96	0.286	3.362	9.508
9.0	0.90	0.10	30	30	-	0.20	0.99	0.89	0.89	0.303	2.938	8.815
10.0	1.00	0.10	25	25	-	0.13	1.36	1.26	1.45	0.319	4.542	14.362
10.0	1.00	0.10	30	30	-	0.17	1.12	1.02	1.05	0.319	3.289	10.400
10.0	1.00	0.10	35	35	-	0.19	0.90	0.80	0.97	0.319	3.038	9.607
10.0	1.00	0.10	40	40	-	0.23	0.75	0.65	0.92	0.319	2.882	9.112
12.0	1.20	0.10	30	30	-	0.18	1.28	1.18	1.15	0.350	3.288	11.390
12.0	1.20	0.10	40	40	-	0.24	0.84	0.74	1.00	0.350	2.859	9.905
12.0	1.20	0.10	25	25	-	0.14	1.60	1.50	1.30	0.350	3.717	12.876
16.7	1.67	0.10	30	30	-	0.24	1.58	1.57	1.36	0.412	3.296	13.470
20.0	2.00	0.10	30	30	-	0.21	1.61	1.51	1.45	0.452	3.211	14.362
3.2	0.60	0.19	30	10	0.2	0.15	0.90	0.71	1.20	0.247	4.852	8.668
3.2	0.60	0.19	30	20	0.2	0.20	0.96	0.78	0.90	0.247	3.639	6.501
3.2	0.60	0.19	30	30	0.2	0.22	0.86	0.67	0.80	0.247	3.235	5.779
3.2	0.60	0.19	40	20	0.2	0.24	0.80	0.61	0.83	0.247	3.356	5.996
3.2	0.60	0.19	30	10	0.5	0.15	0.93	0.75	1.30	0.247	5.257	9.391

Table 1 - Summary of the parameters and results from the numerical simulations with horizontal channel and with different bottom characteristics. Values of basal friction angle for simulations with an erodible layer refer to the internal friction angle of the erodible material. See Figure 4.5.4 for symbol explanation; t_{fin} = time of arrest of motion

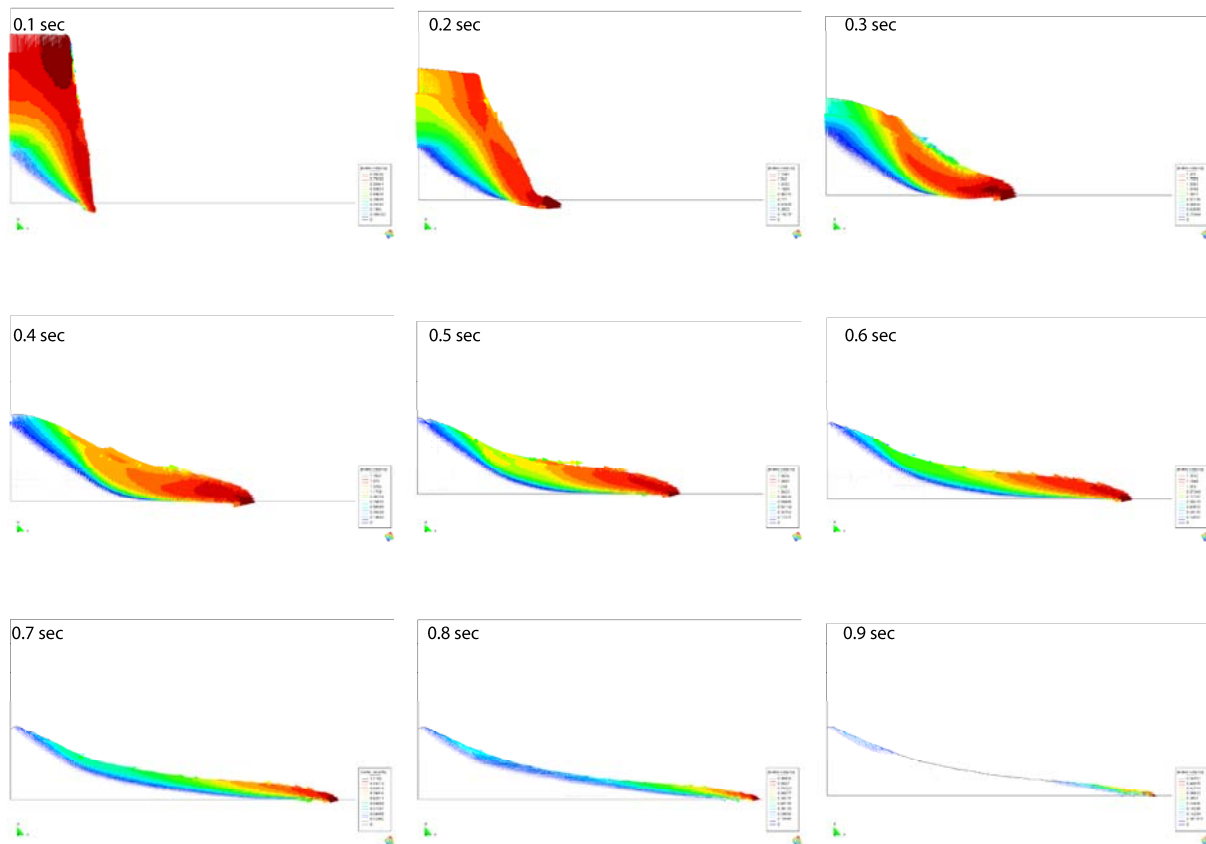


Figure 4.5.7 – Example of numerical results for the collapse of a granular column ($a = 3.2$). Vectors show the computed velocity within the moving mass at different time steps ($\Delta t = 0.1$ sec) since the beginning. Initial wedge failure, successive horizontal spreading and deposition are visible in the figures. At the final steps movement mainly occurs locally and at steeper sectors.

Runout dependence on step aspect ratio and friction angle is shown in Figure 4.5.8 together with laboratory and numerical results from the literature. Our results evidence a linear relationship with coefficient equals to 1.44 (for $\phi=30$ degrees; 0.867 for 40 degrees and 1.77 for 25 degrees, see Figure 4.5.8c) for aspect ratios lower than 4 and a power law relationship above this limit (Figure 4.5.8c). The power law coefficient is inversely related to friction angle and ranges between 1.17 and 2.17. The exponent ranges between 0.68 and 0.77. Values of the exponent are similar to the fixed value (0.67) presented by *Lube et al.* [2005] and *Lajeunesse et al.* [2005]. In any case Figure 4.5.8 shows how our results fit reasonably well the experimental test results over the entire range of simulated aspect ratios and considering a broad range of internal friction angles.

To test the model against the scaling relationships presented by *Lube et al.* [2005, Figure 4.5.8b] and *Lajeunesse et al.* [2005] and the dependence on friction we plot the initial to final height ratio (non dimensional height, Figure 4.5.9a) and the maximum deposit height to initial column width ratio (non dimensional maximum deposit height, Figure 4.5.9b) with respect to the aspect ratio.

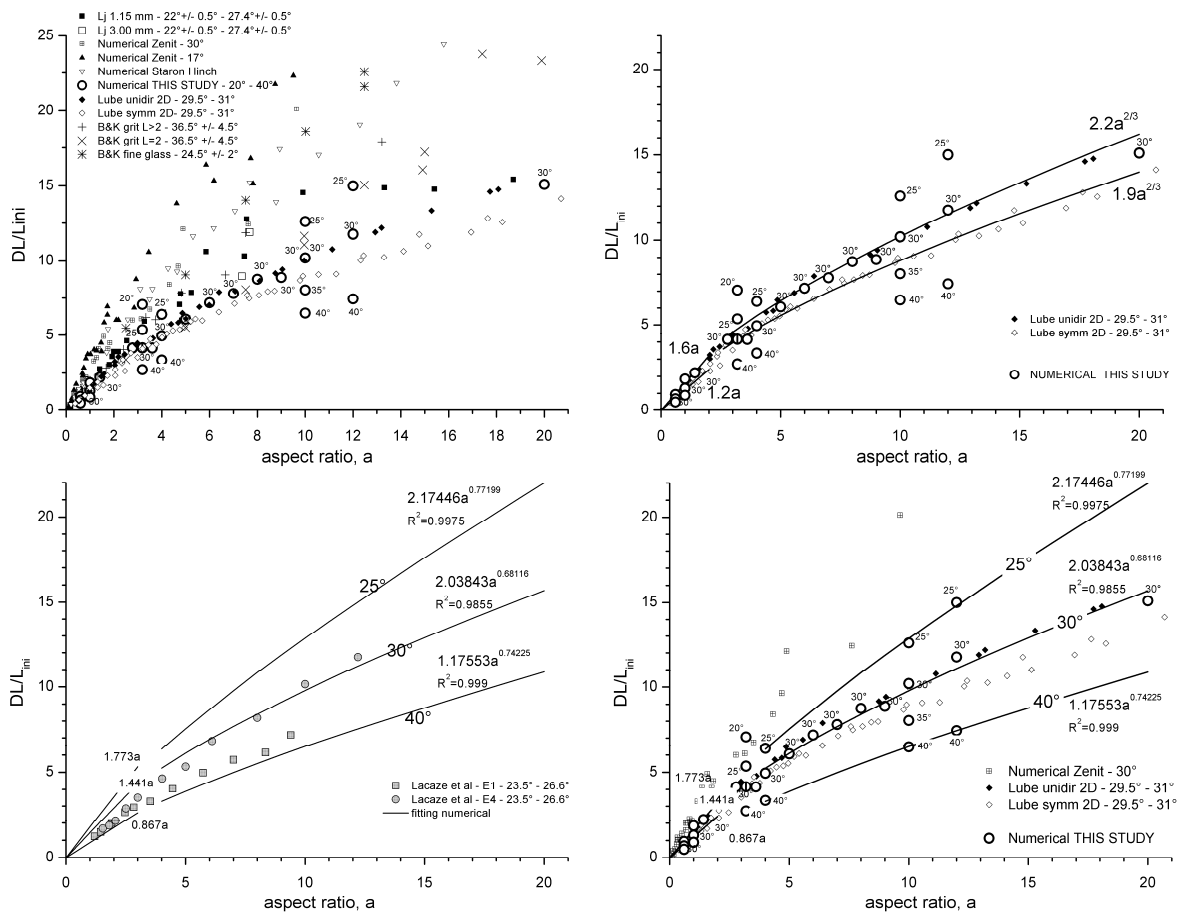


Figure 4.5.8 – Comparison of the results from numerical simulations and experimental data. Nondimensional incremental runout plotted against aspect ratio and (Fig. 4.5.5b) fitting relationships as proposed by Lube et al. [2005] for coarse sand and unidirectional tests with 20 cm wide channel ($2.2a^{2/3}$) and for coarse sand and bidirectional tests with 10 cm wide channel ($1.9a^{2/3}$). Data are shown all together in a) and separately in b), c) and d). Results of the numerical simulation are shown for comparison in each plot and are labelled with the adopted values for the internal friction angle of the material (open circles, see also Table 1). Best fit lines for simulations with different values for the angle of internal friction are shown for $a < 4$ and $a > 4$. Legend explanation: data labels represent: Lj: Lajeunesse et al., 2005; Zenit: Zenit, 2005; Staron Hinch: Staron and Hinch, 2005; Lube: Lube et al., 2005 where symmetric is for series A and unidirectional for series B; B&K: Balmforth and Kerswell, 2005; Lacaze et al.: Lacaze et al., 2008.

Numerical data are in good agreement with experimental data up to aspect ratio values of about 20 even if a certain dispersion in experimental data is observed. The trend of numerical results for the maximum normalized height (Figure 4.5. 8b) is similar to the one presented by *Lajeunesse et al* [2005] with values of the normalized height which tend to a constant value. Again, we observe that the value of the maximum normalized height changes with the internal friction angle for a boundary condition, along a free-slip vertical side [as for test series A, symmetrical two dimensional, by *Lube et al.*, 2005]

Model validation has been completed , for columns with different aspect ratios, by comparing numerical and experimental data concerning the position of the flow front during motion at different times [Figure 4.5.10a; *Lajeunesse et al.*, 2005, *Lube et al.*, 2005] and the total flow duration (Figure 4.5.10b). The time evolution of the flow can be described by plotting the front position at successive instants versus time normalized by the free fall time of the granular column [Figure 4.5.10a, *Lajeunesse et al.*, 2005, $\tau_c = (H_{ini}/g)^{0.5}$]. The simulations show the same time evolution in three steps as described by *Lajeunesse et al.* [2005] for the experimental tests, and characterized by a transient acceleration, a constant velocity spreading, and a progressive deceleration. These phases last for time intervals proportional to τ_c and the numerical results show the same normalized duration for each of the phases recognized experimentally by *Lajeunesse et al.* [2005]. The scaled total flow time (Figure 4.5.10b) has been used [*Lube et al.*, 2005] to analyse the dependence of flow duration on aspect ratio. By fitting the more complete series of the numerical results for an internal friction angle equals to 30 degrees (Table 1 and Figure 4.5.10b), the relationship $3.684 * a^{0.448}$ is obtained.

Velocity distribution within the flowing mass has been obtained by sampling values along profiles (Figures 4.5.11a and 4.5.11b) normal to the instantaneous local failure zone (i.e. the interface between static and flowing regions), being the flow locally parallel to the static/flowing interface. This allows a comparison with experimental results presented for flows on similar geometries [*Midi*, 2004; *Lajeunesse et al.*, 2005; *Lube et al.*, 2007; *Forterre and Pouliquenne*, 2008].

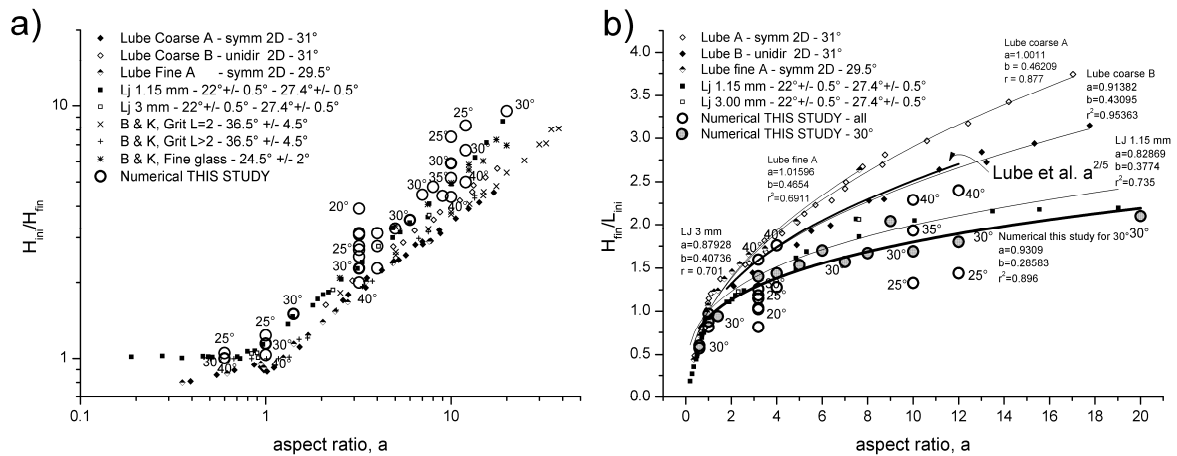


Figure 4.5.9 - a) Initial to final height ratio and b) maximum deposit height to initial column width ratio plotted against aspect ratio. Data from experimental tests is shown [Lube: from Lube et al., 2005; Lj: from Lajeunesse et al., 2005; B&K, from Balmforth and Kerswell, 2005]. Results of numerical simulations, performed with different values for the internal friction angles (open circles with relative values) are shown together with best fitting of the data for 30° internal friction angle.

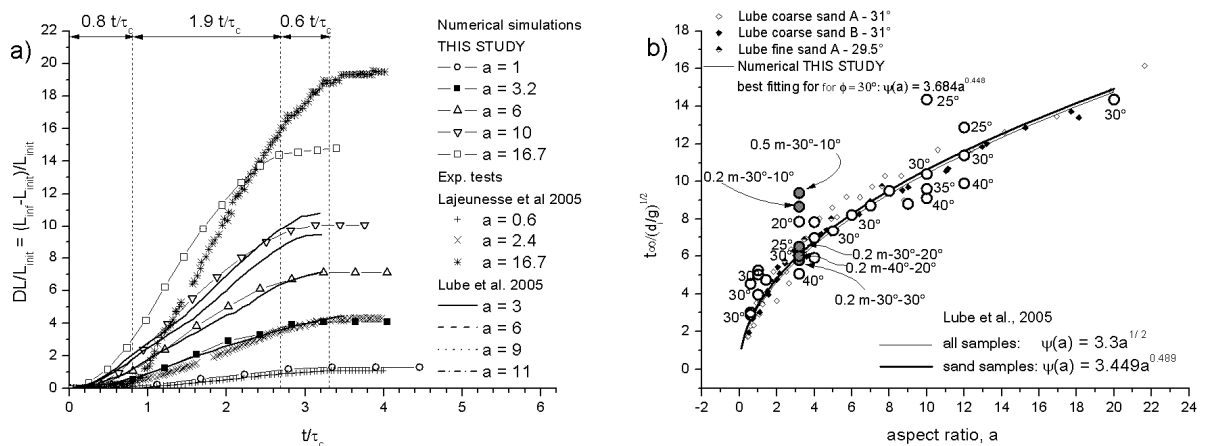


Figure 4.5.10 – a) Normalized runout vs normalized time with evidenced the three time steps as by Lajeunesse et al [2005], b) non dimensional time for the flow front to cease motion vs aspect ratio, where $\tau_c = (H_{ini}/g)^{0.5}$ represents the free fall collapse time. Open circles and grey filled circles are for numerical tests without and with erodible basal layer, respectively. The label for erosion tests shows the thickness of the erodible layer, the internal friction angle of the column material and of the erodible material, respectively. Best fit for simulations with $\phi = 30$ degrees is $3.684 * a^{0.448}$.

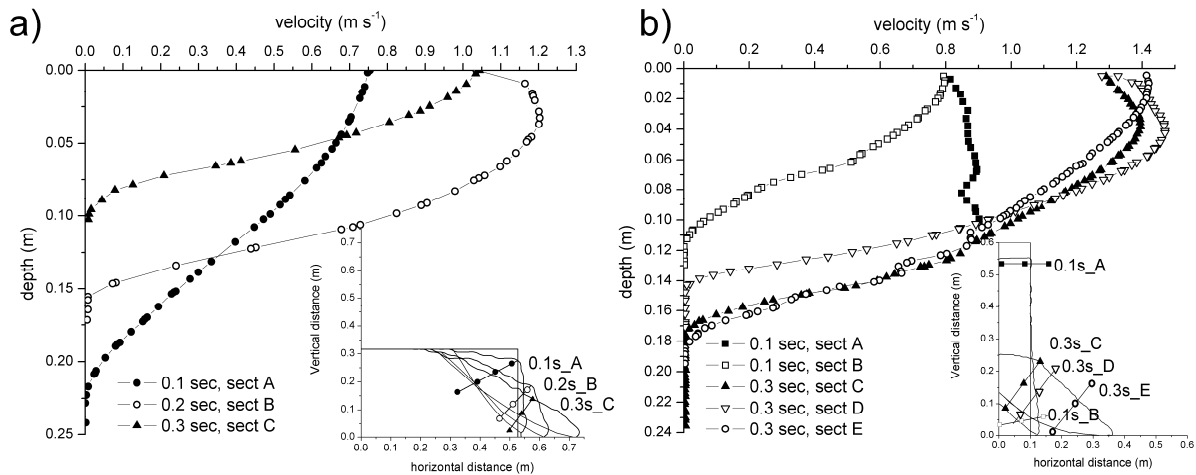


Figure 4.5.11 – Instantaneous velocity profiles for two different tests a) $a = 0.6$ and b) $a = 6$ at different transversal profiles oriented perpendicularly to the failure surface. Depth is the distance from the free surface in a line perpendicular to the failure surface. The time when each profile was measured is shown in the legends. For the case 0.1sec-Sect.A in b) the ordinate axis represents the horizontal distance from the lateral boundary being the section horizontal.

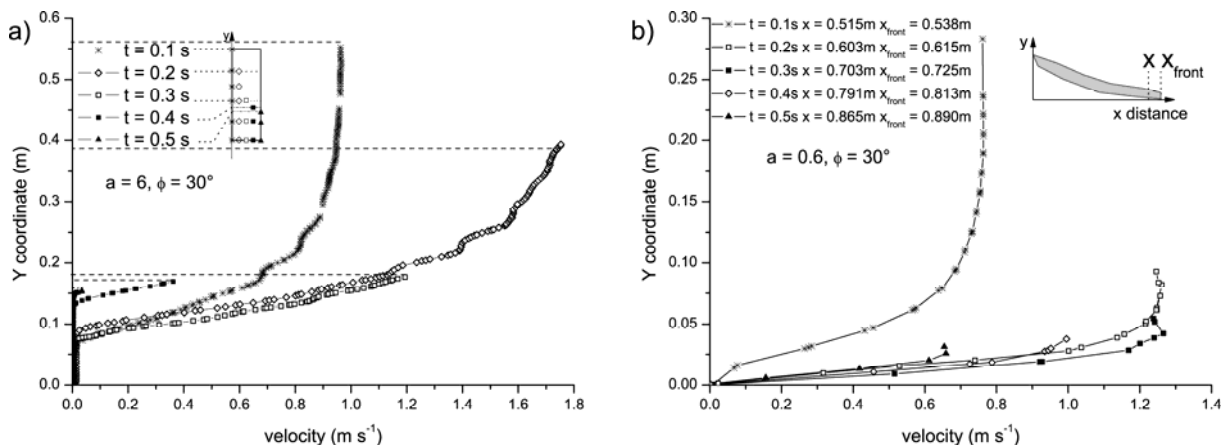


Figure 4.5.12 – Instantaneous velocity profiles for two different tests a) $a = 6$ and b) $a = 0.6$ at different transversal profiles. For case a) velocity is sampled at different time steps (0.1 s to 0.5 s) along a vertical profile laying along the left hand side of the collapsing column ($x = 0$). As a consequence the maximum y coordinate decreases with time with the column collapse. For case b) the velocity is sampled at different time steps (0.1 s to 0.5 s) along different vertical profiles located just behind (coordinate x) the instantaneous leading front (coordinate x_{front})

Simulations show a plug like flow during the vertical free fall for large aspect ratios. During the initial phase of the collapse of a tall column the velocity is constant in the upper part of the column (see Figure 4.5.12a, at 0.1 sec) and rapidly decreases in the lower sector. Successively, the material decelerates and starts moving outward. The velocity at the time step 0.1 sec coincides with the free fall velocity but at 0.2 sec it is already slightly below the corresponding velocity suggesting there is a slight deceleration that continues progressively.

The velocity profiles during the lateral spreading phase along subcircular shear zones agree with those presented in the literature [*Lajeunesse et al., 2005*] with a clear linear trend with depth in the middle and upper sector and an exponential tail towards the static granular layer. The decreasing trend in velocity observed for the more superficial part of the flowing material (Figure 4.5.11b) is probably an artefact related to the linear geometry of the sampling profiles and the slightly circular movement of the material (see Figures 4.5.7 and 4.5.11).

Locally, a plug-like flow in proximity of the flow front is observed. This is shown in Figure 4.5.12b, where the material velocity has been sampled at successive time steps (between 0.1 sec and 0.5 sec) for a test with low aspect ratio (0.6) along a vertical profile located just behind the instantaneous front position. The same type of behaviour has been observed for the entire set of numerical simulations (eg. See Figure 4.5.7).

4.5.3 Collapse of a granular step on erodible layer

Lajeunesse et al. [2006] and *Lucas and Mangeney* [2007] analyzed the similarities between granular step collapse experiments and some large Martian landslides. To verify similarities with other conditions and real case studies, and to generalize the adopted approach and test its validity for real case studies it is necessary to consider the presence of erodible material along the spreading surface [*Crosta*, 1994; *Hungr and Evans*, 2004; *Mangeney et al.*, 2007; *Crosta et al.*, 2008a, b, 2009; *Mangeney et al.*, in press]. Therefore, we collected the available data and we started a series of laboratory tests to analyse the problem of the granular step collapse on an erodible layer. We compared the test results with those obtained from the numerical model. Finally, we collected data for a couple of historical rock-avalanche events and we compare observations with model results under different conditions of the erodible layer (dry or saturated).

4.5.3.1 Experimental setup

The experiments examine two-dimensional granular flows originated by the collapse of rectangular columns.

Following previous experimental work on granular step collapse we performed a series of preliminary laboratory tests in a 2 dimensional setting with a 10 cm gap between vertical sidewalls. The channel has a depth of 800 mm and a length of 2000 mm. We performed experiments by releasing a granular column on a smooth channel base, on a rough surface made by gluing particles to the channel bottom, and on a 5 cm erodible layer deposited on the channel base. The column height and width have been varied through a wide range of values to obtain columns with different values of the aspect ratio (a , between 0.6 and 20). The material has been gently pluviated behind a gate and on the channel base (for experiments on an erodible layer) by controlling the falling height of the material. The bulk density of the pluviated material has been computed for each experiment. We observed a maximum bulk density increase with column height (from 6 to 60 cm) varying in a range of values between 4 and 15 %. The material is maintained in position by a swinging gate that is rapidly opened to start the experiments. A series of tests has been performed with different materials to test the general behaviour, and to verify the erosion and entrainment process during the column

collapse as a function of the material properties. In particular, in the context of this research we present some of the results from tests performed using rice (for the column; grain size 3 ± 0.5 mm) moving on smooth plexiglass surface, or on glued pasta grains or on an erodible layer of pasta grains (sub-spherical elements, gran size 2 ± 0.2 mm). Differences in colour and grain characteristics allow for a simpler visualization of the interface between material forming the collapsing column and the horizontal erodible layer.

Internal friction angle was estimated by inclining a plane with and without particles glued on its surface till downslope motion of the overlying granular layer was observed. Angle of repose was measured from the final slope of wedge shaped piles built up by deposition within the channel. The average value of the internal friction angle for these materials ranges in a narrow interval (angle of repose: 27-33 degrees for rice and 24 - 27 degrees for pasta grains). The friction angle values at the contact between the smooth channel base and rice, and pasta grains are 22 and 19 degrees, respectively. The motion of the collapsing material was recorded at 600 frames per seconds using a high speed camera.

4.5.3.2 Experimental results

Figure 4.5.13 shows experimental results in terms of normalized runout with respect to aspect ratio. The results clearly demonstrate the effect of an erodible basal layer in reducing the material runout. Measured runout distances are always shorter than for the case of smooth basal surface and shorter also for the case of a channel base covered by glued pasta grains. In this last case the front is always characterized by a strong agitation, bouncing and projection of the particles. Furthermore, we notice that the stiffness of the material (e.g. plexiglass, rubber sheet, grains glued on plexiglass or rubber) forming the surface can control the runout. The best fitting relationships are comparable to the experimental results in the literature [Lajeunesse *et al.* 2004, 2005; Lube *et al.* 2004, 2005, 2007; Siavoshi and Kudrolli 2005; Balmforth and Kerswell 2005], both in terms of coefficient and exponent values.

Image analysis techniques have been applied to observe in detail the sectors of the material interested by fast and slower motion, and by deformation and dragging within the erodible layer. Particle velocimetry (PIV) has been applied to obtain velocity vectors from couples of successive images. The results demonstrate that dragging occurs at the base of the moving

material and that no real mixing between the two materials occurs along along the contact surface (see Figure 4.5.14).

Figure 4.5.14 shows some of the results concerning motion of the material at successive time steps (15 steps at 0.0083 sec intervals) and the disturbance induced in the underlying erodible layer. Images of the sector close to the toe of the granular column have been taken at 600 frames per seconds. Analysis of images taken at intervals of 5 frames, by applying PIV (particle image velocimetry), clearly illustrates the progressive displacement, the geometry at the front, and the disturbance in the erodible layer (ie. below the original surface of the erodible layer; see Figure 4.5.14).

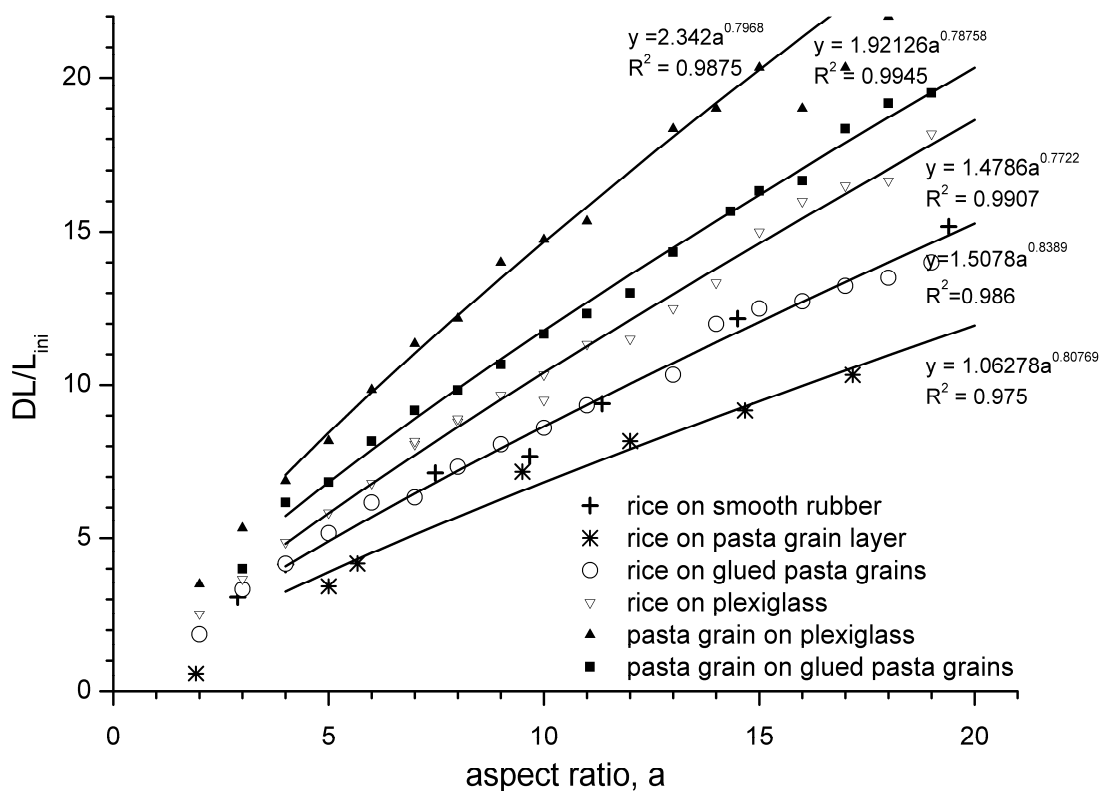


Figure 4.5.13 – Results of laboratory experiments performed with different granular materials and channel base in different conditions (see legend for description). Best fitting curves obtained using allometric functions are shown. The effect of different internal and basal friction angles, as well as of basal dragging and deformation, on normalized runout are visible.

From this series of images we can observe the geometry of the profile and of the disturbed zone. This zone expands progressively together with the material motion and then is shifted in the direction of motion.

Deformation and dragging in the basal layer are evident even for this case of materials with similar properties. Finally, Figure 4.5.14 clearly shows the presence of a slowly moving sector, located behind the fast moving material of the front. This moving material is limited below by a sub-circular boundary. The enclosed sector of material expands progressively, initially more rapidly, and then slowly while migrating in the direction of motion.

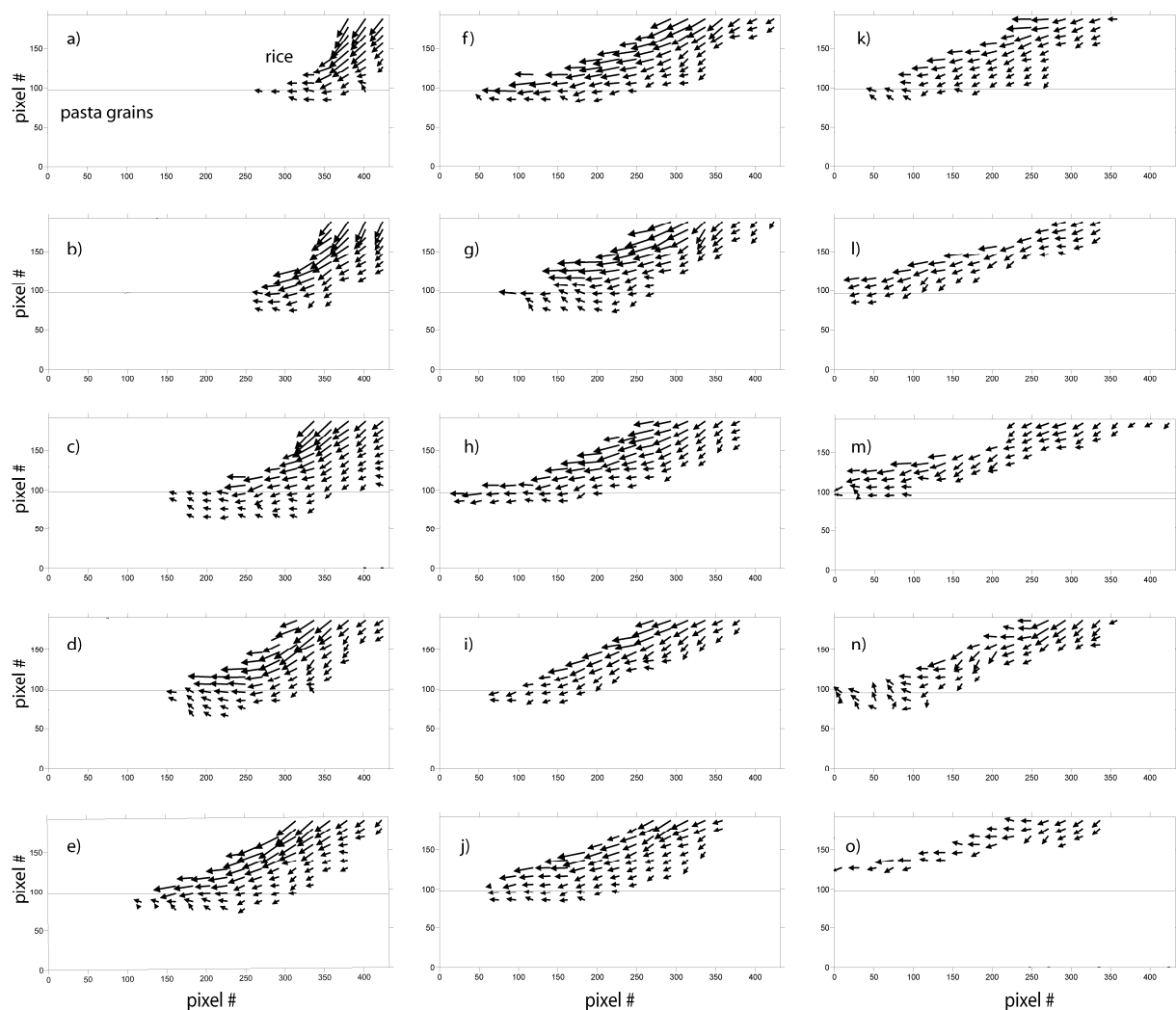


Figure 4.5.14 – Example of material velocity distribution at successive time intervals (0.083 sec) for a test with a rice column moving over an erodible layer made of pasta grains. The horizontal surface of the erodible layer is shown together with the velocity vectors as from PIV-particle image velocimetry.

4.5.3.3 *Numerical results*

Horizontal channel

To validate the model and to extend the analysis to materials with different shear strength, we modelled the collapse of a granular column with fixed aspect ratio ($a = 3.2$) and variable friction angle and thickness of the erodible layer. The internal friction angle of the basal erodible layer was varied between 10 and 30 degrees, with a thickness of 0.2 and 0.5 m for an initial column height of 0.6 m.

Figure 4.5.15 presents the results of some of the performed simulations. In the case of an erodible layer characterized by a low internal friction angle (10 degrees) the front of the advancing material is thinner than for the case of spreading on a hard smooth frictional surface. Initially, the collapsing material sinks within the erodible bed, without evident differences for the different layer thicknesses (2 or 5 cm), and successively it slightly runs up and over the material removed from the erodible layer and pushed at the flow front.

Sinking and ploughing tend to disappear with increasing internal friction angle values. For a 30 degrees material no sinking and erosion are observed and no material is pushed in the front (Figure 4.5.15). A major difference is also represented by the evolution of the interface between static and flowing material. No migration of the interface is observed for the case of a basal layer with low values of internal friction angle. On the contrary, the migration of the interface is observed when no scouring and ploughing occurs along a layer characterized by higher friction angles.

Finally, we observe that the maximum velocity in the moving mass always occurs between 0.2 – 0.3 sec and progressively decreases with time. The maximum velocity is higher for the case of higher internal friction angle even if the motion stops earlier than for the cases with lower friction (see Figure 4.5.16). This is probably the result of the minimized or null sinking, entrainment and material plowing by the moving mass. On the contrary, we observe that the increase in the internal friction angle of the erodible layer causes a decrease in the final runout, and the formation of a slightly thicker toe of the deposit.

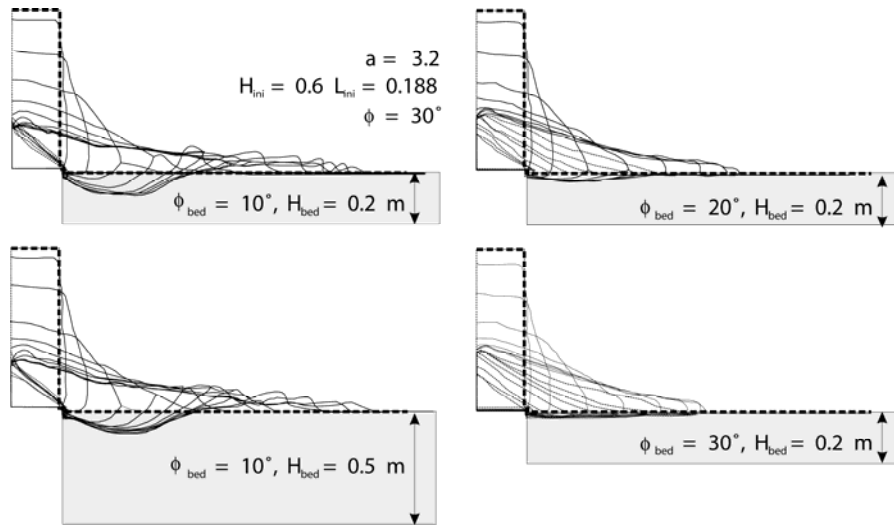


Figure 4.5.15 - Results of the numerical models for the collapse of a granular step ($H_{ini} = 0.6\text{ m}$; $L_{ini} = 0.188\text{ m}$; $a = 3.2$, see Table 1) including the presence of an erodible basal layer (light grey). The layer thickness and internal friction angle have been varied. Time step between each profile is 0.1 sec. The interface between static and moving material is also represented for each instantaneous profile. A completely different behavior is observed for the interface when a low shear strength basal layer is simulated: no deposition is simulated along the interface and no increase in static sector is observed till final arrest.

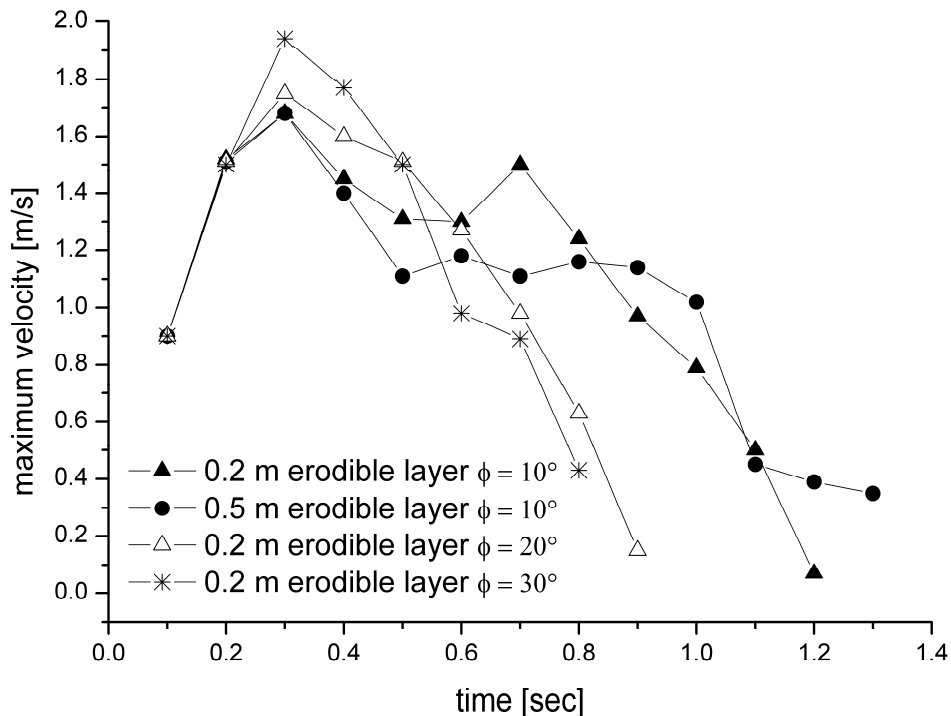


Figure 4.5.16 – Values of the maximum velocity computed for the collapse of a granular step on an erodible layer (see Figure 4.5.13 and Table 1) with different thickness and internal friction angle.

Inclined channel

As stated in the introduction, entrainment is commonly associated with granular flows in different environments with variable conditions. Debris flows, rock and debris avalanches can travel along rocky non erodible surfaces or along talus slopes made of loose material deposited, with a specific thickness, at or close to the angle of repose.

In the following we present some results of numerical simulations performed by releasing instantaneously a column of material according to the geometry shown in Figure 4.5.17 (a and b: with rigid channel bed; c: with erodible layer along the channel; d: comparison).

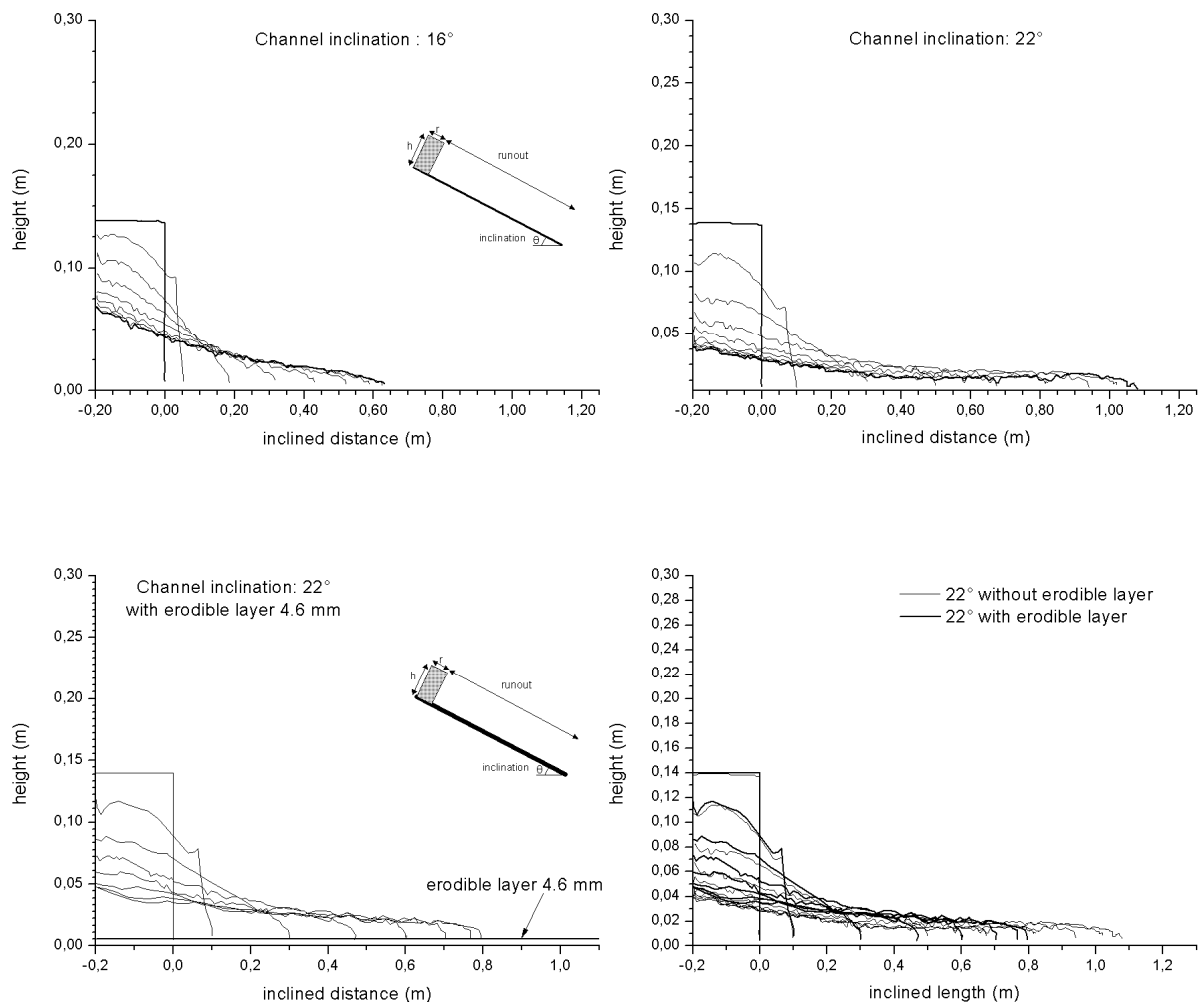


Figure 4.5.17 - Evolution of the material profile for 3 different simulations: a) and b) channel with a rigid base inclined at 16° and 22°, respectively; c) channel covered by a 4.6 mm erodible layer. d) compares the profiles for the two simulations at 22° with and without erodible layer. Time interval is 0.12 s.

Simulations have been run along channels both horizontal and inclined at 10°, 16° and 22°. The material has been modelled as a Mohr-Coulomb material characterized by a friction angle of 26° and a very low cohesion variable between 0 and 24 Pa for channels inclined from 0 up to 22°. In any case this value is quite low when considered for example against the initial vertical stress at the base of the column (e.g. for the case of an horizontal plane equals 1300 Pa). One more series of simulations has been run by considering the presence of a 4.6 mm thick erodible layer placed directly on a smooth channel surface.

The profile evolution for the two cases with channel inclination equals to 16° and 22° is reported in Figure 4.5.17 at successive time steps (time interval = 0.12 s). The profiles are plotted at the same scale, but with a vertical exaggeration to evidence the profile geometry. The case for a 22° channel inclination clearly shows the presence of a blunt front, with the maximum elevation of the frontal sector reached at a distance from the front equal to 15% of the total runout length. Behind this point elevation is progressively decreasing up to a distance equal to about 55% of the runout from the front. From this point the deposit thickness increases progressively up to the maximum value against the uphill side of the column position.

Evolution of the flow for different channel inclinations with time is shown in Figure 4.5.18 and 4.5.19. Inclination is affecting both the maximum velocity and the duration of the flow. Maximum runout distance increases by 5 times passing from a 0° to 22° inclination, while maximum velocity increases of about 30% and total duration doubles. The evolution of the column collapse can be followed through the maximum height values computed at the uphill boundary of the column.

Finally, the quality of the results is checked against experimental data collected by *Lube* [2006] and *Mangeney et al.* [in press] with slightly different settings (vertical column adopted by *Lube* [2006], or column normal to the channel base, *Mangeney et al.* [in print]). By comparing the numerical results with those from these sets of experiments an almost perfect coincidence occurs with the dataset by *Mangeney et al.*, whereas some differences are evident with *Lube* dataset as shown in Figure 4.5.21.

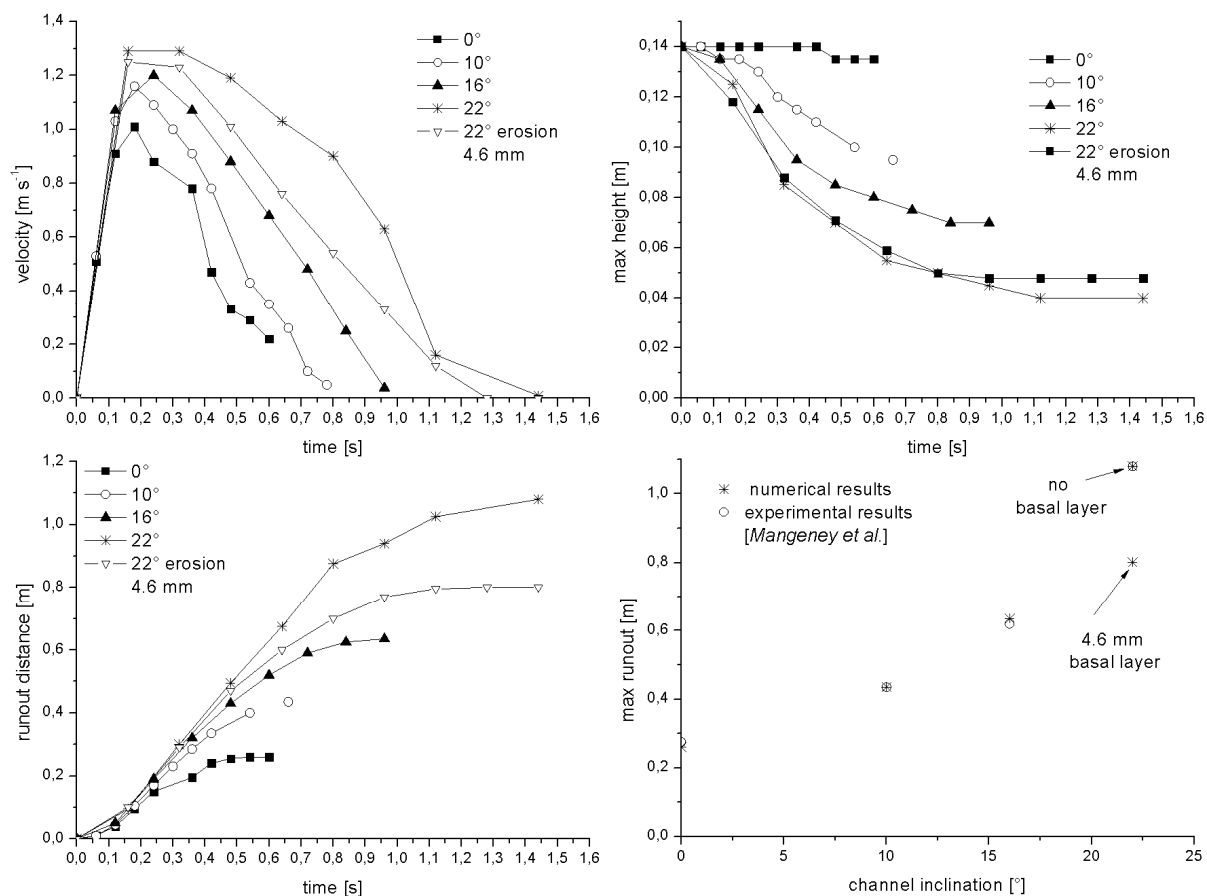


Figure 4.5.18 - Evolution of the front velocity and position with time (a, c) and b) of maximum height of the material (at the left hand boundary of the model. d) Lower right hand plot shows the maximum runout distance with respect to channel inclination. Test results for the 22° inclined channel are shown both for simulation with and without basal erodible layer (4.6 mm in thickness).

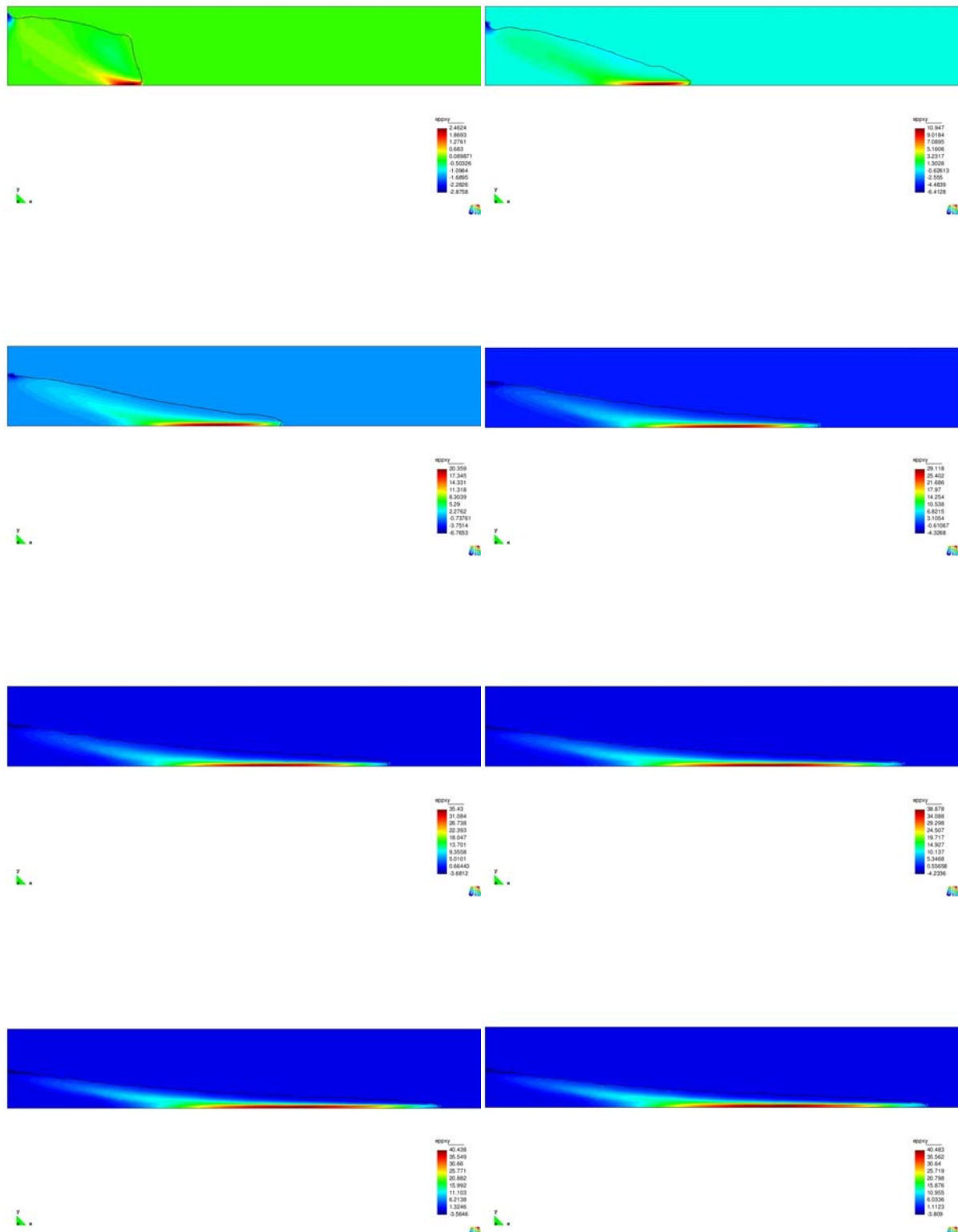


Figure 4.5.19a - Plastic strain distribution for a simulation of a column collapse with $a = 0.7$ along a 16° inclined channel with no erodible layer (time interval = 0.12 s).

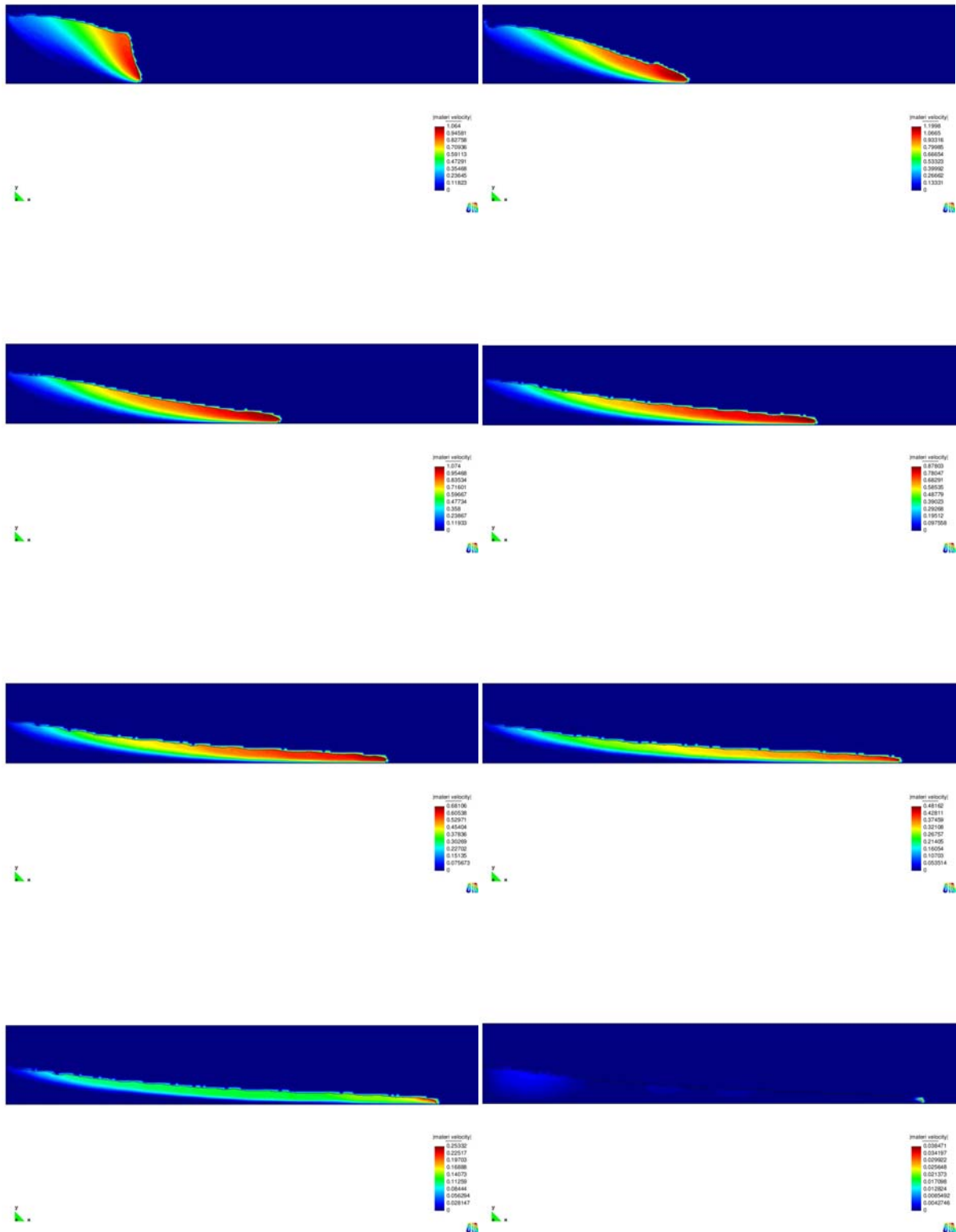


Figure 4.5.19b - Velocity distribution for a simulation of a column collapse with $a = 0.7$ along a 16° inclined channel with no erodible layer (time interval = 0.12 s).

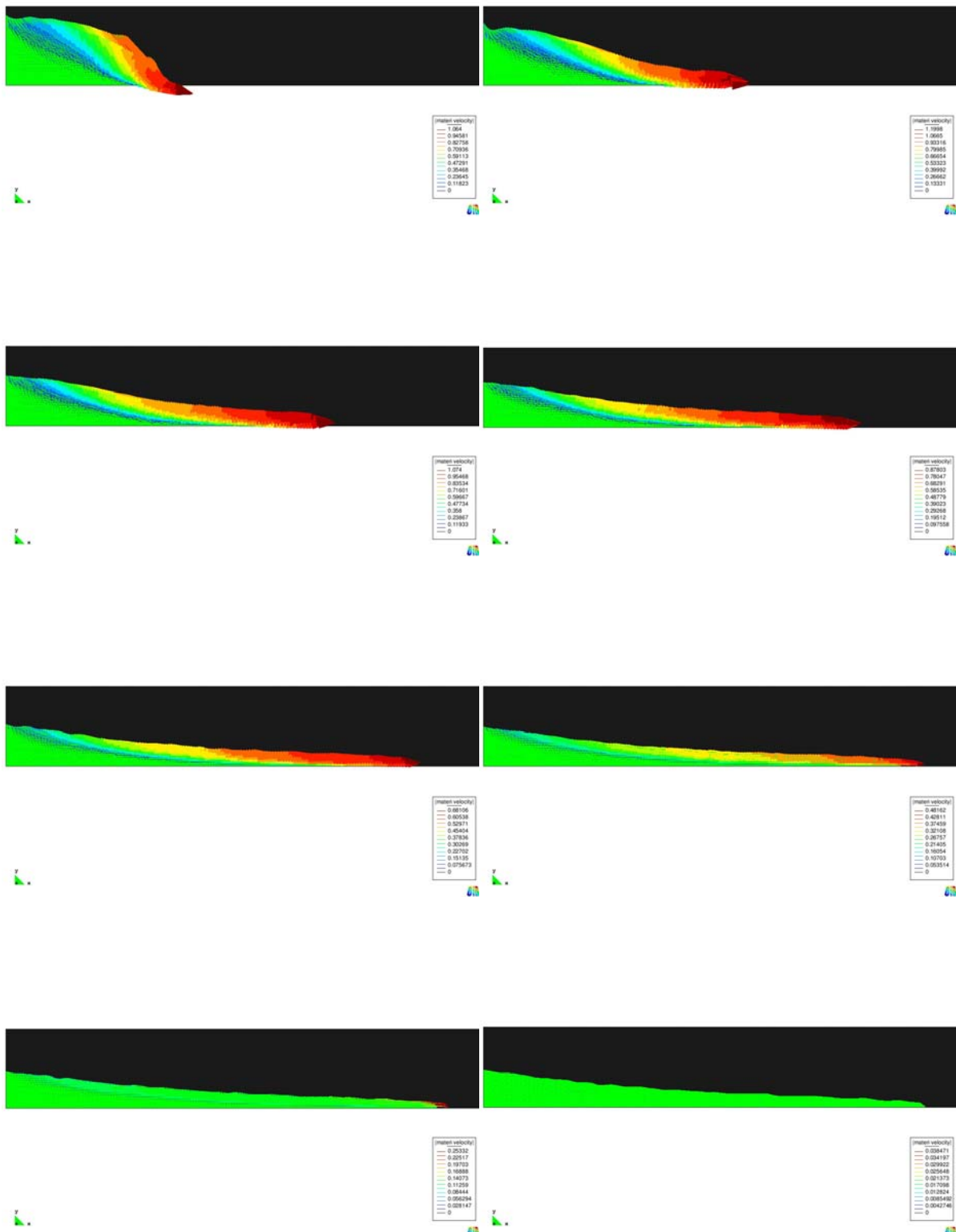


Figure 4.5.19c - Velocity vectors for a simulation of a column collapse with $a = 0.7$ along a 16° inclined channel with no erodible layer (time interval = 0.16 s).

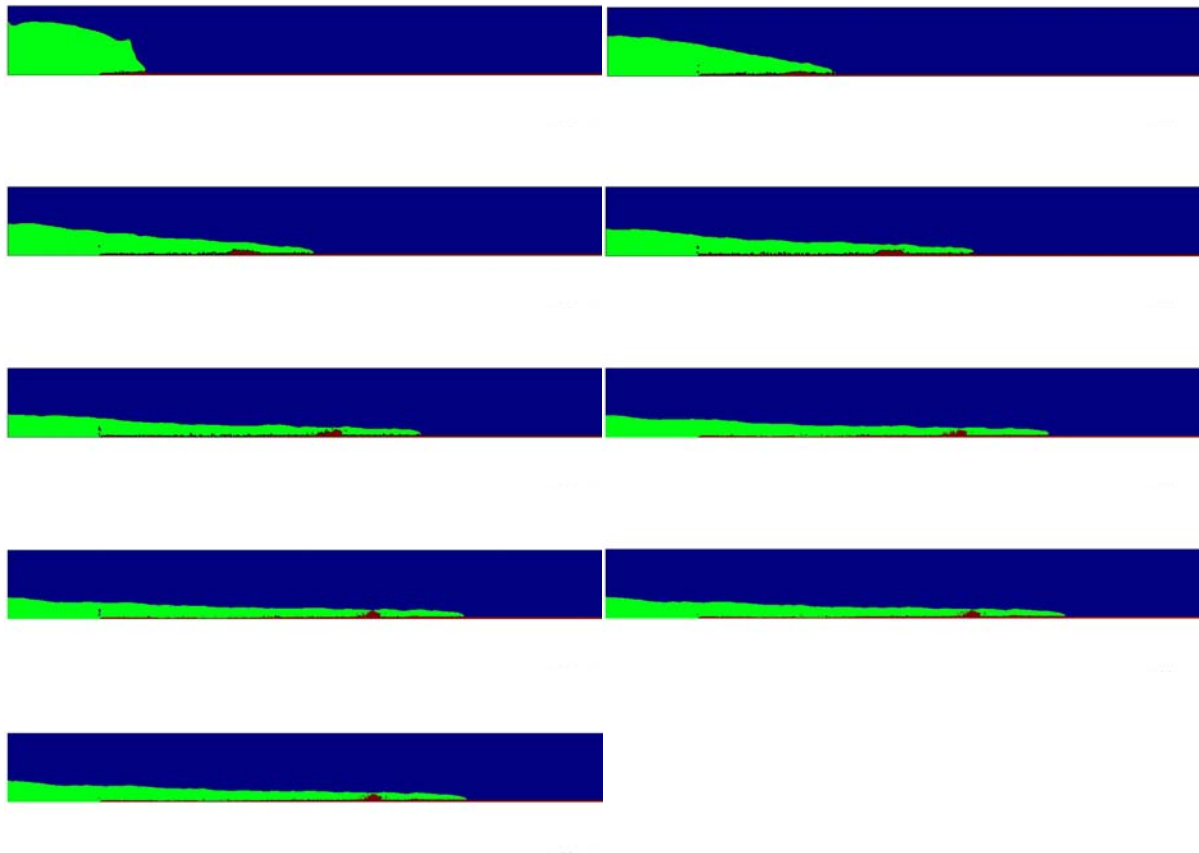


Figure 4.5.19d - Collapsing column and erodible bed material for a simulation of a column collapse with $a = 0.7$ along a 22° inclined channel with a 4.6 mm thick erodible layer (time interval = 0.16 s). A progressive change in the erosion depth is visible in the initial steps together with the formation of a small wave of eroded material which is dragged behind the front.

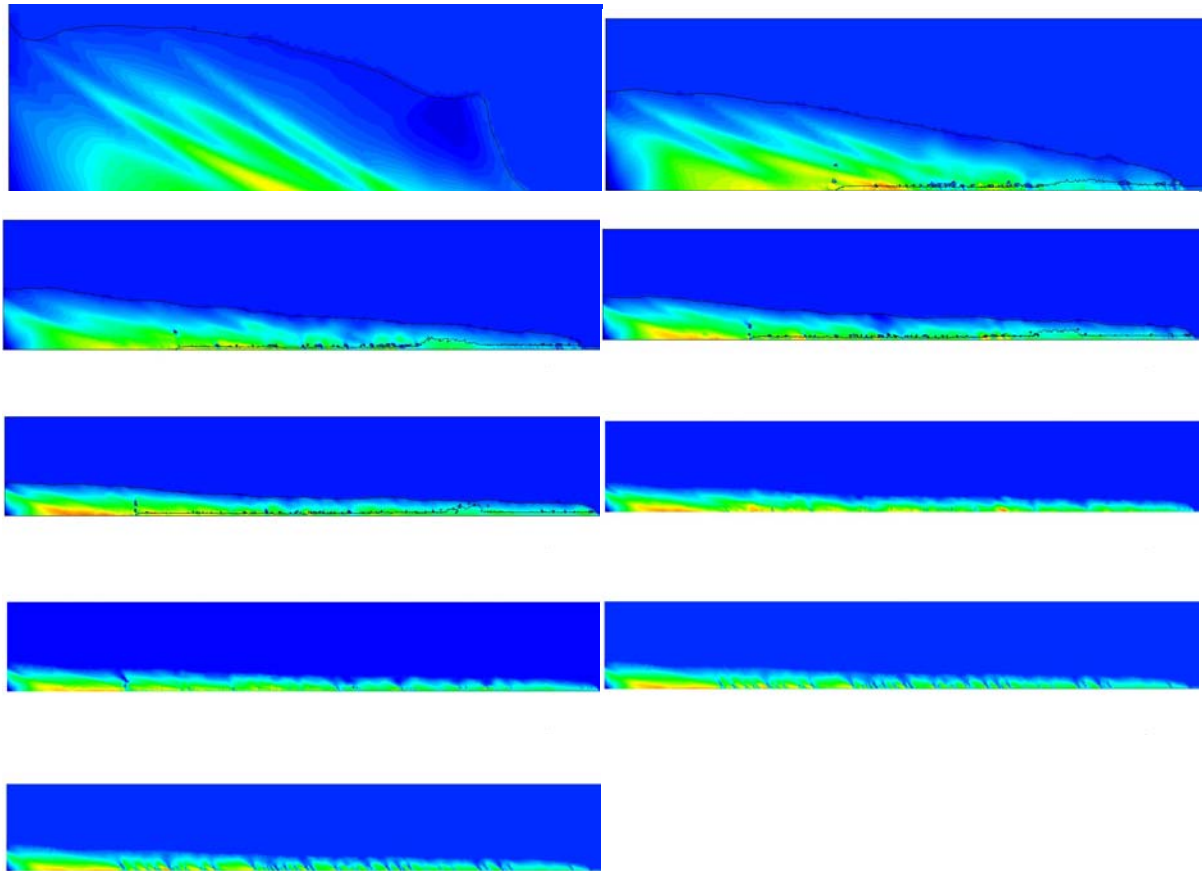


Figure 4.5.19e - Shear stress distribution for a simulation of a column collapse with $a = 0.7$ along a 22° inclined channel with a 4.6 mm thick erodible layer (time interval = 0.16 s). The development of multiple shear bands is evidenced in the initial steps but their increase in number and successive evolution is visible till the arrest of the flow.

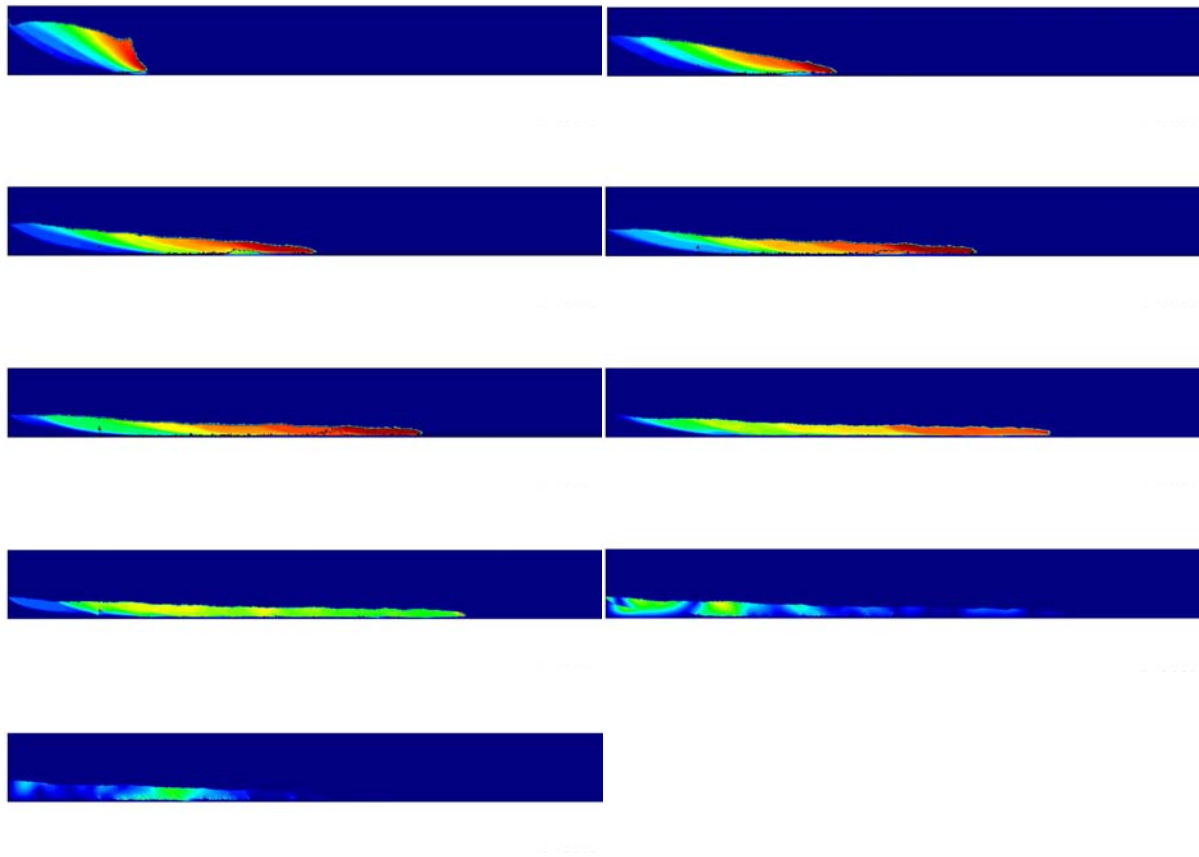


Figure 4.5 - 18f: Velocity field for a simulation of a column collapse with $a = 0.7$ along a 22° inclined channel with a 4.6 mm thick erodible layer (time interval = 0.16 s).

The case of a channel covered by a thin erodible layer and inclined at an angle close to the repose angle of the granular material could simulate some natural condition for a flow over a previously deposited thin layer of material. In the Figure 4.5.19 and 4.5.20, the erosion is shown to occur along the layer. At the beginning the erosion depth is close to the layer thickness but decreases progressively toward the front as this moves forward. This decrease together with the dragging of the eroded material along the interface between the falling mass and the erodible layer, generates a sort of wave along the interface which slowly moves forward. This seems to simulate the experimental observations made by *Mangeney et al.* [in print].

On the other hand, we observe a clear difference between the numerical results and the experimental ones obtained by *Mangeney et al.* [in print] (see Figure 4.5.21). By running the simulation with the same set of properties we obtain a much shorter runout, shorter than for the case of smooth channel. On the contrary, *Mangeney et al.* observed a longer runout with a slightly slower motion. This experimental behaviour is more similar to the case for a granular material for which cohesion is completely eliminated. We suppose that this change in behavior could be ascribed to the fact that the basal channel surface in the experiments has been prepared by gluing a layer of sand grains which can confer a roughness effect not simulated through the friction coefficient assigned at the channel surface. This roughness allows for a steeper angle of repose of the material with respect to the one that can exist on a smooth surface causing arrest of the material in a metastable condition.

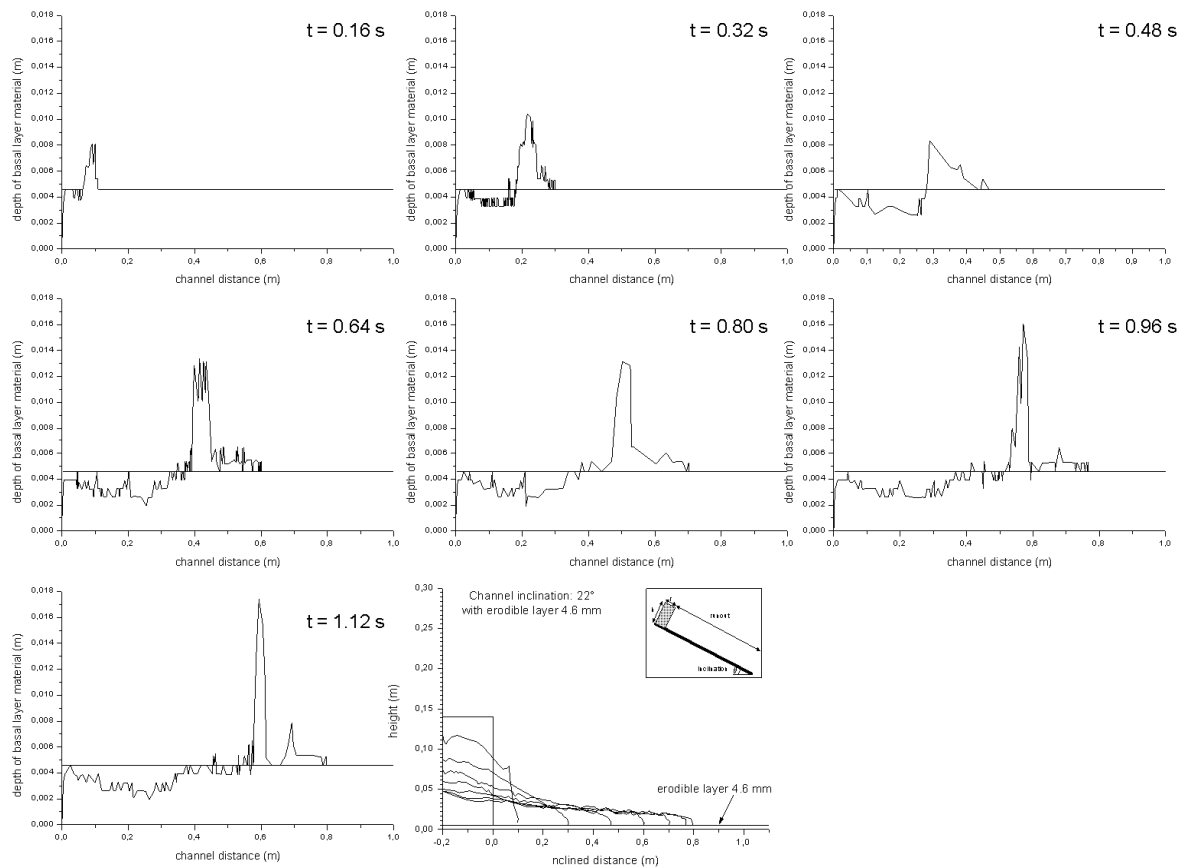


Figure 4.5.20 – Numerical results showing the change in geometry of the interface between released mass (from column collapse) and erodible layer along the channel. The propagation of a wave-like perturbation is shown in terms of position along the channel and elevation of the interface, After 0.64 s since the beginning of motion the distance between the front position and the wave remains roughly constant.

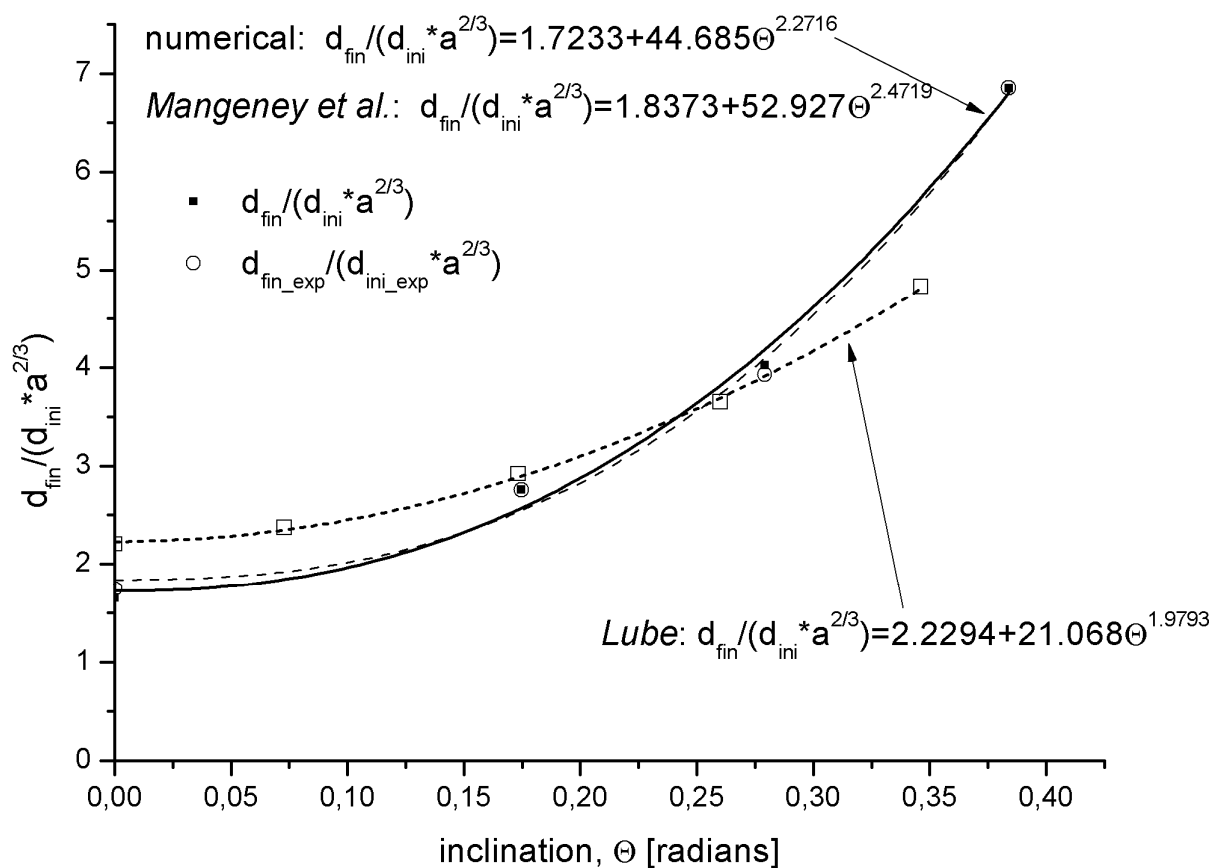


Figure 4.5.21 - Comparison of numerical and experimental results [Mangeney et al., in press; Lube, 2006] in terms of normalized runout vs channel inclination (Θ). Numerical and experimental tests by Mangeney et al. have the same geometry (column normal to the base of the channel, see Figure 4.5.2c) whereas tests by Lube have been performed by using a vertical column (see Figure 4.5.2d).

4.5.4 Arvel case study

4.5.4.1 Description

The Arvel landslide [March 14, 1922, Canton Vaud, Switzerland, *Choffat*, 1929; *Jaboyedoff*, 2003; *Locat et al.*, 2006; *Crosta et al.*, 2008 a, b; Figure 4.5.22] occurred as a single and rapid failure affecting a 120 m high steep rocky cliff of a limestone quarry (brecciated oolitic limestone, black fossiliferous marl and a weak grey limestone). The rockfall/rock-avalanche was characterized by a simple geometry, a steep source and a flat propagation, erosion and deposition areas which were occupied by alluvial deposits (gravelly silt, sand and peat). The alluvial deposits were characterized by a water table located few metres below the surface. The landslide deposit (614,000 m³), 6 to 24 m in thickness, included blocks up to 8,000 m³ immersed in a finer matrix. Folding and faulting of the alluvial deposits were observed on an area of about 8 hectares and up to 340 m beyond the front of the landslide deposit. The upper scarp is narrower than the rest of the detachment zone and the deposit has a fan like geometry. This geometry introduces a certain 3D effect in material redistribution. The maximum horizontal distance, from the top of the main scarp to the tip of the deposit, and the total maximum drop height were about 337 m and 240 m, respectively. A *fahrboschung* (i.e. the angle between the horizontal and the line connecting the upper point of the main scarp with the most distal point of the deposit) of 35.5 degrees has been computed for the landslide but a value of 19.5 degrees is obtained by considering the displacement of the disturbed alluvial deposits. The general setting of the event resembles that of the collapse of a granular step, with aspect ratio of about 3.2, with spreading along a flat horizontal surface made of an erodible material. To verify the similarities between the small scale and large scale collapse behaviours, and the capabilities of the approach for hazard assessment, we ran 2D simulations along a longitudinal profile used by *Choffat* [1929, see Figure 4.5.22] to represent field observations. We assumed a maximum thickness of 30 m for the alluvial deposits and the adopted properties are summarized in Table II. The role of the presence of water within the alluvial deposits and of the excess pore pressures induced by the impact of the rock fall have been examined in *Crosta et al.* [2008] and are summarized in the following.

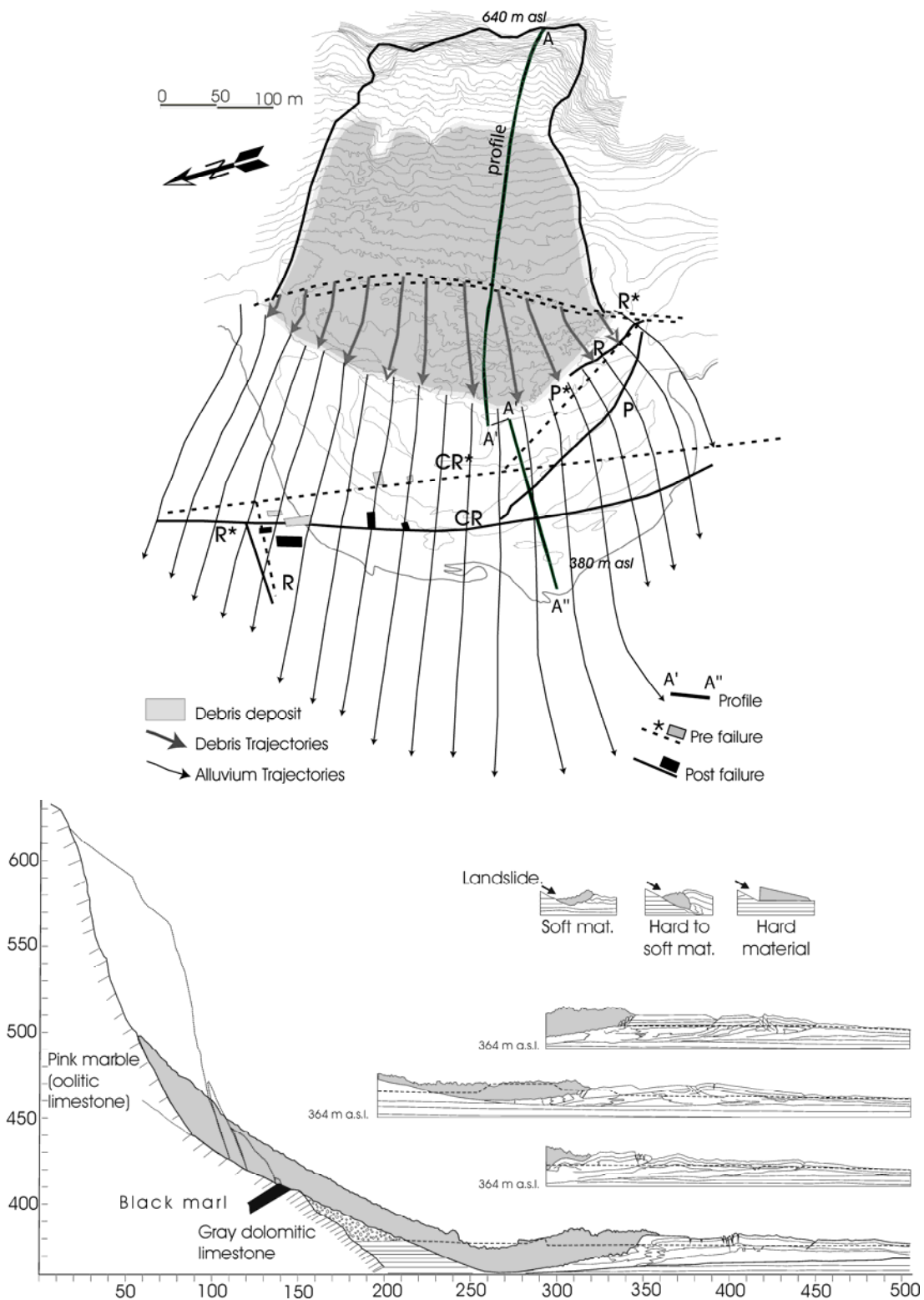


Figure 4.5.22 - Plain view and longitudinal cross section as from data presented by Choffat [1929]. A series of sub-profiles with different orientations is shown in the lower figure

	γ kN/m ³	E GPa	ν	t_c kPa	ϕ_i °	ψ °	c_i kPa	ϕ_p °	ψ_p °	c_p kPa	Rf	Kh ms ⁻¹	Kv
A) Dry alluvial deposits													
slide			0,2	0,0									
mass	19,62	100	3	1	38	0	50	33	0	50	0,5	0,0	0,0
alluvial			0,2	0,0									
deposits	15,07	6	3	1	20	0	50	20	0	50	0,0	0,0	0,0
B) Saturated alluvial deposits													
slide			0,2	0,0									
mass	19,62	100	3	1	38	0	50	33	0	30	0,5	0,0	0,0
alluvial			0,2	0,0									
deposits	17,70	6	3	1	20	0	50	20	0	30	1,0	0,1	0,1
C) Saturated alluvial deposits													
slide			0,2	0,0									
mass	19,62	100	3	1	38	0	50	33	0	30	1,0	0,0	0,0
alluvial			0,2	0,0									
deposits	17,70	6	3	1	20	0	30	20	0	30	1,0	0,1	0,1

Table II – Summary of the properties adopted in the modelling for landslide mass and alluvial deposit materials of the Arvel event. In Model A the alluvial deposits are dry whereas in Models B and C are saturated.

4.5.4.2 Numerical results

The landslide mass moves with regularity along the failure surface. Almost no erosion is observed along the talus slope located immediately at the toe of the rocky cliff. Erosion starts when the dry alluvial deposit is encountered (Figure 4.5.22). The thin layer of eroded alluvial material is pushed with an almost vertical front. Subsequently it is folded over and overcome by the landslide debris (Figure 4.5.23). A rapid decrease in the velocity of the landslide mass is observed at the impact against the alluvial material and this causes an evident slowing down of the rear part of the mass. Finally, the slide debris moves on the ploughed alluvial material with a sub-horizontal contact, 30 to 40 metres long, while a slight rotational instability occurs at the front. Velocity distribution within the landslide and eroded materials has been analyzed in more detail by *Crosta et al.* [2008a]. The motion lasts for about 20 seconds (Figure 4.5.23). The main differences that can be recognized with respect to

Choffat's profile (Figures 4.5.24) are in the position of the rear limit along the slope and in the thickness of the final deposit. These can be controlled by the three dimensional effects or out of plane spreading of the real landslide deposit (Figure 4.5.22) that is not considered in our set of two dimensional simulations. Eventually, the back of the final deposit passes the rear limit mapped by Choffat suggesting a too high energy of the material in this sector when the front comes to rest. This could be partly the result of lack of third dimension in the model.

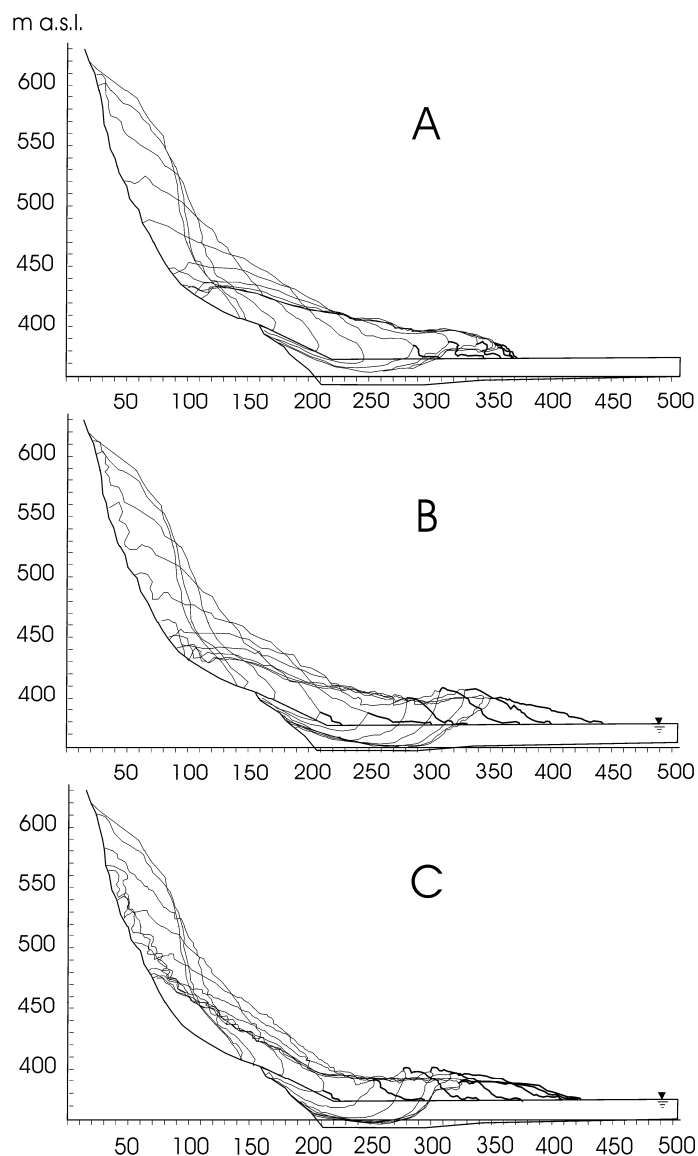


Figure 4.5.23 - Results for simulations adopting different properties and conditions (Models A, B and C as in Table II). Profile of the moving mass is shown every 2 seconds since the movement onset. Contact of the landslide mass with the alluvial deposits is shown together with plowed deposits at the front.

4.5.4.3 Results

The numerical simulations are discussed starting from the results of three different models (see Table II):

A) assuming dry materials (both for the landslide and alluvial deposits) with higher cohesion with respect to Model B and C.

B and C) consider saturated conditions for the alluvial deposits with strength parameters in Model B reduced (by a reduction factor, see Table II) to half their initial values.

Model A – Landslide mass moves with regularity along the failure surface and little erosion is observed along the talus slope immediately at the toe of the rocky cliff. Erosion starts when the mass reaches the dry alluvial deposits (Figures 4.5.23a and 4.5.24). A thin layer of eroded alluvial material is pushed at the front with an almost vertical boundary and is it successively folded over and overcome by the landslide debris. A rapid decrease in the velocity of the landslide mass is observed at the impact against the alluvial material causing an evident deceleration of the tail of the mass. Eventually, the slide debris moves on the ploughed alluvial material with a sub-horizontal contact.

Model B – No relevant talus erosion is observed at the toe of the rocky cliff. The landslide debris sinks in the alluvial deposits while advancing (Figures 4.5.23b and 4.5.24). As a consequence, the debris front is curved and it climbs up becoming sub-vertical at the upper extreme with alluvial material pushed at the front. The contact between landslide debris and alluvial deposits becomes progressively less steep up to reaching a 35° inclination. The front in the alluvial deposits develops in length becoming regularly inclined after having been steeply curved (convex).

A slight instability of the front is observed with a sub-circular velocity distribution. The pore pressure increases rapidly when the debris reaches the alluvial deposits to become controlled eventually by the thickness of the accumulation.

Model C – A different pattern of the velocity in the failing mass is observed in this model, being the velocity in the upper part of the moving mass much higher than in the lower half. This contrast seems the result of the higher and constant resistance mobilized along the failure surface. Differently from the previous models, erosion starts already along the talus slope.

Then, the landslide material plunges into the alluvial deposits with a relatively steep (ca. 65°) contact between landslide debris and alluvial deposits (Figures 4.5.23c and 4.5.24). The debris front is steep whereas that of the alluvial deposits is convex and maintains its shape till the final arrest. The tip of the landslide debris becomes thin and elongated over the ploughed alluvial deposits whereas the alluvial deposits are inclined at about 20°.

Pore pressures increase rapidly at the arrival of the landslide mass over the alluvial deposits but the increase is a lower than observed in model B. Again a small instability along a sub-circular failure surface can be recognized by looking at the velocity distribution.

The landslide geometry is represented in Figures 4.5.23 and 4.5.24, whereas the plot in Figure 4.5.25 is showing the distribution of some points that describe the geometry of the deposit for the 3 different simulations. In the figure we plotted: the position of the tail and of the extreme tip of the deposit, inclusive of the plowed alluvial deposits, the maximum elevation of the deposit, the minimum elevation of the base of landslide deposit.

By comparing the final geometries (Figures 4.5.24 and 4.5.25) with the geometry observed by *Choffat* we note that for:

Model A) the landslide mass remains relatively compact with a surface characterized by a regular slope. The tail reaches the lowest elevation and the front the shortest distance. The maximum erosion depth is the lowest among the values from the different models.

Model B) the deposit is thick but the upper surface is concave; it shows a good agreement with field observations in terms of erosion, maximum debris distance and longer alluvial deposit remobilization.

Model C) the mass is a little bit more elongated (e.g. shortest tail distance and highest elevation), the general upper surface is concave but the farthest half of it is almost sub-horizontal and aligned with the surface of the ploughed alluvial deposits. In general, the model performance is relatively similar to Model B even if the resulting geometry is different. This model results in the best fit of the geometry of the rear half the landslide both in terms of thickness and distances. We note that in the upper part of the profile the 3D effects seem less important than in the frontal part, because of the progressive transversal spreading of the mass.

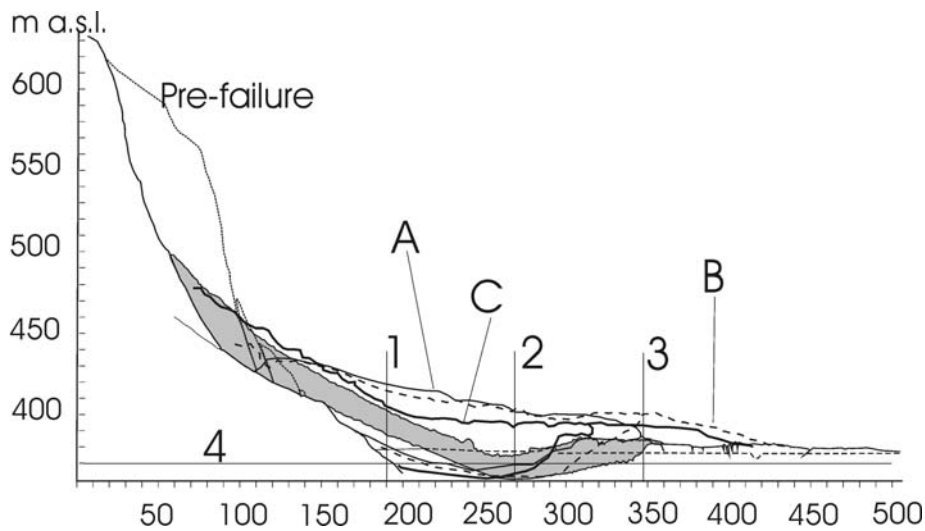


Figure 4.5.24 - Longitudinal cross section along the same profiles as in Figure 4.5.22, with the final profile obtained by the three numerical simulations: A) dry materials; B) saturated alluvial deposits and strength parameters reduced after onset; C) as in B) with no strength reduction.

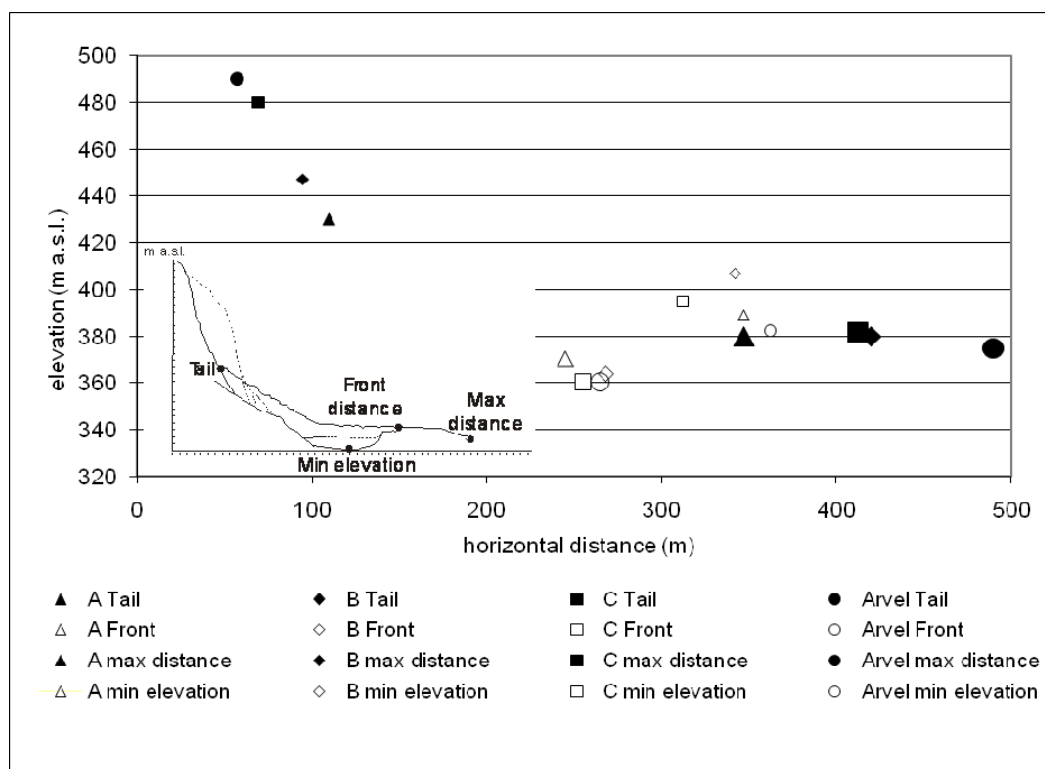


Figure 4.5.25 – Plot of some of the relevant points that describe the geometry of the real deposit and for different simulations (Model A, B and C from Table I): 1) position of the tail of the deposit, 2) position of the extreme tip of the deposit including the plowed alluvial deposits, 3) maximum distance of the front in the alluvial deposit, 4) minimum elevation at the base of landslide deposit.

4.5.4.4 Velocity profiles

To analyse the results of the 3 models, we sampled velocity and pore pressure distribution along three vertical profiles, at different distances from the upper scarp (190 m, 269 m and 346 m), and one horizontal profile placed at 370 m a.s.l. (Figures 4.5.26a, b and c).

Maximum velocity is observed for all the simulations at the toe of the rocky cliff and along the initial part of the alluvial deposits. Model B reaches a maximum velocity of about 25.7 m s⁻¹ followed by Model A with 25.3 m s⁻¹ and Model C with 24.3 m s⁻¹. This is shown by velocity plots along the horizontal section at 370 m a.s.l..

In all the simulations we observe a rapid freezing of the moving mass and a final pattern of the velocities showing a sub-circular front instability. This seems comparable with field observations of secondary slope instabilities within the landslide deposit.

The thickness of the involved alluvial material is evidenced in the velocity plots. Model C presents the lowest material thickness and a strong vertical downward component (y) of velocity close to the slope toe (e.g. at cross section 1, 190 m from the upper scarp, see Figures 4.5.24 and 4.5.25). Maximum y-velocity values occur for Model B where a 50% reduction of the resistance is imposed, followed by Model A (dry alluvial deposits) and then Model C. The velocity plots show that the moving mass is sheared at its interior and that in the later stages tends to move “rigidly” shearing at the contact with the alluvial mattress.

The evolution of the pore pressures within the alluvial material is also shown. Model B is characterised by the high pore pressures for longer times with respect to Model C. The induced increase in pore pressure moves at/with the front of the displaced material and it lasts longer than the landslide duration, being slightly controlled by the final deposit geometry.

4.5.4.5 Comments to Arvel simulations

From the performed simulations we observe that:

- the characteristics of materials that can be entrained strongly control the evolution of rock and debris avalanches; in fact, both the initial impact and the temporary, and final geometry of the landslide debris/alluvial deposit contact surface, change with material properties (or assumed conditions);

- undrained loading plays a relevant role but it is not limited at the debris-alluvial deposits interface and its effect in increasing mobility is counteracted by the erodibility of the alluvial deposits;
- both velocity and thickness of the entrained/pushed materials increase with saturation;
- different behaviours should be expected as a function of depth of alluvial/erodible deposits, volume of the rock avalanche, degree of saturation, mechanical and hydraulic properties;
- different modes of material entrainment have been observed in the field and have been replicated by simulation; in fact, the formation of both wedges and folds of alluvial debris by the bulldozing effect at the front of the rock avalanche material, the basal dragging, and a partial mixing at the front have been simulated. Mixing can induce further changes in behaviour.
- in presence of saturated sediments the erosive process is more intense, the runout is longer and the deformation of alluvial deposits moves farther to the front of the rock-fall-avalanche debris. The excess pore pressures generated within the alluvial deposits, and computed by considering volumetric compression, moves rapidly in the front of the moving landslide mass.

Models B and C give the best result at fitting the observed geometry of the landslide deposit and of the deformed alluvial sediments. Observed differences can result by neglecting the role of 3D effects and the local variability of alluvial properties. This 3D variability is also suggested by the 4 different profiles, presented by Choffat (see [Figure 4.5.22](#)), characterized by different deposit thickness, shape and deformation.

Crosta et al. (2006) show this features and behavior by some illustrative numerical models evidencing the occurrence of shallow erosion, local deposition and ploughing of impacted structures and/or obstacles (see [Figure 4.5.2](#)). We regard this as an interesting step forward in numerical modelling of such phenomena, where only depth averaged models are currently available with entrainment models based on empirical and semi-empirical laws without directly considering some physical and mechanical properties of the erodible substrate.

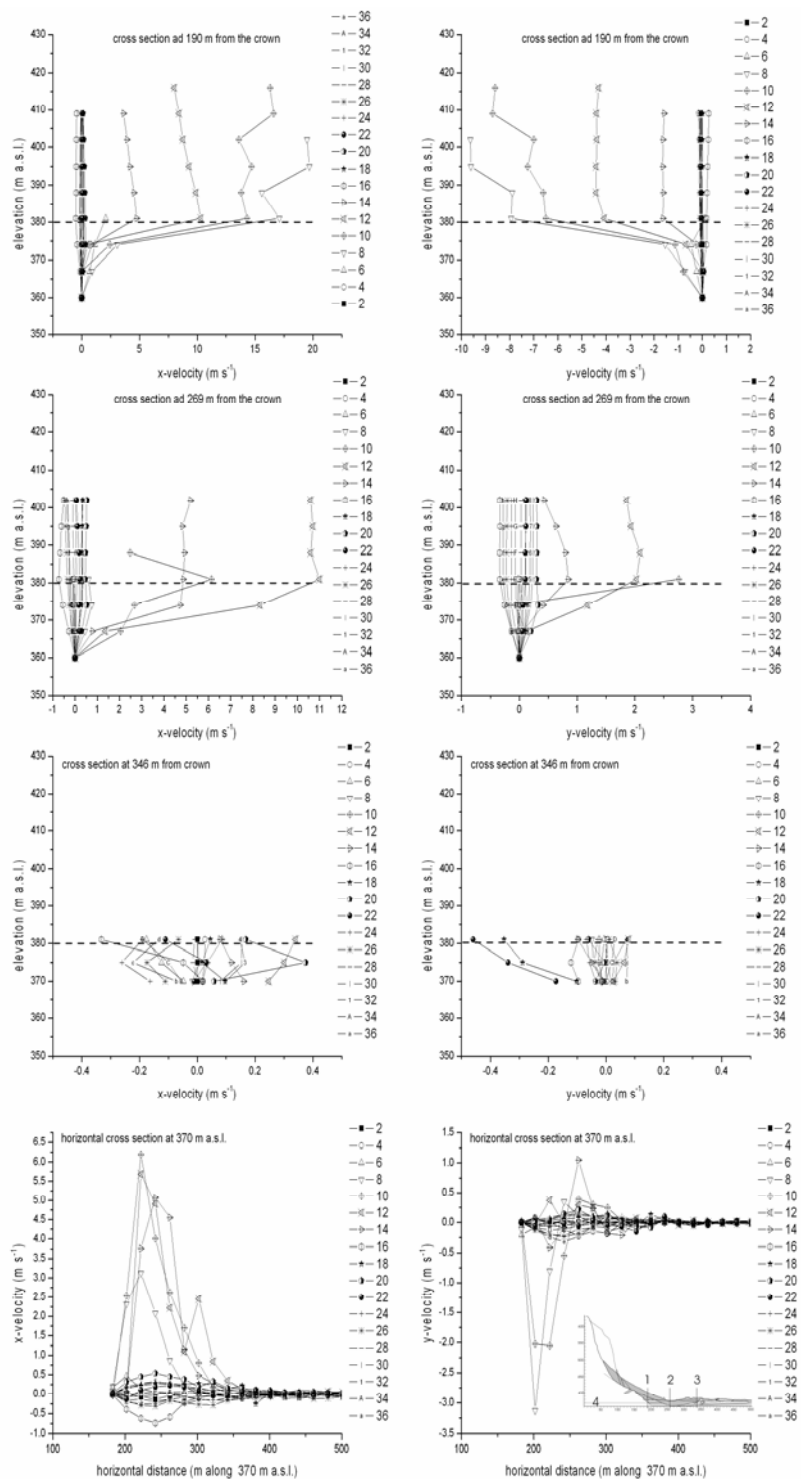


Figure 4.5.26a - Plots of x -velocity and y -velocity components (horizontal and vertical, respectively) for Model A measured at successive time steps (2 sec) along 3 different vertical profiles (# 1 to # 3 at distances of 190 m, 269 m and 346 m from the upper scarp, see Figure 4.5.24 and inset in the lower right plot) and 1 horizontal profile (# 4 at elevation of 370 m a.s.l.). Dashed lines represent the elevation of the alluvial plain before the event.

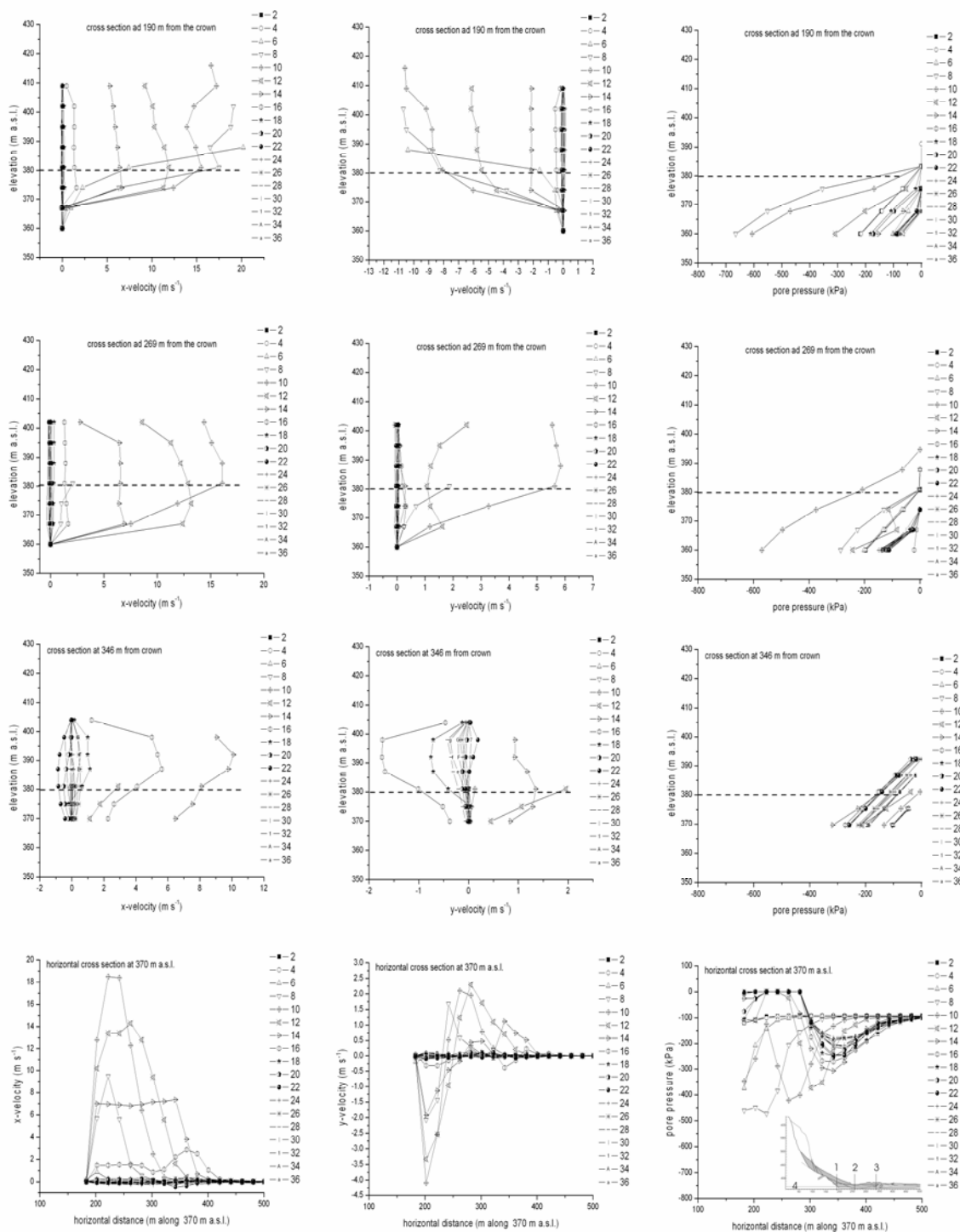


Figure 4.5.26b - Plots of the x -velocity and y -velocity components, and pore pressure for Model B measured at successive time steps (2 sec) along 3 different vertical profiles (# 1 to # 3 at distances of 190 m, 269 m and 346 m from the upper scarp, see Figure 4.5.24 and inset in the lower right plot) and 1 horizontal profile (# 4 at elevation of 370 m a.s.l.). Dashed lines represent the elevation of the alluvial plain before the event.

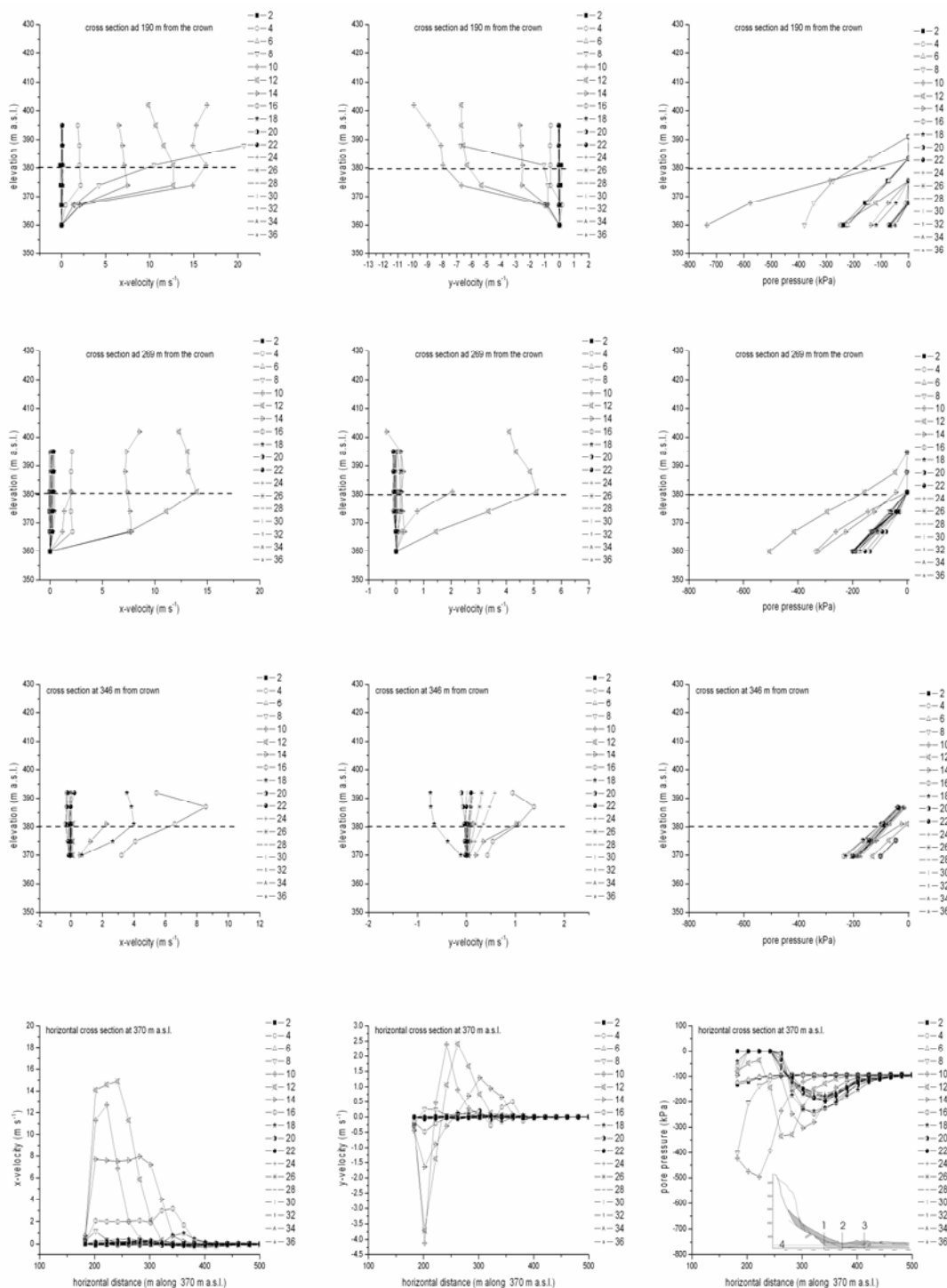


Figure 4.5.26 c - Plots of the x -velocity and y -velocity components, and pore pressure for Model C measured at successive time steps (2 sec) along 3 different vertical profiles (# 1 to # 3 at distances of 190 m, 269 m and 346 m from the upper scarp, see Figure 4.5.24 and inset in the lower right plot) and 1 horizontal profile (# 4 at elevation of 370 m a.s.l.). Dashed lines represent the elevation of the alluvial plain before the event.

4.5.5 Discussion and conclusions

Modelling of the granular step collapse along surfaces of different characteristics is considered important because of the detailed available data and the possibility to study both the evolution in time and space also at very low stress levels. At the same time in its simplicity the test considers the usually large initial drop height typical of many rapid landslides.

The numerical results from application of a continuum elasto-plastic approach are in very good agreement with experimental data. Our numerical scheme is conserving mass (change lower than 3.6%) and its accuracy has been assessed by running simulations with the same material geometry and a different element size. Failure occurs along a clear inclined plane. By increasing the aspect ratio most of the collapsing column moves in a vertical direction with a free fall behavior and only the more external and lower part of the material starts moving outward with a horizontal component.

We are able to simulate the failure along a clear inclined plane (Figure 4.5.5), the initial free fall behavior for high aspect ratios, the progressive increase in size of the static layer (see Figures 4.5.4, 4.5.7 and 4.5.27), the rotational failure mechanism and the progressive thinning of the moving mass as well as the erosion of a basal layer (Figures 4.5.7 and 4.5.17, 4.5.18, 4.5.19 d-f).

The final deposit profile (Figures 4.5.4a, b, c and d, 4.5.6 and 4.5.7) changes both with aspect ratio and internal friction angle. In particular a progressive increase of the aspect ratio causes a larger portion of the mass to move toward the flow front as evidenced in Figure 4.5.4d and observed in the performed experiments. This has also been shown by *Staron and Hinch* [2005] through discrete element modeling.

The validity of the adopted elasto-plastic behavior for the modeling of these types of processes is suggested by the simulations performed by maintaining the same geometry and dimensions of the laboratory tests as well as the physical –mechanical properties of the materials. Recently, *Bui et al.* [2008] successfully adopted elastic plastic constitutive models to simulate large deformation and failure flows through a meshfree particles method.

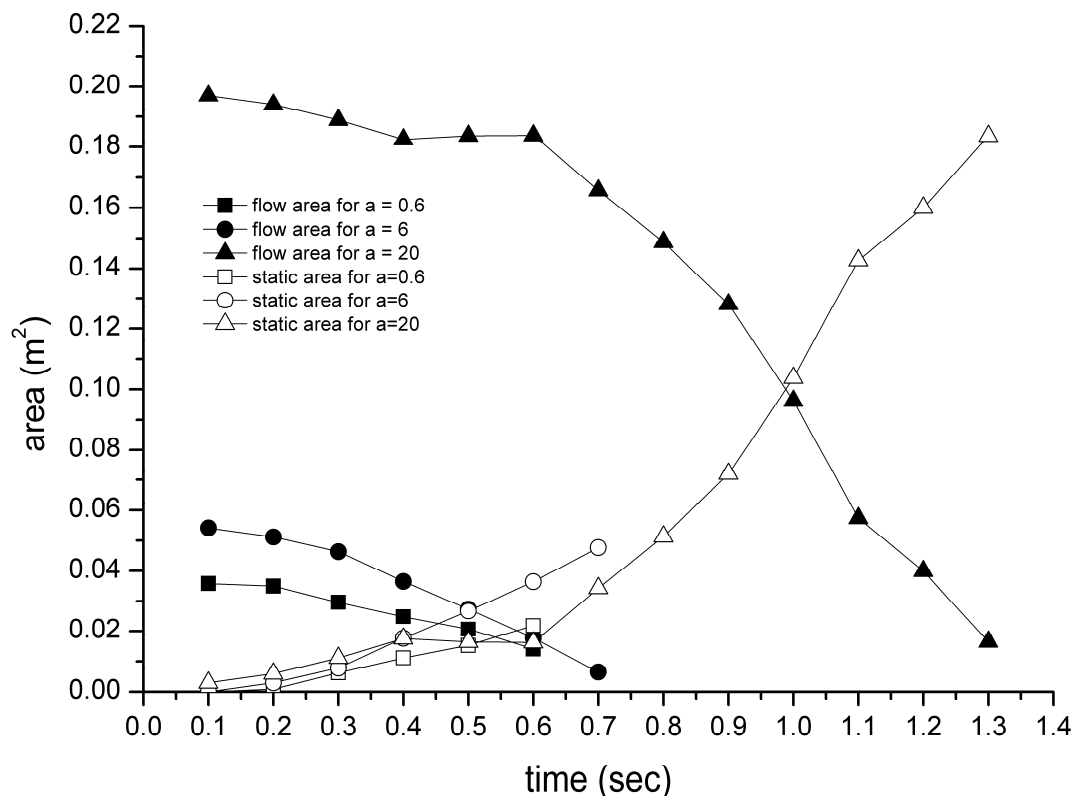


Figure 4.5.27 – Increase with time of the area of the static material (static area, in the legend), and decrease in area of flowing material (flow area) for the three simulations represented in Figure 4.5.4. The change in slope is progressively moved to the right with the increase in aspect ratio so with the duration of the free fall phase.

The general agreement in terms of geometry, pattern of velocity and position at different instants is quite good and have been compared in terms of normalized variables with original experimental data (Figure 4.5.8, 4.5.10) and those from *Lajeunesse et al.* [2004, 2005], *Balmforth and Kerswell* [2005] and *Lube* [2004, 2005]. The results confirm most of the scaling laws proposed by *Lube et al.* [2005], *Lajeunesse et al.* [2005] and *Balmforth and Kerswell* [2005] with slightly different values for the coefficients and exponents. This can be partly associated to the limited range of properties for the tested materials, the larger dispersion of experimental results for larger aspect ratios. On the other hand, the model cannot fully simulate the extreme tapering of the flow front (see Figures 4.5.4 and 4.5.6) observed in experimental tests with cohesionless materials. This can be partly controlled by the size of the adopted mesh size. Furthermore, dependence on material properties and

characteristics of the channel bottom (i.e. smooth, rough, erodible) are demonstrated by experimental results (Figure 4.5.13). At the same time blunt fronts have been observed in some experimental tests [e.g. see *Mangeney et al.*, in print]

Modeling results fit better to the experimental tests than those obtained by discrete element methods [DEM, Figure 4.5.8, *Staron and Hinch*, 2005 and *Zenit*, 2005] for the entire range of simulated aspect ratios. In fact, DEM results [*Staron and Hinch* 2005, *Zenit*, 2005] and the depth averaged models in the literature [e.g.: *Mangeney et al.*, 2004; *Balmforth and Kerswell*, 2005] predict much longer runout than those experimentally observed and the divergence in results increases with the aspect ratio (see for example Figure 4.5.8).

The results clearly show also the change in behavior with the aspect ratio observed in experiments and linked to the different column geometry and behavior in the initial collapse stage (Figures 4.5.4, 4.5.8, 4.5.9, 4.5.10, and 4.5.12).

A certain deviation in the results is observed for the normalized maximum final height of the deposit (see Figures 4.5.9a and b). In general we observe a lower value of final height for small aspect ratios. This could result by the differences in the experimental and numerical boundary conditions assumed along the vertical lateral limits of the model.

The main difference with respect to experimental tests in channeled conditions is represented in Figure 4.5.9b, where the non dimensional maximum deposit height is plotted with respect to a . The numerical model shows a slight deviation in trend for values of aspect ratio larger than 5-6 as for the experimental observations for axis-symmetric conditions [*Lajeunesse et al.*, 2004] even if at larger aspect ratios.

Results show a clear dependence on the adopted internal friction angle (Figures 4.5.6, 4.5.8, 4.5.9 and 4.5.10) but not on basal friction. The runout distance increases with the aspect ratio and it is inversely related to the friction angle (Figures 4.5.6 and 4.5.8). Furthermore, Figure 4.5.6 shows a slight change in the profile geometry with friction angle. In fact, for higher friction angles the profile is more clearly defined by two sectors at different slope, steeper close to the rear boundary.

By fitting the runout numerical results with a power law we obtain an exponent between 0.68 and 0.77 and a coefficient inversely related to friction angle (see Figure 4.5.8). The different

power law relationships between runout and aspect ratio, above a threshold value of $a \approx 4$, for different internal friction angles are:

$$25 \text{ degrees: } \Delta L/L_{ini} = 2.171a^{0.772} \quad (4.5.17a)$$

$$30 \text{ degrees: } \Delta L/L_{ini} = 2.04a^{0.682} \quad (4.5.17b)$$

$$40 \text{ degrees: } \Delta L/L_{ini} = 1.18a^{0.742} \quad (4.5.17c)$$

These results are in good agreement with the empirical relationships proposed in the literature [see eqs. 4.5.3a, 4.5.4a and 4.5.5a] and those obtained by fitting numerical results [see eq. 4.5.6a]. Exponent values are coincident (for internal friction angle = 30 degrees) and slightly higher than those by *Lube et al.* [2005] and *Lajeunesse et al.* [2005] and in any case well within the range of those by *Balmforth and Kerswell* [2005]. The numerical constant varies with friction as suggested by *Lajeunesse et al.* [2005] and by *Balmforth and Kerswell* [2005] and differently by *Lube et al.* [2005].

Numerical results concerning normalized maximum deposit height and flow duration confirm the relationships proposed by *Lube et al.* [2005; see eq. 4.5.4b and Figures 4.5.9a and b].

Figure 4.5.10b presents the best fit for the time for the flow front to cease motion with respect to aspect ratio. The best fit for results relative to simulations with material with a 30 degrees internal friction angle and different aspect ratios is equal to $3.8*a^{0.43}$. This agrees with the two relationships proposed by *Lube et al.* [2005; $3.3*a^{0.5}$] and *Balmforth and Kerswell* [2005; $3*a^{0.5}$].

Figure 4.5.10a for simulations with various aspect ratios and the comparison with experimental data [*Lajeunesse et al.*, 2005, *Lube et al.*, 2005] validate the fact that the column free fall time, τ_c , represents the characteristic time scale also for numerical tests as suggested in the cited literature. This is clearly demonstrated by the three motion phases developing in well determined normalized time intervals ($0.8 t/\tau_c$, $1.9 t/\tau_c$, $0.6 t/\tau_c$). We must mention anyway the problems in the definition of exact flow arrest time.

Velocity profiles at different locations and times are shown in figures 4.5.11 and 4.5.12. These profiles present an exponential lower sector with a rapid increase in velocity and a subsequent linear increment (Figure 4.5.11b) with a rigid plug behavior in the upper column (Figures 4.5.11a and b) and frontal (Figure 4.5.12b) flow sectors.

The general behavior changes considerably either in presence of a rough or of an erodible layer (Figures 4.5.13, 4.5.14 and 4.5.15) and especially as a function of the stiffness of the surface along which the runout occur.

In the case of an inclined rigid channel the model performs quite well. In fact, the results are in very good agreement with experimental observations. Computed runout is coincident with the results reported by *Mangeney et al.* (see Figure 4.5.21) as shown by the interpolating functions:

$$\text{Numerical results: } L_{\text{fin}}/(L_{\text{ini}}*a^{2/3}) = 1.723 + 44.685\Theta^{2.27} \quad (4.5.18a)$$

$$\text{Experimental results: } L_{\text{fin}}/(L_{\text{ini}}*a^{2/3}) = 1.837 + 52.927\Theta^{2.47} \quad [\text{Mangeney et al.}] \quad (4.5.18b)$$

where Θ represents the value of the channel inclination in radians.

On the contrary, the results do not agree with those presented by *Lube* [2006]. This can be attributed to the different release geometry (vertical against normal to channel). The best fitting for Lube data is represented by the following relationship:

$$\text{Experimental results: } L_{\text{fin}}/(L_{\text{ini}}*a^{2/3}) = 2.229 + 21.068\Theta^{1.98} \quad [\text{Lube, 2006}] \quad (4.5.19a)$$

which suggests that runout in this case is a little bit larger for low channel inclinations and the two curves cross each other for inclinations between 11.5° and 17° .

In case of an erodible layer some major differences are observed in the runout distance. This at least till the same set of physical mechanical parameters are adopted with a slight cohesion (a few Pascals) introduced to simulate the rigid channel experiments. In fact, runout increases considerably by eliminating the contribution of cohesion. On the other hand, some of the experimental flow features are reasonably simulated. This is the case of a wave-like motion of the interface between flowing and static erodible layer (Figure 4.5.20).

Laboratory tests are well reproduced by numerical simulations and this suggests the suitability of the model to simulate real case studies. The Arvel case study [*Choffat, 1929*] has been presented because of the geometrical similarities with the step collapse (i.e. very steep initial

motion of the entire mass; Figure 4.5.15) and the presence of a basal erodible layer. Furthermore, it presents a remarkable initial drop height that is similar to the experimental geometry and typical of many rock and debris avalanche events.

Results of these simulations and application of the model to other case studies demonstrate that the model is able to perform robustly in all these conditions overcoming some of the difficulties typical of two dimensional and three dimensional solutions of shallow water equations.

This capability is maintained even if a constant internal friction angle is adopted independent of flow velocity and flow/no flow conditions. This modeling approach already demonstrated its capabilities in modeling case studies of real rock and debris avalanches both in two dimensional [*Crosta et al.* 2003, 2004, 2006, 2008a, b] and three dimensional conditions [*Crosta et al.* 2007]

The application of the above described numerical strategy has several advantages. First of all, only well known material parameters from laboratory tests enter in our scheme, like by example the material friction angle and cohesion, the base friction coefficient. Furthermore, no depth averaging is needed, we straightforward solve the mechanical equations over the present material domain at each timestep.

This complete solution of the mechanical equations comes at the price that more computing power is needed relative to depth averaging approaches. However, our finite element program runs in parallel on shared memory computers, such that advantage is taken of existing and rapidly developing multi-core processors.

4.5.6 References

Ancey, C. (2007) Plasticity and geophysical flows: A review. **J. Non-Newtonian Fluid Mech.**, 142, 4–35.

Ancey, C., (2004) Powder-snow avalanches: approximation as non-Boussinesq clouds with a Richardson-number-dependent entrainment function. **J. Geophys. Res.**, 109, F01005, doi:10.1029/2003JF000052

Ancey, C., Iverson, R.M., Rentschler, M., and R.P. Denlinger (2008), An exact solution for ideal dam-break floods on steep slopes. **Water Resour. Res.**, 44, W01430, doi:10.1029/2007/WR006353.

Balmforth, N. J., and R.R. Kerswell (2005), Granular collapse in two dimensions. **J. Fluid Mech.** 538, 399.

G.D.R. Midi (2004), On dense granular flows. **Eur. Phys. J. E** 14, 341, 2004.

Borzsonyi, T., Halsey, T. C., and R. E. Ecke 803 (2005) Two Scenarios for Avalanche Dynamics in Inclined Granular Layers. **Phys. Rev. Lett.**, 94, 208001.

Borzsonyi, T., Halsey, T. C., and R. E. Ecke (2008) Avalanche dynamics on a rough inclined plane. **Phys. Rev. E**, 78, 011306.

Bouchaud, J.P., Cates, M.E., Ravi Prakash, J. and S.F. Edwards (1994) A model for the dynamics of sandpile surfaces. **J. Phys. I**, 4, 1383

Bouchut, F., Fernandez-Nieto, E.D., Mangeney, A. and P.-Y. Lagrée (2008) On new erosion models of Savage–Hutter type for avalanches. **Acta Mech** 199, 181–208, DOI 10.1007/s00707-007-0534-9

Bui, H.H., Fukagawa, R., Sako, K., Ohno, S. (2008) Lagrangian meshfree particles method (SPH) for large deformation and failure flows of geomaterials using elastic-plastic soil constitutive model. *Int. J. Numer. Anal. Meth. Geomech.*, DOI: 10.1002/nag.688

Campbell, C.S. (2006) Granular material flows – An overview. **Powder Technology**, 162, 208–229

Chen, H., and C.F. Lee (2000), Numerical simulation of debris flows. **Can. Geotech. J.**, 37, 1, 146–160.

Chen, H., Crosta, G. B., and C.F. Lee (2006) Erosional effects on runout of fast landslides, debris flows and avalanches: a numerical investigation. **Geotechnique**, 56, 5, 305–322.

Chen, W.F. and D.J. Han (1988) **Plasticity for structural engineers**. Springer Verlag, N.Y., 606 pp.

Choffat, P. (1929), L'écroulement d'Arvel (Villeneuve) de 1922. **Bulletin de la Société Vaudoise des Sciences Naturelles**, 57, 1, 5-28.

Crosta, G.B. (1994) An example of unusual complex landslide: from a rockfall to a dry granular flow? **Geologica Romana**, 30, 175-184.

Crosta G.B., Imposimato S., and D.G. Roddeman (2003) Numerical modelling of large landslides stability and runout. **Natural Hazards and Earth System Sciences**, 3, 6, 523-538.

Crosta, G. B., Chen, H. and C.F., Lee (2004) Replay of the 1987 Val Pola Landslide, Italian Alps. **Geomorphology**, 60, 1-2, 127-146.

Crosta, G. B., Imposimato, S., Roddeman, D., Chiesa, S., and F. Moia (2005) Small fast moving flow-like landslides in volcanic deposits: the 2001 Las Colinas Landslide (El Salvador). **Engineering Geology**, 79, 3-4, 185-214.

Crosta G.B., S. Imposimato, D.G. Roddeman (2006) Continuum numerical modelling of flow-like landslides. **NATO ARW, Landslides from massive rock slope failure**, Evans, S.G., Scarascia Mugnozza, G., Strom, A., Hermanns, R., (eds) NATO Science Series, Earth and Environmental Sciences, 49, 211-232

Crosta G.B., Frattini P., Imposimato S., and D.G. Roddeman (2007) 2D and 3D numerical modeling of long runout landslides – the Vajont case study. In Crosta G.B., Frattini P. (eds) **Landslides: from mapping to loss and risk estimation**. IUSS Press, Pavia, 15-24.

Crosta, G.B., Imposimato, S., and D.G. Roddeman, (2008a) Approach to numerical modelling of long runout landslides. Hong Kong, GCO, Dec. 2007, Proc International Forum on **Landslide Disaster Management, Landslide Runout Analysis** Benchmarking Exercise, 20 pp.

Crosta, G.B., Imposimato, S., and D.G. Roddeman, (2008b) Numerical modelling of entrainment/deposition in rock and debris-avalanches. **Engineering Geology**, doi:10.1016/j.enggeo.2008.10.004.

Crosta, G. B., Imposimato, S., and D. Roddeman (2009) Numerical modeling of 2-D granular step collapse on erodible and nonerodible surface. **J. Geophys. Res.**, 114,F03020.

Douady, S., Andreotti, B. and A. Daerr (1999) On granular surface flow equations. **Eur. Phys. J. B** 11, 131-142

Doyle, E.E., Huppert, H.E., Lube, G. Mader, H.M., and , S.J. Sparks (2007) Static and flowing regions in granular collapses down channels: Insights from a sedimenting shallow water model. **Phys. Fluids**, 19, 106601.

Denlinger, R. P. and R.M. Iverson (2001) Flow of variably fluidized granular masses across three-dimensional terrain: 2. Numerical predictions and experimental tests. **J. Geophys. Res.** 106, B1, 553-566.

Denlinger, R.P., and R.M. Iverson (2004) Granular avalanches across irregular three-dimensional terrain: 1. Theory and computation. **J. Geophys. Res.**, 109, F01014, doi:10.1029/2003JF000085.

Gardner (1983) Observations on erosion by wet snow avalanches, Mount Rae area, Alberta, Canada. **Arctic and Alpine research**, 15, 2, 271-274.

Gauer, P., and D. Issler (2004) Possible erosion mechanisms in snow avalanches, **Ann. Glaciol.**38, 384–392.

Girolami, L., T.H. Druitt, O.Roche, Z. Khrabrykh (2008) Propagation and hindered settling of laboratory ash flows. **J. Geophys. Res.**, 113, B02202.

Gray, J.M.N.T. (2001) Granular flow in partially filled slowly rotating drums. **J. Fluid Mech.**, 441, 1-29.

Gray, J. M. N. T. Wieland M. and K. Hutter (1999) Gravity-driven free surface flow of granular avalanches over complex basal topography. **Proc. R. Soc. Lond. A**, 455, 1841-1874.

Greve, R. and Hutter, K. (1993) Motion of a granular avalanche in a convex and concave curved chute: experiments and theoretical predictions. **Phil. Trans. R. Soc. Lond. A** 342, 573-600.

Greve, R., Koch, T. & Hutter, K. (1994) Unconfined flow of granular avalanches along a partly curved surface. I. **Theory. Proc. R. Soc. Lond.** A445, 399-413.

Hogg, A. J. (2007) Two dimensional granular 849 slumps down slopes. **Phys. Fluids**, 19, 093301, DOI: 10.1063/1.2762254

Hogg, A.J., and D. Pritchard (2004) The effects of hydraulic resistance on dam-break and other shallow inertial flows. **J. Fluid Mech.**, 501, 179-212.

Hungr, O. (1995) A model for the runout analysis of rapid flow slides, debris flows, and avalanches. **Canadian Geotechnical Journal**, 32, 610–623.

Hungr, O., and S.G. Evans (2004) Entrainment of debris in rock avalanches: an analysis of a long runout mechanism. **Bulletin of the Geological Society of America**, 116, 1240-1252.

Hunter, S.C. (1983) **Mechanics of continuous media**. 2nd. Edition, Ellis Horwood Limited, 640 pp.

Hutter, K., Siegel, M., Savage, S. B. and Nohguchi, Y. (1993) Two-dimensional spreading of a granular avalanche down an inclined plane. **Theory. Acta Mech.** 100, 37-68.

Issler D. (1998) Modelling of snow entrainment and deposition in powder-snow avalanches, **Ann. Glaciol.**26, 253–258.

Iverson, R. M., and R.P. Denlinger (2001) Flow of variably fluidized granular masses across three-dimensional terrain: Part I: Coulomb mixture theory. **J. Geophys. Res.** 106, 537-552.

Jaboyedoff, M. (2003) The rockslide of Arvel caused by human activity (Villeneuve, Switzerland): Summary, partial reinterpretation and comments of the work of Choffat, Ph. (1929): L'écroulement d'Arvel (Villeneuve) de 1922. **Bull. SVSN** 57, 5-28. Quanterra OPEN-FILE REPORT3, http://www.quanterra.org/erosion_hazard.htm.

Jop, P., Forterre, Y., Pouliquen, O. (2005) Crucial role of sidewalls in granular surface flows: consequences for the rheology. **J. Fluid Mech.**, 541, 167-192, doi: 10.1017/S0022112005005987

Kerswell, R. R. (2005) Dam break with Coulomb friction: A model for granular slumping? **Phys. Fluids**, 17, 057101.

Lacaze, L., Phillips, J.C. and R.R. Kerswell (2008) Planar collapse of a granular column: Experiments and discrete element simulations. **Phys. Fluids**, 20, 063302.

Lajeunesse, E., Mangeney-Castelnau, A., and J.P. Vilotte (2004) Spreading of a granular mass on a horizontal plane. **Phys. Fluids**, 16, 2371.

Lajeunesse, E., Monnier, J. B., and G.M. Homsy (2005) Granular slumping on a horizontal surface. **Phys. Fluids**, 17, 103302.

Lajeunesse, E., C. Quantin, P. Allemand, and C. Delacourt (2006) New insights on the runout of large landslides in the Valles-Marineris canyons, Mars, **Geophys. Res. Lett.**, 33, L04403, doi:10.1029/2005GL025168.

Larrieu, E., Staron, L. and E.J. Hinch (2006) Raining into shallow water as a description of the collapse of a column of grains. **J. Fluid Mech.**, 554, 259–270.

Locat, P., Couture, R., Leroueil, S., Locat, J., and M. Jaboyedoff (2006) Fragmentation energy in rock avalanches. **Canadian Geotechnical Journal**, 43, 830-851.

Lube, G., (2006) The flow and depositional mechanisms of granular matter: Experimental and field studies with implications for pyroclastic flows. PhD Thesis, Univ. of Kiel, 160 pp.

Lube, G., Huppert, H., Sparks, S., Hallworth, M. (2004) Axisymmetric collapse of granular columns. **J. Fluid Mech.** 508, 175-199.

Lube, G., Huppert, H., Sparks, S., and A. Freundt (2007) Static and flowing regions in granular collapses down channels. **Phys. Fluids**, 19, 043301.

Lube, G., Huppert, H., Sparks, S., and A. Freundt (2005) Collapses of two-dimensional granular columns. **Phys. Rev. E** 72, 041301.

Lucas, A., and A. Mangeney (2007) Mobility and topographic effects for large Valles Marineris landslides on Mars. *Geophys. Res. Lett.*, 34, L10201, Doi:10.1029/2007GL029835.
Mangeney, A., Heinrich, Ph., and R. Roche (2000) Analytical Solution for Testing Debris Avalanche Numerical Models. **Pure Appl. Geophys.**, 157, 1081-1096.

Mangeney-Castelnaud, A., Vilotte, J.-P., Bristeau, M.O., Perthame, B., Bouchut, F., Simeoni, C., and S. Yerneni (2003) Numerical modeling of avalanches based on Saint-Venant equations using a kinetic scheme, **J. Geophys. Res.** 118, 2527.

Mangeney-Castelnaud, A., Bouchut, B., Vilotte, J.P., Lajeunesse, E., Aubertin, A., and Pirulli, M.,(2005) On the use of Saint-Venant equations for simulating the spreading of a granular mass. **J. Geophys. Res.**, 110, B09103.

Mangeney-Castelnaud, A., Tsimring, L.S., Volfson, D., Aranson, I.S., and B. Bouchut (2007) Avalanche mobility induced by the presence of an erodible bed and associated entrainment. **Geophys. Res. Lett.**, 34, L22401.

Mangeney,A.,Roche, O., Hungr,O., Mangold,N., Faccanoni, G. and Lucas, A., (in press) Erosion and mobility in granular collapse over sloping beds . **J. Geophys. Res.**,

McDougall, S. (2006) A new continuum dynamic model for the analysis of extremely rapid landslide motion across complex 3D terrain. PhD Thesis, Univ. British Columbia, 253 pp.

MIDI GDR (2004) On dense granular flows. Groupement De Recherche Milieux Divisés, **Eur. Phys. J. E**, 14, 341-365, DOI: 10.1140/epje/i2003-10153-0

Pastor, M., J. A. Fernandez Merodo, M. Quecedo, M. I. Herreros, E. Gonzales, and P. Mira (2002) Modelling of debris flows and flow slides. **Numer. Modell. Geomech.**, 6, 1213–1232.

Pitman, E.B., Nichita, C.C., Patra, A.K., Bauer, A.C., Bursik, M. and A. Weber (2003) A model of granular flows over an erodible surface. **Discrete Contin. Dyn. Syst.**, B, 3, 589.

Pouliquen, O., (1999) Scaling laws in granular flows down rough inclined planes. **Phys. Fluids**, 11(3), 542-548.

Pouliquen O, Forterre Y. (2002) Friction law for dense granular flows: application to the motion of a mass down a rough inclined plane. **J. Fluid Mech.** 453:133-151

Pouliquen O, Chevoir F. (2002) Dense flows of dry granular material. **C. R.Physique** 3:163-75

Pouliquen O, Cassar, C ., Jop, P., Forterre Y. and M Nicolas (2006) Flow of dense granular material: towards simple constitutive laws. **Jour. of Statistical Mechanics:Theory and Experiment**, 1742-5468/06/P07020

Pudasaini, S.P., and K. Hutter (2007) **Avalanche dynamics, dynamics of rapid flows of dense granular avalanches.** Springer Verlag, 602 pp.

Rastello M., Ancey C., Ousset F., Magnard R., and Hopfinger, E. J. (2002) An experimental study of particle-driven gravity currents on steep slopes with entrainment of particles. **Natural Hazards and Earth System Sciences**, 2: 181–185

Ritter, A. (1892) Die Fortpflanzung der Wasserwellen. *Zeit. Vereines Deutsch. Ing.*, 36(33), 947-954

Roddeman, D.G. (2008), **TOCHNOG user's manual**. FEAT, 255 pp., www.feat.nl/manuals/user/user.html.

Sailer, R., Fellin, W., Fromm, R., Jorg, P., Rammer, L., Sampl, P., Schaffhauser, A. (2008) Snow avalanche mass-balance calculation and simulation-model verification. **Annals of Glaciology**, 48, 183-192

Savage, S.B. (1979) Gravity flow of cohesionless granular materials in chutes and channels. **J. Fluid Mech.**, 92, 53-96.

Savage S.B., Hutter K (1989) The motion of a finite mass of granular material down a rough incline. **J. Fluid Mech.** 199, 177–215.

Savage S.B., Hutter K (1991) The dynamics of avalanches of granular materials from initiation to run out. Part I: Analysis. **Acta Mech.** 86, 201–223.

Siavoshi, S., and A. Kudrolli (2005) Failure of a granular step. *Phys. Rev. E* 71, 051302.
Sovilla, B. and P. Bartelt. (2002) Observations and modelling of snow avalanche entrainment. **Natur. Hazards Earth Syst. Sci.**, 2(3–4), 169–179.

Sovilla, B., S. Margreth and P. Bartelt. (2007) On snow entrainment in avalanche dynamics calculations. **Cold Reg. Sci. Technol.**, 47(1–2), 69–79.

Staron, L., and J. Hinch (2005) Study of the collapse of granular columns using DEM numerical simulation. **J. Fluid Mech.** 545, 1–27.

Staron, L. (2008) Mobility of long-runout rock flows: a discrete numerical investigation. **Geophys. J. Int.**, 172, 455-463.

Tai, Y. C. Kuo, C. Y. (2008a) A new model of granular flows over general topography with erosion and deposition. **Acta Mech.**, 199, 71–96, DOI 10.1007/s00707-007-0560-7

Tai, Y. C. and Y.C. Lin (2008b) A focused view of the behaviour of granular flows down a confined chute into the horizontal run-out zone. *Phys. Fluids*, 20, 123302

Thompson, E.L., and H.E. Huppert (2007) Granular column collapses: further experimental results. **J. Fluid Mech.**, 575, 177-186

Zenit, R. (2005) Computer simulation of the collapse of granular columns. **Phys. Fluids**, 17, 031

4.6 CALIBRATION OF RHEOLOGICAL PARAMETERS FOR VOLCANIC AND GLACIAL ROCK AVALANCHES

4.6.1 Introduction

Replicating the behavior of fast moving landslide is primarily aimed at defining the areas which are prone to landslide propagation at varying magnitude (i.e. flow velocity and depth). The rheological properties required to describe the flow behavior are mostly empirical and they do not directly describe the material properties, but the macroscopic behavior of the approximated or “equivalent fluid”. Even assuming a frictional model, the approximated fluid requires an “apparent friction angle” to replicate the “excess travel distance” observed in the field (Hsu, 1975). For these reasons, the rheological parameters are calibrated through back-analysis of real landslide case studies rather than measured. Even if the modeling procedure usually consists on reproducing the features of a past event through a back-analysis procedure, in some cases it could be necessary to forecast the flow propagation without a preventive calibration of the model parameters. In these cases, a set of consistent events can provide a range of admissible values for the rheological parameters to be applied in similar conditions.

We present the numerical modeling of the propagation phase of several rock debris avalanches that originated in different environments: (i) rock and debris avalanches originated from the failure of volcanic edifices (volcanic debris avalanches) and (ii) rock and debris avalanches which mostly propagated over glacial ice (glacial rock avalanches). The modeled events are chosen from the historical rock and debris avalanches best-described in the literature and best preserved in the field.

4.6.1.1 The numerical model

We use DAN 3D (McDougall and Hungr 2004), a quasi-3D extension of the existing 2D model DAN-W which satisfactorily models debris avalanches in different environments (e.g. McDougall, 2006; McDougall et al., 2006). The model uses a meshless, Lagrangian numerical method adapted from Smoothed Particle Hydrodynamics to discretize and solve the depth-averaged equations of motion for an “equivalent fluid”, a hypothetical material governed by simple rheological relationships.

The momentum equations consider a constant frictional internal rheology, governed by an internal friction angle, and a user-selected basal rheology, as provided by several alternative rheological kernels (Hungr, 1995). The internal shear strength allows simulating strain-dependent, non-hydrostatic, anisotropic internal stresses due to 3D deformation of material. The basal rheology is controlled by one or two parameters, depending on the selected kernel, which must be adjusted by a trial and error calibration procedure.

Based on previous analyses of large rock avalanches, the frictional, Voellmy rheologies (Hungr and Evans, 1996) are alternatively considered for the basal shear stress in this work. In addition, the plastic rheology (Kelfoun and Druitt, 2005) has been used to model volcanic debris avalanches.

The frictional rheology assumes the resisting shear force, τ , to depend only on the effective normal stress, σ . The frictional equation is expressed as:

$$\tau = \sigma(1 - r_u) \tan \varphi \quad (4.6.1)$$

where the pore-pressure ratio, r_u , and the dynamic friction angle, φ , are the rheological parameters to be introduced in the model. The pore-pressure ratio derives from the pore pressure, u , normalized by the total bed-normal stress at the base, σ . The pore-pressure ratio and the dynamic friction angle can be alternatively expressed by one single variable denoted as bulk basal friction:

$$\varphi_b = \arctan[(1 - r_u) \tan \varphi] \quad (4.6.2)$$

thus reducing the basal resistance equation to:

$$\tau = \sigma \tan \varphi_b \quad (4.6.3)$$

The Voellmy rheology describes the total resistance as a sum of a frictional and a turbulent term:

$$\tau = \sigma \mu + \frac{\rho g v^2}{\xi} \quad (4.6.4)$$

The frictional term relates the shear stress to the normal stress through a friction coefficient, μ , which is analogous to $\tan \varphi_b$. The turbulent term summarizes all velocity-dependent factors of flow resistance, and is expressed by the square of the velocity and the density of the debris through a turbulence coefficient, ξ .

The plastic rheology assumes the resistance is given by constant shear strength, c :

$$\tau = -c \quad (4.6.5)$$

The rheological parameters (basal friction angle, φ , and pore pressure ratio, r_u for the frictional rheology; frictional, μ , and turbulent coefficients, ξ , for the Voellmy rheology, and shear strength for the plastic rheology) are allowed to change along the path. The change is specified by reference to elevation ranges.

4.6.1.2 Data and methods

SRTM and ASTER data provides the present topography used for the modelling at an horizontal resolution of 3 arcseconds (<90 m) and 1 arcsecond (<30 m), respectively. The satellite data provide the post event topographies. The topographies of the volcano edifices are eventually modified for removal of other volcanic products placed after the collapse event (e.g. dome creation, effusion lava). We modify the original terrain data to reconstruct the pre-event topography in the area interested by detachment and deposition outlined by available maps and morphological evidences. In several cases, data are available about the pre-event topography or the deposit thickness. With no specific data available, the topography is adjusted within the known path extent so as to match the estimates of the mobilized volumes

in the detachment and in the deposition zone and to provide a smooth transition to the neighbouring topography.

The back analyses of the rheological parameters were performed to match (i) the total runout distance reached by the debris avalanche (i.e. the horizontal distance between the scar high point to the furthest point reached by the avalanche) and (ii) the aerial extent of the deposition. In the case of volcanic debris avalanches, the area covered by the propagation is generally preferred to the deposition extent because the proximal end of the deposition is often buried by volcanic material either ejected as secondary product of the failure or as post-collapse volcanic deposits, resulting uncertain in most of the cases. Other data eventually used for the back analyses are the deposit thicknesses and distribution.

Glacial and volcanic rock and debris avalanches are recently gaining more attention because of their recognised prominence and frequency. Millions of people live on top of debris avalanche deposits produced by volcanic edifice collapses (Siebert, 2002), where future collapses are possible. They mobilize large volumes and the produced morphological features (i.e. scars and tongue-shaped accumulation of coarse rock debris) are often well preserved. These features were often misinterpreted as result of glacial or other volcanic processes. Moreover, both are characterized by a greater mobility compared to events evolving in non-glacial, non-volcanic environments (Evans and Clague, 1999; Crosta et al, 2005).

4.6.2 Volcanic debris avalanches

Sector or flank collapse of volcanic edifices is a common and major catastrophic event for many acid volcanos. Recent, prominent, disasters that occurred at Mount St Helens (May 1980; Voight, 1981), at Casita (Nicaragua, October 1998; Kerle and van Wyk de Vries, 2001), at Soufriere Hills (Montserrat, December 1997; Boudon et al., 2007) underline the hazard posed by collapse events around volcano edifices. Volcanic collapses are ubiquitous and occur in a wide variety of volcanic environments and tectonical settings (Ui, 1983; Siebert, 1984; McGuire, 1996).

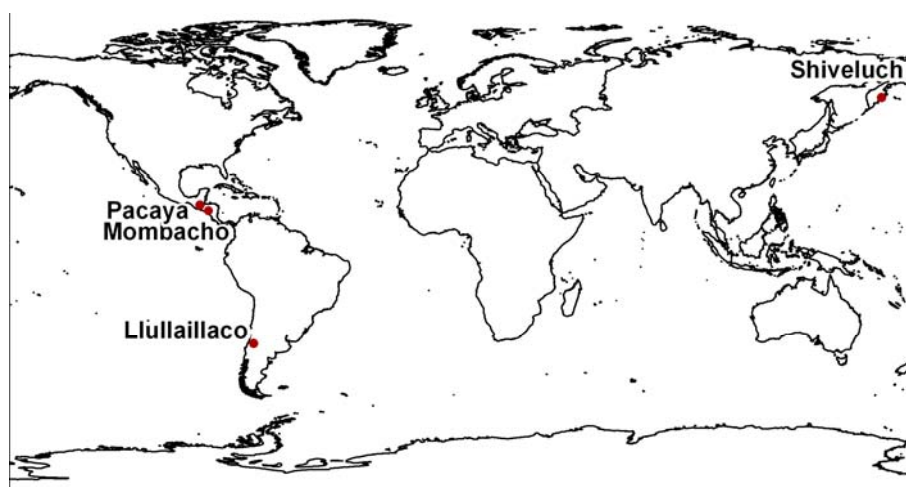


Figure 4.6.1 – Location of the collapsed volcano edifices considered for the modeling.

Table 1. Debris avalanche volumes reported in the literature for the selected events compared to the ones supposed for the modelling.

	Volume event [km ³]	Volumes in the model [km ³]	
		Source	Deposit
<i>Shiveluch</i>	1.25	1.15	1.25
<i>Llullaillaco</i>	1.5-2	1.75	1.85
<i>El Crater</i>	1.8	1.6	1.8
<i>Las Isletas</i>	1.2	0.98	1.2
<i>Pacaya</i>	0.6-0.85	0.75	0.88

Irrespective of the initial geometry (shallow or deep flank or sector collapse), most failures develop as rock slides and debris avalanches, characterized by the fast movement of large volumes of rock and debris over great distances. Subaerial avalanches of 1-10 km³ in volume can travel as much as 100 km affecting areas of up to 1500 km² (Siebert, 1984; Stoops and Sheridan, 1992).

Because of their high mobility and gigantic magnitudes, debris avalanches originating from collapses of volcanic edifices produce severe threat and damage (Siebert, 1996). The adoption of the DAN 3D and similar models to volcanic debris avalanches is supported by the many similarities between volcanic and non-volcanic events (morphology and texture of the deposits, evidences of flow structures, etc.) suggesting similar emplacement mechanisms (Hayashi and Self, 1992). Nevertheless, volcanic debris avalanches present elements of complexity which lack in their non-volcanic counterparts. Volcanic debris avalanches are often larger than non-volcanic ones and the transport phase may be influenced by variable water content and or by thermodynamic effects or degassing caused by active volcanic processes (Bursik et al., 2005).

The modelled cases are selected from a database of 118 collapse events recognized from satellite images and collected from literature records (Figure 4.6.1). The events differ with respect to their morphological constrains, materials, triggering conditions and styles of failure. The collapses date from late Pleistocene (Llullaillaco) to the present (Shiveluch). The volumes involved in the event and the corresponding volumes considered in the models are listed in table 1. We reconstructed the pre event topography making the assumption of a 10-20% increase of volume due to fragmentation from the source to the deposition.

4.6.2.1 Llullaillaco debris avalanche (Argentina), late Pleistocene

Cerro Llullaillaco (6739 m a.s.l.) is an active stratovolcano at the Chile-Argentina border. Its SE flank failed during late Pleistocene producing a 1.5-2.0 km³ debris avalanche.

The failure was first reported by Wood and Francis (1988) and then described by Richards and Villeneuve (2001). A smaller debris avalanche took place on the NE flank, but no information is available for the timing and volume of the event. The edifice is composed of

dacitic lava flows variably altered and oxidized, permanently covered by an ice cap above approximately 6000 m a.s.l..

The collapse was immediately preceded by volcanic activity, as evidenced by the presence of fused dacitic blocks at the proximal end of the deposit. The deposit is exceptionally well preserved and contains juvenile dacitic blocks at its proximal end. The presence of old volcanic structures (Cerro Rosado to the north and Cerro 5074 to the south) forced the debris avalanche to runup (over 200 m on to Cerro Rosado) and to bifurcate and flow towards the Salina de Llullaillaco (sloping $2^{\circ} \pm 1^{\circ}$). The two branches, in which the mass divided, travelled 23- 25 km far from the slide scarp, while a separate lobe 50 m thick formed on the north-western slope of Cerro 5074. The deposit halted quite abruptly (the toe rise up 10 m above the Salina de Llullaillaco), with steep and sharply defined margins, and maximum thickness within 50- 60 m (Richard and Villeneuve, 2001). The deposit halted quite abruptly (the toe rise up 10 m above the Salina de Llullaillaco) and presents prominent longitudinal ridges and high tide-marks against obstacles. The deposit margins are sharply defined and steep resembling the feature typical of high yield strength materials. The distal end limit of the northern branch, flowing within the Salina de Llullaillaco, is indistinct and uncertain because of the mobility of the salt flats.

A lower estimate of the maximum velocity, which allows the vertical runup on to Cerro Rosado, is about 90 ms^{-1} (Richards and Villeneuve, 2001). The velocity, v , has been calculated according to the equation $v = (2gh)^{0.5}$, where g is the acceleration due to gravity and h is the runup height.

A source volume of 1.75 km^3 is considered for the modeling. The frictional rheology ($\phi=4.6^{\circ}$, null pore pressure) correctly reproduces the runup on to Cerro Rosado and the runout propagation of the two branches which formed after flow bifurcation (Figure 4.6.2).

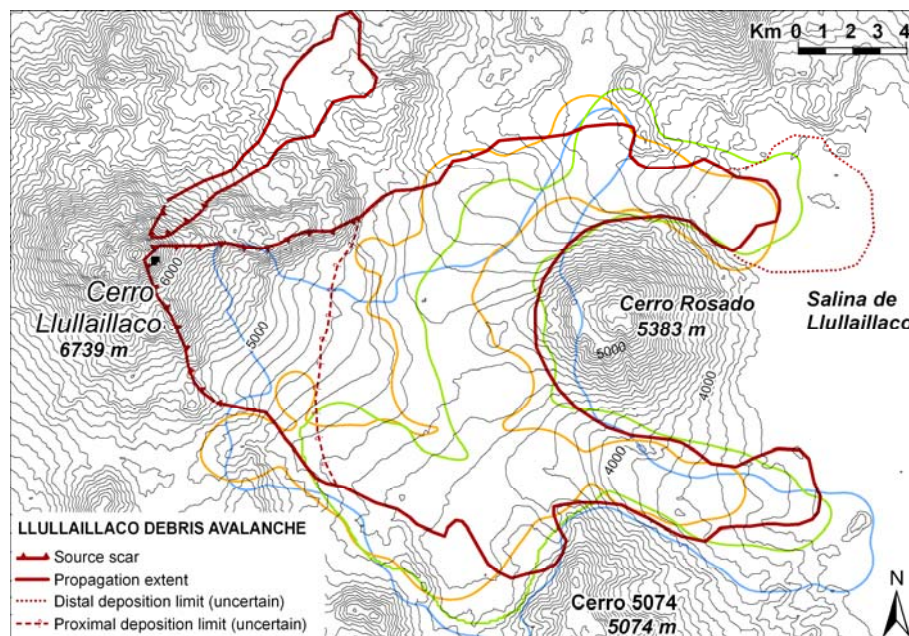


Figure 4.6.2 - Outline map of the debris avalanche deposits obtained assuming the frictional (green), Voellmy (orange), and plastic (blue) rheologies compared against the debris-avalanche deposits from the field data (in brown).

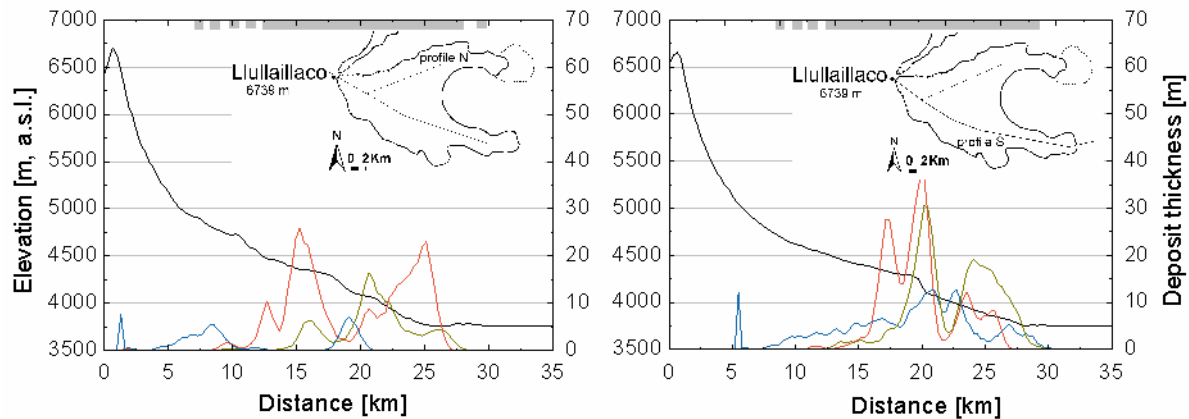


Figure 4.6.3 - Profiles of the final deposit thickness obtained by the frictional (green), Voellmy (orange) and plastic (blue) rheologies along the indicated travel paths. The grey bars at the top of the graphs indicate the extent of certain (continuous bar) and uncertain (discontinuous bar) deposition.

The maximum thicknesses resulting from the modeling slightly exceed 50 m and are observed in correspondence to the topographic obstacles, Cerro Rosado and Cerro 5074, in agreement with several exposures of the deposit (circles in Figure 4.6.4 b; Richard and Villeneuve, 2001). In the model, the flow reaches a maximum velocity of 90-95 ms^{-1} before impacting the obstacles. These velocities are comparable to field measurements. The main discrepancy against field data is relative to the mode of deposition that does not occur in the vicinity of the edifice, whereas the overall deposit extent is underestimated by 14% (Figure 4.6.3).

The other rheologies replicate the proximal deposition but they fail to predict the flow dynamics as well as the distal deposition (volumetric distribution of the material in the two branches, their respective travel distances, and the runup on to Cerro Rosado). The flow velocities in the vicinity of the obstacle are higher (e.g. 120 ms^{-1} , for the plastic model) or lower (e.g. 65 ms^{-1} , for the Voellmy model) than estimated from energy balance considerations. The deposition starts in proximity of the source area so that the deposit spreads over a larger area with thickness lower than observed in the field. Because of the low flow velocity both the run up and travel distance of the southern branch are under-predicted. The Voellmy and plastic rheologies underestimate the deposit extent by 15% and 3%, respectively.

4.6.2.2 Mombacho debris avalanche (Nicaragua): El Crater and Las Isletas, undated

Mombacho (1344 m a.s.l.) is an active stratovolcano located in Nicaragua, rising above the Lake Nicaragua (31 m a.s.l.).

Debris avalanche deposits on two sides of the volcano reveal multiple lateral failures (van Wyk de Vries and Francis; 1997; Shea et al., 2008). El Crater debris avalanche affects the S flank of the edifice. The avalanche on the NE flank created the Las Isletas archipelago. The

events are undated, forest cover indicates a minimum age of 1000 years for both (van Wyk de Vries and Francis, 1997).



Figure 4.6.4 - Outline map of the debris avalanche deposits obtained assuming the frictional (green), Voellmy (orange), and plastic (blue) rheologies compared against the debris-avalanche deposits from the field data (in brown).

The two events differ in their triggering mechanisms and type of material involved. None of the events was accompanied by explosive or magmatic activity and none shows evidences of water presence during transport. El Crater avalanche (1.75 km^3) initiated as a slump failure entirely developed within the cone, and involved intensively altered lavas and hydrothermal clays. The lack of confinement allowed the avalanche to spread freely along 3° slope topography, thinning until stoppage. Las Isletas avalanche (1.2 km^3) probably initiates along a bedding plane within the ignimbrite basement. The failure plane cuts the volcanic edifice down to the base. Outward gravitational spreading of the basement was responsible for the failure (van Wyk de Vries and Francis, 1997). El Crater debris avalanche deposited unconstrained. In the case of Las Isletas, the material mainly deposited into the lake with uncertain limits (Shea et al., 2008).

Moreover, the flow into the lake may have affected the mode of spreading.

The two deposits contain large amounts of clay which originates from the hydrothermally-altered source material (El Crater) or from the pumice-rich unit which forms the substratum (Las Isletas). The absence of confinement favors extensional dynamics during transport (Figure 4.6.3 c, d), attested by the presence of normal faults and hummocky surfaces in the upper layer of both the deposits. No evidences of basal erosion exist for the two events, and no information is available about the maximum thickness or distribution of the deposits, and flow velocities. The propagation extent is the main element for the back analyses in both the cases.

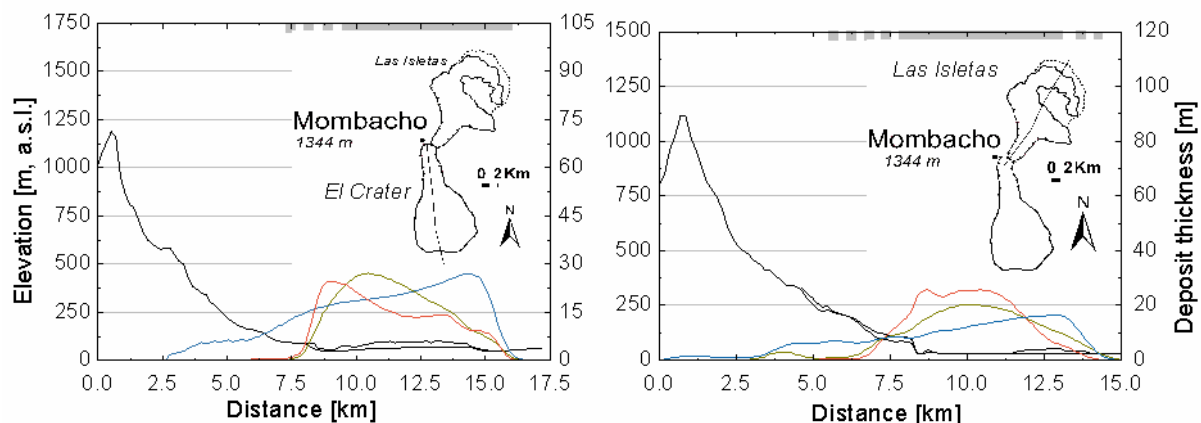


Figure 4.6.5 - Profiles of the final deposit thicknesses obtained by the frictional (green), Voellmy (orange) and plastic (blue) rheologies along the indicated travel path. The grey bars at the top of the graphs indicate the extent of certain (continuous bar) and uncertain (discontinuous bar) deposition.

The source volumes assumed in the model are 1.6 km^3 and 0.98 km^3 for El Crater and Las Isletas debris avalanches, respectively (Figure 4.6.4). For all the rheologies, a westward component dominates the initial phase of the avalanche movement at the exit of the source area affecting the final deposit extent.

The distribution of the deposits is similar among the models with a somewhat larger maximum thickness for the frictional rheology (Figure 4.6.5). Assuming a frictional rheology, the back analyses of the two events provide similar parameters (basal friction angle of 4.3° and 4.5° for El Crater and Las Isletas, respectively, and null pore pressure for both cases). The best-fitting Voellmy parameters are $\mu=0.08$, $\xi=1000 \text{ m s}^{-2}$ for El Crater, and $\mu=0.15$, $\xi=500 \text{ m s}^{-2}$ for Las Isletas.

For El Crater debris avalanche, the frictional model overestimates the propagation and final deposition extent by 7%. Larger extents (exceeding the observation by 16%-25%) are predicted by the plastic and Voellmy rheologies. These differences are given by the larger lateral spreading in the case of the Voellmy model and by the occurrence of deposition in the vicinity of the edifice in the case of the plastic model. Las Isletas debris avalanche mainly deposits at the entrance into the lake. All the models roughly estimate the aerial extent of the deposition.

The thickness reaches its maximum (slightly over 50 m) at the proximal end of the deposit and then thins towards the margins in case of El Crater debris avalanche. Maximum flow velocities of $90\text{-}100 \text{ ms}^{-1}$ are reached by the two models. The Las Isletas debris avalanche mainly deposits at the entrance into the lake, the maximum thickness being in the area of the archipelago. The discrepancies in the deposit distribution with respect to reality are partly related to the path-topography reconstruction (the elevation within the lake is fixed at the water surface) and partly to the additional complexity provided by the spreading within the lake. On the other hand, the limits of the debris-avalanche deposit within the lake are uncertain and may extend further on the eastern side (Shea et al., 2008). Maximum velocities of $75\text{-}80 \text{ ms}^{-1}$ are modelled by the frictional rheology, and velocities of $65\text{-}70 \text{ ms}^{-1}$ assuming Voellmy.

4.6.2.3 *Pacaya debris avalanche (Guatemala), late Holocene*

Pacaya (2600 m a.s.l.) is an active stratovolcano located in Guatemala which collapsed between 595 and 1555 yr BP (Katayama and Matias, 1995).

The failure occurred on the SW flank of Pacaya, which grew within the ancestral edifice (Figure 4.6.3d). The source is partially filled by post-collapse MacKenney cone and associated lava flows. The deposit probably exceeds 0.65 km^3 in volume (Vallance et al., 1995; Katayama and Matias, 1995) and is characterized by numerous hummocks and 5-10 m levées.

Most of the avalanche deposited on the south flank, along the Metapa valley for 25 km and in a lobe of about 20 km^2 , to depths large as 50-120 m in the upper valley (Vallance et al., 1995), while part of the avalanche flowed to the west (Katayama and Matias, 1995).

We assume a debris-avalanche volume of 0.75 km^3 (Katayama and Matias; 1995) at the source. The Voellmy rheology ($\mu=0.003$, $\xi=1200 \text{ ms}^{-2}$) better predicts the deposit extent (figures 6). Most of the material propagates along the Metapa valley, where the deposit reaches thicknesses of about 60 m (figures 7). In the other models most of the material stops in the upper sector of the Metapa valley preventing the formation of the terminal lobe observed at the confluence

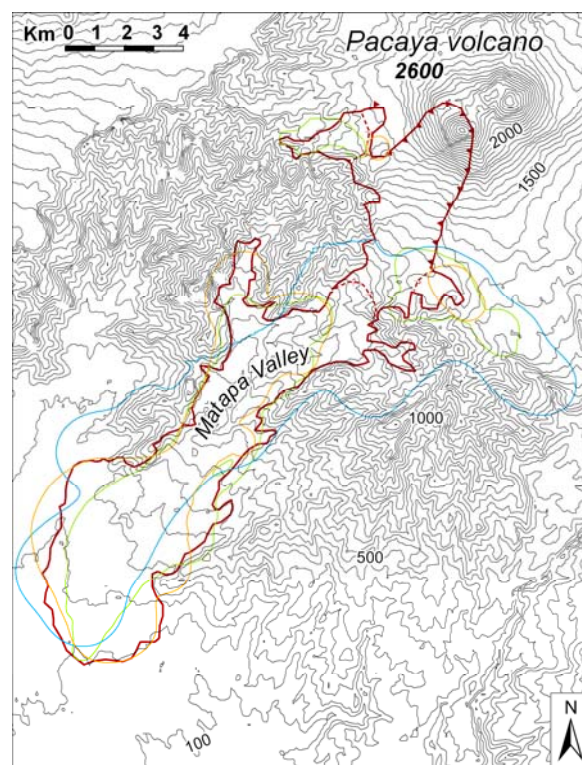


Figure 4.6.6 - Outline map of the debris avalanche deposits obtained assuming the frictional (green), Voellmy (orange), and plastic (blue) rheologies compared against the debris-avalanche deposits from the field data (in brown).

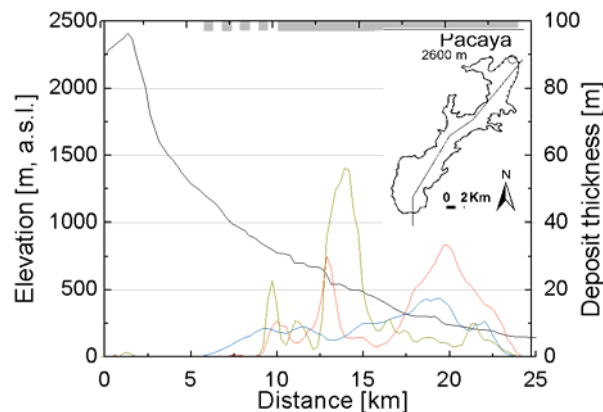


Figure 4.6.7 - Profiles of the final deposit thicknesses obtained by the frictional (green), Voellmy (orange) and plastic (blue) rheologies along the indicated travel path. The grey bars at the top of the graphs indicate the extent of certain (continuous bar) and uncertain (discontinuous bar) deposition.

into the main valley. Assuming the material as frictional, deposit up to 85-90 m thick forms in the upper valley, close to the observed maximum thicknesses (locally up to 120 m). Assuming the material as plastic, part of the deposition occurs on the east flank of the volcano, along El Chupadero, a tributary of Rio Metapa. This is in contrast to the observations.

4.6.2.4 Shiveluch debris avalanche (Kamchatka), 1964

Shiveluch is the northernmost active volcano of the Kamchatka peninsula. The volcano rises isolated in the Central Kamchatka depression, and it is composed by the Old Shiveluch (3283 m a.s.l.) and Young Shiveluch (2800 m a.s.l.) edifices. Old Shiveluch shows a giant horseshoe-shaped crater broadly opened to the south which is the result of a massive earlier edifice failure about 10 ka BP (Belousov et al., 1999). Young Shiveluch is the active sector of the volcano nested in the Old Shiveluch crater.

The volcano experienced multiple edifice failures (Ponomareva et al., 1998), most recently in 1964 (Belousov et al., 1999). All the failures occurred in the same, southern direction and some were accompanied by minor phreatic eruptions early in the failure process. The overlapping deposits from these events cover an area of 200 km² (Ponomareva et al., 1998).

The 1964 sector failure started as a 1.25 km³ retrogressive landslide with the leading block transforming into a debris avalanche. Laterally unconfined, the debris avalanche spread radially to distances exceeding 15 km, forming a thinning fan-shaped body. The last-released blocks did not completely disintegrate and came to rest in the newly formed horseshoe-shaped caldera (Belousov et al., 1999). Apart from the deposit limits, no other information is available.

We modelled the detachment of 1.15 km³ of material. The extent of the deposit is well reproduced by the frictional model (mismatch in the areal extent is within 4%) with $\phi=7.5^\circ$ and null pore pressure, and the plastic model ($c=75$, with a mismatch lower than 3%), whereas the Voellmy rheology overspreads laterally and overpredicts the aerial extent by 35% (Figure 4.6.8). The maximum thickness exceeds 35-40 m with slightly higher values for the frictional

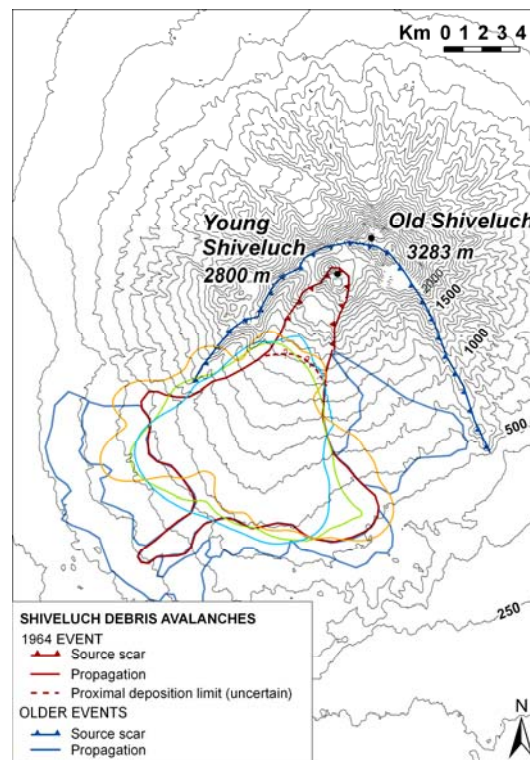


Figure 4.6.8 - Outline map of the debris avalanche deposits obtained assuming the frictional (green), Voellmy (orange), and plastic (blue) rheologies compared against the debris-avalanche deposits from the field data (in brown).

rheology (Figure 4.6.9). Maximum velocities exceeding $75\text{-}80\text{ ms}^{-1}$ and $60\text{-}65\text{ ms}^{-1}$ are attained by the frictional and Voellmy rheology, respectively. The frictional and plastic rheologies differ for the thickness distribution: it thins down along the volcano flank for the frictional, whereas it thickens for the plastic.

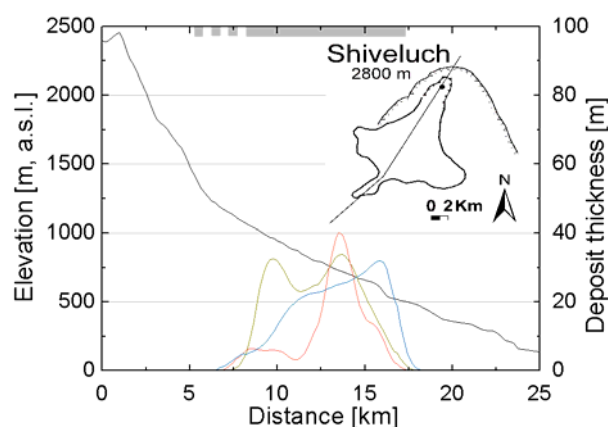


Figure 4.6.9 - Profiles of the final deposit thicknesses obtained by the frictional (green), Voellmy (orange) and plastic (blue) rheologies along the indicated travel path. The grey bars at the top of the graphs indicate the extent of certain (continuous bar) and uncertain (discontinuous bar) deposition.

4.6.3 Glacial Rock avalanches

Combined rock-ice avalanches usually evolve from major rock falls in glacial environments that entrain large volumes of ice and snow. Most of these landslides probably initiate as topples and falls, but rapidly transform into rock avalanches as they travel over glaciers (Couture and Evans, 2002; Schwab et al., 2003) and undergo remarkable thinning. Rock avalanches that travel over glaciers may have anomalously long runouts due to low friction at the debris-glacier interface (Evans and Clague, 1988; Huggel et al., 2005)

The behavior of the rock avalanche, its moisture content and patterns of deposition, were affected by travel over ice. Rock avalanches in glacial environments have considerably longer travel distances in glacial than in non-glacial environments due to possible interactions with and transformations of ice, snow and water. The mobility of rock avalanches in glacial environments has been observed to increase by about 25% (Evans and Clague, 1988), compared to non-glacial environments. The mobility is increased by the low friction at the interface of the moving debris and ice. Friction may be further reduced as water films form, and pore pressures develop, at the base of the debris due to frictional heating or compression of snow on the glacier surface (Geertsema et al., 2006).

Triggers may include intense rainfall, earthquakes, and permafrost degradation. The volumes of the events modelled are listed in table 2.

Table 2. Debris avalanche volumes reported in the literature for the selected events compared to the ones supposed for the modelling.

	Volume event [M m ³]	Volumes in the model [M m ³]	
		Source	Deposit
<i>Alaska, March 1964 earthquake</i>			
<i>Sherman</i>	25-30	26.4	27.8
<i>Martin River 2</i>	11.2	11.9	11.9
<i>Martin River 3</i>	8.8	8.6	8.9
<i>Martin River 4</i>	15.5	15.2	16
<i>Martin River unnamed 1</i>	8.9	8.6	8.8
<i>Martin River unnamed 2</i>	6.0	5.9	6.1
<i>Martin River unnamed 3</i>	4.2	4.2	4.4
<i>Baring 3</i>	8.0	7.8	8.1
<i>Baring 2</i>	12.1	11.8	12.4
<i>Alaska, Denali 2002 earthquake</i>			
<i>Black Rapids, west</i>	9.9	9.7	9.9
<i>Alps</i>			
<i>Becca d Luseny</i>	1.0	0.95	1.0
<i>Thurwieser</i>	2.0-2.5	2.0	2.5

4.6.3.1 The March 1964 Alaska earthquake

The March 27, 1964 earthquake was one of the strongest ever recorded in North America. Its Richter magnitude, computed by different observatories was from 8.3 to possibly as high as 8.75, the duration of strong shaking was timed or estimated as from 1.5 to 7 minutes (Eckel, 1970). As interpreted by Wyss and Brune (1967), the earthquake rupture propagated in a series of events, with six widely distributed "epicenters". Energy was released by the earthquake itself over a broader area than has previously been observed (Plafker, 1965a; Plafker and Mayo, 1965).

Almost 2,000 avalanches and snow slides were seen on post earthquake aerial photographs examined by Hackman (1965). Rockfalls occurred over a very broad area as a result of the earthquake (Post, 1967). Most of these rockfalls and rockslide avalanches were minor in both size and importance. The largest ones propagate above the Sherman, Martin River, Bering, Steller, Allen glaciers (Post, 1967), and range in volume from 4.2 M m³ to 24.8 M m³.

The extent of the avalanches was mapped from field surveys and aerial-photographic investigations (Post, 1967). In most of the cases, an estimation of the mobilized volume is missing. We reconstruct the event volumes from the extent of the deposits assuming the deposition extent vs volume should be comparable to the one observed for other ice-rock avalanche events of similar size. The avalanches initially descended very steep slopes and attained high velocities; the rock debris spread out over surficial features of the glacier surfaces without greatly modifying them; and the gradients of the avalanches on the glacier surface were very low, yet the material traveled very long distances (Post, 1967).

Ice-rock avalanches on Sherman Glacier

One of the largest of the many avalanches triggered by the Alaska earthquake of 27 March 1964 was the Sherman landslide, 130 km east of the epicentre of the earthquake.

A steeply dipping, pervasively jointed, tabular block of massive sandstone and argillite roughly 450 m long, 300 m wide, and 150 m thick that comprised the west face and uppermost 50 m of a Matterhorn-like peak (1207 m a.s.l.), now informally called "Shattered Peak", was shaken free along a bedding surface and plunged 600 m down the 40-degree slope below to slide as far as 5 km north-westward across the gently sloping, snow-covered terminal reach of the Glacier (Shreve, 1966). The mass of shattered rock debris and minor amounts of admixed ice and snow spread out in a trapezoidal, partially digitate lobe having an average width of about 1.5 km, a maximum width of nearly 3 km, and a relatively uniform thickness of 3 to 6 m. The volume has been evaluated in 25-30 M m³ (Plafker, 1965; Shreve, 1966). The debris avalanches propagated 5.6 km along the glacier, surmounting a spur ridge rising 140 m at its southern edge, and climbing 25 m up the opposite valley wall at its northern edge. The Sherman landslide covers about 50% of the ablation area of the Sherman glacier (Post, 1967) with a highly insulating blanket of debris, which by July 1965 had already prevented the normal loss of several meters of ice.

Other, smaller ice-rock avalanches triggered by the same 1964 earthquake event involved the Shattered Peak.

We modelled a volume of 26.4 M m³ and a single rheology along the entire path. The material descends from the Shattered peak to the glacier, where the deposition started (Figure 4.6.10). On the glacier, the debris accelerates to velocities of 100-105 ms⁻¹, which are required to

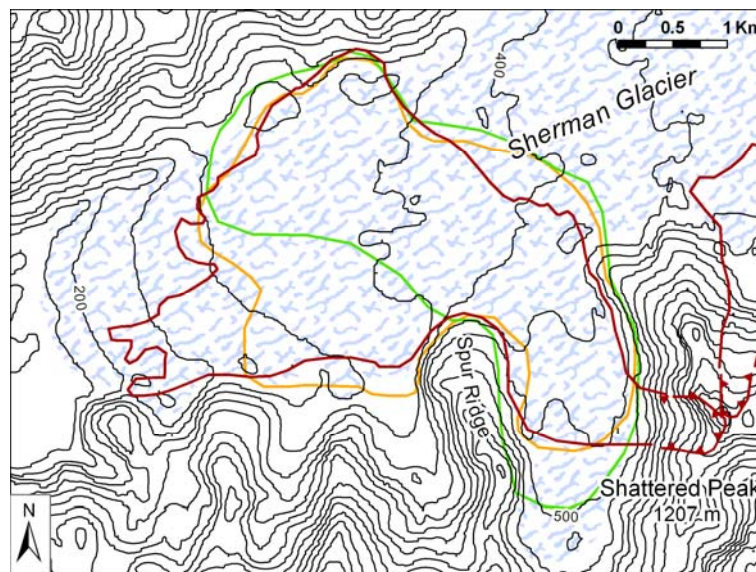


Figure 4.6.10 - Outline map of the debris avalanche deposits obtained assuming the frictional (green) and Voellmy (orange) rheologies compared against the debris-avalanche deposits from the field data (in brown).

overpass the Spur Ridge. Nonetheless, most of the material is channelled within the lateral moraines along the glacier to widen at the confluence with the Sherman Glacier.

The Voellmy rheology better replicates the propagation, and it let a deposit of low thickness (the maximum thickness is 4.5 m), along the entire path. Assuming a frictional rheology the deposition is larger at the base of the Shattered Peak, where the deposit reaches thickness of 10-12 m, whereas the deposit extends above the Sherman glacier is underestimated. The flow velocities obtained in the model are compatible with the value of 95 ms^{-1} at the base of the Shattered Peak and 52 ms^{-1} in correspondence of the Spur Ridge suggested by Shreve (1966).

Ice-rock avalanches on Martin River Glacier

The Martin River Glacier is located in south-central Alaska. The nearest town, Cordova, is approximately 96 km west of the glacier terminus. The Martin River Glacier received several major avalanches (Tuthill, 1966, Post, 1966). Together these probably contain about 24 million m^3 of broken rock. About 5% of the glacier surface was covered with rock debris. For each event, the area of propagation is mapped with an estimate of the volume involved in the movement.

We modelled six ice-rock avalanche events with volumes between 4.2 M m^3 and 15.2 M m^3 . Without other data available, the back analyses have been performed on the maximum runout and on the propagation extent (Figure 4.6.11). For the modelling, we assumed friction angles between 7° and 11° . In the Voellmy model, the frictional coefficient varies between 0.04 and 0.1, whereas the turbulent coefficient varies between 0.04 and 0.1 ms^{-2} . The topography exerts a strong control on the deposit distribution. The deposits are thin (generally they do not exceed 12-15 m) and widespread.

Ice-rock avalanches on Bering Glacier

Five ice-rock avalanches occurred on the flanks of the Mt. Steller, in the Bering Glacier. The largest avalanche (Mt. Steller, number 3) is 6.5 km in length, has a maximum width of 2 km, and contains at least 10 million m³ of rock. From a maximum source altitude of nearly 3,000 m, the rock debris descended slopes of about 43° for 600 m. On reaching the glacier, the material swept out with a gradient decreasing to less than 2° in the last 3 km.

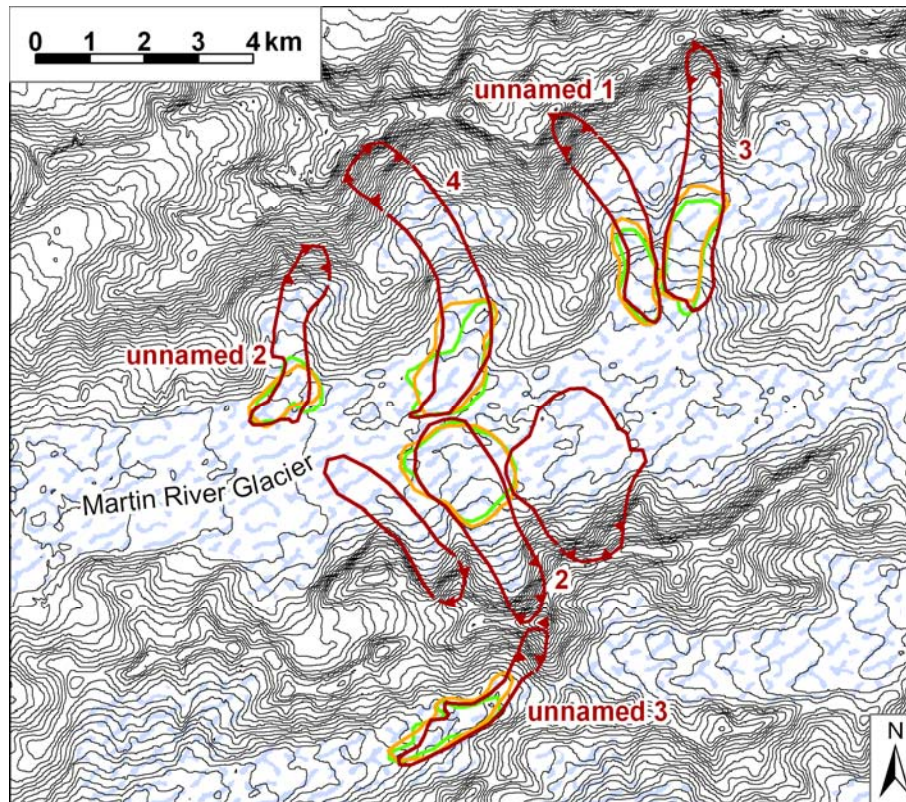


Figure 4.6.11 - Outline map of the debris avalanche deposits obtained assuming the frictional (green) and Voellmy (orange) rheologies compared against the debris-avalanche deposits from the field data (in brown).

We modeled the rock avalanches 2 and 3, assuming source volumes of 7.8 and 11.8 M m³, respectively. Again, the back analyses have been performed on the runout distance and on the propagation (Figure 4.6.12). For the modelling, we assumed friction angles between 6.8° and 8.8° for event 2 and 3, respectively. Assuming a Voellmy rheology, the best fitting parameters are $\mu=0.05$ and $\mu=0.02$, whereas $\xi=1000$ for both the cases.

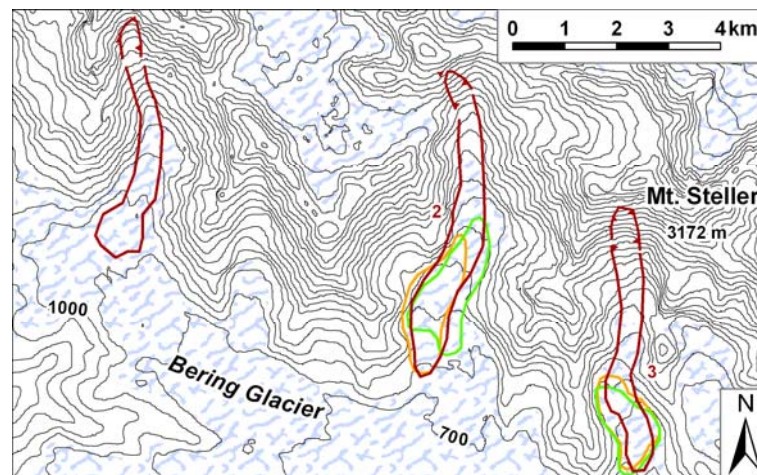


Figure 4.6.12 - Outline map of the debris avalanche deposits obtained assuming the frictional (green) and Voellmy (orange) rheologies compared against the debris-avalanche deposits from the field data (in brown).

4.6.3.2 Denali earthquake (Alaska), 2002

Shortly after midday on November 3, 2002, a magnitude 7.9 earthquake ruptured the Denali Fault in the rugged Alaska Range. Called the Denali Fault earthquake, this shock was the strongest ever recorded in the interior of Alaska.

The earthquake triggered an unusual pattern of landslides and liquefaction effects. The landslides were primarily rock falls and rock slides that ranged in volume from a few cubic meters to the 40 million-cubic-meter and contain mixtures of fractured rock, soil, ice, and snow. Landslides were concentrated in a narrow zone about 30 km wide around the fault rupture zone over its entire 300 km length. The large majority of were shallow rock falls and rock slides from steep slopes.

The most spectacular landslides triggered by the shaking were large rock avalanches having volumes of several million cubic meters that were deposited on the Black Rapids, McGinnis, and West Fork Glaciers (Jibson et al., 2006).

Black Rapids rock avalanche

The earthquake triggered three large and several smaller rock avalanches from steep granitic slopes that form the southern edge of the valley occupied by the Black Rapids Glacier (Jibson et al., 2006). The Denali Fault extends through this valley, and so the landslides occurred within a few hundred meters of the fault trace. They cascaded down steep rock slopes, crossed a lateral moraine and a medial moraine, and then spread out about 2.5 km across the glacier-filled valley, coming to rest near the opposite valley wall. The deposits were uniformly thin, about 3 m in most areas. The debris overpasses a 50 m high medial moraine, indicating that the avalanches were moving at least 45 ms^{-1} . The rock avalanches crossed the glacier and then turned and flowed some hundreds of meters down the valley on the glacier surface. The margins of the deposits are sharply defined and average 2–3 m in height.

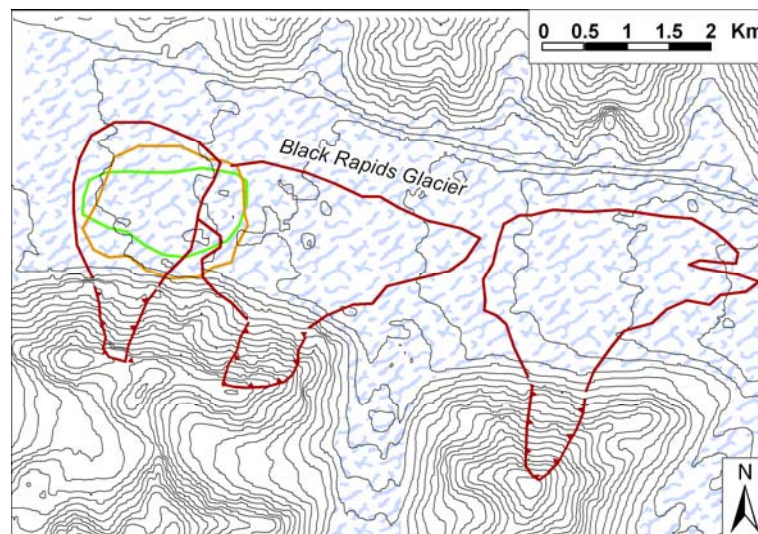


Figure 4.6.13 - Outline map of the debris avalanche deposits obtained assuming the frictional (green) and Voellmy (orange) rheologies compared against the debris-avalanche deposits from the field data (in brown).

We modeled the east most ice-rock avalanche with a volume of 9.7 M m^3 (Figure 4.6.13). The back analyzed parameters are 9° for the friction angle assumed in the frictional rheology and 0.08 and 1000 for the frictional and turbulent coefficient assumed in the Voellmy model. In both the cases, the deposit spreads with maximum thicknesses lower than 8 m and mean thicknesses of 3.2 and 4 m for the Voellmy and frictional rheology, respectively.

4.6.3.3 Rock avalanches on glaciers in the Alps

Rock fall represents a relevant hazard in high mountain areas that is expected to increase due to permafrost degradation caused by present atmospheric warming (Haeberli et al., 1997). Warming and thawing of perennially frozen rock walls can affect their stability (Gruber et al., 2004). Rock avalanches developing on high alpine environments may involve large volumes of material and move over long distances of several kilometres.

We present the modeling of two events occurred in the Italian Alps.

Luseney rock avalanche (Aosta Valley, Northwest Italy), 1952

The Becca di Luseney rock avalanche occurred on June, 1952 from the W-SW flank of the Becca di Luseney (Valpelline, Western Italian Alps) from an elevation of 3100 m a.s.l.. The detachment involved a rock volume estimated in 1 M m^3 . The rock avalanche travelled for 3 km, partially above a today extinct glacier, descending for about 1450 m. The debris came to rest near the opposite valley wall, after going up for 100 m. The main deposition occurred in the Poullaye gorge, with thicknesses of 6-7 m, and in the main valley, where it spread for a length of about 1 km and with thicknesses of 6-7 m. The accumulation blocked the valley and determined the formation of a lake of 0.3 M m^3 of water that overtopped after three days.

Propagating along the glacier, the rock avalanche entrained ice and debris, as demonstrated by the ice blocks founded in the deposit

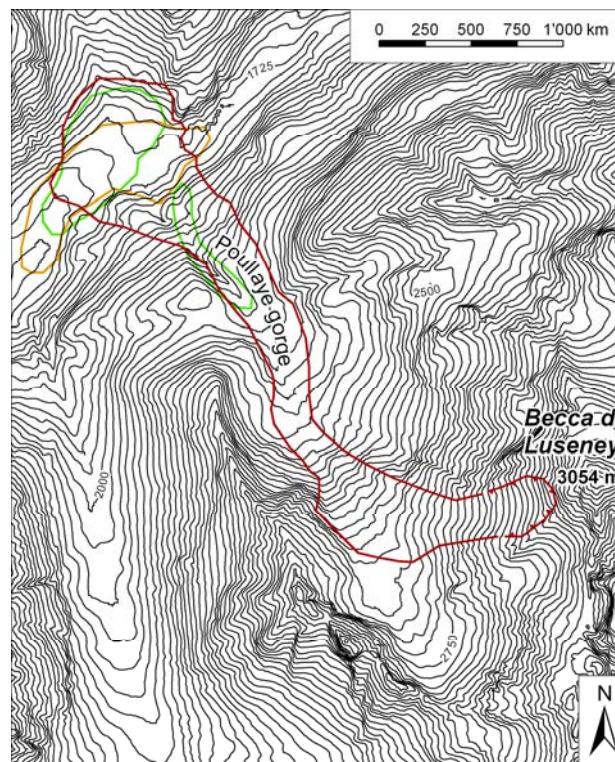


Figure 4.6.14 - Outline map of the debris avalanche deposits obtained assuming the frictional (green) and Voellmy (orange) rheologies compared against the debris-avalanche deposits from the field data (in brown).

We modelled a mass of 0.95 M m^3 in volume (Figure 4.6.14). The frictional rheology correctly replicates the deposition along the Poullaye gorge. Assuming a Voellmy rheology, all the material deposited in the valley. The runup obtained from the modeling is about 80 m for the frictional and 65 m for the Voellmy rheologies. The maximum deposit thickness in the valley is about 7-9 m.

The back analyzed parameters are 9° for the friction angle assumed in the frictional rheology and 0.08 and 1000 for the frictional and turbulent coefficient assumed in the Voellmy model. In both the cases, the deposit spreads with maximum thicknesses lower than 8 m and mean thicknesses of 3.2 and 4 m for the Voellmy and frictional rheology, respectively.

Thurwieser rock avalanche (Upper Valtellina, Central Italy), 2004

The Thurwieser rock avalanche occurred on September 18th, 2004 on the Southern flank of Punta Thurwieser (3658 m a.s.l.) in the Italian Central Alps (Sosio et al., 2008). The initial source volume (2 M m^3) consists mainly of dolostone and black limestone that detached between approximately 3.250–3.600 m a.s.l.. No exceptional meteorological event occurred in the area with temperature slightly warmer than the average. Rock fall activity was increasing progressively during the preceding few years along the southern flank of the peak and this convinced alpine guides to abandon a classical climbing route on the peak.

The avalanche travelled for about 2.9 km along the Marè valley covered by glacial ice in the upper part (Zebrù and Gran Zebrù Glaciers for about 0.6–0.65 km), and then exposed rock

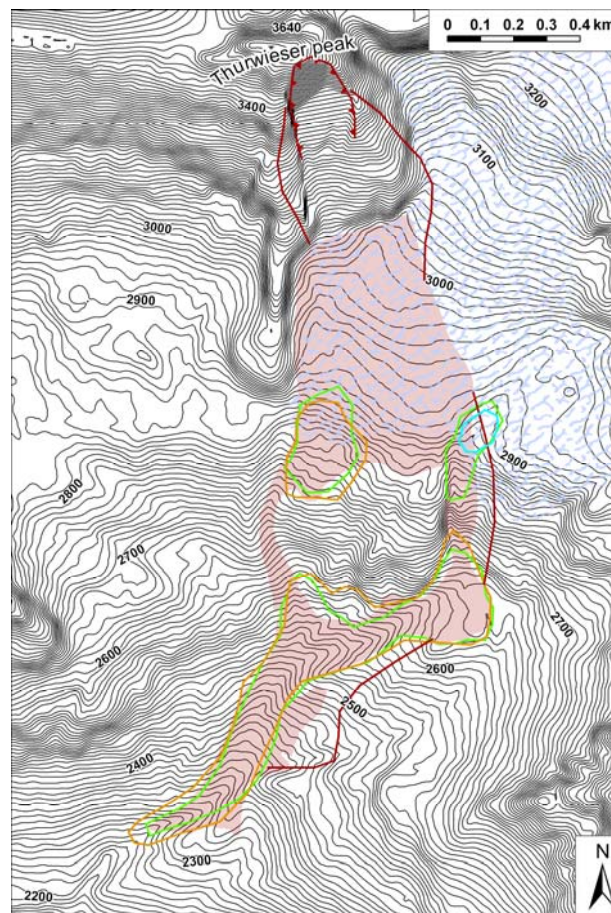


Figure 4.6.15 - Outline map of the debris avalanche deposits obtained assuming the frictional (green) and Voellmy (orange) rheologies compared against the field data (in brown). The lines identify the limits of the source area and of the propagation, the light brown in background identifies the deposition extent.

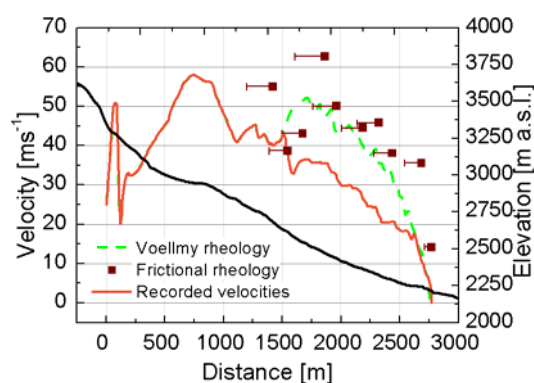


Figure 4.6.16 - Velocities simulated along the path against the velocities calculated by the video for the dusty front. The error bars represent the uncertainty related to the time lag between the dusty which is seen from the timed photos and the granular front.

(about 0.5 km) and glacial deposits (about 1 km). Most of the landslide debris accumulated on and adjacent to the glacial deposits, its propagation being controlled by Little Ice Age lateral moraines. The landslide is documented by a series photos and video recordings which allowed reconstructing almost the full evolution of the propagation. Among the data available are: (i) the landslide velocity at several locations evaluated from timed photos and energy conservation arguments in correspondence of obstacles; (ii) the time duration of the event; (iii) the thickness distribution of the deposit.

We modelled a volume of 2 M m^3 of debris (Figure 4.6.15). The rheology has been assumed as Voellmy for the track above the glacier, then it changes and the Voellmy and frictional rheology have been alternatively considered.

Both the models reproduce quite satisfactorily the longitudinal spreading of the debris along the path. Just below the glacier, the mass is roughly divided in two branches, each following a pre-existing topographic incision confined by the outcropping rock in the upper part, and by the lateral moraine in the lower part. The propagation takes approximately 75 and 90 s considering respectively the frictional and Voellmy rheologies for the track behind the Glacier. The duration obtained from the models compares to the estimation obtained from the video (80-90 s). Both the models overestimate the debris thickness at the base of the outcrops, but recognize the zone of maximum thickness along the path. The spreading above the ice is quite consistent with the debris deposit observed in the field, with deviations of less than 10% in terms of the total width.

The longitudinal profile results are shown as thickness and velocity profiles plotted for the frictional and Voellmy rheologies and compared to the observations of the final distribution and velocity of the debris (Figure 4.6.16).

4.6.4 DISCUSSIONS AND CONCLUSIONS

A number of factors are critical for the modeling and could have influenced the initial phases of the propagation and the final distribution of the deposit, particularly at the proximal end. The exact modeling of this part of the flow is important for reaching a complete modeling and test the rheological material, but is much less important as the modeling purpose is hazard and risk assessment. The reconstruction of the pre event topography from the original data is critical, especially in the areas interested by debris avalanche deposition and, for volcanic edifices, by post-collapse eruptive phenomena. At the same time, the resolution of the topographic data can control the results in terms of rheological parameters, time of mise en place, runout, and deposit features. The mode of failure (possible multiple failures, influence on the debris avalanche propagation due to toreva detachment or other volcanic processes) is another element of complexity which is not easily taken in consideration.

The nature of the failed material, the presence of juvenile material, the thickness and availability of erodible materials, the failure mechanism and the local environmental conditions (e.g. presence of lake, glaciers) strongly influence the emplacement. Nonetheless the diversity of the cases presented, the parameters derived from the back-analyses span a narrow range among each group (i.e volcanic, glacial) and they significantly differ from those typical of rock/debris avalanches evolving in other conditions.

Table 3. Rheological parameters back analyzed for the modelled events of volcanic collapse.

	Volume [km ³]	Internal friction angle	Frictional rheology	Voellmy rheology	
			Bulk friction angle [°]	Frictional coeff. [-]	Turbulent coeff. [ms ⁻²]
<i>Shiveluch</i>	1.25	10	7.5	0.03	500
<i>Lullaillaco</i>	1.5-2.0	10	5.5	0.03	1100
<i>El Crater</i>	1.8	10	5.8	0.02	1000
<i>Las Isletas</i>	1.2	10	5.5	0.04	1100
<i>Pacaya</i>	0.65-0.85	10	5.0	0.03	1200

The frictional rheology replicated the diversity of volcanic debris avalanches here considered with little variation in the back analyzed parameters (table 3). Assuming frictional rheology, the basal friction angles obtained by the back- analyses are significantly lower ($3^\circ < \phi < 7.5^\circ$) than those commonly used for non-volcanic debris avalanches ($11^\circ < \phi < 31^\circ$, McDougall 2006). Intermediate parameters are required for debris avalanches entraining deposits ($8^\circ < \phi < 13^\circ$) or partly propagating over ice ($10^\circ < \phi < 20^\circ$).

The presence of glacial ice plays a substantial role in increasing the mobility of the rock avalanche and must be accounted for in the modelling (Evans and Clague, 1988; Huggel et al., 2005). The Voellmy model is suggested to replicate the flow motion along the glacial ice, where the resistance has to be reduced to properly enhance the flow mobility. Values of $\mu=0.02-0.08$ and $\xi=1000-2000 \text{ ms}^{-2}$ provided the best results (Table 4).

Table 4. Rheological parameters back analyzed for the events of glacial rock avalanches.

	Volume [M m ³]	Internal friction angle	Frictional rheology	Voellmy rheology	
			Bulk friction angle [°]	Frictional coeff. [-]	Turbulent coeff. [ms ⁻²]
<i>Alaska, March 1964 earthquake</i>					
<i>Sherman</i>	25-30	35.0	5.6	0.03	2000
<i>Martin River 2</i>	11.2	35.0	9	0.04	1000
<i>Martin River 3</i>	8.8	35.0	8.5	0.05	1000
<i>Martin River 4</i>	15.5	35.0	7	0.05	1500
<i>Martin River unnamed 1</i>	8.9	35.0	11	0.1	1000
<i>Martin River unnamed 2</i>	6.0	35.0	9	0.04	800
<i>Martin River unnamed 3</i>	4.2	35.0	9.5	0.04	1000
<i>Baring 3</i>	8.0	35.0	8.8	0.05	1000
<i>Baring 2</i>	12.1	35.0	6.8	0.02	1000
<i>Alaska, Denali 2002 earthquake</i>					
<i>Black Rapids, west</i>	9.9	35	9.0	0.08	1000
<i>Alps</i>					
<i>Becca d Luseney</i>	1.0	35.0	9.0	0.08	1000
<i>Thurwieser</i>	2.0	35.0	12.0	0.05	1000

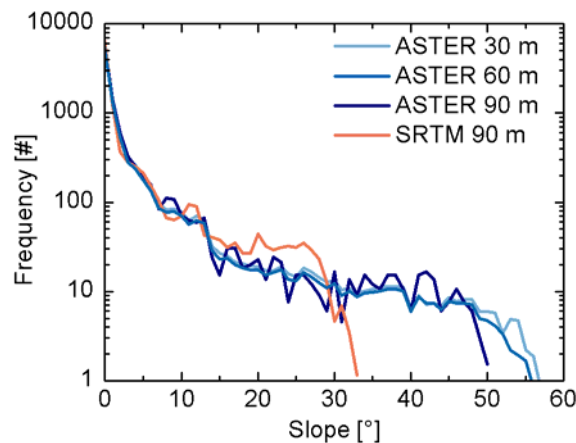


Figure 4.6.17 – Slope frequency plot for the area interested by the propagation of the El Crater (Mombacho Volcano) debris avalanches generated from the ASTER (original and resampled) and SRTM topographic data.

The effect of the cell size of the basal topography is scarcely relevant when the resampling is performed on the same original data. In the case of Mombacho, the back analysed parameters slightly increase (the bulk friction angle change from 5.8° to 6.0°) at increasing the cell size from 30 m to 90 m. We suppose that the lower values required to replicate the debris avalanche event over the finest topography serve to balance the larger roughness of the more detailed terrain. The back analysed parameters differ more at changing the data origin (i.e. ASTER vs SRTM), even at the same cell size. In this case the bulk friction angle change from 6.0° (ASTER data resampled to 90 m) to 4.6° (90 m SRTM data) is due to the different topography of the source area as defined by the two satellite datasets (Figure 4.6.17). High slopes are less represented in the SRTM topography than in the ASTER ones, suggesting lower energy available at the motion starting or shorter steep slope sectors available to accelerate the material.

4.6.5 REFERENCES

- A. Belousov, M. Belousova, B. Voight Multiple edifice failures, debris avalanches and associated eruptions in the Holocene history of Shiveluch volcano Kamchatka, Russia, **Bull. Volcanol.**, 61, 324-342 (1999)
- M. Bursik, A. Patra, E.B. Pitman, C. Nichita, J.L. Macias, R. Saucedo, O. Girina Advances in studies of dense volcanic granular flows, **Reports on Progress in Physics** 68(2), 271-301 (2005)
- Couture R., Evans S.G. (2002) A rock topple–rock avalanche, near Goat Mountain, Caribou Mountains, British Columbia, Canada, Proceedings, 9th Congress, International Association of Engineering Geology and the Environment, Durban, South Africa, Conference CD.
- Crosta, G.B. Imposimato, S. Roddeman, D. Chiesa, S. Moia, F. (2005) Small fast-moving flow-like landslides in volcanic deposits: The 2001 Las Colinas Landslide (El Salvador). **Eng. Geol.**, 79 3-4, 185-214.

-
- Eckel, E. B., 1970, The Alaska earthquake, March 27, 1964: Lessons and conclusions: **U.S. Geol. Survey Prof. Paper** 546, 57 p.
- Evans, S.G., Clague, J.J., 1988. Catastrophic rock avalanches in glacial environments. In: Bonnard, C. (Ed.), Proceedings **5th International Symposium on Landslides**, 11–15 July, Lausanne, Switzerland. Balkema, Rotterdam, pp. 1153–1158.
- Evans SG, Clague JJ (1999) Rock avalanches on glaciers in the Coast and St. Elias Mountains, British Columbia. In: Proceedings of the 13th **Annual Vancouver Geotechnical Society Symposium**, Vancouver, pp 115–123
- Geertsema, M., Clague, J.J., Schwab, J., Evans, S.G., 2006. An overview of recent large catastrophic landslides in northern British Columbia. **Eng. Geol.** 83, 120–143.
- Gruber S., Hoelzle M., Haeberli W. (2004). Rock wall temperatures in the Alps: modelling their topographic distribution and regional differences. **Permafr. Periglac. Process.** 15(3) 299Y307.
- Hackman, R.J., (1965) Interpretation of Alaskan post- earthquake photographs. **Photogrammetric Engineering**, 31, 604-610.
- Haeberli W., Wegmann M., Vonder Muhll D., (1997). Slope stability problems related to Glacier shrinkage and permafrost degradation in the Alps, **Eclogae Geol. Helv.** 90: 407Y414.
- Hayashi JN, Self S (1992) A comparison of pyroclastic flow and debris avalanche mobility. **J Geophys Res** 97:9063 9071.
- Huggel, C., Zraggen-Oswald, S., Haeberli, W., Kaab, A., Polkvoj, A., Galushkin, I., Evans, S.G., 2005. The 2002 rock/ice avalanche at Kolka/Karmadon, Russian Caucasus: assessment of extraordinary avalanche formation and mobility, and application of QuickBird satellite imagery. **Nat. Hazards Earth Syst. Sci.** 5 (2), 173–187.
- Hungr O, Evans SG, (1996) Rock avalanche runout prediction using a dynamic model. In: Senneset. (Ed.), Procs., **7th. International Symposium on Landslides**, Trondheim, Norway, 1:233-238.
- Hungr, O., 1995. A model for the runout analysis of rapid flow slides, debris flows, and avalanches. **Can. Geotech. J.** 32, 610–623.
- Hsü K.J., 1975. Catastrophic debris streams, sturzstroms generated by rockfalls. **Geol. Soc. Am. Bull.** 86, 129–140.
- Jibson, R.W., Harp, E.L., Schulz, W., Keefer, D.W., 2006. Large rock avalanches triggered by the M 7.9 Denali Fault, Alaska, earthquake of 3 November 2002. **Eng. Geol.** 83 (1–3), 144–160.
- Katayama S, Matias O, (1995) Tephra stratigraphic approach to the eruptive history of Pacaya volcano, Guatemala, Sci Rpt Tohoku Univ, **7th Ser (Geog)**, 45: 1-41.
- Kelfoun K, Druitt TH (2005) Numerical modeling of the emplacement of Socompa rock avalanche, Chile. **J Geophys Res** 110, B12202.1-12202.
- McDougall S (2006) **A new continuum dynamic model for the analysis of extremely rapid landslide motion across complex 3d terrain**. PhD thesis, University of British Columbia, Vancouver.

- McDougall S, Hungr O (2004) A model for the analysis of rapid landslide motion across three dimensional terrain. **Can Geotech J.**, 41, 1084-1097.
- McDougall, S., 2006. A new continuum dynamic model for the analysis of extremely rapid landslide motion across complex 3d terrain. Ph.D. Thesis, University of British Columbia, 253 p.
- McGuire WJ (1996) Volcano instability: a review of contemporary themes. In: McGuire WJ., Jones AP, Neuberg J (eds) Volcano Instability on the Earth and other Planets, **Geological Society Special Publication**, 1–24.
- Plafker G., Mayo L.R. (1965) Tectonic deformation, subaqueous slides and destructive waves associated with the Alaskan March 27, 1964 earthquake-an interim geologic evaluation: **U.S. Geol. Survey, Open-File Report**, 19 p.
- Plafker, George, 1965, Tectonic deformation associated with the 1964 Alaska earthquake : **Science**, 148, 1675-1687.
- Ponomareva VV, Pevzner MM, Melekestsev IV (1998) Large debris avalanches and associated eruptions in the Holocene eruptive history of Shiveluch volcano, Kamchatka, Russia. **Bull Volcanol** 59(7), 490-505.
- Post A (1967) The Alaska earthquake March 27, 1964: effects on hydrologic regimen. **U. S. Geological Survey Professional Paper** 544-D.
- Richards JP, Villeneuve M (2001) The Llullaillaco volcano, northwestern Argentina: construction by Pleistocene volcanism and destruction by edifice collapse. **J Volcanol Geotherm Res** 105:77-105.
- Schwab, J.W., Geertsema, M., Evans, S.G., 2003. Catastrophic rock avalanches, westcentral B.C., Canada. **3rd Canadian Conference on Geotechnique and Natural Hazards**, Edmonton, AB, pp. 252–259.
- Shea T, van Wyk de Vries B, Pilato M (2008) Emplacement mechanisms of contrasting debris avalanches at Volcán Mombacho (Nicaragua), provided by structural and facies analysis. **Bull Volcanol** 70, 899-921.
- Shreve, R. L., 1966, Air-layer lubrication of large avalanches **Cabs. Geol. Soc. America Spec. Paper** 87, p. 154.
- Siebert L (1984) Large volcanic debris avalanches: characteristics of source areas, deposits and associated eruptions, **J Volcanol Geotherm Res** (22), 163-197.
- Siebert L (1996) Hazards of large volcanic debris avalanches and associated eruptive phenomena. In: Scarpa R Tilling RI (eds) **Monitoring and Mitigation of Volcanic Hazards**, Berlin. Springer–Verlag, 541-572.
- Siebert L (2002) Landslides resulting from structural failure of volcanoes. In: Evans SG De Graff JV (eds) Catastrophic landslides: Effects, Occurrence, and Mechanisms **Geol Soc Amer Rev Eng Geol**, 15: 209–235.
- Sosio R, Crosta GB, Hungr O (2008) Complete dynamic modelling calibration for the Thurwieser rock avalanche (Italian Central Alps). **Eng. Geol.**, 100(1-2), 11-26.
- Stoopes GR, Sheridan MF (1992) Giant debris avalanches from the Colima Volcanic Complex, Mexico: implication for long-runout landslides (>100 km). **Geology**, 20, 299-302.
-

Tuthill, S. J., 1966, Earthquake origin of superglacial drift on the glaciers of the Martin River area, southcentral Alaska. **Jour. Glaciology**, 6 (43) 83-86.

Ui T (1983) Volcanic dry avalanche deposits - identification and comparison with non-volcanic debris stream deposits. **J Volcanol Geotherm Res.**, 18, 135-150.

Vallance JW, Siebert L, Rose WI, Girón J, Banks NG (1995) Edifice collapse and related hazards in Guatemala. **J. Volcanol. Geotherm. Res.**, 66, 337-355.

van Wyk de Vries B, Francis PW (1997) Catastrophic collapse at stratovolcanoes induced by gradual volcano spreading. **Nature** 387, 387–390.

Wood CA, Francis PW (1985) Large volcanic debris avalanche deposits in the Central Andes. **EOS** 66, pp. 410.

Wyss M., Brune J.N., (1967) The Alaska earthquake of 28 March 1964: a complex multiple rupture. **Bull. Seismol. Soc. Am.** 57, 1017–1023.

D1.7 Landslide runout

Appendix I – Overview of run-out models for landslide hazard and risk assessment

The following organisations contributed to the work described in this deliverable:

Lead partner responsible for the appendix:

ITC

Deliverable prepared by:

Byron Quan Luna

Partner responsible for quality control:

ICG/NGI

Deliverable reviewed by:

Dieter Issler

CONTENTS

1	Introduction	3
2	Run-out models	4
2.1	Empirical models	4
2.2	Application of empirical methods to regional risk assessments in past studies	12
2.3	Analytical models	14
2.4	Numerical models	15
3	Classification of numerical run-out models.....	18
3.1	Classification based on the solution dimension (1D, 2D or 3D)	18
3.2	Classification based on the solution reference frame (Eulerian or Lagrangian)	18
3.3	Classification based on the flow rheology	20
4	An overview of selected dynamic run-out models.....	22
5	Run-out models for hazard analysis in a Quantitative Risk Assessment (QRA).....	25
6	References	28

1 INTRODUCTION

Run-out analysis can be defined as the prediction of landslide dynamics and consequences. In recent times, the numerical models for simulating debris-flow run-out have been increasingly used for elaborating risk and hazard maps. These tools support public authorities managing landslide hazards. Computer modeling allows them to study a range of potential scenarios in advance in the framework of Quantitative Risk Assessment (QRA), to design proper strategies for mitigation and to inform the affected populations of these natural hazards so that they can respond appropriately.

Knowing the extent of the endangered area is very important in a QRA. This requires accurate prediction of the run-out behavior of the landslide in question, such as how far and how fast the landslide will travel. The run-out behavior can be described by a set of spatially distributed quantitative parameters. For the purpose of landslide risk assessment, these parameters mainly include (Hung, 1995):

- Area potentially affected by the landslide;
- Spatial distribution of maximum velocity;
- Pressure
- Depth of the moving mass;
- Depth of deposits.

Once the risk from a landslide is assessed, measures may be taken to mitigate the risk to the community. The community faced with a landslide might have several strategies to deal with it, and these strategies may be grouped into: planning control; engineering works; acceptance (tolerance); and monitoring and warning systems. Planning control aims at reducing the expected number of elements at risk; the engineering solution strategy is to reduce either the occurrence probability of a landslide or its spatial impact. The acceptance strategy considers losses as unavoidable or acceptable while the monitoring and warning system strategy reduces the number of expected elements at risk by evacuation in advance of failure.

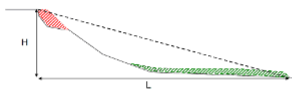
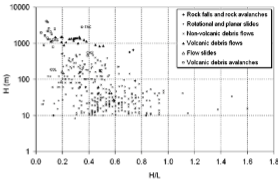
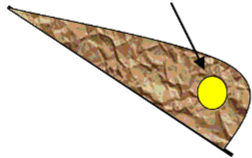
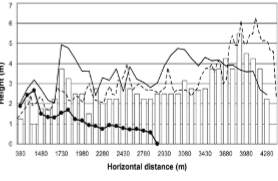
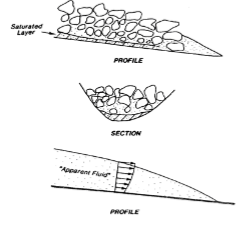
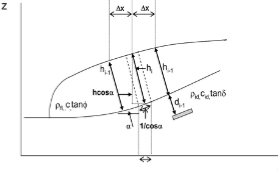
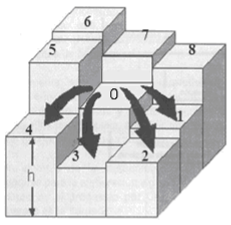
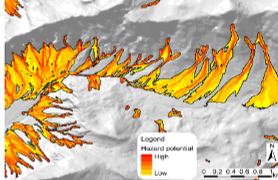
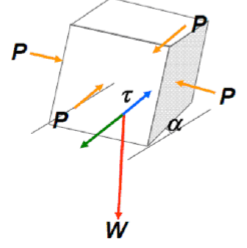
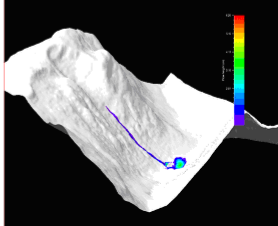
2 RUN-OUT MODELS

Several approaches have been developed to model fast gravitational mass movements in order to assess their characteristics, intensities and run-out. These approaches vary with respect to the required scope of the assessment, the scale of analysis, the available input data and the extent of the outputs required. A very important part of any landslide risk assessment is a quantitative estimate of post-failure motion defining distance, material spreading and velocity as a function of the assumed scenario that defines the initial conditions. It should be understood that the movement of a landslide is complex and more than one flow regime may be operating at any given time, and different processes may prevail at different locations of a given event. For this reason, no universal run-out model exists, i.e., no single model can adequately describe all the movement types. However, the developed methods give a good systematic approach to assessing the spreading, extension and impact that a landslide can generate. These methods can be divided into *empirical methods*, *analytical methods* and *numerical methods*. A good overview of methods for run-out modeling is given by Hungr et al. (2005) and Hürlimann et al. (2008). The main characteristics of the various methods are summarized in Fig. 1.

2.1 EMPIRICAL MODELS

Empirical methods for assessing landslide run-out are usually based on extensive amounts of field observations and on statistical analysis of the relationships between the run-out distance and different landslide mechanisms, their morphometric parameters, the volume of the landslide mass, and the characteristics of the terrain. Empirical approaches are based on simplified assumptions and are relatively easy to apply over large areas. Empirical methods can be subdivided into i) *heuristic methods*, ii) *the mass-change method* and iii) *the angle-of-reach method*.

Heuristic methods are based on the assumption that the spatial extent of past landslides on a given slope provides a first estimate of the spatial extent of future landslides with corresponding frequency (Hungri et al., 2005). Field work and photo interpretation are classical procedures used to define the spatial distribution and extent of past landslides. This approach will work best in situations where landslides are frequent and their occurrence does not change

Dimension of calculations	Type of methods	Inputs	Outputs
1-D	<p>Empirical methods</p> <ul style="list-style-type: none"> • Heuristic • Angle of reach • Mass-change 	<ul style="list-style-type: none"> • Volume • Topographic profile • Visual, fieldwork and geomorphologic interpretation 	<ul style="list-style-type: none"> • Maximum run-out • Area of deposit  <p>(Devoli <i>et al.</i>, 2009)</p>
	<p>Analytical methods (point mass models)</p> 	<ul style="list-style-type: none"> • Rheologic parameters • Topographic profile 	<ul style="list-style-type: none"> • Maximum run-out • Velocity 
	<p>Numerical methods (continuum approach)</p>  <p>(Hungri, 1995)</p>	<ul style="list-style-type: none"> • Rheologic parameters • Topographic profile • Volume 	<ul style="list-style-type: none"> • Maximum run-out • Velocity • Impact pressures • Flow depth 
2-D	<p>Flow routing methods</p> 	<ul style="list-style-type: none"> • DEM (Digital elevation model) 	<ul style="list-style-type: none"> • Pxy= probability of each cell to be affected by a flow • Flow trajectories and extension of deposits  <p>(Horton <i>et al.</i>, 2008)</p>
	<p>Numerical methods</p> 	<ul style="list-style-type: none"> • DEM • Rheologic parameters • Volume 	<ul style="list-style-type: none"> • Extension of deposit • Velocity • Flow depth • Impact pressures 

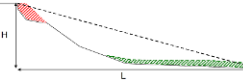
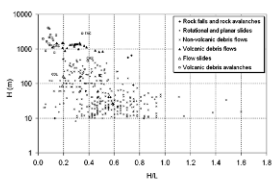
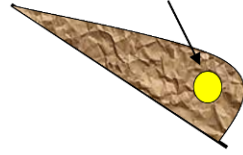
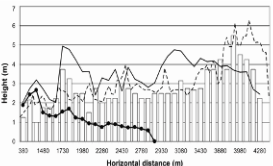
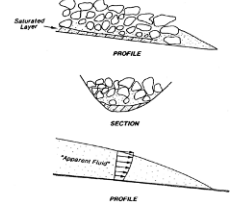
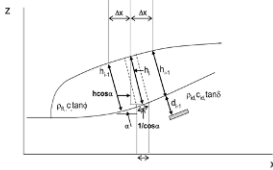
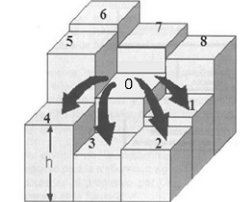
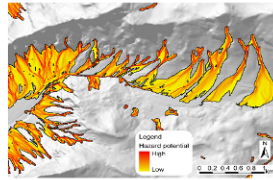
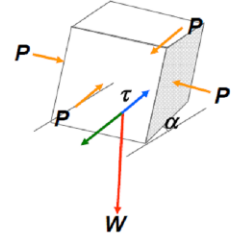
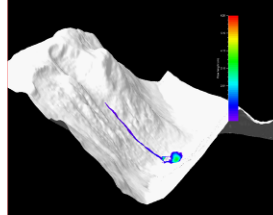
Dimension of calculations	Type of methods	Inputs	Outputs
1-D	<p>Empirical methods</p> <ul style="list-style-type: none"> • Heuristic • Angle of reach • Mass-change 	<ul style="list-style-type: none"> • Volume • Topographic profile • Visual, fieldwork and geomorphologic interpretation 	<ul style="list-style-type: none"> • Maximum run-out • Area of deposit • Flow depth  <p>(Devoli <i>et al.</i>, 2009)</p>
	<p>Analytical methods (point mass models)</p> 	<ul style="list-style-type: none"> • Rheologic parameters • Topographic profile 	<ul style="list-style-type: none"> • Maximum run-out • Velocity 
	<p>Numerical methods (continuum approach)</p>  <p>(Hungri, 1995)</p>	<ul style="list-style-type: none"> • Rheologic parameters • Topographic profile • Volume 	<ul style="list-style-type: none"> • Maximum run-out • Velocity • Impact pressures • Flow depth 
2-D	<p>Flow routing methods</p> 	<ul style="list-style-type: none"> • DEM (Digital elevation model) 	<ul style="list-style-type: none"> • Pxy= probability of each cell to be affected by a flow • Flow trajectories and extension of deposits  <p>(Horton <i>et al.</i>, 2008)</p>
	<p>Numerical methods</p> 	<ul style="list-style-type: none"> • DEM • Rheologic parameters • Volume 	<ul style="list-style-type: none"> • Extension of deposit • Velocity • Flow depth • Impact pressures 

Fig. 1. Schematic overview of run-out modeling methods and the dimensions of their calculation domains.

properties (topography, geomorphology, and lithology) of the mountainside so fundamentally that the frequency and/or size of future landslides in the same slope changes considerably. The foremost example is small and moderate-sized debris flows in catchments where rockfalls due to weathering provide a quasi-continuous and quasi-constant source of mobilizable material in the channel.

The mass-change method is based on the fact that as the landslide debris moves down slope, the initial volume/mass of the landslide is being modified through loss or deposition of material, and that the landslide debris halts when the volume of the actively moving debris becomes negligible (Cannon and Savage, 1988). They determined the average mass/volume-change rate of landslide debris by dividing the difference of the volumes of mobilized material and of the final deposit by the length of the debris trail. This method does not explicitly account for the mechanics of the entrainment/deposition process.

The angle-of-reach method is based on the angle of the line connecting the escarpment of the landslide source to the distal margin of the displaced mass (Fig. 2). The angle of reach is also used as an index of efficiency for the dissipation of energy and so is inversely related to mobility. Once the release source, volume and direction of the flow are known and the most probable angle of reach has been selected, the length of the run-out can be estimated.

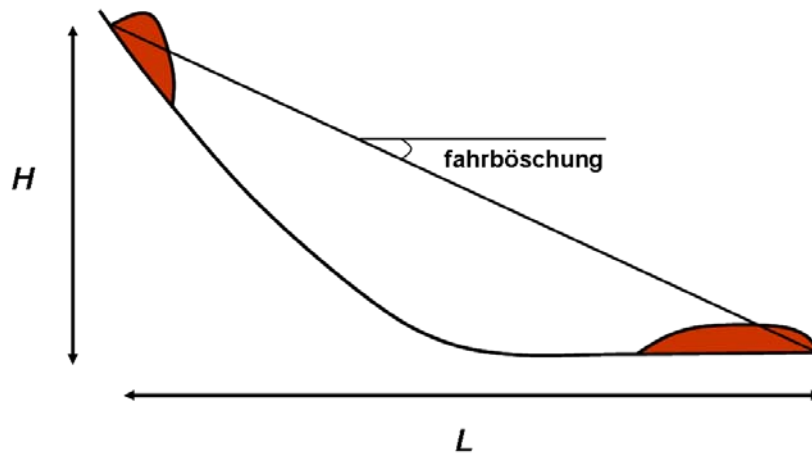


Fig. 2. Schematic representation of the angle of reach or fahrböschung. H is the elevation difference between the escarpment and the toe of the deposit, and L is the length of the horizontal projection of the line connecting these two points.

When the landslide source and potential landslide volume are known, the travel distance can be obtained from the following expression:

$$L = \frac{H}{\tan \alpha}, \quad (1)$$

In addition, other empirical expressions have been proposed based on the inverse relationship between the tangent of the reach angle (H/L) and the landslide volume (e.g. Devoli et al., 2008). These relations generally assume a reduction of H/L with a volume increase:

$$\log(\tan[\alpha]) = A + B \log V, \quad (2)$$

where A and B are constants and V is the landslide volume.

Because of the large range and inconsistent pattern of the volume values, the correlation coefficients of the relationship between volume and H/L may be too small to be used for runout prediction. In order to improve the regression equations, Corominas (1996) performed an analysis using more homogeneous landslide populations. Landslides were split into different groups according to their predominant propagation mechanism (rock falls and avalanches, translational slides, debris flows and earth flows) and the characteristics of the path (i.e. unobstructed, channeled, forested, obstructed by an opposite slope, etc.). The regression

equations showed a noticeable improvement. The reasons that explain the scattering are manifold: (i) different motion mechanisms; (ii) different material properties, plus residual strength is not considered; (iii) pore fluid pressures are not accounted for; (iv) simplified morphology; and (v) a variety of path constraints. However, the angle-of-reach approach is the most commonly used method in assessing the run-out of landslides due to its simplicity and straightforward results.

Besides the run-out length, statistical methods can be used to estimate other landslide run-out characteristics as well. Rickenmann (1999) also used regression equations and proposed a series of empirical relations for debris flows to estimate the peak discharge, the mean flow velocity, the total travel distance, and the run-out distance on the fan. In addition, the spreading pattern of the flow and deposition can also be estimated. This requires more detailed morphological parameters accounting exclusively for site-specific conditions. Similar to the volume–angle of reach approach, statistical correlations between volume and deposit area have also been proposed by Iverson et al. (1998) with the LAHARZ model. LAHARZ is a GIS code and is based on a semi-empirical model which delineates lahar inundation hazard zones (i.e. areas drawn to depict probable inundations during a lahar event) on a Digital Elevation Model (DEM). The program uses two semi-empirical equations calibrated by statistical analysis of the cross-sectional area inundated by a lahar, A (Eq. 3), and the planimetric area inundated by a lahar, B (Eq. 4), measured for 27 lahar deposits located at nine volcanoes in the USA, Mexico, Colombia, Canada and Philippines (Iverson **et al.**, 1998). These equations are constrained by physical scaling arguments assuming a flow that moves downstream as an evolving, translating waveform of constant bulk density, mass and volume (Iverson **et al.**, 1998). The equations are:

$$A = \alpha_1 V^{\frac{2}{3}} \quad (3)$$

$$B = \alpha_2 V^{\frac{2}{3}} \quad (4)$$

where V is the volume of the lahar, $\alpha_1 = 0.05$ (constant value), $\alpha_2 = 200$ (constant value).

The method for selecting a starting point in LAHARZ is based on an energy cone ratio, namely the H/L ratio, where H is the drop height of the volcano and L is the distance away from the center of the summit at which lahars begin depositing. When a volume is entered into the model, the material is deposited in each cross section until the average area for that volume is reached. The remaining material is then passed to the next cross section and the process is repeated until the average planimetric area for that given volume has been reached. LAHARZ uses the mass conservation principle, meaning that the volume of material used as initiation volume equals the volume of the deposit.

One of the most recent efforts to map debris-flow susceptibility in two dimensions at intermediate scales is the software Flow-R developed by Horton et al. (2008) at the University of Lausanne, Switzerland. This software uses a GIS-based approach that couples automatic detection of the source areas and a simple assessment of the debris flow spreading (Kappes et al., 2011). Flow-R attempts to visualize existing or potential new susceptibility zones at a regional scale with limited data and without any notion of intensity or occurrence probability. The Flow-R model is divided in two modules: (1) *source area identification*, where the sediment availability is linked to the lithology type; the upslope contributing area is considered as a function of the water input; and the slope angle, the plan curvature and the land use map are added to increase the detection accuracy; (2) *spreading area assessment*, where the software selects each calculated source area and spreads the corresponding starting mass over the terrain. The spreading can be mathematically estimated by two types of algorithms. Algorithms of the first type are called flow routing algorithms, which determine the path that the debris flow will follow. Algorithms of the second type determine the runout distance. Flow direction algorithms distribute the flow from one cell to its eight neighbors. Some conditions are defined so that there is always at least one cell in which the flow can run; runout-distance algorithms only determine whether that mass flows further or stops. The runout distance algorithms inside the model are energy-based calculations that determine whether a part of the debris flow can potentially reach another cell or not. Flow-R does not consider the release volume in its routing calculation routines. Thus, run-out distance calculation is

based on the energy balance (per unit mass), a constant loss function and a maximum velocity threshold (Horton et al., 2008):

$$E_{\text{kin}}^i = E_{\text{kin}}^{i-1} + \Delta E_{\text{pot}}^i - E_{\text{loss}}^i \quad (5)$$

where i numbers the time step, E_{kin} is the kinetic energy, ΔE_{pot} is the change in potential energy and E_{loss} denotes a constant energy dissipation rate times the timestep.

Another way to express the spatial susceptibility considering the area affected by the arrival of landslide debris was proposed by Li (1983). An approximate proportionality was found between the volume (V) of the landslide debris and the area (A) covered by it. The following empirical equation was derived for V measured in m^3 and A measured in m^2 :

$$\log A = 1.9 + 0.57 \log V. \quad (6)$$

Empirical methods assess the interactions between the characterizing factors of the source area, the travel path (topography and morphology), the landslide volume, and the travel distance. Based on the information gathered via field observation or image interpretation, statistical analyses are performed. These analyses result in statistical functions that express directly or indirectly the mobility of the moving mass. However, a common problem with the empirical methods is that the scatter of the data is too large for anything but very preliminary predictions of the travel distance. The flexibility of the empirical methods allows them to be applied in landslide susceptibility and hazard mapping at local to medium scale but as they do not provide kinematic parameters (velocity, kinetic energy) of the landslides, these approaches can hardly be applied to site-specific analyses and in quantitative risk assessment. Another disadvantage of the empirical-statistical methods is the demand for reliable data with cumbersome information like release source point, toe deposition point, and starting and final volume.

2.2 APPLICATION OF EMPIRICAL METHODS TO REGIONAL RISK ASSESSMENTS IN PAST STUDIES

Medium-scale analysis, which provides maps at the scale between 1:10 000 and 1: 50 000 (van Westen et al., 2006) can provide an initial overview of the hazard in a specific area. The

goal of a medium-scale analysis is to identify all the potentially unstable areas as accurately as possible and the down-slope regions probably affected by the flow. This analysis should be used as a first assessment for the potential impact zones and to give an indication of where further local studies should be carried out with more detail.

In the past, several studies of rapid mass movements and debris flows in mountainous environment at medium scale successfully used empirical-statistical methods to calculate the run-out.

Miller and Burnett (2008) used available digital elevation and land-cover data (DEMs at 10 m resolution and 25 m satellite imagery) to assess debris-flow run-out paths at a regional scale. They presented a model for using these data to calculate empirical probabilities for debris-flow run-out over flow paths determined from the DEM and showed how these probabilities can be combined over all sources to estimate the potential for debris-flow delivery to stream reaches throughout entire channel networks. The model was calibrated and model predictions were compared to field-mapped debris-flow travel paths from study sites in the Coast Range of Oregon, USA. Their model predicts debris-flow probability over channel-reach scales that can be aggregated to basin-scale measures of debris-flow potential.

Strîmbu (2011) presented a travel distance model for debris flows based on information collected in southeastern British Columbia, Canada. The model incorporates a variable that represents terrain morphology by a single number. The terrain morphology was defined by a site-specific character, providing a process-based representation of local conditions. Multiple regression analysis was used to assess the dependence of event travel distance on terrain morphology, slope, stand height, terrain curvature and canopy closure.

Following a similar approach, Tang et al. (2012) proposed an empirical regression model for preliminary estimates of the maximum run-out length and lateral width of debris flow in fans for an earthquake-affected region. From the September 24, 2008 rainfall event in the

Wenchuan (Biechuan County, China) earthquake area, 46 debris-flow catchments with well-defined debris-flow deposits on alluvial fans were selected for the analysis. Their model estimated debris-flow run-out zones from easily measurable topographic parameters and sediment supply in a drainage basin. Among the terrain parameters used for the prediction of the characteristics of debris flow run-out zones, the volume of removable sediment was the most important factor for establishing an applicable prediction model. To determine the variables needed for the prediction of debris flow run-out characteristics on alluvial fans, multiple regression analysis was used to establish models for the prediction of the characteristics of debris-flow run-out zones.

Conway et al. (2010) used iso-maps and associated field observations, to determine a relationship between ground slope and patterns in deposition volume in the Westfjords of Iceland. They used their finding as a basis for an empirical model that allows estimating the total travel distance and final thickness of future debris flows.

Toyos et al. (2007) based their approach to simulating the maximum run-out of debris flows on the events that occurred in May 1998 in the area of Sarno, southern Italy. Flow mobility ratios (H/L) were derived from the x , y , z coordinates of the lower-most limit of the source areas (i.e. the apex of the alluvial fan) and the distal limit of the flows. They performed a regression analysis that showed a correlation between the estimated flow volumes and mobility ratios. As mentioned before, thanks to their simplicity, statistical and empirical models are often the method of choice and constitute a well established approach for assessing the hazard at a medium scale (Liu et al., 2002; Castellanos, 2008).

2.3 ANALYTICAL MODELS

Analytical methods include different formulations based on lumped mass approaches in which the debris mass is assumed to be concentrated in a single point. The simplest type of analytical method is the sled model (Sassa, 1988), which assumes that all energy loss during debris movement is due to friction and that the landslide can be described as a dimensionless

body moving down the profile of the path. The movement is controlled by a single resultant force, lumping together the gravity driving force and all movement resistance. The ratio of the vertical to horizontal displacement of the center of gravity of the block equals the friction coefficient used in the analysis. This method can provide an effective means for the calculation of run-out distance, velocity and acceleration of debris movement. Sassa (2000) improved the sled model by considering the effect of pore fluid pressures at the sliding plane. The apparent friction angle in the improved sled model can be expressed as the combined effects of the internal friction angle of debris material, and the motion-induced pore pressure. Hutchinson (1986) developed a model for the prediction of run-out distances of flows in loose, cohesionless materials by assuming that the shape of a debris flow is a uniformly spread-out sheet. In the model, the basal resistance of the debris mass is assumed to be purely frictional, and the excessive fluid pressure in the debris mass is assumed to be dissipating according to one-dimensional consolidation theory. As debris moves down-slope, the shear resistance on the sliding plane increases due to dissipation of excessive pore pressure. The debris mass decelerates when the resultant force along the sliding plane becomes negative, i.e., opposite to the velocity. The analytical approaches provide an estimate of the velocity profile and acceleration of the landslide (Hungr, 1995), which can be used to estimate impact pressures.

2.4 NUMERICAL MODELS

These models are based on fluid mechanics and solve the equations of mass and momentum conservation numerically after discretizing them in both space and time. The stresses in the momentum conservation equation are determined from the assumed constitutive law of the flowing material. Most models are based on a “continuum approach” that considers the loose, unsorted, multiphase material of a landslide as a continuum. A continuum approach offers the possibility to model the dynamics of debris flows using an “equivalent” fluid, whose rheological properties are such that the bulk behavior of the numerically simulated flowing mass approximates the expected bulk behavior of the real mixture of the solid and fluid phases (Hungr and McDougall, 2009).

Savage and Hutter (1989) developed a continuum-mechanical theory (also known as the Savage–Hutter model) capable of describing the evolving geometry of a finite mass of a granular material and the velocity distribution as it slides down an inclined plane (Pudasaini and Hutter, 2007). In the Savage–Hutter model, the mass and momentum are averaged over the depth and a scaling analysis is performed with respect to the aspect ratio of the flowing mass, considered to be small. This allows modeling the flow by a Saint-Venant-type system (shallow water equations) derived in a reference frame linked to an inclined plane (Bouchut et al., 2008). The depth-averaged shallow water equation approach using different solvers has been applied commonly for numerical simulations of rapid mass movements over complex topographies (e.g. Briukhanov et al., 1967; Cheng and Lee, 2000; Iverson and Denlinger, 2001; Crosta et al., 2003; Mangeney et al., 2005; Pitman and L  , 2005; Pudasaini and Hutter, 2007; Pastor et al., 2009; Hungr and McDougall, 2009; Medina et al., 2008; Begueria et al., 2009; Christen et al., 2010). Depth averaging allows representing the rheology of the flow as a single term that expresses the frictional forces that act at the interface between the flow and the bed. Under the shallow water assumption, different types of solutions (1D and 2D) for fast gravitational flows can be derived from the momentum equation for unsteady fluid flow, evaluating the dynamic equilibrium for a single column (or discretized unit) isolated from the flowing mass:

$$\frac{\partial h}{\partial t} + \frac{\partial(hu)}{\partial x} + \frac{\partial(hv)}{\partial y} = 0, \quad (7)$$

$$\frac{\partial u}{\partial t} + u \frac{\partial u}{\partial x} + v \frac{\partial u}{\partial y} = -g \left(S_x + k \frac{\partial h}{\partial x} + S_f q_x \right), \quad (8)$$

$$\frac{\partial v}{\partial t} + u \frac{\partial v}{\partial x} + v \frac{\partial v}{\partial y} = -g \left(S_y + k \frac{\partial h}{\partial y} + S_f q_y \right), \quad (9)$$

where h is the flow thickness, (u, v) are the x and y components of the depth-averaged velocity (m/s). Equation (7) is the mass balance equation. The momentum equations (8) and (9) are expressed in terms of acceleration (m/s^2), where g is the acceleration due to gravity. The first term on the left side of the equation represents the local acceleration, expressing the time rate of change at a fixed position. The second and third terms on the left side of the equation

represents the convective acceleration, i.e. the time rate of change due to change in position in the spatial field. The first term between the brackets represents the acceleration due to gravity, and $S_x = \tan \alpha_x$ and $S_y = \tan \alpha_y$ are the bed slopes in the x and y directions, respectively. The spatial derivative in the second term is the pressure acceleration, i.e. the time rate of change due to pressure differences within the flow. Non-hydrostatic normal stresses were introduced by Savage and Hutter (1991), who assumed that the moving mass is frictional and undergoes plastic deformation according to the Rankine theory:

$$K_a = \frac{1 - \sin \varphi}{1 + \sin \varphi}, \quad K_p = \frac{1 + \sin \varphi}{1 - \sin \varphi} \quad (10)$$

The term k in Eqs. (8) and (9) is the earth pressure coefficient. It ranges between two extreme values corresponding to the active and passive states in the Rankine theory, i.e. $k_a \leq 1 \leq k_p$ given in Eq. (10). These values depend on the internal friction angle, φ , of the mixture (Savage and Hutter, 1989). S_f is the flow resistance gradient, which accounts for momentum dissipation within the flow due to frictional stress at the bed. The terms q_x and q_y are directional coefficients:

$$q_x = \frac{-u}{\sqrt{u^2 + v^2}}, \quad q_y = \frac{-v}{\sqrt{u^2 + v^2}} \quad (11)$$

where the minus sign before u and v ensures that S_f opposes the direction of the velocity.

One of the advantages of the numerical methods is that they compute the movement of the flow over irregular terrain with a good compromise between computing effort and accuracy. Besides this, the computed output of the models provides the intensity of the landslide, which can be coupled directly to vulnerability or damage-stage functions for quantitative risk assessment. Numerical models also provide the opportunity to investigate run-out frequencies and magnitudes of landslides in the absence of documented former events: One has to assume a probability distribution (on the basis of geotechnical investigations) for the release volume and obtains the probability distribution function for the landslide travel distance from the model.

3 CLASSIFICATION OF NUMERICAL RUN-OUT MODELS

Dynamic run-out models can be classified in many ways, but the main classification schemes commonly refer to (i) the solution dimension (1D, 2D, 3D) (ii) the choice of reference frame (i.e., Eulerian models using a reference frame at rest with respect to the terrain or Lagrangian models where the reference frame moves with the sliding mass, or (iii) the basal rheology.

3.1 CLASSIFICATION BASED ON THE SOLUTION DIMENSION (1D, 2D OR 3D)

The majority of dynamic models use an approach known as depth-averaging, in which the governing mass and momentum balance equations are integrated with respect to the flow depth. Stresses are assumed to increase linearly with depth below the top surface of the flow, which is usually assumed to be stress free, and shear stresses in the depth-wise direction are neglected (Savage and Hutter, 1991). This is based on the assumption that the depth varies gradually and is small relative to the length and width of the landslide. Depth-averaging combined with the shallow flow assumption essentially eliminates one dimension, the depth-wise dimension, from the governing mass and momentum balances. One-dimensional depth-averaged models analyze the movement considering the topography as a longitudinal section of the terrain with a pre-defined width while two-dimensional models consider the topography in both the streamwise and cross-stream directions.

3.2 CLASSIFICATION BASED ON THE SOLUTION REFERENCE FRAME (EULERIAN OR LAGRANGIAN)

The equations of motion can be formulated in two different frames of reference: Eulerian or Lagrangian. An Eulerian reference frame is fixed in space, analogous to an observer standing still as a landslide passes. Models formulated in an Eulerian framework require the solution of a more complex form of the governing equations using a dense, fixed computational grid. The Eulerian approach is the conventional method in computational fluid dynamics. A Lagrangian reference frame moves with the local velocity, analogous to an observer riding on top of a landslide. This method simplifies the governing equations and does not sacrifice

computational resources in void zones. When using the Lagrangian reference (also called material reference), the material velocity and acceleration are expressed in the form

$$\mathbf{V}(\mathbf{X}, t) = \frac{D\boldsymbol{\zeta}(\mathbf{X}, t)}{Dt} \quad (12)$$

and

$$\mathbf{A}(\mathbf{X}, t) = \frac{D\mathbf{V}(\mathbf{X}, t)}{Dt} = \frac{D^2\boldsymbol{\zeta}(\mathbf{X}, t)}{Dt^2}, \quad (13)$$

where V is the velocity; A is the acceleration; \mathbf{X} the referential position; $\boldsymbol{\zeta}$ is the motion that can be viewed as a transport of points from the reference configuration to the current configuration during a specific time interval $[0, t]$. Then, the displacement \mathbf{U} of a particle located at \mathbf{X} is expressed as

$$\mathbf{U}(\mathbf{X}, t) = \boldsymbol{\zeta}(\mathbf{X}, t) - \mathbf{X}. \quad (14)$$

In the Eulerian approach, attention is given to a fixed region in space and the material motion is observed within this region as time proceeds. The quantities of interest are expressed in terms of the spatial coordinates \mathbf{x} and time t . The velocity and acceleration can be described as

$$\mathbf{v} = \mathbf{v}(\mathbf{x}, t) \quad (15)$$

and

$$\mathbf{a} = \mathbf{a}(\mathbf{x}, t). \quad (16)$$

The displacement \mathbf{u} can be expressed as

$$\mathbf{u}(\mathbf{x}, t) = \mathbf{x} - \boldsymbol{\zeta}^{-1}(\mathbf{x}, t). \quad (17)$$

The Lagrangian approach is economical in the sense that the flow is computed only where the flowing mass is presently located, while computation in the Eulerian approach a priori comprises the entire area that may be affected by the flowing mass in the course of the event. (More advanced models restrict computation to the domain active at any given point in time and typically achieve speed-up factors between 2 and 5.) A possible disadvantage of the Lagrangian schemes, especially in 2-dimensional depth-averaged and fully 3-dimensional computations, is the increasing distortion of the computational grid due to shearing that may require frequent remeshing. Eulerian models also are at an advantage if the flow solution

exhibits shocks, i.e. discontinuities of the field variables. Special shock-capturing numerical techniques have been developed that resolve shock fronts fairly precisely and maintain high accuracy outside the shock region. The only practically used technique for handling shocks in Lagrangian schemes is adding artificial viscosity, i.e., diffusion to stabilize the solution at the expense of physical correctness. This is a serious concern in many geophysical mass flows where shocks commonly occur at bends or during the impact on obstacles.

3.3 CLASSIFICATION BASED ON THE FLOW RHEOLOGY

In depth-averaged flow models, the rheology of the flowing material enters only in the expression for the frictional forces that act at the interface between the flow and the bed, and through "form factors" or so-called Boussinesq coefficients in the advection term of the momentum balance equation. Most currently used models neglect these latter coefficients, even though they may have a considerable effect in certain situations.

Different rheological assumptions can be adopted in the models. The most commonly used ones are:

- The "**Frictional**" (or "Coulomb") resistance based on the relation of the effective shear and normal stress at the base and the pore fluid pressure:

$$S_f = \tan \varphi', \quad (18)$$

$$\tan \varphi' = (1 - r_u) \tan \varphi, \quad (19)$$

where S_f is the unit base resistance, r_u is the pore-pressure ratio which is equal to the bed pore water pressure divided by the bed normal total stress; and φ is the dynamic basal friction angle.

- The frictional-turbulent "**Voellmy**" resistance proposed initially for snow avalanches (Voellmy, 1955) and used for granular cohesionless materials with or without the presence of a pore fluid. This model features a velocity-squared resistance term (turbulent coefficient ζ) similar to the Chézy resistance for turbulent water flow in open channels, and a Coulomb-like

friction (apparent friction coefficient $\mu = \tan \varphi'$, where $\tan \varphi'$ is given by (19)). The basal shear stress is calculated as

$$S_f = \tan \varphi' + \frac{\mathbf{u}^2}{\xi h}, \quad (20)$$

where S_f again is the unit base resistance, $\tan \varphi' = \mu$ is the friction coefficient, \mathbf{u} is the flow velocity ($L T^{-1}$) and ξ is the turbulent friction coefficient ($L T^{-2}$). The parameters μ and ξ are constants whose magnitudes depend, respectively, on the flow properties and the roughness of the flow surface (Christen et al., 2010). Various authors have used the run-out from granular avalanches to estimate the friction coefficients of the Voellmy model (McDougall and Hungr, 2005).

- The visco-plastic **Bingham**-type resistance relationship applicable for plastic clay-rich material (Jiang and LeBlond, 1993; Imran et al., 2001; Malet et al., 2004; Pastor et al., 2009). The Bingham model is a function of flow depth, velocity, constant yield strength (τ_c) and dynamic viscosity (η). A linear stress-strain rate relationship is assumed once the yield strength is exceeded. The mean flow velocity is derived from the linear increase of shear stress with depth (Coussot, 1997). According to Rickenmann et al. (2006), a clay fraction (particle size less than 40 μm) greater than 10% is necessary for a flow material to behave like a Bingham fluid. The basal shear stress is calculated as

$$S_f = \frac{1}{\rho g h} \left(\frac{3}{2} \tau_c + 3\eta \frac{\|\mathbf{u}\|}{h} \right), \quad (21)$$

where τ_c is a constant yield strength due to cohesion, ρ is the density of the flow, and η is the viscosity parameter (Jiang and LeBlond, 1993). The yield stress and the viscosity of the flow are closely related to the concentration of solids.

A linear relationship between shear rate and shear stress may not be the most appropriate one for clay-rich materials, which exhibit shear-thinning at low and moderate shear rates. Better agreement with rheological laboratory measurements on clay materials is obtained with a Herschel–Bulkley non-linear relationship,

$$\tau = \tau_c + \eta \dot{\gamma}^n, \quad (22)$$

where $\dot{\gamma}$ is the shear rate (in the case of simple shear), $n > 0$ is the rheological exponent, and the viscosity coefficient η has dimensions Pa s^{-n} . Typical rheological exponents for clay-rich materials are $n = 0.3 \dots 0.5$.

- The “**Quadratic**” resistance model that incorporates a turbulent contribution to the yield and the viscous term already defined in the Bingham equation (O’Brien et al., 1993). The basal shear stress is calculated according to

$$S_f = \frac{\tau_c}{\rho g h} + \frac{K \eta}{8 \rho g h^2} \|\mathbf{u}\| + \frac{n^2 \mathbf{u}^2}{h^{\frac{4}{3}}}, \quad (23)$$

where \mathbf{u} is the depth-averaged velocity, h the flow depth; η the viscosity of the fluid, which is a function of the sediment concentration by volume, K is a dimensionless resistance parameter that equals 24 for laminar flow in smooth, wide, rectangular channels, but increases with roughness and irregular cross section geometry; and n is the Manning coefficient that takes into account the turbulent and dispersive components of the flow.

A more thorough description of rheologies that are commonly used for simulating debris flows can be found in (Naef et al., 2006) and (Hung and McDougall, 2009).

4 AN OVERVIEW OF SELECTED DYNAMIC RUN-OUT MODELS

Several dynamic run-out models have been developed in the past and the approaches for landslide modelling have been improved. These models have evolved from simple hydrodynamic models to more complex models that include various methods accounting for internal strength, entrainment and rheology variations. Table 1 gives an overview of some well-known commonly used 2D run-out dynamic models. They were classified based on their implementation and scheme of their entrainment rates. “Defined entrainment rate” means that the amount of entrained material is specified a priori by the user while “Process-based entrainment rate” means that the amount of entrained material is calculated dynamically by a

prescribed relationship between the relevant dynamical variables (e.g., velocity, flow height, bed shear stress) and the entrainment rate. Other characteristics of the models are also summarized: basal rheology, solution approach, reference frame of solution and variation of rheology along the flow path.

Most of the above mentioned models were applied in an important benchmarking exercise on landslide debris run-out and mobility modeling that was carried out in 2007 at the International Forum on Landslide Disaster Management in Hong Kong. The main goal of this exercise was to assess whether the field of run-out modeling is on its way towards establishing some degree of commonality among different methods used by various groups and to highlight the main progress in that topic (Hung et al., 2007). In that exercise, 13 research groups that work on the topic of run-out analysis participated by performing simulations of twelve different case studies. The participants were free to select the model and case studies that were most convenient with respect to their resources. The main results were presented during the forum and also discussed in a round table. The main points during that discussion were the following:

Table 1. An overview of several 2D dynamic numerical run-out models.

Model	Rheology	Solution approach	Reference Frame	Variation of rheology	Entrainment rate
MADFLOW (Chen and Lee, 2007)	Frictional, Voellmy and Bingham	Continuum Integrated	Lagrangian with mesh	no	Defined
TOCHNOG (Crosta et al., 2003)	Frictional (elastoplastic model)	Continuum Differential	Eulerian–Lagrangian (adaptive mesh)	yes	Process based
RAMMS (Christen et al., 2010)	Voellmy	Continuum Integrated	Eulerian	yes	Process based and defined
DAN3D (Hung and McDougall, 2009)	Frictional, Voellmy and Bingham	Continuum Integrated	Lagrangian meshless	yes	Defined
FLATMODEL (Medina et al., 2008)	Frictional and Voellmy	Continuum Integrated	Eulerian	no	Process based
SCIDDICA S3-hex (D'Ambrosio et al., 2003)	Energy based	Cellular Automata	Eulerian	no	Process based
3dDMM (Kwan and Sun, 2006)	Frictional and Voellmy	Continuum Integrated	Eulerian	yes	Defined
PASTOR model,	Frictional,	Continuum	Lagrangian	yes	Defined

(Pastor et al., 2009)	Voellmy and Bingham	Integrated	meshless		
MassMov2D (Begueria et al., 2009)	Voellmy and Bingham	Continuum Integrated	Eulerian	yes	Defined
RASH3D (Pirulli and Mangeney, 2008)	Frictional, Voellmy, Quadratic	Continuum Integrated	Eulerian	no	No entrainment rate is used
FLO-2D (O'Brien et al., 1993)	Quadratic	Continuum Integrated	Eulerian	no	No entrainment rate is used
TITAN2D (Pitman and Lê, 2005)	Frictional	Continuum Integrated	Lagrangian with mesh	no	No entrainment rate is used
PFC (Poisel and Preh, 2007)	Inter-particle and particle wall interaction	Solution of motion of particles (distinct element method)	Distinct element method	no	No entrainment rate is used
VolcFlow (Kelfoun and Druitt, 2005)	Frictional and Voellmy	Continuum Integrated	Eulerian	no	No entrainment rate is used

- Run-out modeling is very sensitive to the topography and the resolution of the computational domain. Mesh refinement methods will help to improve the modelling results.
- Run-out models need to be computationally efficient.
- The momentum-based formulation in continuum models is still the most reliable approach for run-out modelling.
- All of the presented models either use the Eulerian or the Lagrangian approach. Although both methods have their advantages and disadvantages, they are usable and promising.
- Well documented events can be accurately back-calculated by existing run-out models, but forward-analyses lead to widely diverging results.
- More data from real landslides is needed to refine the models and their parameterization.
- Reliable guidelines need to be worked out for selecting suitable rheological models and their parameters for different types of landslides.

5 RUN-OUT MODELS FOR HAZARD ANALYSIS IN A QUANTITATIVE RISK ASSESSMENT (QRA)

Different approaches and methods have been developed in the past for quantitative risk analysis using dynamic run-out models. A central point therein is that the vulnerability of the elements at risk is described in a quantitative or qualitative manner. In this direction, Bell and Glade (2004) performed a quantitative risk analysis (focusing on the risks to life) in north-western Iceland for debris flows and rock falls. Their approach to quantifying the hazards is based on empirical and process modeling that resulted in specific run-out maps. The hazard zones were determined based on the recurrence interval of the respective processes. For the determination of the respective levels of vulnerability, a semi-quantitative approach defined by matrices was used based on available literature and the authors' past findings (Glade, 2003). Their calculated vulnerability levels were incorporated into a consequence analysis that included the definition of elements at risk, the determination of spatial and temporal probabilities of impact, and the seasonal occurrence of the event.

Calvo and Savi (2008) proposed a method for risk analysis in a debris flow-prone area in Ardenno (Italian Alps), utilizing a Monte Carlo procedure to obtain synthetic samples of debris flows. To simulate the propagation of the debris flow on the alluvial fan, the FLO-2D model (O'Brien et al., 1993) was applied and probability density functions of the outputs of the model (i.e., forces) were obtained. Three different vulnerability functions were adopted to examine their effect on risk maps.

Muir et al. (2008) presented a site-specific case study of quantitative risk assessment for an undeveloped area in Hong Kong, where various scenarios were generated with different source volumes and sets of rheological parameters derived from back analyses of similar landslides in Hong Kong. Debris mobility modelling was performed using the Debris Mobility Model (DMM) software developed by the Geotechnical Engineering Office (Kwan and Sun, 2006); this model is an extension of Hungr's (1995) DAN model. They derived probability distributions from the run-outs of past events and calculated the probability

distribution of debris mobility for each volume class. Regarding the vulnerability, they used an ‘Overall Vulnerability Factor’ (OVF) and the average number of vulnerable individuals in a given facility directly hit by a landslide. The OVF was derived from the landslide volume, location of the elements at risk and the protection a facility can offer. Individual risk was calculated as the product of the frequency of a flow affecting the facility and the vulnerability of the most vulnerable individual, summed over all scenarios. They also calculated the societal risk.

Castellanos (2008) performed a local risk assessment based on the back-analysis of one historical landslide in Cuba. Based on the parameters obtained from the modelling of past events, run-out simulations were carried out with a beta version of the MassMov2D software (Begueria et al., 2009) for twelve potential zones. Vulnerability curves based on the depth of the flow and the conditions of the buildings were generated using detailed building typology characteristics and run-out results; and economic risk values were computed for three scenarios.

Zimmermann (2005) described Switzerland’s new approach of natural hazards and risk management using the Sörenberg debris flow as an example. For the Sörenberg event, hazard maps were prepared according to scenarios corresponding to three probability classes. The scenarios were based on past events and field verification. Debris-flow run-out was simulated using a random walk approach (Gamma, 2000) by applying a simple model that assumes that the motion is mainly governed by two frictional components: a sliding friction coefficient and a turbulent friction coefficient that is determined by a Chézy-type relation (Rickenmann, 1990). Results of the modeling were displayed as intensity maps. Swiss federal recommendations provide definite criteria for the intensity classes, which are based on the height and the velocity of the flow. Specific restrictions on land-use plans and extra requirements in the building codes are associated with these intensity classes.

Jakob and Weatherly (2005) quantified debris flow hazard and risk on the Jonas Creek fan in the State of Washington, U.S.A. They constructed frequency-magnitude graphs to build different return period scenarios as an input to a debris flow run-out model. The FLO-2D model was used to calculate maximum flow depths and velocities. Intensity maps were developed based on the model outputs for each simulated scenario. Potential deaths were calculated assuming that in the high-intensity areas the vulnerability is equal to 1, while the vulnerability is equal to 0 in the medium and low-intensity zones.

In terms of risk management, Crosta et al. (2005) carried out a cost-benefit analysis for the village of Bindo in the Valsassina valley (Central Pre-Alps, Italy) where a part of an active slope is still a threat. They identified different mitigation plans such as a defense structure, monitoring and a combination of both. They built hazard scenarios with a method that couples a stability analysis with a run-out assessment for different potential landslides. The stability analysis was performed using a 2D numerical code, and the run-out was simulated with the quasi-three-dimensional finite element method of Chen and Lee (2000) in the Lagrangian frame of reference. The different scenarios were compared with a scenario where no mitigation action was introduced. A cost-benefit analysis of each scenario was performed considering the direct effect on human life, houses and lifelines.

The recent work using physics-based numerical modeling in the framework of risk analysis suggests that dynamic run-out models (if correctly used) are a valuable tool when attempting to quantify the risk. Together with a good understanding of the slope processes and their relationship with other conditional factors, the detailed results from the run-out models can be used in a hazard analysis to estimate the spatial probability of the flow affecting a certain location as well as the intensity (flow depth, velocity, impact pressure). Results obtained from the run-out modeling are directly involved as factors that influence and affect the vulnerability of an exposed element. However, a major limitation is that quantitative vulnerability information for landslides is difficult to obtain due to the large variability in landslides types,

the difficulty in quantifying landslide magnitude, and the scarcity of precise historical damage records (van Westen et al., 2006; Douglas, 2007).

6 REFERENCES

- Beguiria, S., van Asch, Th. W. J., Malet, J.-P., and Grondahl, S., 2009. A GIS-based numerical model for simulating the kinematics of mud and debris flows over complex terrain. *Nat. Haz. Earth Syst. Sci.* **9**, 1897–1909.
- Bell, R. and Glade, T., 2004. Quantitative risk analysis for landslides – Examples from BÍldudalur, NW-Iceland. *Nat. Haz. Earth Syst. Sci.* **4**, 117–131.
- Bouchut, F., Fernandez-Nieto, E. D., Mangeney, A., Lagrée, P.-Y., 2008. On new erosion models of Savage-Hutter type for avalanches. *Acta Mech.* **199**, 181–208.
- Briukhanov, A. V., Grigorian, S. S., Miagkov, S. M., Plam, M. Ya., Shurova, I. Ya., Eglit, M. E. and Yakimov, Yu. L., 1967. On some new approaches to the dynamics of snow avalanches. In: Ôura, H (ed.), *Physics of Snow and Ice*, Proc. Intl. Conf. Low Temperature Science, Sapporo, Japan, 1966. Vol. I, Part 2, pp. 1223–1241.
- Calvo, B. and Savi, F., 2008. A real-world application of Monte Carlo procedure for debris flow risk assessment. *Comp. & Geosci.* **35**(5), 967–977.
- Castellanos Abella, E. A., 2008. Local landslide risk assessment. Multi-scale landslide risk assessment in Cuba. Utrecht, Utrecht University, ITC Dissertation 154, 193–226.
- Cannon, S. H. and Savage, W. Z., 1988. A mass change model for debris flows. *J. Geol.* **96**, 221–227.
- Chen, H. and Lee, C. F., 2000. Numerical simulation of debris flows. *Can. Geotech. J.* **37**, 146–160.
- Christen, M., Kowalski, J., and Bartelt, P., 2010. RAMMS: Numerical simulation of dense snow avalanches in three-dimensional terrain. *Cold Regions Sci. Technol.* **63**, 1–14.
- Corominas, J., 1996. The angle of reach as a mobility index for small and large landslides. *Can. Geotech. J.* **33**, 260–271.
- Conway, S. J., Decaulne, A., Balme, M. R., Murray, J. B. and Towner, M. C., 2010. A new approach to estimating hazard posed by debris flows in the Westfjords of Iceland. *Geomorph.* **114**(4), 556–572.
- Coussot P., 1997. *Mudflow Rheology and Dynamics*. IAHR monograph. Balkema, Rotterdam; 260. pp
- Crosta, G. B., Imposimato, S., and Roddeman, D., 2003. Numerical modelling of large landslides stability and runout. *Nat. Haz. Earth Syst. Sci.* **3**(6), 523–538.

- Crosta, G. B., Frattini, P., Fugazza, F., Caluzzi, L., and Chen, J., 2005. Cost-benefit analysis for debris avalanche risk management. In: Hungr, O., Fell, R., Couture, R., and Eberhardt, E. (eds.): *Landslide Risk Management*. Taylor & Francis, London, pp. 533–541.
- Devoli, G., De Blasio, F., Elverhøi, A., and Høeg, K., 2009. Statistical analysis of landslide events in Central America and their run-out distance. *Geotech. Geol. Eng.* **27**(1), 23–42.
- Douglas, J., 2007. Physical vulnerability modelling in natural hazard risk assessment. *Nat. Haz. Earth Syst. Sci.* **7**, 283–288.
- Gamma, P., 2000. DF-Walk: Ein Murgang-Simulationsprogramm zur Gefahrenzonierung. Geographica Bernensia G66. University of Bern, Berne, Switzerland (in German).
- Glade, T., 2003. Vulnerability assessment in landslide risk analysis. *Die Erde* **134**, 123–146.
- Heim, A., 1932. Bergsturz und Menschenleben. Beiblatt zur Vierteljahrsschrift. Fretz & Wasmuth Verlag, Zürich. 218 pp.
- Horton, P., Jaboyedoff, M., and Bardou, E., 2008. Debris flow susceptibility mapping at a regional scale. In: 4th Canadian Conference on Geohazards, Université Laval, Quebec, Canada.
- Hungr, O., 1995. A model for the runout analysis of rapid flow slides, debris flows, and avalanches. *Can. Geotech. J.* **32**, 610–623.
- Hungr, O. and McDougall, S., 2009. Two numerical models for landslide dynamic analysis. *Computers & Geosci.* **35**, 978–992.
- Hungr, O., Corominas, J., and Eberhardt, E., 2005. Estimating landslide motion mechanisms, travel distance and velocity. In: *Landslide Risk Management*. O. Hungr, R. Fell, R. Couture and E. Eberhardt (eds.). Taylor and Francis, London. Pages.99–128.
- Hungr, O., Morgenstern, N., and Wong, H. N., 2007. Review of benchmarking exercise on landslide debris runout and mobility modelling. In: *The 2007 International Forum on Landslide Disaster Management*. Ho & Li (eds.), ISBN 978-962-7619-30-7.
- Hürlimann, M., Rickenmann, D., Medina, V., and Bateman, A., 2008. Evaluation of approaches to calculate debris-flow parameters for hazard assessment., *Eng. Geol.* **102**, 152–163.
- Hutchinson, J. N., 1986. A sliding-consolidation model for flow slides. *Can. Geotech. J.* **23**, 115–126.
- Imran, J., Harff, P. and Parker, G., 2001. A numerical model of submarine debris flows with graphical user interface. *Computers Geosci.* **27**(6), 717–729.
- Iverson, R. M. and Denlinger, R. P., 2001. Flow of variably fluidized granular masses across three-dimensional terrain. 1. Coulomb mixture theory. *J. Geophys. Res.* **106**(B1), 537–552.
- Iverson, R. M., Schilling, S. P., and Vallance, J. W., 1998. Objective delineation of lahar-inundation hazard zones. *Geol. Soc. Amer. Bull.* **100**, 972–984.
-

- Jakob, M., and Weatherly, H., 2005. Debris flow hazard and risk assessment, Jones Creek, Washington. *In: Hungr, O., Fell, R., Couture, R., Eberhardt, E. (eds.), Landslide Risk Management.* Taylor & Francis, London, pp. 533–541.
- Jiang, L. and LeBlond, P., 1993. Numerical modelling of an underwater Bingham plastic mudslide and the waves it generates. *J. Geophys. Res.* **98**(C6), 10303–10317.
- Kappes, M. S., Malet, J.-P., Remaître, A., Horton, P., Jaboyedoff, M., and Bell, R., 2011. Assessment of debris-flow susceptibility at medium-scale in the Barcelonnette basin, France, *Nat. Haz. Earth Syst. Sci.* **11**, 627–641, doi:10.5194/nhess-11-627-2011.
- Kwan, J. S .H. and Sun, H .W., 2006. An improved landslide mobility model. *Can. Geotech. J.* **43**, 531–539.
- Li, T., 1983. A mathematical model for predicting the extent of a major rockfall. *Z. Geomorph.* **24**, 473–482.
- Liu, X., Yue, Z. Q., Tham, L. G., and Lee, C. F., 2002. Empirical assessment of debris flow risk on a regional scale in Yunnan province, southwestern China. *Env. Management* **30**(2), 249–264.
- Malet, J.-P., Remaître, A., and Maquaire, O., 2004. Runout modeling and extension of the threatened area associated with muddy debris flows. *Geomorphologie: relief, processus, environnement* **3**, 195–210.
- Mangeney, A., Bouchut, F., Vilotte, J. P., Lajeunesse, E., Aubertin, A., and Pirulli, M., 2005. On the use of Saint-Venant equations for simulating the spreading of a granular mass. *J. Geophys. Res.* **110**, B09103, doi:10.1029/2004JB003161.
- McDougall, S., and Hungr, O., 2005. Dynamic modelling of entrainment in rapid landslides. *Can. Geotech. J.* **42**, 1437–1448.
- Medina, V., Hürlimann, M., and Bateman, A., 2008. Application of FLATModel, a 2D finite volume code, to debris flows in the northeastern part of the Iberian Peninsula. *Landslides* **5**, 127–142.
- Miller, D. J. and Burnett, K. M., 2008. A probabilistic model of debris-flow delivery to stream channels, demonstrated for the Coast Range of Oregon, USA. *Geomorphol.* **94**(1–2), 184–205.
- Muir, I., Ho, K. S. S., Sun, H. W., Hui, T. H. H., and Koo, Y. C., 2006. Quantitative risk assessment as applied to natural terrain landslide hazard management in a mid-levels catchment, Hong Kong. *In: Nadim, F., Pöttler, R., Einstein, H., Klapperich, H., and Kramer, S. (eds.), Geohazards, ECI Symposium Series, vol. P07, pp. 1–8.*
- Naef, D., Rickenmann, D., Rutschmann, P., and McArdell, B. W., 2006. Comparison of flow resistance relations for debris flows using a one-dimensional finite element simulation model. *Nat. Haz. Earth Syst. Sci.* **6**, 155–165.
- O’Brien, J.S., Julien, P.Y., and Fullerton, W.T., 1993. Two-dimensional water flood and mudflow simulation. *J. Hydr. Eng.* **119**(2), 244–261.
-

- Pastor, M., Haddad, B., Sorbino, G., Cuomo, S., and Drempetic, V., 2009. A depth-integrated, coupled SPH model for flow-like landslides and related phenomena. *Int. J. Numer. Anal. Meth. Geomech.* **33**, 143–172.
- Pitman, B. E. and Lê, L., 2005. A two-fluid model for avalanche and debris flow. *Phil. Trans. R. Soc. A* **363**, 1573–1601.
- Pudasaini, S. P. and Hutter, K., 2007. *Avalanche Dynamics – Dynamics of Rapid Dense Granular Avalanches*. Springer-Verlag, Berlin.
- Rickenmann, D., 1990. Debris flows 1987 in Switzerland: modelling and sediment transport. IAHS Publication No. 194, pp. 371–378. International Association of Hydrological Sciences, Christchurch, New Zealand.
- Rickenmann, D., 1999. Empirical relationships for debris flows. *Nat. Haz.* **19**(1), 47–77.
- Rickenmann, D., Laigle, D. McArdell, B. W., and Hübl, J., 2006. Comparison of 2D debris-flow simulation models with field events. *Computat. Geosci.* **10**, 241–264.
- Sassa, K., 1988. Geotechnical model for the motion of landslides. In: Proc. Vth ISL, Lausanne, pp. 37–55.
- Sassa, K. and Wang, F., 2000. A modified geotechnical simulation model for the areal prediction of landslide motion. *Ann. Disas. Prev. Res. Inst.*, Kyoto Univ., 43 B-1.
- Savage, S. B. and Hutter, K., 1991. The dynamics of avalanches and granular material from initiation to run-out. Part I: Analysis. *Acta Mech.* **86**, 201–223.
- Scheidegger, A., 1973. On the prediction of the reach and velocity of catastrophic landslides. *Rock Mechanics* **5**, 231–236.
- Shreve, R. L., 1968. The Blackhawk landslide. Geological Society of America, Special Paper 108.
- Strîmbu B., 2011. Modeling the travel distances of debris flows and debris slides: quantifying hillside morphology. *Ann. For. Res.* **54**(1), 119–134.
- Tang, C., Zhu, J., Chang, M., Ding, J., and Qi., X., 2012. An empirical-statistical model for predicting debris-flow runout zones in the Wenchuan earthquake area. *Quat. Intl.* **250**, 63–73, doi:10.1016/j.quaint.2010.11.020.
- Toyos, G., Oramas Dorta, D., Oppenheimer, C., Pareschi, M. T., Sulpizio, R., and Zanchetta, G., 2008. GIS-assisted modelling for debris flow hazard assessment based on the events of May 1998 in the area of Sarno, Southern Italy: II. Velocity and dynamic pressure. *Earth Surf. Proc. Landforms* **33**(11), 1693–1708.
- van Westen, C. J., van Asch, Th. J. W., and Soeters, R., 2006. Landslide hazard and risk zonation – why is it still so difficult? *Bull. Eng. Geol. Env.* **65**, 167–184.
- Voellmy, A., 1955. Über die Zerstörungskraft von Lawinen (On the destructive force of snow avalanches). *Schweiz. Bauzeitung* **73**, 159–165, 212–217, 246–249, 212–285.
-

Zimmermann, M. N., 2005. Analysis and management of debris-flow risks at Sörenberg, Switzerland. *In: Jakob, M., and Hungr, O. (eds.): Debris-Flow Hazards and Related Phenomena*, Praxis, Springer, Berlin, Heidelberg, pp. 615–634.



Appendix II to Deliverable D1.7

Landslide runout: Guidelines for using a simple propagation code

Work Package 1.5 Runout Models

Deliverable/Work Package Leader: FUNAB

Revision: 0

February 2012

Rev.	Deliverable Responsible	Controlled by	Date
0	Manuel Pastor	Leonardo Cascini	2 Feb 2012

SUMMARY

Deliverable D1.7 belonging to WP1.5 has presented an state of the art of those propagation models which presents a good balance between complexity and computer time. The deliverable addressed topics such as mathematical modelling, rheological modelling and numerical modelling. Two main categories of models were studied: (i) Full 3D models, useful to study the 3D flow structure, and (ii) simplified depth integrated models. The former are expensive because the large extension covered by many landslides, and the non linear nature of the mathematical problem, requiring implicit integration of the constitutive equations. Concerning the latter, the time of computation is of the order of minutes in an average personal computer. The technique used – SPH- allowed different degrees of approximation depending on the number of nodes used in the discretization. In the limit, a 1 particle model can be used as a block model.

Deliverable D.1.7 was complemented by deliverable D1.9, where suitable guidelines for end users were provided, recommending them how to avoid the most classic errors.

During the past months, the FUNAB group has been working on preparing a version of the SPH code used in the group, in order to illustrate in a more effective way the use of SPH codes for landslide propagation.

The purpose of this Appendix – which is a complement to deliverables D1.7 and D1.9 – already approved by the EC- is to enrich the information provided to all SAFELAND partners. It is delivered as a learning and research tool, all other uses being out of the scope of this package.

Note about contributors

The following organisations contributed to the work described in this deliverable:

Lead partner responsible for the deliverable:

FUNAB

Fundación Agustín de Betancourt ETS de Ingenieros de Caminos
Universidad Politécnica de Madrid (Spain)

Deliverable prepared by:

(i) FUNAB (M.Pastor, T.Blanc, M.J.Pastor, M. Sánchez,
D.Manzanal and V.Drempetic)

Partner responsible for quality control:

University of Salerno

Deliverable reviewed by:

Leonardo Cascini

CONTENTS

1. INTRODUCTION

2. THEORETICAL BACKGROUND

3. THE GEOFLOW_SPH © CODE

3.1 Introduction. Code structure

3.2 Data files

3.3 Output files. Postprocessing

4. EXAMPLE 1. THE FRANK ROCK AVALANCHE

4.1. Description

4.2 Data files

4.3 Results

4.4 References

5. EXAMPLE 2. THE TSING SHAN DEBRIS FLOW (2000)

5.1. Description

5.2 Data files

5.3 Results

6. RUNNING THE CODE

7. POSTPROCESSING

1 INTRODUCTION

Deliverable D1.7 belonging to WP1.5 has presented an state of the art of those propagation models which presents a good balance between complexity and computer time. The deliverable addressed topics such as mathematical modelling, rheological modelling and numerical modelling. Two main categories of models were studied: (i) Full 3D models, useful to study the 3D flow structure, and (ii) simplified depth integrated models. The former are expensive because the large extension covered by many landslides, and the non linear nature of the mathematical problem, requiring implicit integration of the constitutive equations. Concerning the latter, the time of computation is of the order of minutes in an average personal computer. The technique used – SPH- allowed different degrees of approximation depending on the number of nodes used in the discretization. In the limit, a 1 particle model can be used as a block model.

Deliverable D.1.7 was complemented by deliverable D1.9, where suitable guidelines for end users were provided, recommending them how to avoid the most classic errors.

During the past months, the FUNAB group has been working on preparing a version of the SPH code used in the group, in order to illustrate in a more effective way the use of SPH codes for landslide propagation.

The purpose of this Appendix – which is a complement to deliverables D1.7 and D1.9 – already approved by the EC- is to enrich the information provided to all SAFELAND partners. It is delivered as a learning and research tool, all other uses being out of the scope of this package.

2 THEORETICAL BACKGROUND

We will provide here, for the sake of completeness, a short review where the main assumptions of the code are presented.

2.1 Depth Integrated model with coupled pore pressures

Many flow-like catastrophic landslides have average depths which are small in comparison with their length or width. In this case, it is possible to simplify the 3D propagation-consolidation model described above by integrating its equations along the vertical axis. The resulting 2D depth integrated model presents an excellent combination of accuracy and simplicity providing important information such as velocity of propagation, time to reach a particular place, depth of the flow at a certain location, etc.

Depth integrated models have been frequently used in the past to model flow-like landslides. It is worth mentioning the pioneering work of Hutter and coworkers (Savage and Hutter, 1991; Hutter and Koch 1991), and those of Laigle and Coussot (1997), Mc Dougall and Hungr 2005, and the authors (Pastor et al 2002, 2008, Quecedo et al 2004). We will use the reference system given in Fig. 2.1 where we have depicted some magnitudes of interest which will be used in this section.

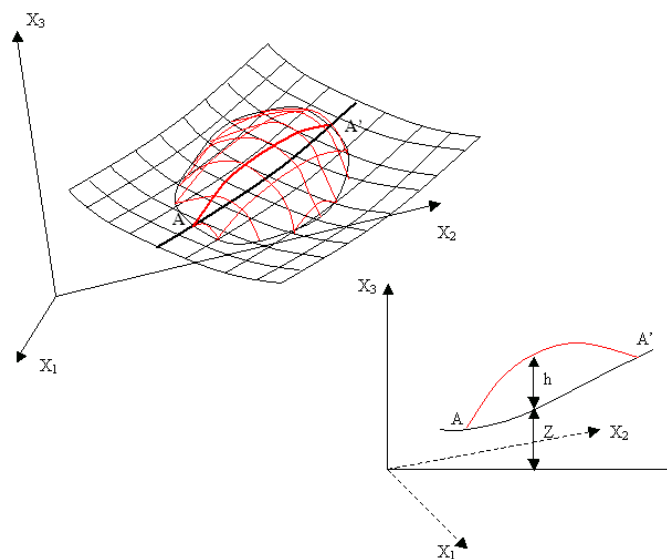


Figure 2.1 Reference system and notation used in the analysis

It is worth mentioning the difficulty of obtaining directly a Lagrangian form of the depth integrated equations, because the vertical integration is not performed in a material volume. Sometimes, it has been found convenient to refer to an equivalent 2D continuum having as velocities of their material points the depth integrated velocities. This cannot be considered as a Lagrangian formulation, because the moving points have no exact connection with material particles. It can be denominated either “quasi lagrangian”, or arbitrary lagrangian eulerian

(ALE) formulation. To derive a quasi lagrangian formulation of the depth integrated equations, we will first introduce a “quasi material derivative” as:

$$\frac{\bar{d}}{dt} = \frac{\partial}{\partial t} + \bar{v}_j \frac{\partial}{\partial x_j}$$

from where we obtain the “quasi lagrangian” form of the balance of mass, depth integrated equation as

$$\frac{\bar{d}h}{dt} + h \frac{\partial \bar{v}_j}{\partial x_j} = e_R \quad \text{where } e_R \text{ is the erosion rate } [L^{-1}]$$

The balance of momentum equation is

$$h \frac{\bar{d}}{dt} \bar{v}_i - \frac{\partial}{\partial x_i} \left(\frac{1}{2} b_3 h^2 \right) = \frac{1}{\rho} \frac{\partial}{\partial x_j} (h \bar{\sigma}_{ij}^*) + b_i h + \frac{1}{\rho} |N^B| t_i^B - e_R \bar{v}_i$$

where we have introduced the decomposition

$$\sigma_{ij} = -\bar{p} \delta_{ij} + \sigma_{ij}^* \quad \text{with } \bar{p} = \frac{1}{2} \rho b_3 h \text{ and } \bar{\sigma}_{ij}^* = \bar{\sigma}_{ij} + \bar{p} \delta_{ij}$$

The term t_i^B is the i-th component of the normal stress acting on the basal surface, and $|N^B|$ is

$$|N^B| = \left(\frac{\partial Z}{\partial x_1}^2 + \frac{\partial Z}{\partial x_2}^2 + 1 \right)^{1/2} \quad \text{where } Z \text{ is the height of the basal surface.}$$

It is important to note that we have to include the effect of centripetal accelerations, which can be done in a simple manner by integrating along the vertical the balance of momentum equation, and assuming a constant vertical acceleration given by V^2/R , where V is the modulus of the averaged velocity and R the main radius of curvature in the direction of the flow. Finally, after integrating the vertical consolidation equation in depth we arrive at:

$$\frac{\bar{d}}{dt} (\bar{p}_w h) = c_v \frac{\partial p_w}{\partial x_3} \Bigg|_Z^{Z+h}$$

Next, assuming an approximation of the pore pressure as

$$p_w(x_1, x_2, x_3, t) = \sum_{k=1}^{N_{pw}} P_k(x_1, x_2, t) N_k(x_3)$$

from where, taking

$$N_k(x_3) = \cos \frac{(2k-1)}{2h} \pi (x_3 - Z) \quad k = 1, Npw$$

and keeping only the first term, we have:

$$p_w(x_1, x_2, x_3, t) = P_1(x_1, x_2, t) \cos \frac{\pi}{2h} (x_3 - Z)$$

from where we obtain the depth integrated equation

$$\frac{d\bar{P}_1}{dt} = \frac{\pi^2}{4h^2} c_v P_1$$

which is the quasi-lagrangian form of the vertically integrated 1D consolidation equation. It is important to note that the results obtained above depend on the rheological model chosen, from which we will obtain the basal friction and the depth integrated stress tensor $\bar{\sigma}_{ij}^*$.

2.2 Rheological models

When obtaining the depth integrated equations described in the preceding Section, we have lost the flow structure along the vertical, which is needed to obtain both the basal friction and the depth integrated stress tensor. A possible solution which is widely used consist of assuming that the flow at a given point and time, with known depth and depth averaged velocities has the same vertical structure than a uniform, steady state flow. In the case of flow-like landslides this model is often referred to as the infinite landslide, as it is assumed to have constant depth and move at constant velocity along a constant slope. This infinite landslide model is used to obtain necessary items in our depth integrated model. We will present next some models frequently found in landslide propagation modelling.

2.2.1 Bingham fluid

In the case of Bingham fluids, there exists an additional difficulty, because it is not possible to obtain directly the shear stress on the bottom as a function of the averaged velocity. The expression relating the averaged velocity to the basal friction for the infinite landslide problem is,

$$\bar{v} = \frac{\tau_B h}{6\mu} \left(1 - \frac{\tau_Y}{\tau_B}\right)^2 \left(2 + \frac{\tau_Y}{\tau_B}\right)$$

where μ is the viscosity, τ_Y the yield stress, and τ_B the shear stress on the bottom. This expression can be transformed into

$$P_3(\eta) := \eta^3 - (3+a)\eta + 2 = 0$$

where we have introduced $\eta = h_p/h$ which is the ratio between the height of the constant velocity region or plug to the total height of the flow, and the non dimensional number a defined as

$$a = \frac{6\mu\bar{v}}{h\tau_y}$$

It is first necessary to obtain the root of a third order polynomial. To decrease the computational load, several simplified formulae have been proposed in the past. The authors introduced in Pastor et al. (2004) a simple method based on obtaining the second order polynomial which is the best approximation in the uniform distance sense of the third order polynomial, which is given by

$$P_2(\eta) = \frac{3}{2}\eta^2 - \left(\frac{57}{16} + a\right)\eta + \frac{65}{32}$$

Knowing the non dimensional number a , the root is obtained immediately.

2.2.2 Frictional fluid

One simple yet effective model is the frictional fluid, especially in the case where it is used within the framework of coupled behaviour between soil skeleton and pore fluid. Without further additional data it is not possible to obtain the velocity distribution. This is why depth integrated models using pure frictional models cannot include information concerning depth integrated stresses $\bar{\sigma}$. Concerning the basal friction, it is usually approximated as

$$\tau_b = -\sigma_v \tan \phi \frac{\bar{v}_i}{|\bar{v}|}$$

where σ_v is the normal stress acting on the bottom. Sometimes, when there is a high mobility of granular particles and drag forces due to the contact with the air are important it is convenient to introduce the extra term. proposed by Voellmy's (Voellmy 1955), which includes the correction term $\frac{\rho g v^2}{\xi}$ where ξ is the Voellmy turbulence parameter.

In some cases, the fluidized soil flows over a basal surface made of a different material. If the friction angle between both materials δ is smaller than the friction angle of the fluidized soil, the basal shear stress is given by:

$$\tau_b = -\rho'_d g h \tan \phi_b \frac{\bar{v}_i}{|\bar{v}|}$$

where the basal friction ϕ_b is

$$\phi_b = \min(\delta, \phi)$$

This simplified model can implement the effect of pore pressure at the basal surface. In this case, the basal shear stress will be:

$$\tau_b = -\left(\sigma'_v \tan \phi_b - p_w^b\right) \frac{\bar{v}_i}{|\bar{v}|}$$

We can see that the effect of the pore pressure is similar to decreasing the friction angle.

2.2.3 Cohesive-Frictional fluids

The cohesive-frictional model proposed in 3D by the authors (Pastor et al 2009) particularizes for the case of a simple shear flow to

$$\sigma_{11} = \sigma_{22} = \sigma_{33} = -p$$

$$\sigma_{13} = \sigma_{31} = s + \mu_{CF} \left(\frac{\partial v_1}{\partial x_3} \right)^m$$

where $s = c \cos \varphi + p' \sin \varphi$.

Two particular cases of interest are the Bingham fluid ($\varphi = 0$ $c = \tau_y$ $m = 1$) and the Herschel Bulkley fluid. For flow of granular materials we will use $c = 0$ $m = 2$. The basal friction term results on (Pastor et al 2009)

$$\tau_b = \rho_d' g h \cos \theta \tan \varphi + \frac{25}{4} \mu_{CF} \frac{\bar{v}^2}{h^2}$$

which is a law of similar structure than Voellmy's

$$\tau_b = \left\{ \rho_d' g h \cos \theta \tan \varphi + \rho g \frac{\bar{v}^2}{\zeta} \right\}$$

where ζ is a material parameter. If we compare both expressions, we can see that both incorporate a quadratic term depending on the averaged velocity.

In above, we have defined for convenience $\rho_d' = \rho_d - \beta_w \rho_w$, where $\rho_d = (1-n)\rho_s$, and the pore pressure in excess to the hydrostatic is written as $\Delta p_w = \beta_w \rho_w$.

2.2.4. Erosion

One important aspect in the behaviour of catastrophic landslides and related phenomena is the erosion. This complex phenomena requires a rheological or constitutive behaviour of the interface, and depends on variables such as the flow structure, density, size of particles, and on how close are the effective stresses at the surface of the terrain to failure. We have used here the simple yet effective law proposed by Hungr 1995 which gives the erosion rate as $E_t = E_s h \bar{v}$ where E_s can be obtained directly from the initial and final volumes of the

material and the distance traveled as $E_s \approx \frac{\ln(V_{final}/V_0)}{\text{distance}}$. Units of erosion coefficient are L^{-1}

It is also worth mentioning other erosion laws proposed by Blanc (2008), Issler and Jóhannesson (2010) and Issler and Pastor (2011)

2.3 Numerical model: the SPH technique.

To analyze the propagation of a fast landslide over a terrain, there are two main alternatives. The first is eulerian, and is based on a structured (Finite Differences) or unstructured grid (Finite Elements and Volumes) within which the material flows. The main problem here is the need of a very fine computational mesh for both the terrain information and for the fluidized soil. Lagrangian methods allow the separation of both meshes, with an important economy of computational effort. If we combine a Lagrangian method with a mesh based discretization technique, we will find problems as soon as the mesh deforms, making necessary to use mesh refinement. As alternative, meshless methods, which do not rely on meshes, avoids distortion problems in an elegant way. In this work, we have used a meshless method referred to as the smoothed particle hydrodynamic or SPH. As in any meshless method, information is linked to moving nodes. We will describe next the method in a very succinct way. Smoothed particle hydrodynamics (SPH) is a meshless method introduced independently by Lucy (1977) and Gingold and Monaghan (1977) and firstly applied to astrophysical modelling, a domain where SPH presents important advantages over other methods. SPH is well suited for hydrodynamics, and researchers have applied it to a variety of problems, like those described in Gingold and Monaghan (1982), Monaghan et al. (1999), Bonet and S. Kulasegaram (2000) and Monaghan et al. (2003), just to mention a few. SPH has been also applied to model the propagation of catastrophic landslides (Bonet and Rodriguez-Paz, 2005; McDougall , 2006; McDougall and Hungr, 2004) however in both cases, the analysis did not incorporate hydro mechanical coupling between the solid skeleton and the pore fluid, which has been proposed by the authors (Pastor et al 2008).

2.4 An SPH method for depth integrated equations

We will introduce a set of nodes $\{x_k\}$ with $K = 1..N$ and the nodal variables:

- h_I height of the landslide at node I
- \bar{v}_I depth averaged, 2D velocity
- t_I^b surface force vector at the bottom
- $\bar{\sigma}_I^*$ depth averaged modified stress tensor
- P_{1I} pore pressure at the basal surface

If the 2D area associated to node I is Ω_I , we will introduce for convenience:

- (i) a fictitious mass m_I moving with this node $m_I = \Omega_I h_I$
- (ii) and, an averaged pressure term \bar{p}_I , given by $\bar{p}_I = \frac{1}{2} b_3 h_I^2$

It is important to note that m_I has no physical meaning, as when node I moves, the material contained in a column of base Ω_I has entered it or will leave it as the column moves with an averaged velocity which is not the same for all particles in it.

There are several possible alternatives for the equations, according to the discretized form chosen for the differential operators results. We will show those obtained with the third symmetrized forms:

$$\frac{\overline{dh}_I}{dt} = h_I \sum_J \frac{m_J}{h_J} v_{IJ} \text{grad} W_{IJ} \text{ where we have introduced } v_{IJ} = v_I - v_J$$

Alternatively, the height can be obtained once the position of the nodes is known as:

$$h_I = \langle h(x_I) \rangle = \sum_J h_J \Omega_J W_{IJ} = \sum_J m_J W_{IJ}$$

The discretized balance of linear momentum equation is:

$$\begin{aligned} \frac{\overline{d}}{dt} \overline{v}_I &= - \sum_J m_J \left(\frac{p_I}{h_I^2} + \frac{p_J}{h_J^2} \right) \text{grad} W_{IJ} \\ &+ \frac{1}{\rho} \sum_J m_J \left(\frac{\sigma_I}{h_I^2} + \frac{\sigma_J}{h_J^2} \right) \text{grad} W_{IJ} + b + \frac{1}{\rho h_I} |N^B| t_I^B \end{aligned}$$

Finally, the SPH discretized form of the basal pore pressure dissipation is:

$$\frac{\overline{d}}{dt} P_{1I} = - \frac{\pi^2 c_v}{4h_I} P_{1I}$$

So far, we have discretized the equations of balance of mass, balance of momentum and pore pressure dissipation. The resulting equations are ODEs which can be integrated in time using a scheme such as Leap Frog or Runge Kutta (2nd or 4th order).

2.5. References

- Blanc, T. (2008). Numerical simulation of debris flows with the 2D SPH depth-integrated model, Master's thesis, Institute for Mountain Risk Engineering, University of Natural Resources and Applied Life Sciences, Vienna, Austria
- Bonet, J and Kulasegaram, S. (2000) "Correction and stabilization of smooth particle hydrodynamics methods with applications in metal forming simulations", *Int. J. Numer. Meth. Engng.*, 47, pp. 1189-1214
- Bonet, J., Rodríguez Paz, M.X. (2005). "A corrected smooth particle hydrodynamics formulation of the shallow-water equations". *Computers and Structures* 83, pp. 1396 – 1410.
- Gingold, R.A. and Monaghan, J.J (1982), Kernel estimates as a basis for general particle methods in hydrodynamics, *J. Comput. Phys.* 46 (1982) 429
- Hungr, O. (1995). "A model for the runout analysis of rapid flow slides, debris flows, and avalanches" . *Canadian Geotechnical Journal*, 32: 610-623.

-
- Hutter, K., Koch, T. (1991). Motion of a granular avalanche in an exponentially curved chute: experiments and theoretical predictions. *Phil. Trans. R. Soc. London, A* 334, pp 93 – 138.
- Issler, D. and Jóhannesson, T. (2010). Dynamically consistent entrainment and deposition rates in depth-averaged gravity mass flow models. (submitted for publication)
- Issler, D. and Pastor, M., Interplay of entrainment and rheology in snow avalanches – a numerical study. *Annals of Glaciology* 52(58) 2011
- Laigle, D., Coussot, P. (1997). Numerical modelling of mudflows. *Journal of Hydraulic Engineering, ASCE*, 123 (7), pp. 617 – 623.
- Lucy, L.B. (1977). A numerical approach to the testing of fusion process. *Astronomical Journal*, Vol. 82, pp. 1013 – 1024.
- McDougall, S. (2006), “A new continuum dynamic model for the analysis of extremely rapid landslide motion across complex 3D terrain”, PhD Thesis, University of British Columbia
- McDougall, S., Hungr, O. (2004). A Model for the Analysis of Rapid Landslide Motion across Three-Dimensional Terrain. *Canadian Geotechnical Journal*, 41 n 12, pp. 1084 – 1097.
- Monaghan, J.J, Cas, R. F., Kos, A., and Hallworth, M.,(1999) “Gravity currents descending a ramp in a stratified tank”, *J. Fluid Mech.*, 379, pp.36–39
- Monaghan, J. J.; Kos, A., and Issa, N. (2003) “Fluid Motion Generated by Impact”, *Journal of Waterway, Port, Coastal, and Ocean Engineering ASCE* 129, pp. 250–259.
- Pastor, M., Quecedo, M., Fernández Merodo, J.A., Herreros, M.I., González, E., Mira, P. (2002). Modelling Tailing Dams and mine waste dumps failures. *Geotechnique*, Vol.LII, N.8, pp. 579 – 592.
- Pastor, M., Quecedo, M., González,E., Herreros, I., Fernández Merodo, J.A., and Mira, P. (2004), “A simple approximation to bottom friction for Bingham fluid depth integrated models”, *Journal of Hydraulic Engineering ASCE*, Vol. 130, No. 2, pp. 149-155
- Pastor, M., Haddad B., Sorbino G. and Cuomo S. (2008), “A depth integrated coupled SPH model for flow-like landslides and related phenomena”, *Int.J.Num.Anal.Meth.Geomech.* 33:143–172
- Pastor, M., Blanc, T. and Pastor, M.J (2009), A depth-integrated viscoplastic model for dilatant saturated cohesive-frictional fluidized mixtures: Application to fast catastrophic landslides *J. Non-Newtonian Fluid Mech.* 158 (2009) 142–153
- Quecedo, M., Pastor, M., Herreros, M.I., Fernández. Merodo, J.A. (2004). Numerical modelling of the propagation of fast landslides using the Finite Element Method. *Int. J. Num. Meth. Eng.*, Vol. 59, Issue 6, pp. 755 – 794.
- Savage, S.B., Hutter, K. (1991). The dynamics of avalanches of granular materials from initiation to runout. Part I: Analysis. *Acta Mechanica* 86, pp. 201 – 223.
- Voellmy, A. (1955) “Über die Zerstörungskraft von Lawinen”. *Schweizerische Bauzeitung*, 73, pp. 212-285

3 THE GEOFLOW_SPH © CODE

3.1 Introduction. Code structure

Many flow-like catastrophic landslides The code developed at Madrid during the past years, called GEOFLOW_SPH © has been written in Fortran 90, using a modular structure which allows easy connection with other modelling codes developed by the group.

It consists of the following set of modules:

- (i) SPH_FEM_Driver_2012
- (ii) SPH_MAIN_2012
- (iii) SPH_SW_2012
- (iv) SPH_FEM_topo_2012
- (v) SPH_FEM_Driver_time_vars_2012
- (vi) SPH_Main_Vars_2012
- (vii) SPH_SW_Vars_2012

The main module, controlling the flow of the code and the interaction with other SPH and FEM modules is SPH_FEM_Driver, which prepares and controls an auxiliary module of control variables called SPH_FEM_Driver_time_vars.

This main module calls routines concerning general SPH integration techniques belonging to the module SPH_MAIN, which in turn prepares and uses a set of general SPH variables belonging to the module SPH_Main_Vars.

It is important to note that this main SPH module can drive not only the depth integrated routines which belong to GEOFLOW_SPH code, but to other modules used for Navier Stokes problems, for instance.

Then, the module SPH_SW contains all the subroutines related to depth integrated problems, which is the case of the shallow landslides.

Finally, there is an ad hoc module called SPH_FEM_topo, prepared to deal with terrain geometry.

The GEOFLOW_SPH code solves the SPH equations corresponding to a set of computational nodes where information of the landslide is stored: heights, averaged velocities and basal pore pressured as stored for each SPH node.

There is a a topographic structured mesh formed of bilinear quadrilaterals, at which nodes we store the terrain height, it gradients (or slopes), and second order derivatives used to compute the terrain curvature along the direction of propagation.

3.2 Data files

The code uses a set of ASCII data files which have to be prepared in order to run a problem. The data files share a problem name, which we will assume to be “**myproblem**”.

In this theoretical case, the input files would be:

myproblem.MASTER.DAT
myproblem.TOP
myproblem.DAT
myproblem.PTS

which will be described next. Please do notice that this is not intended to be a complete manual of GEOFLOW_SPH code, but rather a vehicle to learn how to use it step by step, beginning with particular cases.

In order to illustrate file structure, we will consider a particular case, that of Tsing Shan debris flow which occurred in Hong Kong in 2000.

3.2.1 Terrain data: TsingShan.TOP

The data file **TsingShan.TOP** contains the topographic data. It has the following structure:

type of topography		
11		
Nr of Pts in DTM	representative grid spacing	
18271	5	
X coord	Y coord	Z coord
813.250,00	826.700,00	195,25
813.255,00	826.700,00	192,82
813.260,00	826.700,00	190,26
813.265,00	826.700,00	187,77
813.270,00	826.700,00	185,45
813.275,00	826.700,00	183,34
813.280,00	826.700,00	181,82
	...	
813975,00	827300,00	64,93
813980,00	827300,00	63,58
813985,00	827300,00	62,24
813990,00	827300,00	60,97
813995,00	827300,00	59,74
814000,00	827300,00	58,52
Terrain dependent Properties		
0,00		

Note 1: The type of information arrangement is 11, and consists of 18271 points (nodes have not to be arranged in a structured manner) from which we will obtain a topographical grid with a spacing of 5 m.

Note 2. It is possible in the code to have some properties as dependent on the value of Z coordinate (for instance, when an avalanche crosses a glacier). As this feature will not be used here, the value has been set to zero.

Note 3. We will provide the files for two cases: Frank avalanche and Tsing Shan debris flow (2000). Both of them have exactly the same format. Files are named **T08.top** and **T10.top**, respectively.

3.2.2 General control data: TsingShan.MASTER.dat

This data file controls the code execution. It is important to notice that GEOFLOW_SPH belongs to a suite of codes developed at Madrid where there are other modules for depth integrated Finite Elements, 3D solid dynamics finite elements, and 3D SPH solid. Therefore, some of the options will be set to zero, as the other modules are not used.

1			
Tsing Shan 2000			
if_sph	if_gfl	if_tgf	
1	0	0	
SPH_problem_typ	SPH_t_integ_AI		
e	g		
1	4		
sph problem name			
T10			
BLOCK 1			
dt	time_end	maxtimesteps	
0.1	80.00	1000000	
print_step	save_step	plot_step	
25	25	25	
dt_sph	ic_adapt		
0.1	1		
Ntime curves	max pts in curves		
0	6		
FINAL BLOCK			
dt	time_end	maxtimesteps	
-1	2.00	100000	

Note 1. We start this file with a number (1 in this case) which indicates how many text lines describing the problem follow. This line of text contains “Tsing Shan 2000” string.

Note 2. Next set of information consists of 3 integers (**if_sph if_gfl** and **if_tgf**) which indicates the code the modules which will be used in the analysis. In our case it is the sph module only, so we set if_sph to 1, and the two other values to zero.

Note 3. Next set of information parameters refer to the SPH model type, which is depth integrated, so `SPH_problem_type = 1`, and the integration scheme to be used, `SPH_t_integ_Alg` which is set to 4 as we will use a 4th order Runge-Kutta integration scheme.

Note 4. `sph problem name` provides the name of the file where SPH algorithm data will be stored. In this case, it is “t10”.

Note 5. It is possible to use several blocks in the analysis, even though here we will use a single block. A block provides information on time steps, and on time history input (histograms) which are used if nodes are injected in the domain following a particular histogram.

As we can be running at the same time several interacting concurrent modules, we have a first controlling time increment which will be used as reference, mainly for output. We provide `dt`, `time_end` and maximum number of timesteps, which here have been selected as 0.1 80 and 1000000. In order to avoid excessive output, we limit writing to files to one step every 25. Here, only `print_step` and `plot_step` are used.

An important parameter is the time increment which will be used by SPH. As the algorithm used in the analysis is explicit, `dt_sph` will have to fulfill some restrictions. Here we have taken the classical CFL condition, setting

$$dt_sph = \min(\text{spacing} / \sqrt{gh})$$

where `spacing` is the SPH nodal spacing and `h` is the height of the landslide. For instance, if nodes have an initial spacing of 10 m, and the maximum depth of the landslide is 20 m, the limit timestep will be

$$dt_sph = (10 / \sqrt{20g}) = 0.7139 \text{ For safety, we would use a value of 0.1.}$$

An interesting feature of the code is that it can change adaptively the time step value, by setting `ic_adapt` to 1, as we have done here.

As no time curves for histograms will be used, we set `Ntime_curves` to zero, the value of `max_pts_in_curves` not being used (it is however mandatory to provide an integer value, 6 in this case)

The blocks input finish with the final block information given in the table.

3.2.3 SPH data: TsingShan. dat

This file provides the control data required for both SPH and SPH_SW modules. It is important to remark that name of the file has been provided in the MASTER.DAT file.

1

Tsing Shan 2000 debris flow

SW algorithm

0

nhist

0

ndimn

2

ic_soil	ic_water	ic_vps	ic_abs
1	0	0	0

Soil unkno h_inf_SW

7

0.1

Landslide File

TsingShan

sph algorithm	search neighbours	h update	weigh f type
2	2	2	1

Dens.Algorithm	av_vel	dummy	nor_dens
1	1	0	0

P1. gravity	P2 dens	P3 Voellmy	P4 Erosion	P5 rheology	P6 Tauy0	P7 Visco K
9.8	2000.	500	97.e-4	7	0	0

P8 Mu	P9 tan(fi_inf)	P10 h_frict0	P11	P12 tan(Fi_0)	P13 Bcons	P14
0	0.18	0,001	0	0,18	0	0

P15 h_comp
0,001

K0 activated?

0

icpwp

0

coarse mesh saving utility?

0

control points?

0

output filter	1.hs	2.disp	3.v	4.Pw	5 eros	6..Z
---------------	------	--------	-----	------	--------	------

1	1	0	0	0	0
7..hrel	8..hw	9..eta	10.. hs+hw	11 dummy	12...dummy
0	0	0	0	0	0

T_change_to_W
1.e+12

Note 1. sph problem name has been given in the MASTER.DAT file.

Note 2. As in the case of the MASTER.DAT file, we provide first the number of lines which describe the problem (as many as necessary). In this case, we just use the name of the problem being solved.

Note 3. **nhist** is a variable which provides the number of histograms which will be used in case we need them. Here is 0, as we are giving a description of the landslide mass.

Note 4. **ndimn** is the number of dimensions of the problem solved, which can be 1 or 2, as in this case.

Note 5. **ic_soil**, **ic_water**, **ic_vps** and **ic_abs** refer to special features that the code can analyze. We use **ic_soil** = **1** when we have a landsliding mass of soil, **ic_water** = **1** when we want to consider masses of soil and water –as in the case of waves in reservoirs triggered by landslides-

Note 6. **soil_unkno** refers to the way the landslide is described. Type 7 is a particular case, the information will be given when describing file **myproblem.pts**. The control variable **h_inf_SW** is used to provide a limit for landslide depth, in order to improve model efficiency. In some cases, we have observed that the digital terrain model may include depths of tens of meters together with some spurious depths of the order of milimeters.

Note 7. Next set of control variables refer to SPH techniques. **sph_algorithm** allows the user to choose between several alternatives to discretize gradients. We recommend to use this symmetrized alternative, where the gradient of a scalar function (pressure, for instance) is approximated as

$$\text{grad } \phi_I = \rho_I \sum_J m_J \left\{ \frac{\phi_J}{\rho_J^2} + \frac{\phi_I}{\rho_I^2} \right\} \text{grad } W_{IJ}$$

In above equation, ϕ_I is the function evaluated at node I, m_J the associated volume of node J (associated area multiplied by landslide depth), ρ_J the landslide depth at node J, and $\text{grad } W_{IJ}$ the gradient of the smoothing function W centered at node J and evaluated at node I. The parameter **search_neighbours** controls the searching algorithm allowing the code to know which particles are interacting. Code 2 refers to the algorithm developed at Madrid,

which uses a background mesh of boxes. Next, `h_update` describes how the smoothing length will be updated. Here we have chosen the updating algorithm proposed by Benz in 1990,

where $dh = -\frac{1}{ndimn} \cdot \frac{h}{\rho} d\rho$, `h` being the smoothing length. Finally, there are three options for the weight function `W`, that corresponding to the value `weigh_f_type = 1` being a cubic spline.

Note 8. Updating of landslide depth can be used by two alternative procedures: (i) integrating the mass conservation equation `Dens.Algorithm = 0` or by evaluating it from the heights of the neighbour nodes, `Dens.Algorithm = 1`. Spurious oscillations can be damped out by averaging the velocity of the nodes, which correspond to `av_vel = 1`. The dummy parameter included in the line is not used. Finally, `nor_dens = 1` can be used to correct the height in zones close to boundaries, and it is not used here, so we take it as 0.

Note 9. The next set of data is mostly material parameters. We will concentrate in the case being studied here, where we have assumed a frictional fluid with a Voellmy's turbulent viscosity. The values are the following:

P1 Gravity acceleration 9,8 m/s²

P2 Density of the mixture 2000 Kg/m³

P3 Voellmy's coefficient of turbulent viscosity 500 m/s²

P4 Hungr's erosion coefficient $97e-4 \text{ m}^{-1}$. Note that the erosion rate as $E_t = E_s h \bar{v}$ where E_s can be obtained directly from the initial and final volumes of the material and the distance traveled as $E_s \approx \frac{\ln(V_{final}/V_0)}{\text{distance}}$. Units of erosion coefficient are L^{-1}

P5 Rheology type. 7 means a frictional fluid, with Voellmy's turbulent viscosity added if P3 is different from zero.

P6, P7 and P8 are parameters for Bingham fluids. Here are set to zero.

P9 and P12 are the tangents of the initial and final friction angles. They are the same, and have been kept for compatibility with old versions where the pore pressure dissipation was approximated in a crude way.

P13 is a vertical consolidation coefficient, taken as zero as no pore pressures are considered in this case.

P10 and P15 are limits for depth of the landslide, to avoid dividing for very small values when obtaining the bottom friction.

P11 and P14 are not used, and are set to zero.

Note 10. `K0_activated` is a control parameter which has been included to account –in a future version- for active and passive horizontal stress coefficients.

Note 11. The parameter `icpwp` informs the code, when set to 1, that a coupled analysis is being performed. Here it is zero.

Note 12. The `coarse_mesh_saving_utility` parameter allows a restricted output when the topographic mesh is too fine, in order to avoid excessive output volume. The computations are carried out in the fine mesh describing the topography, but the output is given on a coarser mesh.

Note 13 In some cases, control points are needed in order to know there the time history of landslide height. Here we do not consider it, so the parameter is set to zero.

Note 14. In order to avoid excessive output data, we can select using the filtering vector `output_filter` those variables we want to be in the output. here we have selected just heights and displacements.

Note 15. Finally, the code uses a value for special cases not considered here which is set to $e+12$.

3.2.4 Landslide data: TsingShan. pts

This file provides the data of the landslide mass. In some cases, the information is limited, and we are given only a simple region (rectangular) where the depth is constant. This case correspond to the parameter **soil_unkno=7** described in myfile.dat. The structure of the file is the following.

```
1
Tsing Shan 2000 debris flow

npoin source grid spacing deltax delty facthsm1
4          10          0.5      0.5      2

--- X ---   --- Y ---   -- h --
813302,5    827224,5    1,3
813302,5    827230,5    1,3
813322,5    827224,5    1,3
813322,5    827230,5    1,3
```

Note 1. As in the case of the MASTER.DAT file, we provide first the number of lines which describe the problem (as many as necessary). In this case, we just use the name of the problem being solved.

Note 2. We provide the 4 points describing the rectangle, we assume a typical grid spacing of 10 m, and we want to generate points inside the rectangle spaced 0.5 m both in x and in y. Finally, the smoothing length of SPH is taken as multiplied by a factor of 2.

Note 3. We provide the X and Y coordinates of the points describing the rectangle, together with landslide heights at them

4 THE FRANK SLIDE AT ALBERTA, CANADA (1903)

4.1 Description

During 2007, the Hong Kong Geotechnical Office organized a benchmarking exercise aiming to assess the accuracy of numerical and constitutive models. The participants were provided a detailed digital terrain elevation map, including the original position of the mobilized mass and the final position of the deposit.

One of the tests (number 8) is the Frank slide, a rock avalanche which happened in in Canada in 1903. It is the event causing a larger number of victims in Canadian history. It consisted of a rock avalanche involving approximately 36 million of cubic meters of fragmented limestone which detached from the ridge of Turtle Mountain. The front extension was 700 m, and it travelled downhill 800 m, forming a deposit with an average thickness of 18 m. with an extension of 1.7 km wide and 2 km long. Concerning velocity of propagation, there is no available information, but McConnell and Brock (1904) who reported the event, estimated a propagation time less than 100 seconds, according to witnesses. The Frank slide has been described extensively by Cruden and Hungr (1986).



Fig 4.1 The Frank slide (from Cruden and Hungr 1986)

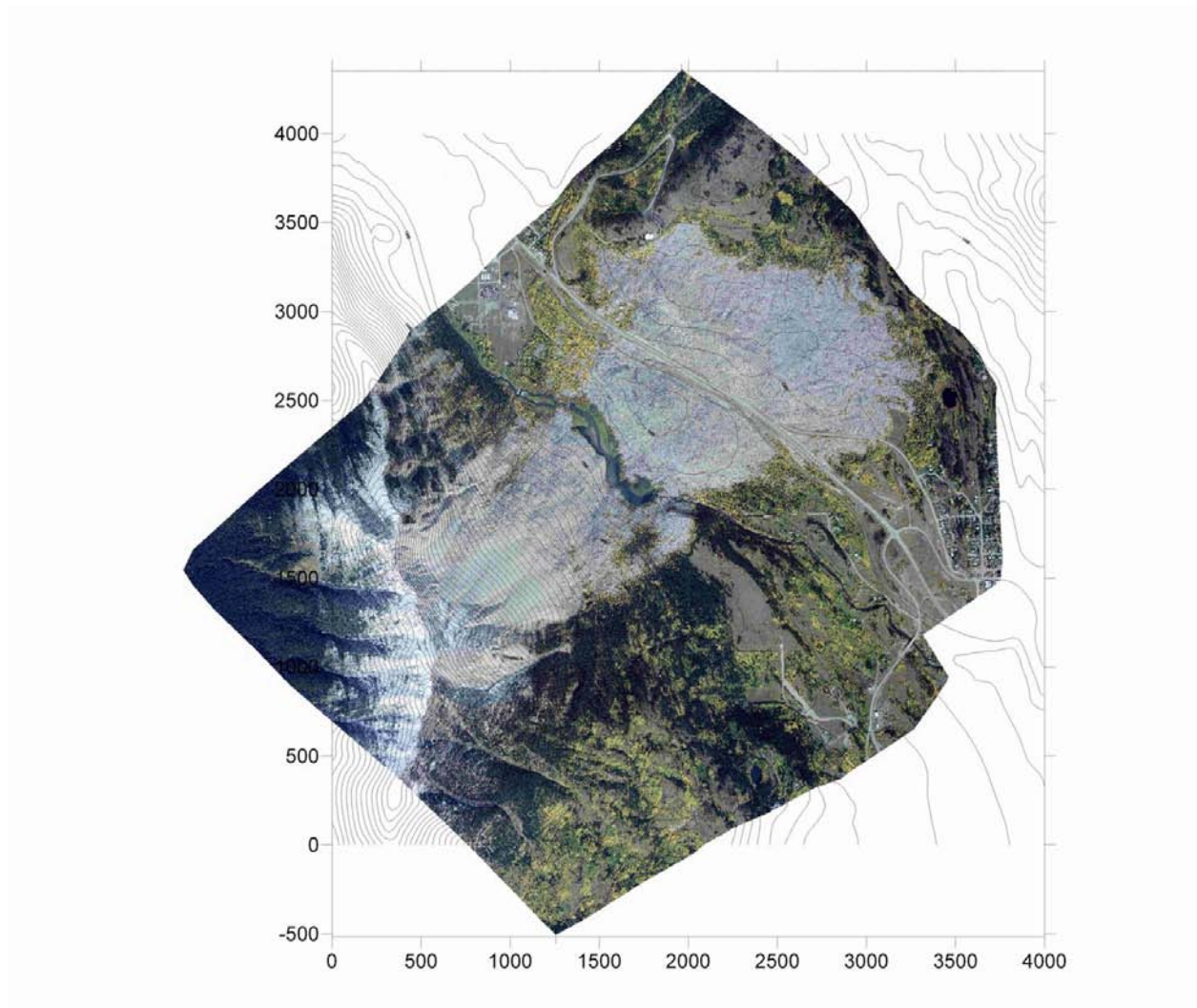


Fig.4.2 Orthophoto of the area provided to participants on the benchmark activity

4.2 Modelling and data files

Modellers were provided with (i) a digital terrain model describing the situation before landslide took place, based on historic photographs and maps, and (ii) a full topographical description of the sliding mass. The grid spacing was 20 m. in both x and y directions.

From the excel files provided describing both the topography and the avalanching mass, we have prepared two files, which have been named Frank.top and Frank.pts.

Concerning the former, **Frank.top**, its structure is very similar to that described in section 3.2.1. The file has 40401 points, spaced uniformly at 20 m. As before, we will not require properties depending on the terrain.

type of topography		
11		
Nr of Pts in DTM	representative grid spacing	
40401	20	
X coord	Y coord	Z coord
0,00	0,00	1.881,92
20,00	0,00	1.888,97
40,00	0,00	1.900,57
60,00	0,00	1.914,39
80,00	0,00	1.929,05
100,00	0,00	1.943,13
120,00	0,00	1.955,25
...		
3900,00	4000,00	1571,49
3920,00	4000,00	1574,17
3940,00	4000,00	1575,82
3960,00	4000,00	1577,26
3980,00	4000,00	1578,55
4000,00	4000,00	1579,32
Terrain dependent Properties		
0,00		

The initial mass of the avalanche is described in the file **Frank.pts**, which we reproduce below. The data structure used here is different from that of Tsing Shan debris flow, because we have been given the X and Y coordinates of a set of 1500 together with the avalanche depth at them. Note that we provide the factor characterizing the smoothing length for the points, which is 2. The value of the parameter **Soil unkno = 6**, and is given in file **Frank.dat**

npoin source	deltx	fact hsml
1500	20	2
X coordinate	Y coord.	avalanche depth h
800	1480	99,87
740	1260	99,81
880	1380	99,79
440	1580	99,71
440	1540	99,52
640	1680	99,22
...		

The SPH data is given in file **Frank.dat**, which we reproduce below. It is very similar in structure and contents to that used for the Tsing Shan debris flow, the only changes being highlighted in bold blue. Therefore, it is advisable to create this file from another, modifying the required data.

1

Frank slide

SW algorithm

0

nhist

0

ndimn

2

ic_soil	ic_water	ic_vps	ic_abs
1	0	0	0

Soil unkno **h_inf_SW**

6

0.1

Landslide File

Frank

sph algorithm	search neigh	h update	weigh f type
2	2	2	1

Dens.Algorithm	av_vel	virt_part	nor_dens
1	1	0	0

P1. gravity	P2 dens	P3 cmaning	P4 Erosion	P5 rheology	P6 Tauy0	P7 Visco K
9.8	2000.	0	0	7	0	0

P8 Mu	P9 tan(fi_inf)	P10 h_frict0	P11	P12 tan(FI_0)	P13 Bcons	P14
0	0,218	0,001	0	0,218	0	0

P15 h_comp
 0,001

K0 activated?

0

icpwp

0

coarse mesh saving utility?

0

control points?						
0						
output filter	1.hs	2.disp	3.v	4.Pw	5 eros	6..Z
	1	1	0	0	0	0
	7..hrel	8..hw	9..eta	10.. hs+hw	11 dummy	12...dummy
	0	0	0	0	0	0
T_change_to_W						
1.e+12						

Finally, the time stepping and other control data are given in file **Frank.MASTER.dat**, which we give below.

1		
Frank slide		
if_sph	if_gfl	if_tgf
1	0	0
SPH_problem_type	SPH_t_integ_Alg	
1	4	
sph problem name		
Frank slide		

BLOCK 1			
dt	time_end	maxtimesteps	
0.1	80.00	100000	
print_step	save_step	plot_step	
25	25	25	
dt_sph	ic_adapt		
0.1	1		
Ntime curves	max pts in them		
0	6		

FINAL BLOCK			
dt	time_end	maxtimesteps	
-1	2.00	100000	

4.3 Results

Concerning the results of the computations, (i) The final position agrees well, (ii) the width and length of the deposit are 1300 and 2000 m, to be compared to the measured values of 1700 and 2000 m. reported. Concerning the depth, we have obtained depths ranging from 0 to 28 m, which compare well with those reported. Computed propagation time is 80 s., of the order of magnitude reported by eye witnesses.

We provide in figure 4.1 a topographical map showing the landslide path and the position of the sliding mass, together with the computed final position of the nodes. Figure 4.2 provides the contours of depth in the deposit.

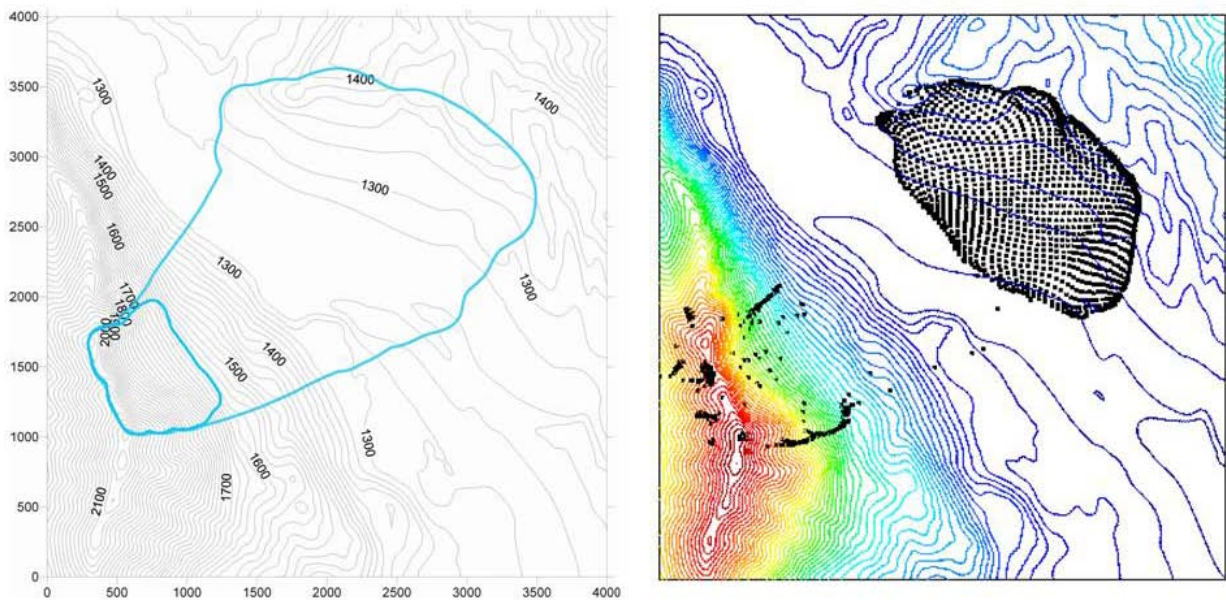


Figure 4.1. Frank Slide: Topography and landslide track (left), and final position of the SPH nodes (right)

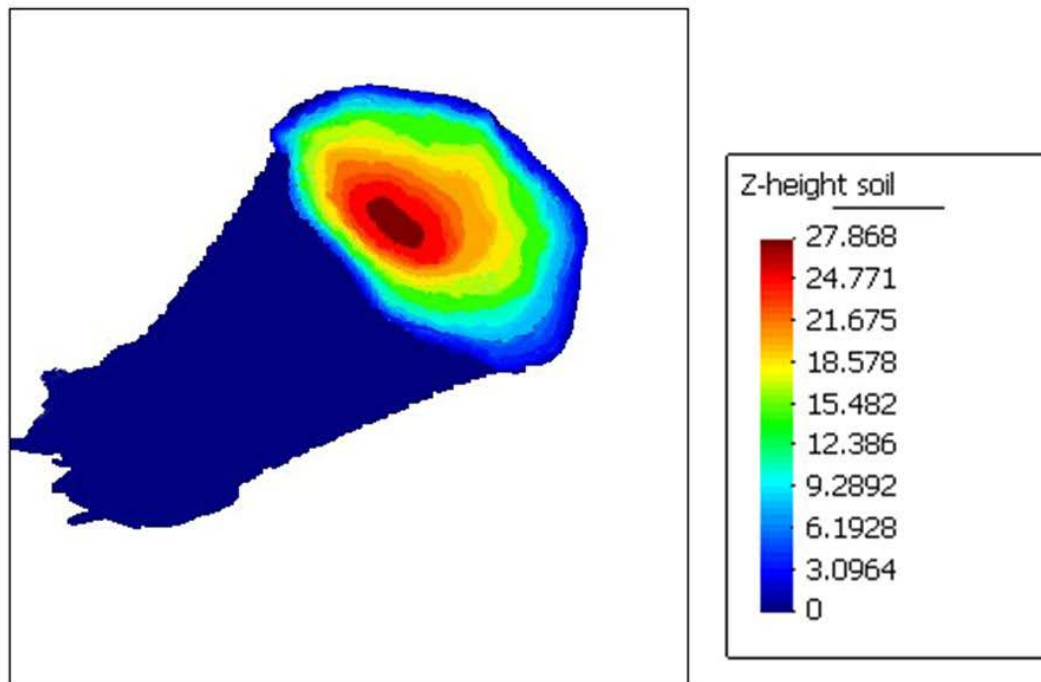


Figure 4.2. Frank Slide: Track of the rockslide (dark blue) and deposit depths

4.4 References

McConnell, R.G., and Brock, R.W., The great landslide at Frank, Alberta, in Annual Report for the year 1902–1903: Department of the Interior, Government of Canada Sessional Paper 25 (1904), p. 1–17.

Cruden, D.M. and Hungr, O., The debris of the Frank Slide and theories of rockslide-avalanche mobility. Canadian Journal of Earth Sciences, 23 (1986) 425-432.

5 THE TSING SHAN DEBRIS FLOW, HONG KONG (2000)

5.1 Description

the Tsing Shan debris flow which occurred in Hong Kong on the 14th April 2000. This analysis is based on the information found both in the package provided by Hong Kong Geotechnical Office and the report by King (2001).

This debris flow took place following rains which triggered more than 50 landslides in the area. The accumulated rainfall was 160 mm. The terrain was vegetated, and consisted of colluvial boulders. One important feature of this event is the strong erosion which made the initial mass to increase from 150 to 1600 cubic meters. Figure 5.1, taken from King (2001) provides two general views of the debris flow. One important aspect is the bifurcation of the flow which can be observed in the pictures.



Figure 5.1 : General view of the 2000 Tsing Shan debris flow. (King 2001)

5.2 Modelling and data files

The data files used for this analysis were:

- (i) TsingShan.top with the terrain data. This file has been commented in Section 3.2.1

We have selected a grid spacing of 5 m for the terrain model, which is that of the data provided to the participants by the Hong Kong Geotechnical Office. As we mentioned in the deliverable D.1.9, the results are very much sensitive to the this value. Indeed, if we had chosen a value of 10 m. the results would have been absolutely different, as no branching would have been predicted in the model. We suggest the reader repeats the test case, but using a grid spacing of 10 m. The results are given below in fig.5.3

(ii) TsingShan.MASTER.dat contains the time stepping and control data, see Section 3.2.2

(iii) TsingShan.dat contains the sph data, and it has been described in Section 3.2.3

(iv) TsingShan.pts provides a description of the source zone, see Section 3.2.4.

In order to model the materil of this debris flow, we have used a frictional fluid model, with $\tan \phi = 0.18$, zero cohesion and a coefficient of Voellmy's turbulent viscosity of 500 m/s².

We have chosen the Hungr's erosion model, using an erosion coefficient of $97e-4 \text{ m}^{-1}$.

Note that the erosion rate as $E_t = E_s h \bar{v}$ where E_s can be obtained directly from the initial and

final volumes of the material and the distance traveled as $E_s \approx \frac{\ln(V_{final}/V_0)}{\text{distance}}$.

5.3 Results

The results of the simulation are given in Figure 5.2 which provides information regarding both the position and depths of the final deposit and the track. One peculiarity of this debris flow is the bifurcation in two branches, which is a feature difficult to capture in simulations. The computed path depicted in figure 5.2 shows the branching. In figure 5.2, it can be seen that the deepest deposit was formed at the end of the lower south branch, with a maximum depth of 1.8 m. Regarding velocities, there is no available information. The model predicts a time of propagation close to 120 s. Considering that the runout was 900 m in the lowest branch, the average velocity is close to 30 km/h. The report provides a total mass deposited in the south branch of 500 cubic meters, while the computation provides a value of 525 cubic meters. Concerning the total volume of eroded soil, the report estimates it as 1600 cubic meters, while the computations provide a value of 1550.

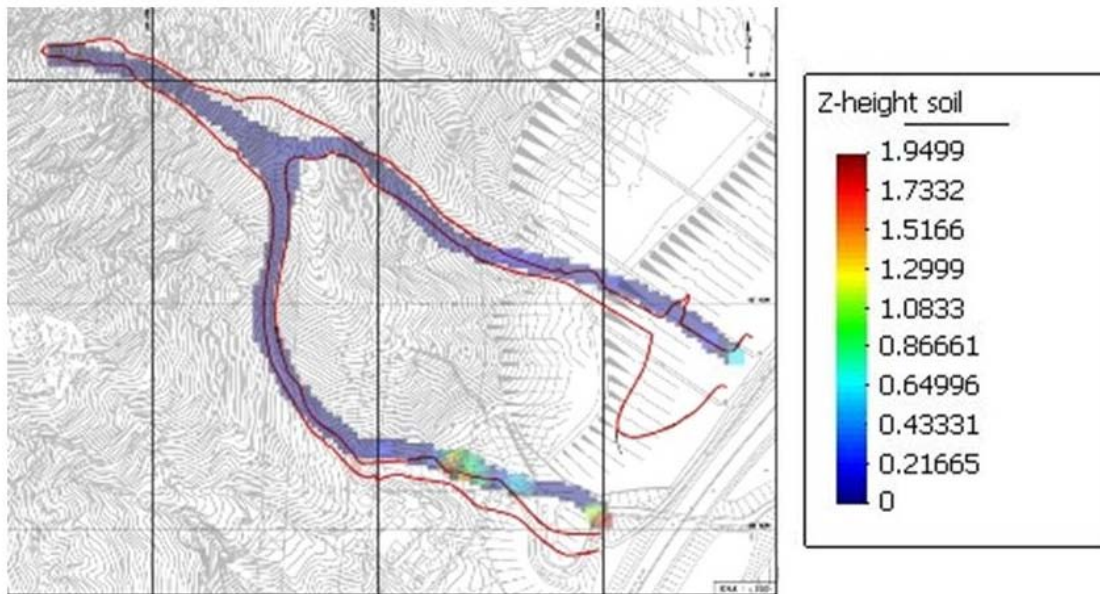


Fig 5.2 Tsing Shan debris flow: Model predictions vs. field observations.

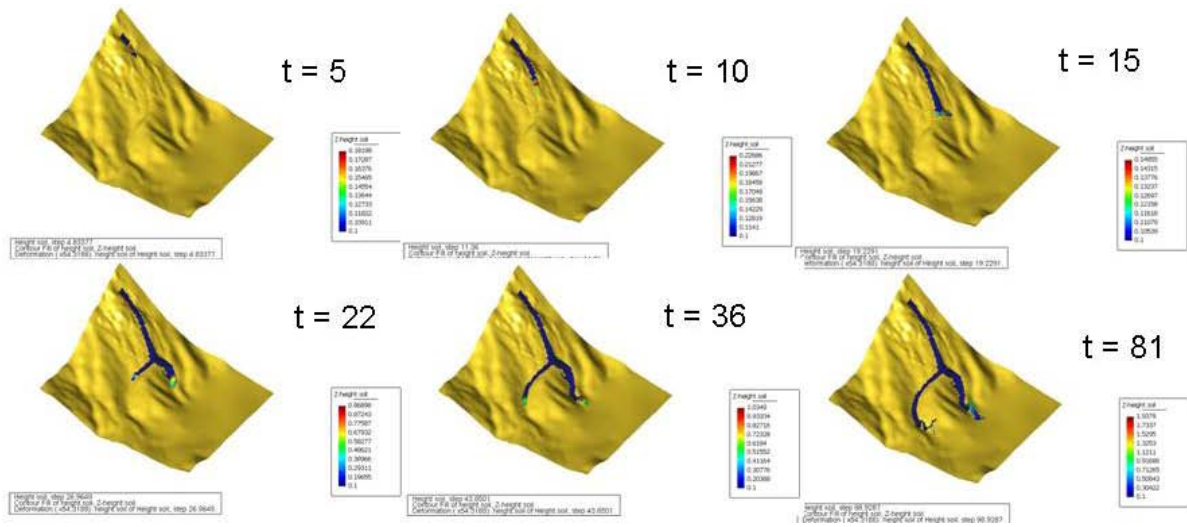


Fig.5.3 Perspective of the Tsing Shan debris flow of 200.

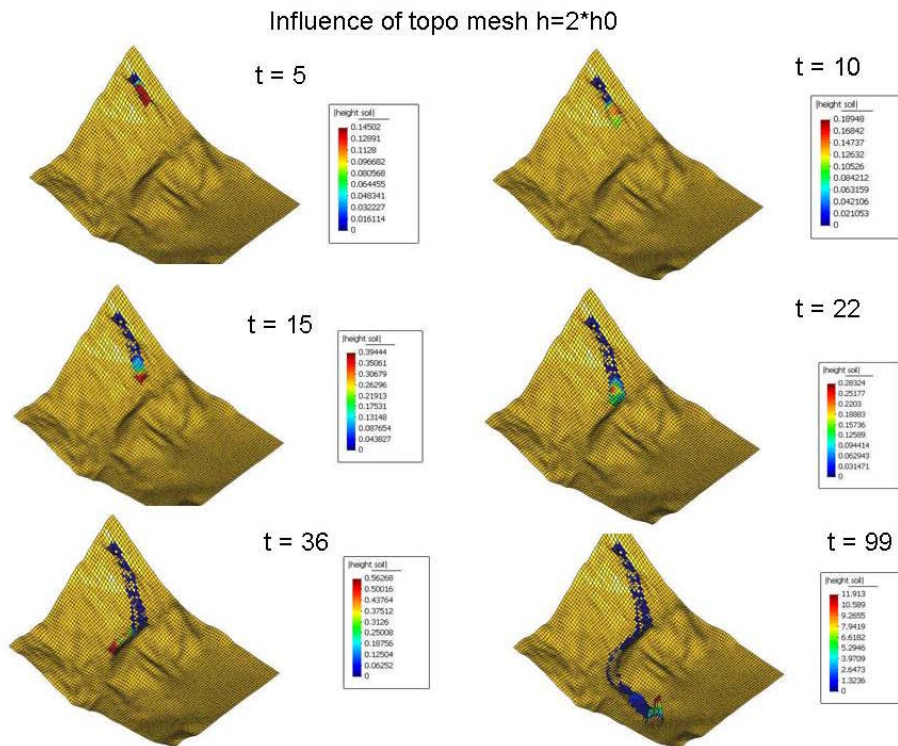


Fig. 5.4. Tsing Shan debris flow: Unrealistic model predictions vs. field observations with a grid spacing of 10 m.

5.4 References

King, J.P. (2001), The 2000 Tsing Shan Debris Flow, Report LSR 3/2001, Planning Division, Geotechnical Engineering Office, Civil Engineering and Development Department, The Government of the Hong Kong Special Administrative Region

6 RUNNING THE CODE

This Section is intended to provide information on the necessary steps to run the code. We will use the Frank slide case to illustrate it.

First of all, it is advisable to prepare a work directory where we will have:

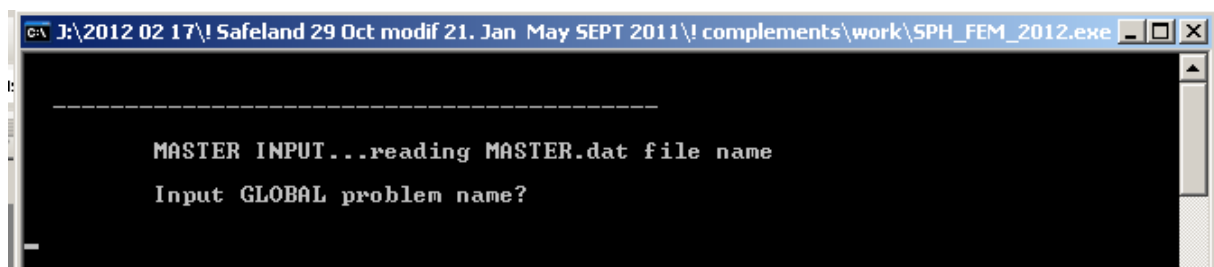
(i) The code: Geoflow_SPH.exe

(ii) The data files:

- Frank.dat
- Frank.MASTER.dat
- Frank.dat
- Frank.pts

All of them have been described above.

To run the code, we will type: Geoflow_SPH and then RETURN.
A new screen will appear.



```
C:\J:\2012 02 17\! Safeland 29 Oct modif 21. Jan May SEPT 2011\! complements\work\SPH_FEM_2012.exe
-----
MASTER INPUT...reading MASTER.dat file name
Input GLOBAL problem name?
```

where we will be required to input the name of the MASTER.dat file. Note that it is only the name that we have to provide, Frank in this case.

Then, the code provides some information and ask us to input the name of the terrain file, which is Frank as the data where we have the terrain data is Frank.top

```
-----  
MASTER INPUT...reading MASTER.dat file name  
Input GLOBAL problem name?  
Frank  
MASTER file name for data is Frank  
-----  
NOTICES  
-----  
** central integration routine removed  
** Added in RK4 and RKWir a call to a filtering routine...  
which avoids average velocity over nodes behind gates...  
Routine is get_npoin0_SW  
** Can use icadaptdt= 0, 1, 0r 2 v+c  
labs dimensioned to 1000  
routine check abs just to check, useless  
** Call to get Z which is in TOPO module  
ramp ONLY FOR AKNES FILE to avoid BCs in TOPO  
smoothing factor for slope in topo  
modified int forces to put in p(i) h*Z,i  
** NORMALIZED RHO also normalizes drho in con dens  
** RK10 changed for prescribed velocity - study drho  
we have introduced a new routine which substitutes con and sum density  
water is con and soil sum  
-----  
TOPO module  
Input the problem name <TOPO mesh> ?
```

It takes a bit of time for the code to prepare the topographical information which will be used by SPH.

Once it starts running, we will see the screen (we plot only the new information)

```
-----  
      TOPO module  
Input the problem name <TOPO mesh> ?  
Frank  
-----  
      SPH INPUT...reading file.dat name  
sph file name for data is   Frank  
-----  
.....  
Initial volume <SW> or mass = 2.9732808E+07  
.....
```

We are informed that code is reading the Frank.dat file, and gives us the initial volume of the landslide: 2.97 e07 cubic meters.

The code continues its output, which consists of blocks as:

```
.....  
Initial volume <SW> or mass = 2.9732808E+07  
.....  
statistics from sph main grid_find  
time= 2.697499      dt= 0.3681960  
max interactions= 55 at pic      1242  
min interactions= 13 at pic      1  
average 44.35476  
Total pairs : 0  
Pics w/o interaction: 0  
sph output  
time step_sph is 14 time_sph = 3.065695  
dt_sph= 0.3681960 MASS = 2.9732808E+07  
vtemp = 18.20655  
.....  
statistics from sph main grid_find  
time= 5.337295      dt= 0.3997418  
max interactions= 68 at pic      898  
min interactions= 7 at pic      3  
average 46.37773  
Total pairs : 0  
Pics w/o interaction: 0  
sph output  
time step_sph is 21 time_sph = 5.737037  
dt_sph= 0.3997418 MASS = 2.9732808E+07  
vtemp = 33.50607  
.....
```

The code stops, showing the screen

```
.....
statistics from sph main grid_find
time= 79.30830 dt= 0.7178546
max interactions= 90 at pic 1585
min interactions= 0 at pic 1
average 44.86797
Total pairs : 0
Pics w/o interaction: 96

program stopped OK
Fortran Pause - Enter command<CR> or <CR> to continue.
```

We type <CR> (Return, or Intro key), and the command window closes.

Examining the files which have been produced, we will find:

(a) Files of .chk type, which are used in case of input errors for debugging

(b) Topographical information files:

- Frank3d.flavia.bon and Frank3d.flavia.res
- Frank.flavia.dat and Frank.flavia.res

(c) Auxiliary output files:

- Frank.1.res Frank.2.res Frank.3.res

(d) The plotting files prepared for GID postprocessor:

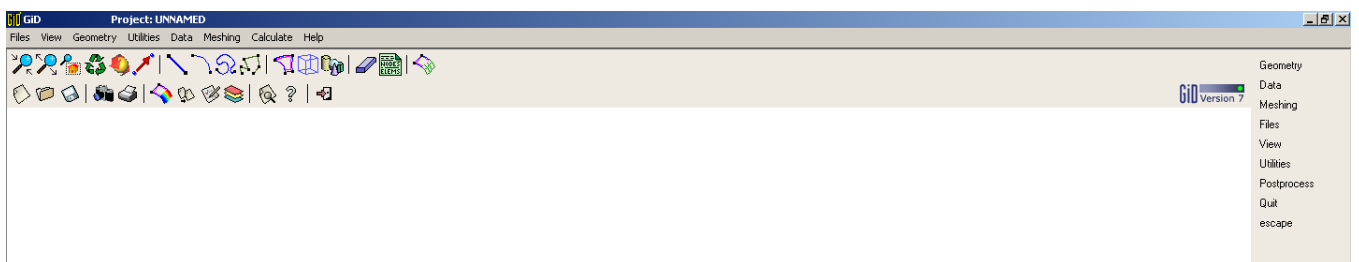
- Frank.post.msh and Frank.post.res

7 POSTPROCESS

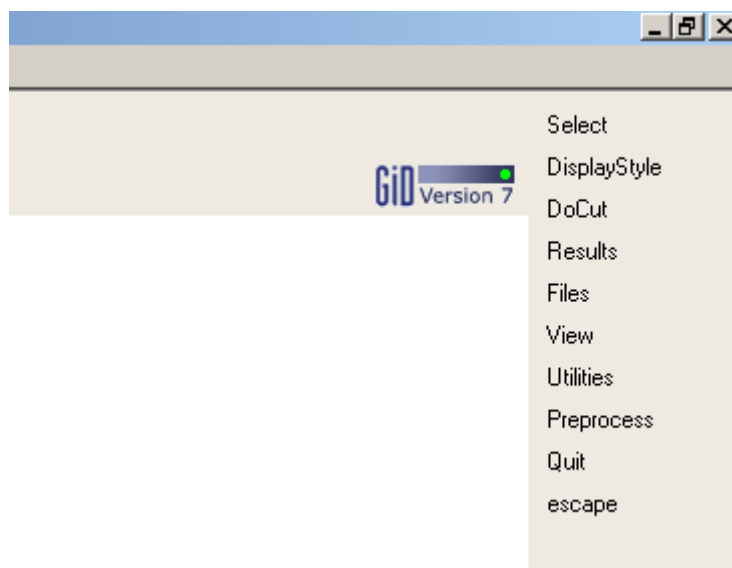
The code prepares output files which can be viewed with the GID Postprocessing software. GID can be obtained at CIMNE website <http://gid.cimne.upc.es/> , where both evaluation and educational versions can be downloaded.

The version we have used in this case is the 7th, the code being provided in the package. Note that in order to use it an evaluation licence has to be obtained.

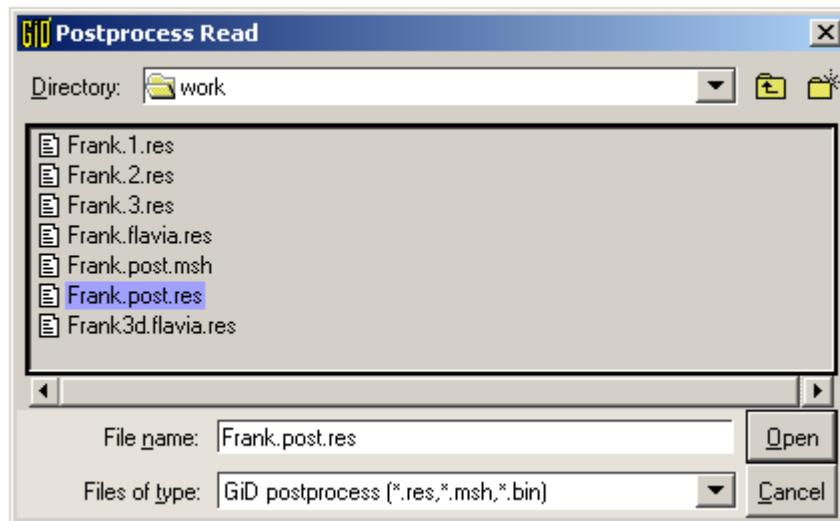
In order to run GID, we will click on GID icon. The initial screen depends on the version, but it will look like the following:



We will go to postprocess, clicking on the options toolbar located on the right,



Then, using the Files -> Read option, we will load Frank.post.res file



GiD will then read the output file, and we will be able to proceed with the analysis of the results.

We are aware that explaining all GiD options is out of the scope of this document. However, it is important to point out some useful hints.

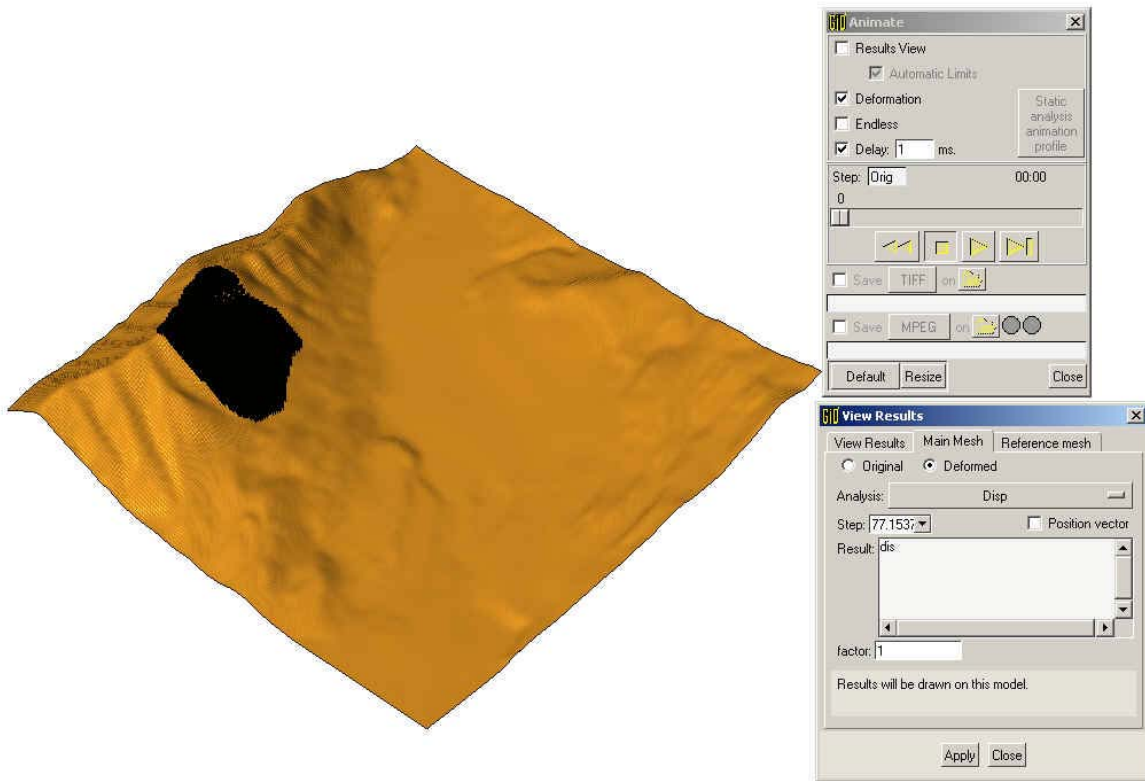
(i) When the topographic mesh is very dense, plotting of the results will be obscured by the mesh. It can be solved by choosing plotting of the results without mesh, which is done using the upper tool bar as illustrated below



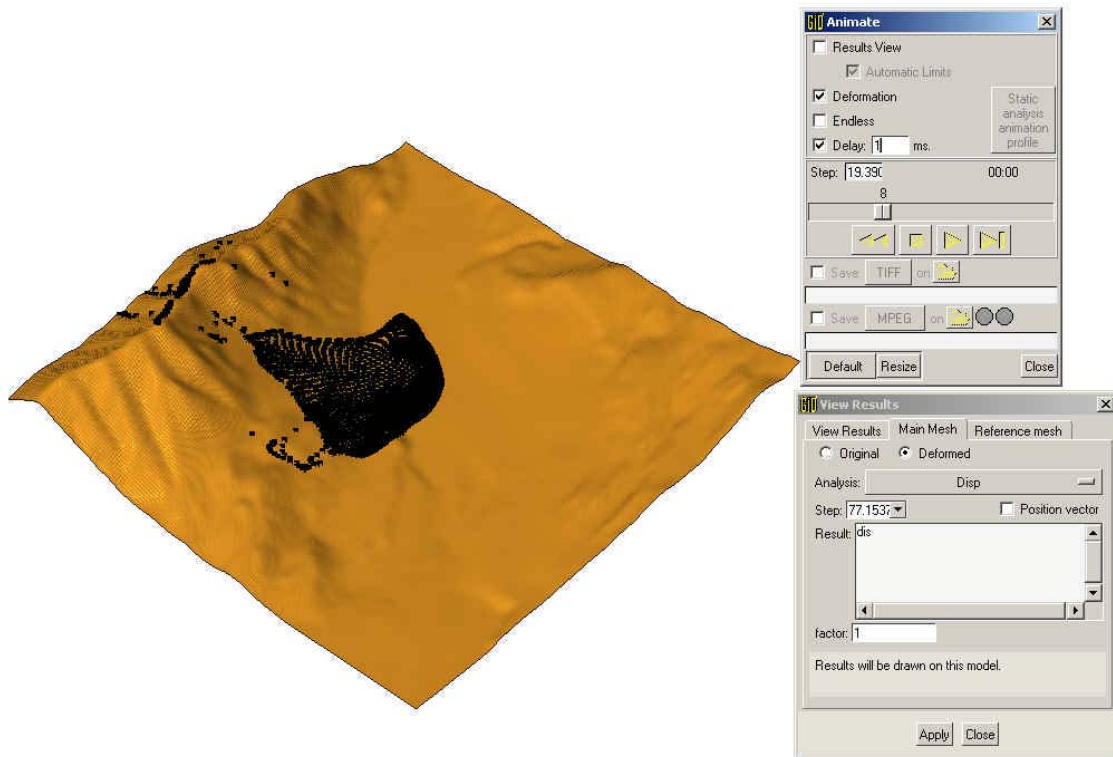
(ii) When preparing films, it is convenient to set to 1 ms the time between frames, otherwise the viewing time would be too long.

(iii) If we want to study the propagation of the landslide, we will select in the View Results window the main mesh submenu, then the "deformed" option, then "Disp" for displacements,

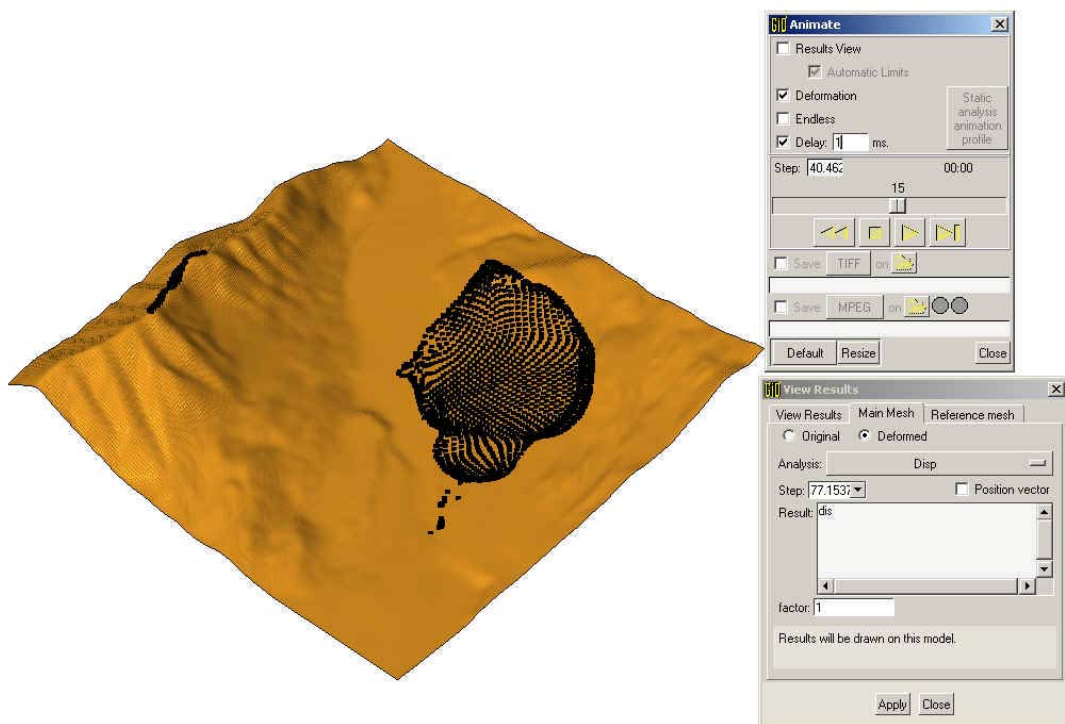
the deformation factor being 1. We illustrate the propagation of Frank slide in the next figures, which correspond to different times.



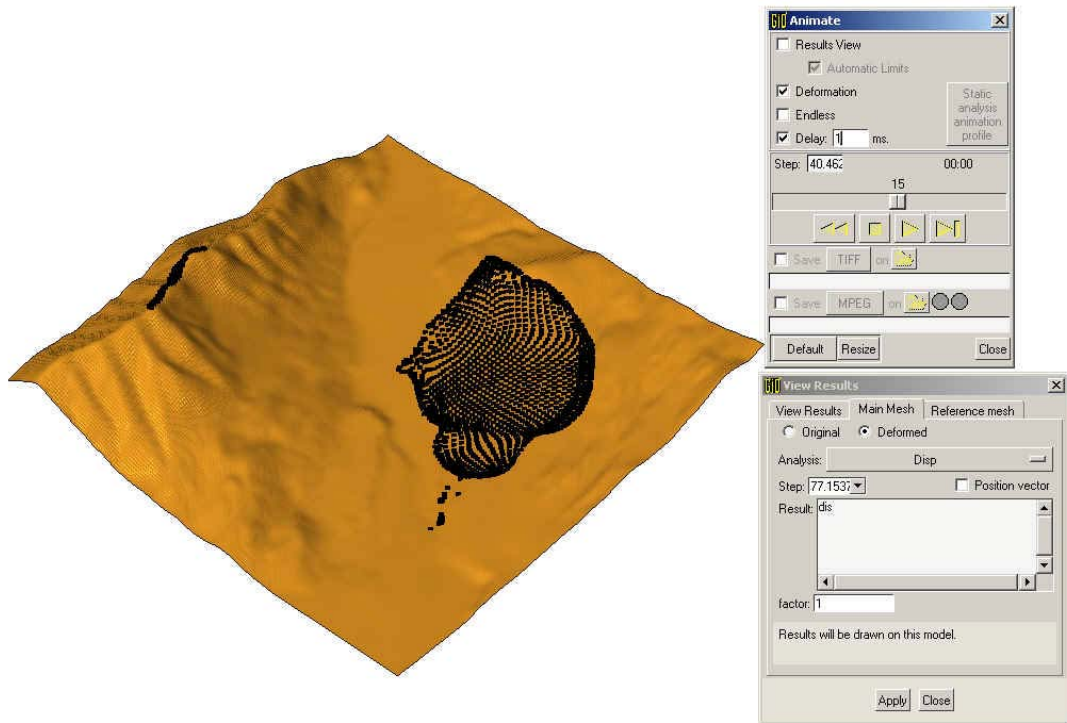
Propagation of Frank slide. (a) Position of SPH nodes at time $t = 0$ s.



Propagation of Frank slide. (b) Position of SPH nodes at time $t = 19.33$ s.



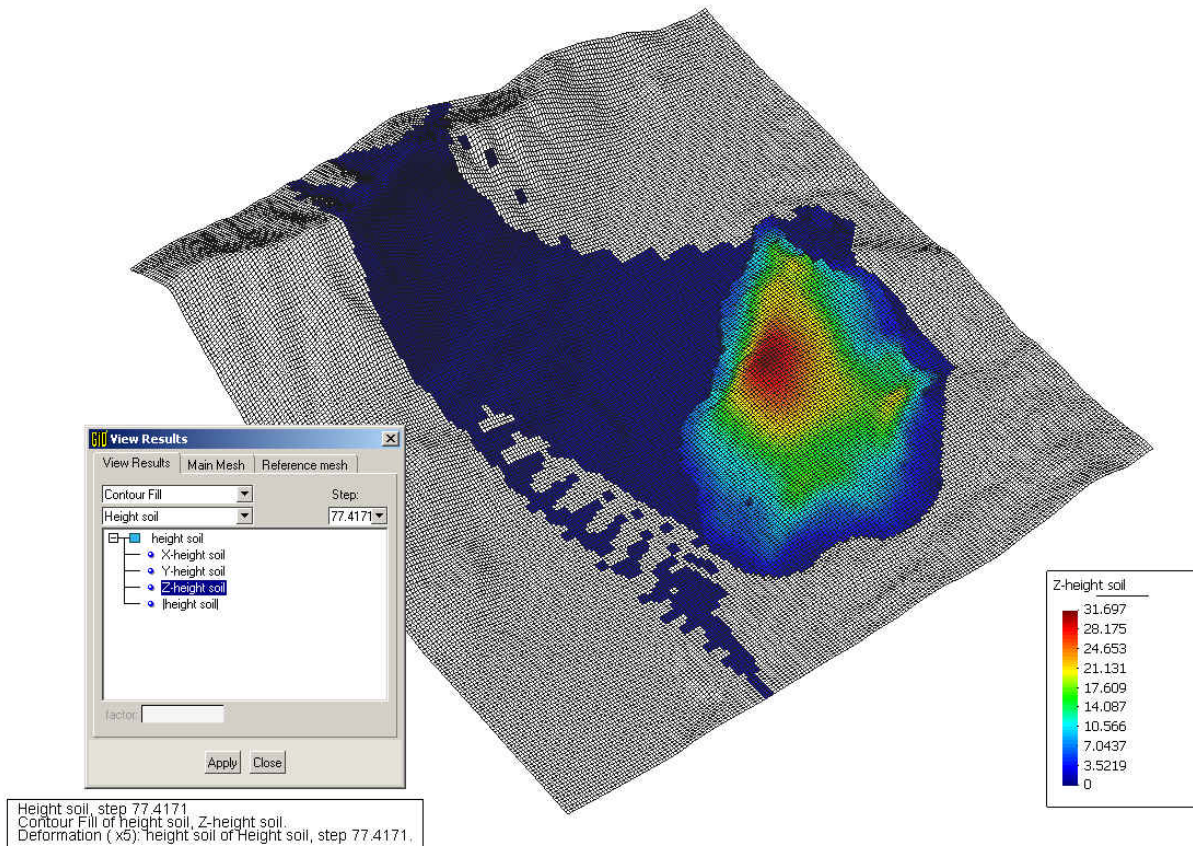
Propagation of Frank slide. (c) Position of SPH nodes at time $t = 40$ s.



Propagation of Frank slide. (d) Position of SPH nodes at time $t = 77$ s.

(iv) In order to view the depth of the landslide, we will select In the View Results tab the variable soil depth, then the "contour fill" option. A graphical scale will appear on the right.

(v) By default, the XY plot is presented. This perspective can be changed by clicking on the right bottom of the mouse, selecting "rotate", then "trackball". The figure is then rotated according to the mouse movements. To finish, hit the "ESC" key on the keyboard.



Propagation of Frank slide. (e) Landslide depths at $t = 77$ s.